Advances in Civil Engineering

Advances in Mine Backfill 2021

Lead Guest Editor: Lijie Guo
Guest Editors: Tingting Zhang, Qianqian Wang, and Qi Jia

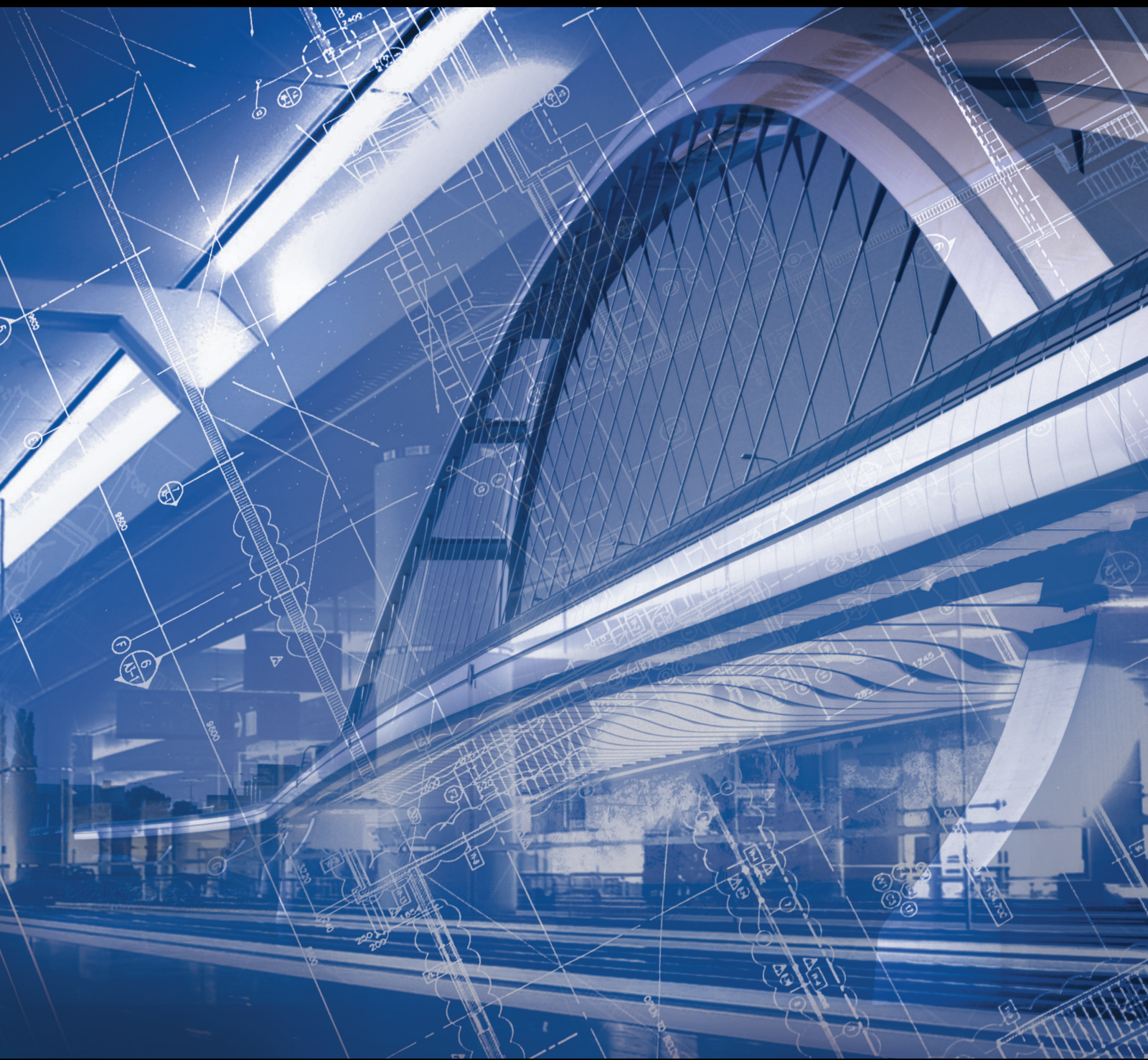

Advances in Mine Backfill 2021

Advances in Civil Engineering

Advances in Mine Backfill 2021

Lead Guest Editor: Lijie Guo
Guest Editors: Tingting Zhang, Qianqian Wang, and Qi Jia

Contents

Analysis of Crustal Stress and Its Influence on the Stability of the Deep Tunnel in the Huanaote Mining Area
Mingde Zhu, Yantian Yin, Chao Peng, Li Cheng, Yingjie Hao, Kuikui Hou, Haoqin Zhang, and Jie Zhang
Research Article (22 pages), Article ID 4077305, Volume 2022 (2022)

Study on Backfill Acoustic Emission Characteristics and Source Location under Uniaxial Compressive
Caixing Shi, Yicheng Wu, Lijie Guo, Yue Zhao, and Wenyuan Xu
Research Article (9 pages), Article ID 2706897, Volume 2022 (2022)

Hindawi
Advances in Civil Engineering
Volume 2022, Article ID 3934398, 10 pages
https://doi.org/10.1155/2022/3934398

Research Article

Distribution of In Situ Stress in Northwest Jiaodong Peninsula

Xingquan Liu,[1,2] **Huanxin Liu**,[1,2] **Chao Peng**,[1,2] **Xi Wang**,[1,2] **Yuyun Fan**,[1,2] **Mingwei Jiang**,[1,2] **and Yantian Yin**[1,2]

[1]*Deep Mining Laboratory of Shandong Gold Group Co. Ltd, Laizhou 261442, China*
[2]*Shandong Key Laboratory of Deep-Sea and Deep-Earth Metallic Mineral Intelligent Mining, Laizhou 261442, China*

Correspondence should be addressed to Huanxin Liu; ssdxmb@163.com

Received 17 December 2021; Revised 18 May 2022; Accepted 29 August 2022; Published 26 September 2022

Academic Editor: Qi Jia

In order to study the present state of the tectonic stress field in northwest Jiaodong Peninsula, the characteristics of the ground stress distribution along depth were analyzed with the method of regression analysis. A total of 164 items of in situ stress measurement data were collected. There are mainly two types of in situ stress states, one is $\sigma_H > \sigma_h > \sigma_v$ and the other is $\sigma_> \sigma_v > \sigma_h$, and the type of in situ stress state is related to the depth. The principal stresses σ_H, σ_h, and σ_v increase approximately linearly with depth, and the stress gradients are 0.0556, 0.0248, and 0.0346, respectively. The lateral pressure coefficients *K*H, *K*h, and *K*av vary approximately hyperbolically with the increase in depth and approach 1.99, 1.12, and 1.56, respectively. The ratio of half of the maximum horizontal differential stress to the average horizontal principal stress μ_d varies linearly with the increase of depth and approaches the value of 0.33. The maximum shear stress τ_m increases approximately linearly with depth, and the stress gradients are 0.0146. The ratio of horizontal principal stress difference with vertical stress on 1000 m–2000 m is 0.5– 0.7. In addition, the maximum level of principal stress advantage direction in the northwest Jiaodong Peninsula is nearly E–W.

1. Introduction

In situ stress is the natural stress existing in the crust undisturbed by engineering, also known as the initial stress of rock mass, absolute stress, or original rock stress. The in situ stress state is an important index to characterize engineering geological disasters, earthquake preparation, and mine safety construction. The study of in situ stress measurement and its distribution characteristics is a basic and very important work in the process of underground engineering construction. The measured data of in situ stress can not only directly reflect the characteristics of the regional in situ stress field but also help to explain the problems of fault activity, crustal movement, and the dynamic source of plate evolution. The northwest Jiaodong Peninsula is located in the easternmost part of Shandong Province, which is the third largest gold-producing region in the world. The complex geological structure of the area is not conducive to mining activities. Despite the particular importance of in situ stress measurement in this area, it is still vacant. The distribution law of regional in situ stress is the foundation for underground engineering construction. Scholars have carried out many studies on regional in situ stress. Sandiford et al., respectively, conducted in situ stress studies in Southeast Australia, Japan Island, South Africa, and the Qinshui Basin [1–4]. After the in situ stress measurement method was introduced in China, many earthquake-prone areas and resource-intensive areas have carried out a lot of work. Many scholars have also studied the local stress field characteristics in the Shandong area. Zheng [5] carried out in situ stress measurements near the coast of the southern Bohai Sea. Liu [6] measured the in situ stress of the sea working face of Beizao mine. Cai and Qiao measured gold mines such as Sanshandao [7, 8]. But in the Jiaodong Peninsula, especially in the northwest Jiaodong Peninsula where rare metal resources are enriched, the in situ stress characteristics are still blank. In order to fully grasp the distribution characteristics of the in situ stress field in the northwest Jiaodong Peninsula, the distribution characteristics of the in situ stress field in this area were analyzed based on the in situ stress

measurement data of the author and others for many years. In particular, the data from the Sanshandao gold mine, Linglong gold mine, and Xincheng gold mine provide important support for this paper. The research results fill the gaps in the characteristics of in situ stress in the Jiaodong Peninsula and provide reliable data for mine engineering construction, tunnel construction, and the study of earthquake focal mechanisms in the area.

2. Geological Tectonic Environment in the Northwest of Jiaodong Peninsula

Shandong is located in the east of the north China block, in the Jiaodong Peninsula between the Bohai Sea and the Huanghai Sea, and is affected by the joint push of the Pacific plate and the Philippine plate. There were a long evolutionary history and complex geological tectonic environment in the area, including the stable ancient land block of the Archean, the Paleozoic Proterozoic activity zone, and the stable Paleozoic land surface sea deposition in Claratong [9]. The NNE-trending and NE-trending faults are the main faults in the northwestern Jiaodong Peninsula. NE-trending faults have the characteristics of right-lateral strike-slip and mainly exhibit compressive-torsional activities including the Yishu fault zone (NNE-trending) and the Zhaoping fault zone (NE-trending). Figure 1 shows the basic pattern of active fracture structures in Shandong Province, some of which are still active at the present stage [11, 12]. These faults have an obvious control effect on the regional formation, tectonic movement, magmatic activity, and mineral distribution.

The Shandong section of the Tanlu fault zone runs between western Shandong, Jiaodong plots, and the Sulu super high voltage metamorphic zone, the fracture zone extending about 360 km towards N(10°~25°)E. Affected by the Tanlu fault belt, the geological environment of the northwest Jiaodong Peninsula and the south Bohai Sea area is more complex. However, this area is an important mineral resource area in China, especially for rare and precious metals. The Jiaodong Peninsula is located at the intersection of mainland East Asia and the western Pacific plate. It is a tectonic shear belt related to the East Asian mainland and the western Pacific activity belt. It is controlled by the regional counterclockwise torsional stress field, forming an active region of the Neocathaysian system. The geotectonic is located in the Jiaodong uplift area of the second uplift zone of the giant tectonic zone of the Neocathaysian system, adjacent to the Tanlu fault zone in the west, the Bohai Bay Basin in the north, the Pacific plate in the east, and the Dabieshan-Sulu super high voltage metamorphic zone in the south [13, 14]. Multistage tectonic magmatic activity in the Jiaodong region has developed a crisscross complex tectonic network. The base structure in the area is a Qixia anticlinorium and fracture structure composed of Precambrian formation, and its tectonic line direction is near the EW direction. Controlled by the collision orogenic and subduction region structural stress field, the fracture structure system is dominated by NE and NNE to the fracture structure. There are 7 fault zones in the region, in turn from west to east, namely, Sanshandao-Cangshang fault, Xincheng-Jiaojia fault, Zhaoyuan-Pingdu fault, Qixia fault, Muping–Jimo fault, Jinniu Mountain fault, and Mishan fault. The first four are in the west of Jiaodong, and the overall trend is in the NE direction. The latter two are located in the eastern part of Jiaodong and generally move towards the near-SN direction. The Muping–Jimo fault is in the junction zone, which is a boundary fault and generally towards the NE direction [15].

3. Source and Cause of In Situ Stress in the Northwest of Jiaodong Peninsula

In situ stress is a general term for stress within the Earth, which is the distribution of in situ stress within a spatial range [16–20]. The formation of in situ stress is mainly related to various dynamic processes of the Earth. The geological activities in the northwest Jiaodong Peninsula are frequent and the geological conditions are very special, which makes the source of regional in situ stress more complicated. But long after in situ stress was proposed, it was widely believed to be only related to overburden weight. Until 1950s, Hast proposed that the in situ stress is not only the vertical stress formed by the overlying strata but also the horizontal stress caused by tectonic stress [21]. For the first time in the tunnel, we proposed that the horizontal stress is much greater than the vertical principal stress, and it was gradually recognized that the tectonic movement is a major factor in forming the in situ stress [22–24]. A number of studies have found that influenced by the collision and extrusion of the Indian plate and the Eurasian plate, the distribution of the maximum principal stress in China is obviously regular. Ma [25] according to the unity and stability of the principal stress direction and the relation of three principal stresses with depth, with the obvious turning area and the principal stress value or stress gradient as the boundary, the crust stress area is divided (Figure 2).

The northwest Jiaodong Peninsula is on the eastern coast of China. This region is a complex of geological records formed in important geological periods, which are preserved by ancient plots after multistage insertion, superimposition, and denudation, with a variety of structural combinations and styles [26–29]. The basic structural frame appears in the basin ridge, from north to south, Longkou Basin, Jiaobei uplift, and Jiaolai Basin. This structural pattern is the response to the Mesozoic mantle uplift and the lithosphere thinning in the crust. During the T3-K1 period, the region with a tectonic extrusion-extension effect was obvious [30], and the extrusion-extension model of the accordion structure in the Jiaodong area was formed.

After a large number of field investigations and experimental studies, the main tectonic activities of the Jiaodong Peninsula were divided into four periods. Stress characteristics are characterized by extrusion and extension interaction [31, 32]. The first period is mainly extrusion, which can be divided into two stages: NW-SE in the early stage and near S-N in the late stage. ① Early stage near NW-SE extrusion, forming the left-line translation fault in the NNE-SSW direction. ② Late stage near S-N extrusion, mainly

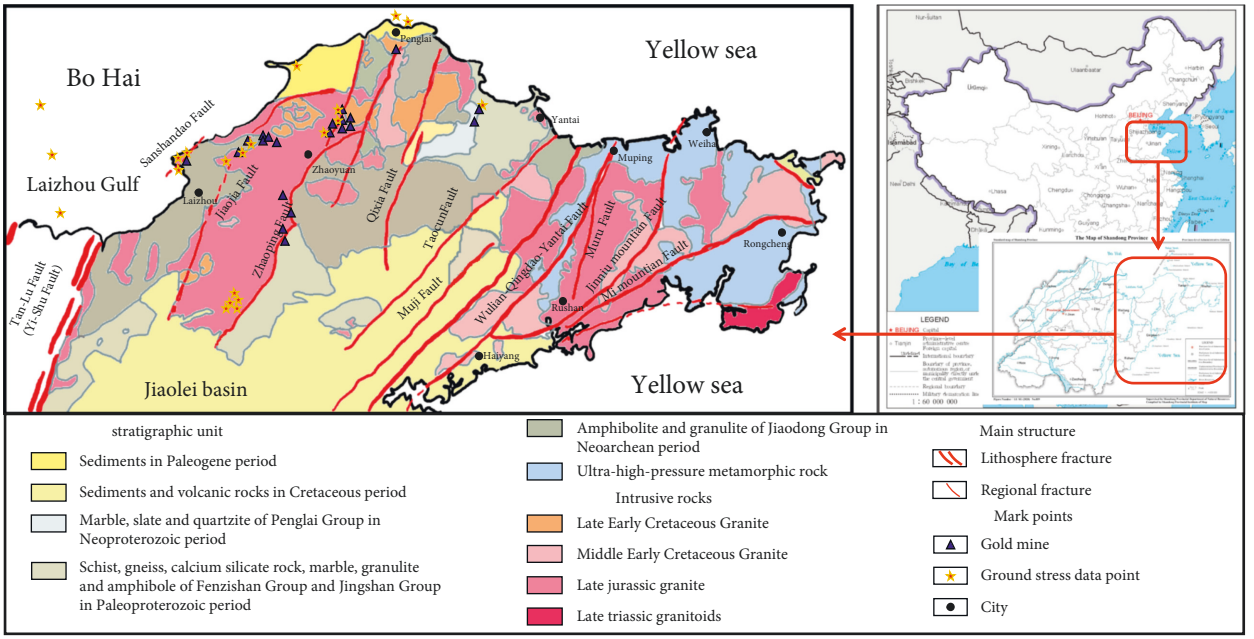

Figure 1: Outline diagram of the new structure in Shandong Province [10].

Figure 2: Current in situ stress zoning in China [25].

forming associated NWW-SEE dextral strike-slip faults and nearly S-N dextral strike-slip faults [33, 34]. The second period shows the transformation from NE-SW extrusion to NE-SW extension, which is reflected by the main positive fault in the Zhaoyuan-Pingdu fault band. The third period shows NW extension. The fourth period is near-E-W extrusion and near-S-N extension, and the NE direction fault in the region is mainly the right translation motion. In the field observation, a large number of E-W structures can be seen in the early stages of the extrusion structure. From the late Jurassic to the early Cretaceous period, Jiaodong plot shows the tectonic mechanical properties from extrusion to extension periodicity, the periodic change constantly changing and adjusting the stress field in the area [35, 36].

Through statistical analysis of the dominant direction of the maximum horizontal principal stress in the Jiaodong block, combined with the existing research results, it is found that the dominant direction of the maximum horizontal principal stress in the region is the NEE-SWW direction (consistent with the focal mechanism solution [37–39]).

4. The Law of In Situ Stress Distribution in the Northwest Jiaodong Peninsula

There are many places similar to the characteristics of seismic activity in the Shandong and North China blocks, among which the seismic activity of the two has a relatively significant correspondence in time [11]. However, due to the existence of the Tanlu fault zone, the Shandong region has its own particularity. Especially in the Jiaodong region, the difference between this region and the western Shandong region not only exists in stratum distribution but also in in situ stress. The following will be analyzed for the in situ stress distribution law in the northwest Jiaodong Peninsula.

4.1. Type Laws of In Situ Stress Field Distribution. Through the collection and measurement of data from the oil field, mine, geophysical research, and meteorological research, 164 items of in situ stress measurement data (depth from 4.7 m to 2300 m) were obtained by hydraulic fracturing methods and stress relief methods, as shown in Figure 3. The maximum horizontal principal stress in each group is greater than the vertical principal stress. It can be seen that the horizontal stress in the northwest Jiaodong Peninsula is dominant within the measurement depth, belonging to the typical structural stress field type. Among these, the magnitude relationship of three principal stresses in 40 groups was $\sigma_H > \sigma_h > \sigma_v$. Accounting for 24.4% of the total groups, they belong to the inverse fracture stress state, which is conducive to the gestation and activity of the inverse fault. The magnitude relationship of the three principal stresses in the remaining 124 groups is $\sigma_H > \sigma_v > \sigma_h$, accounting for 75.6% of the total number of groups, belongs to the slip stress state, and is conducive to the breeding and activity of the slip fault.

After analyzing the data by using the mathematical statistical analysis method, it is also found that when the depth is less than 300 m, the reverse-fault stress state dominates. In the depth range of 300 ~ 450 m, the distribution of the reverse fracture stress state is roughly equal to that of the strike-slip stress state. When the depth exceeds 450 m, the stress state is mainly a striking slip. It can be seen with the increase of depth that the vertical principal stress gradually changes from the minimum principal stress to the intermediate principal stress, and the stress state type gradually changes from the $\sigma_H > \sigma_h > \sigma_v$ to the $\sigma_H > \sigma_v > \sigma_h$.

4.2. The Variation Laws of Principal Stress with Depth. Since the vertical stress in the hydraulic fracturing data is estimated by the weight of the upper rock layer, only the data from the stress relief method are used to analyze the laws of vertical principal stress with depth. The relationship between the maximum horizontal principal stress, the minimum horizontal principal stress, and the vertical principal stress with depth is fitted by linear. The results are as follows:

$$\sigma_H = 0.0556H - 0.7772\,(\mathrm{R2} = 0.7924), \tag{1}$$

$$\sigma_v = 0.0346H - 1.6137\,(\mathrm{R2} = 0.9043), \tag{2}$$

$$\sigma_h = 0.0248H + 1.0504\,(\mathrm{R2} = 0.8319). \tag{3}$$

In the formula, H is the depth (m) and R is the correlation coefficient. The variation laws of principal stress with depth are shown in Figure 4. Due to the different aspects of geological conditions, topography, and rock properties, there is some dispersion of in situ stress measurement data. Equations (1)–(3) show that the correlation coefficient R2 of the three principal stress fitting equations is approximately greater than 0.8, with a high degree of linear correlation, indicates the approximate linear growth of in situ stress with the increase of depth, and also reflects the obvious change of the growth law of in situ stress from the depth range of meters to a few kilometers.

4.3. The Varies Laws Lateral Pressure Coefficient with the Depth. The lateral pressure coefficients are also widely used to characterize the in situ stress states at a point underground. Based on the ratio of σ_H, σ_h, $(\sigma_H + \sigma_h)/2$ with σ_v (collectively referred to the lateral pressure coefficient), the variation of in situ stress state with depth in the northwestern Jiaodong Peninsula is analyzed, which is denoted as KH, Kh, and Kav, respectively. The equations (4)–(6) of the three lateral pressure coefficients in hyperbolic form ($K = a/H +$, where a, b is the regression coefficient) are as follows:

$$K_{\mathrm{H}} = \frac{573.07}{H} + 0.2819, \tag{4}$$

$$K_h = \frac{397.32}{H} - 0.00283, \tag{5}$$

$$K_{\mathrm{av}} = \frac{379.47}{H} + 0.2069. \tag{6}$$

Figure 5 shows the distribution and fitting curves of the three lateral pressure coefficients with depth. As can be seen

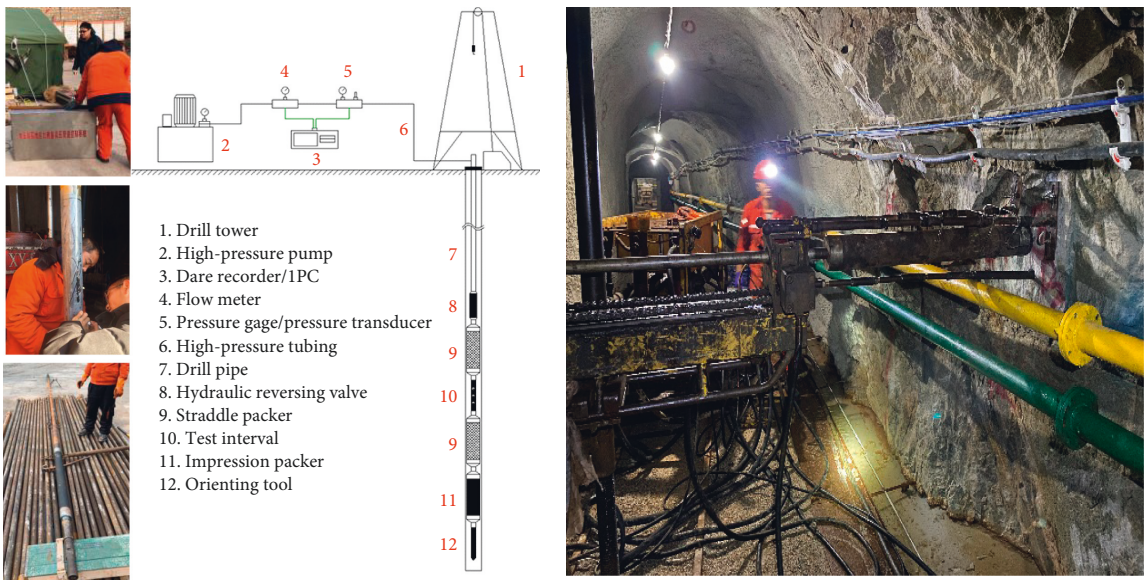

Figure 3: In situ stress measurement work. (a) Hydraulic fracturing method; (b) stress relief method.

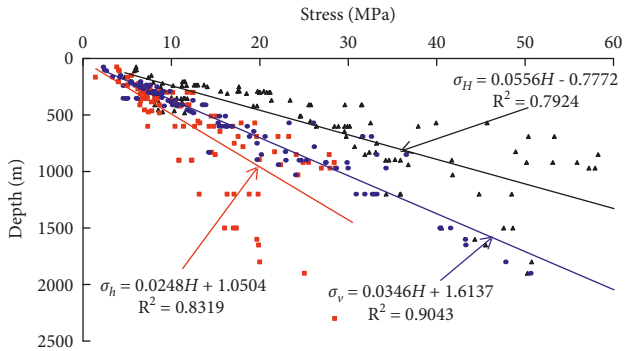

Figure 4: Variation of principal stress with depth.

from the figure, the distribution laws of K_H, K_h, and K_{av} are relatively discrete. The value of K_H is 0.68 to 4.76, average 1.99, the value of K_h is 0.39 to 2.91, average 1.12, and the value of K_{av} is 0.61 to 3.69, average 1.56.

Overall, both the dispersion and values of the three lateral pressure coefficients tended to decrease with increasing depth, whose changes were nonlinear. The results show that the three lateral pressure coefficients will likely tend towards a stable value with increasing depth. When $H < 1000$ m, the value of K_H is mostly greater than 2. When $1000 < H < 3500$ m, the range of K_H from 1.2 to 2.0 and the range of K_h from 0.5 to 1.0 are consistent with previous studies [40]. It can therefore be seen that in the shallow, tectonic stress is dominant, and as the depth increases, the in situ stress state gradually changes from the tectonic stress dominant state in the shallow part to the deep near hydrostatic pressure state.

4.4. The Variation Law of Relative Magnitude of Horizontal Differential Stress with Depth. The relative size of the horizontal difference stress μ_d ($\mu_d = (\sigma_H - \sigma_h)/(\sigma_H + \sigma_h)$) is a parameter related to the crust destruction state, which indicates the relative size of the maximum shear stress in the horizontal surface, which can reflect the crust shear stress state in the region to a certain extent. It is reasonable as the mechanical basis for judging the active fracture instability sliding. It can help better understand the characteristics of the tectonic stress field within the region. The results are as follows:

$$\mu_d = \frac{536.58}{H} - 0.0389. \quad (7)$$

Figure 6 shows the distribution law of μ_d with depth. As can be seen from Figure 5, the distribution is relatively discrete. The range is 0.09 ~ 0.65, with an average value of 0.33, mainly concentrated in the range of 0.09 ~ 0.49. The range of value is 0.34 ~ 0.52 in the depths greater than 1500 m, with an average of 0.41. The range of value is 0.09 ~ 0.65 in the depth range of 0 ~ 1500 m, with an average of 0.32. It can be seen that the fluctuation range of the value less than 1500 m is larger, and the fluctuation range of the value gradually decreases with the increase in depth. Relevant research [41] shows that if the value in the crust exceeds 0.5 ~ 0.7, shear sliding failure may occur. Except for some data points, the value of the northwest Jiaodong Peninsula is basically 0.1~0.5. It can be inferred that under the current in situ stress state, the possibility of shear sliding failure of the faults in the region is small most of the time.

4.5. The Variation Law of Ratio of Horizontal Principal Stress Difference with Vertical Stress with Depth. The horizontal principal stress difference determines the shear stress in the rock mass. The relationship between the ratio of principal stress difference and vertical stress and depth is shown in

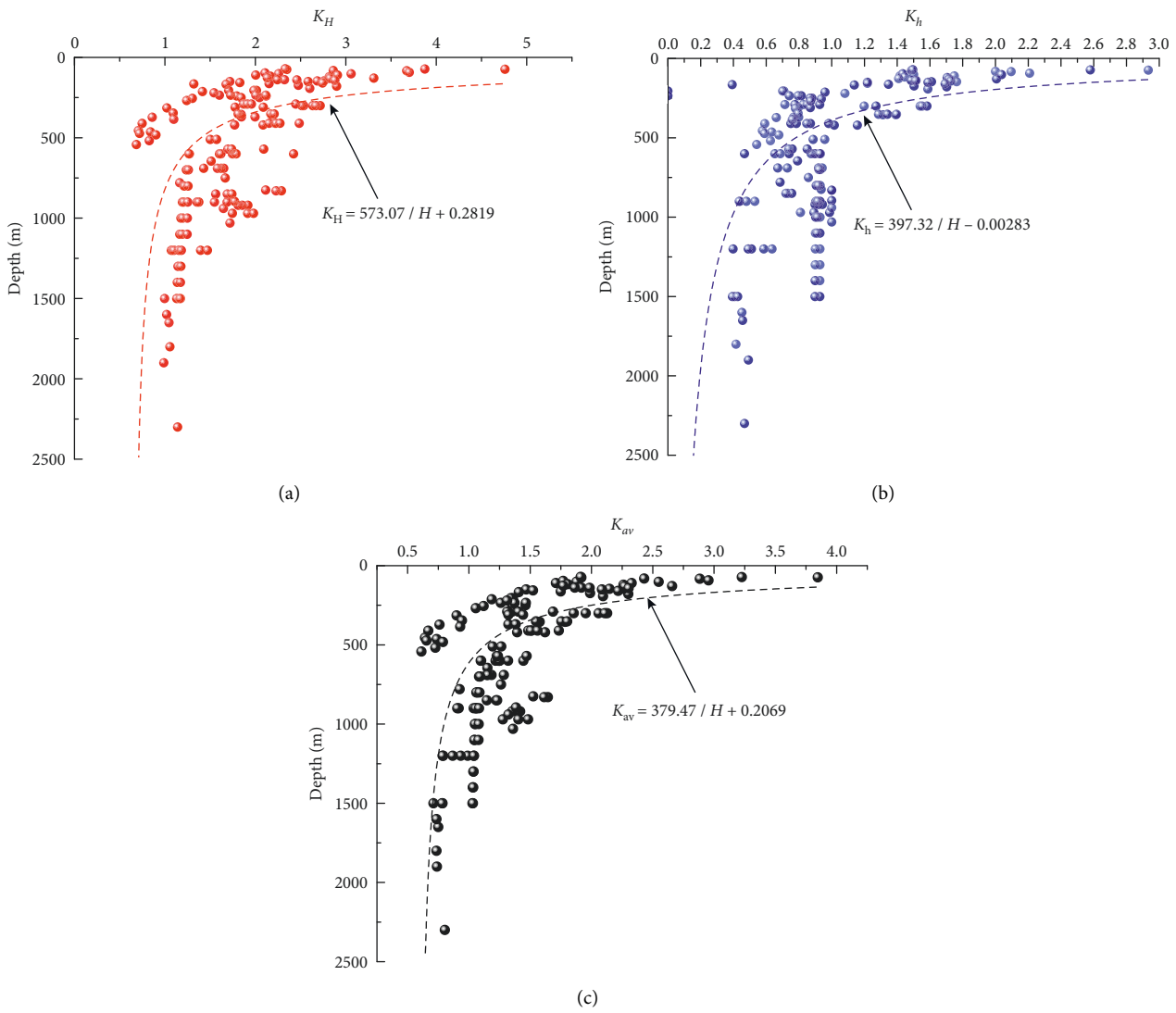

Figure 5: Distribution laws of lateral pressure coefficient with depth and fitting curve. (a–c) Maximum, minimum, and average horizontal lateral pressure coefficients with the depth, respectively.

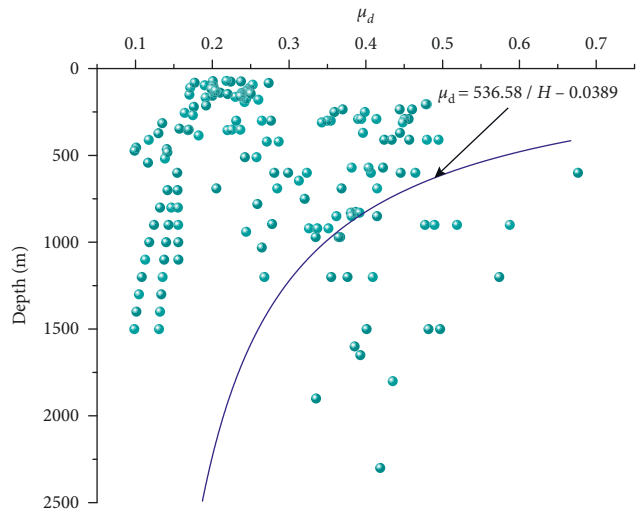

Figure 6: Relative magnitude of horizontal differential stress versus depth distribution and fitting curve.

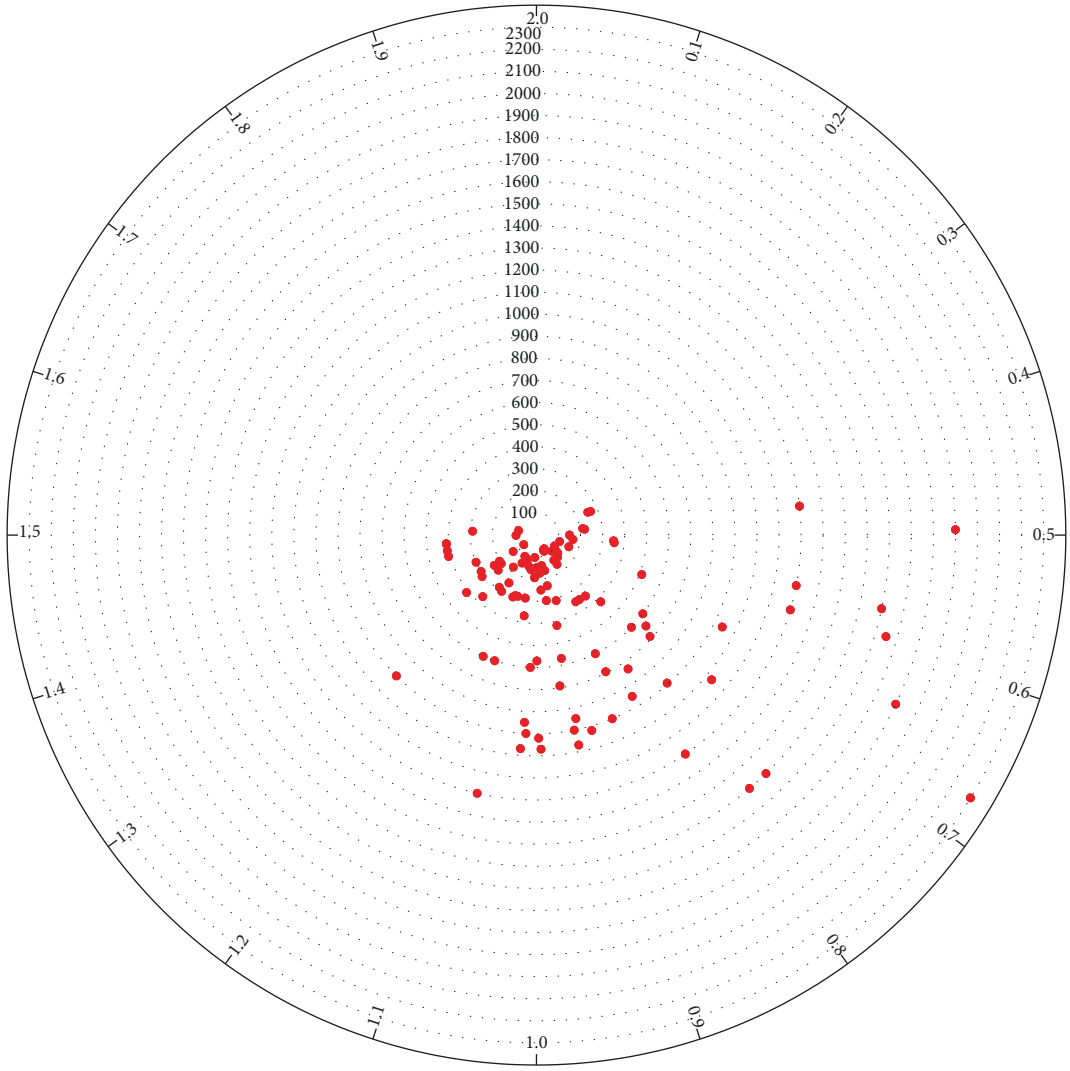

Figure 7: Distribution of the ratio of maximum and minimum principal stress difference and vertical stress with buried depth.

Figure 7. Shear failure is a common form of rock failure. The $K_{H\text{-}h}$ ratio of principal stress difference and vertical gradient is greater. The higher the shear stress of rock mass, the greater the probability of damage.

In all data points, the maximum $K_{H\text{-}h}$ value is 1.52, and the minimum value is 0.34. There are 18 data points where $K_{H\text{-}h} \leq 0.5$, accounting for 10.9% of the total. There are 146 data points where $0.5 < K_{H\text{-}h} \leq 1.1$, accounting for 73.2%, of which 120 are within $0.7 < K_{H\text{-}h} \leq 1.1$. There are 26 data points where $1.1 < K_{H\text{-}h} \leq 1.7$, accounting for 15.9%.

As shown in the above analysis and Figure 6, the $K_{H\text{-}h}$ of shallow ground is very discrete. With the development of the deep ground, $K_{H\text{-}h}$ is mostly concentrated between 0.7 and 1.0 in the range of 400 ~ 1000 m. The discreteness of $K_{H\text{-}h}$ gradually decreases in the range of 1000 ~ 2000 m, basically stable between 0.5 and 0.7. It is predicted through analysis that within a certain period of time, the rock mass can be guaranteed to be in a relatively stable state.

4.6. The Variation Law of Maximum Shear Stress with Depth. The maximum shear stress is 1/2 of the difference between the maximum and minimum principal stress, and the relationship with depth is shown in Figure 8. The relationship between maximum shear stress and depth is obtained by data regression,

$$\tau_m = \frac{\sigma_1 - \sigma_3}{2} = 0.014646H - 1.647993. \quad (8)$$

As can be seen from the figure, the maximum shear stress generally increases with depth. At the same time, an obvious discrete occurs. For all that, the discretization tends to decrease with depth. The reason for this phenomenon may be the scattered distribution of measuring points in the shallow, and these points are affected by the surface environment, coupled with the measurement results obtained by different methods which are quite different. So, the shallow shear stress distribution discretization is large. Although the number of measuring points in the deep is small, the distribution in the deep is more concentrated than that in the shallow, which greatly reduces the dispersion of the shear stress distribution.

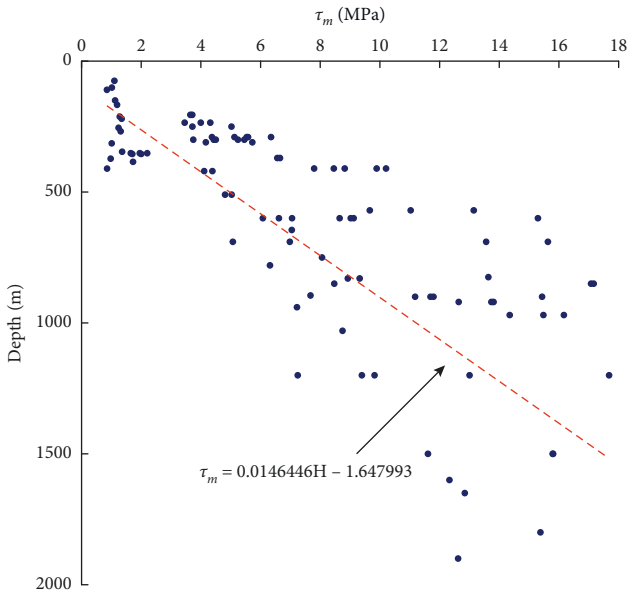

Figure 8: Distribution of maximum shear stress with depth and fitting curve.

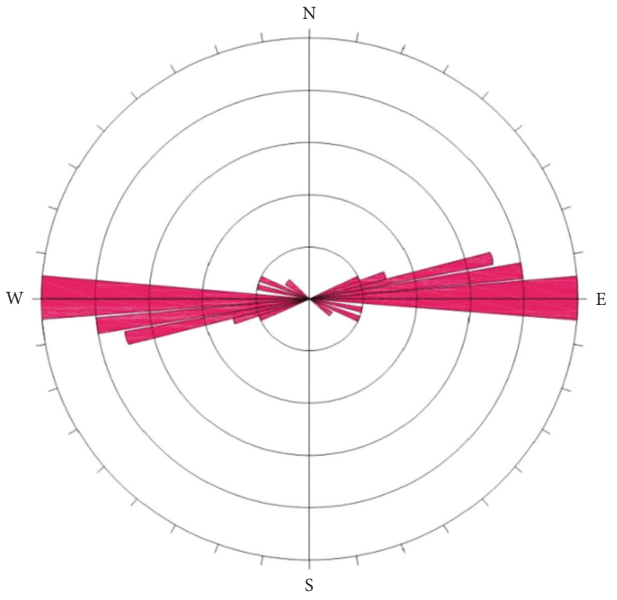

Figure 9: Distribution characteristics of the maximum horizontal principal stress direction in the northwest Jiaodong Peninsula.

4.7. The Distribution Characteristics of the Maximum Horizontal Principal Stress Direction. According to statistics, the maximum level of principal stress in the northwest Jiaodong Peninsula is generally close to EW and NEE-SWW, accounting for about 76.2% of the whole data, among which the near-E-W (70°~110°/250°~290°) is about 65.1%, the NEE-SWW about 11.1%, and the remaining directions about 23.8%. Figure 9 shows the rose chart of the direction of principal stress advantage in the northwest Jiaodong Peninsula. The figure shows that the overall direction of

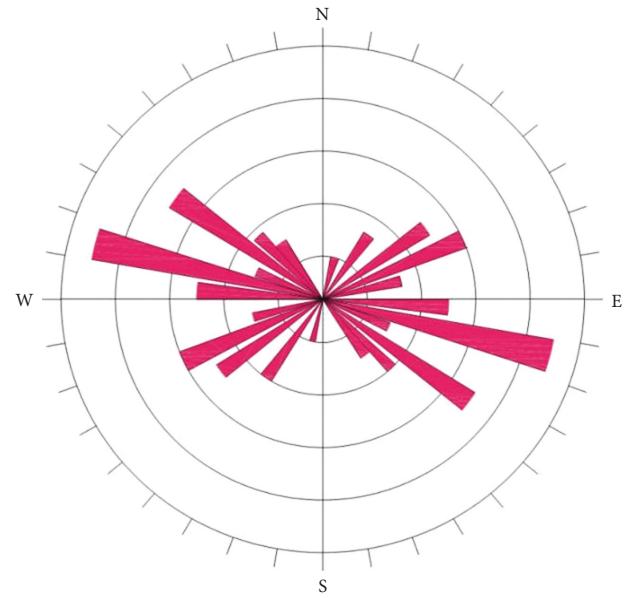

Figure 10: Distribution characteristics of the maximum horizontal principal stress direction in Shandong Provinces.

principal stress advantage in the northwest Jiaodong Peninsula is near E-W, and NWW-SEE also occupies a considerable proportion. This result is similar to the direction of the maximum horizontal principal stress in Shandong province, as shown in Figure 10 [10].

5. Conclusion

(1) By processing the 164 groups of data obtained by hydraulic fracturing methods and stress relief methods, the distribution law of the in situ stress field in the northwest Jiaodong Peninsula is got. The relationship among maximum principal stress, minimum principal stress, and vertical principal stress is analyzed by using the mathematical statistics method. In this area, the $\sigma_H > \sigma_h > \sigma_v$ gradually develops into the $\sigma_H > \sigma_v > \sigma_h$ below −450 m.

(2) The variation relationships of the maximum horizontal principal stress, the minimum horizontal principal stress, and the vertical principal stress with depth, respectively, are $\sigma_H = 0.0556H - 0.7772$, $\sigma_v = 0.0346H - 1.6137$, and $\sigma_h = 0.0248H + 1.0504$, respectively. The distribution laws of maximum, minimum, and average lateral pressure coefficients are in accordance with $K_H = 573.07/H + 0.2819$, $K_h = 397.32/H - 0.00283$, and $K_{av} = 379.47/H + 0.2069$.

(3) According to the obtained data, the relative magnitude of horizontal differential stress and the distribution law of maximum shear stress related to the fracture of surrounding rock are further studied, which are respectively $\mu_d = 536.58/H - 0.0389$ and $\tau_m = 0.014646H - 1.647993$. At the same time, it is also analyzed that the variation law of the ratio of horizontal principal stress difference with vertical

stress with depth concentrated in 0.7–1.0 at 400–1000 m and stabilized in 0.5–0.7 at 1000–2000 m. It is inferred that although the shear stress increases linearly with the increase of depth, there will be no shear dislocation failure in the rock stratum within 1500m.

(4) Through analysis, it is found that the directions of maximum horizontal principal stress in the northwestern Jiaodong Peninsula are EW and NEE-SWW, accounting for about 76.2% of all data [42].

Data Availability

The data used to support the findings of this study are available from the corresponding author upon request.

Conflicts of Interest

The authors declare that they have no conflicts of interest.

Acknowledgments

This research was funded by Major Basic Projects in Shandong Province (ZR2021052400019) and the Major Science and Technology Innovation Project of Shandong Province (2019SDZY05).

References

[1] M. Sandiford, M. Wallace, and D. Coblentz, "Origin of the in-situ stress field in south-eastern Australia," *Basin Research*, vol. 16, no. 3, pp. 325–338, 2004.

[2] T. Kanagawa, S. Hibino, T. Ishida, M. Hayashi, and Y Kitahara, "4. In situ stress measurements in the Japanese islands: over-coring results from a multi-element gauge used at 23 sites," *International Journal of Rock Mechanics and Mining Sciences & Geomechanics Abstracts*, vol. 23, no. 1, pp. 29–39, 1986.

[3] N. C. Gay, "In-situ stress measurements in Southern Africa," *Tectonophysics*, vol. 29, no. 1-4, pp. 447–459, 1975.

[4] Z. P. Meng, J. C. Zhang, and R. Wang, "In-situ stress, pore pressure and stress-dependent permeability in the southern Qinshui Basin," *International Journal of Rock Mechanics and Mining Sciences*, vol. 48, no. 1, pp. 122–131, 2011.

[5] H. X. Zheng, X. H. Zhang, T. H. Zhao, X. H Gao, and J Qi, "Geostress distribution and stress accumulation in Bohai strait and adjacent area," *Chinese Journal of Rock Mechanics and Engineering*, vol. 36, no. 2, pp. 357–369, 2017.

[6] G. L. Liu, Z. J. Tian, and G. J. Li, "Measurement and analysis on ground stress of mining expanded area in Beizao mine under sea," *Coal Science and Technology*, vol. 39, no. 9, pp. 26–29, 2011.

[7] L. Qiao, Z. H. Ouyang, X. P. Lai, and M Shengjun, "In-situ stress measuring and its result analysis in Sanshandao gold mine of China," *Journal of University of Science and Technology Beijing*, vol. 6, pp. 569–571, 2004.

[8] S. H. Wang, M. F. Cai, S. J. Miao, and Z. H Ouyang, "Results and their analysis of in-situ stress measurement in Sanshandao gold mine," *China Mining Magazine*, vol. 10, pp. 46–48, 2003.

[9] M. C. Song, "The composing, setting and evolution of tectonic units in Shandong province," *Geological Survey and Research*, vol. 31, no. 3, pp. 165–175, 2008.

[10] P. Li, Q. F. Guo, H. T. Liu, and X. Q Jiang, "Characteristics of current in-situ stress field and stress accumulation in Shandong region," *Chinese Journal of Rock Mechanics and Engineering*, vol. 36, no. 9, pp. 2220–2231, 2017.

[11] Y. E. Li, L. J. Chen, and S. W. Wang, "Temporal and spatial variations of apparent stress in Shandong province, China," *Earthquake*, vol. 35, no. 2, pp. 80–90, 2015.

[12] L. Zhang, C. Y. Zhou, F. J. Wang, and J Shou-qing, "Characteristics of stress field in each subregion of Shandong area," *North China Earthquake Sciences*, vol. 22, no. 4, pp. 12–15, 2004.

[13] H. T. Chao, J. L. Li, O. W. Cui, and Q. Y Zhao, "Characteristic slip behavior of the holocene fault in the central section of the Tanlu fault zone and the characteristic earthquakes," *Inland Earthquake*, vol. 8, no. 4, pp. 297–304, 1994.

[14] H. T. Chao, J. L. Li, O. W. Cui, and Q. Y Zhao, "Mode of motion of the holocene fault in weifang-jiashan segment of the Tanlu fault zone and earthquake-generating model," *Journal of Seismological Research*, vol. 20, no. 2, pp. 218–226, 1997.

[15] L. J. Yan, G. Zhu, S. Z. Lin, and T Zhao, "Neotectonic activity and formation mechanism of the Yishu fault zone," *Scientia Sinica*, vol. 44, no. 7, pp. 1452–1467, 2014.

[16] C. Fairhurst, "-situ stress determination—an appraisal of its significance in rock mechanics," in *Stephansson. Proceedings of the International Symposium on Rock Stress and Rock Stress Measurements*Stockholm Sweden, 1986.

[17] J. A. Hudson and C Cooling, "In Situ rock stresses and their measurement in the U.K.—Part I. The current state of knowledge," *International Journal of Rock Mechanics and Mining Sciences & Geomechanics Abstracts*, vol. 25, no. 6, pp. 363–370, 1988.

[18] O. Stephansson, "Rock stress in the fennoscandian shield," *Comprehensive Rock Engineering, Oxford Pergamon Press*, vol. 3, pp. 445–459, 1993.

[19] P. Aleksandrowski, O. H. Inderhaug, and B. Knapstad, *Tectonic Structures and Well-Bore Breakout Orientation*, pp. 29–37, Proc. 33rd US Symp, Rotterdam, 1992.

[20] K. Sugawara and Y. Obara, "Measuring rock stress," *Comprehensive Rock Engineering*, vol. 3pp. 533–552, Oxford, 1993.

[21] N. Hast, "The state of stresses in the upper part of the earth's crust," *Engineering Geology*, vol. 2, no. 1, pp. 5–17, 1967.

[22] W. R Judd, *Rock Stress, Rock Mechanics and Research. State of Stress in the Earth's Crust*, Elsevier, New York.USA, 1964.

[23] M. L. Zoback, M. D. Zoback, J. Adams et al., "Global patterns of tectonic stress," *Nature*, vol. 341, no. 6240, pp. 291–298, 1989.

[24] Z. Y. Zhang, X. T. Wang, and L. Wang, *Engineering Geological Analysis Principle*, pp. 56–78, Geological Publishing House, Beijing, 1994.

[25] X. Y. Ma, *Outline of Lithosphere Dynamics of China*, pp. 33–40, Geological Publishing House, Beijing, 1987.

[26] H. T. Chao, J. L. Li, Q. Y. Zhao, and Z. W Cui, "Active folds in the Yishu fault zone and their relations to active faults," *Journal of Seismological Research*, vol. 21, no. 3, pp. 261–267, 1998.

[27] W. Shi, Y. Q. Zhang, and S. W. Dong, "Quaternary activity and segmentation behavior of the middle portion of the tan-Lu fault zone," *Acta Geoscientia Sinica*, vol. 24, no. 1, pp. 11–18, 2003.

[28] Z. C. Wang, R. G. Jia, Z. M. Sun, and S. H. I Rong-hui, "Geometry and activity of the anqiu-zhuli segment of the anqiu-juxian fault in the Yishu fault zone," *Seismology and Geology*, vol. 27, no. 2, pp. 212–220, 2005.

[29] Z. C. Wang, D. L. Wang, and H. T. Xu, "Geometry features and latest acticities of the north segment of the anqiu-juxian fault[J]," *Seismology and Geology*, vol. 37, no. 1, pp. 176–191, 2015.

[30] P. Zhang, L. S. Wang, H. S. Shi, L. M Li, and H. M Tan, "The mesozoic-cenozoic tectonic evolution of the Shandong segment of the tan-Lu fault zone[J]," *Acta Geologica Sinica*, vol. 84, no. 9, pp. 1316–1323, 2010.

[31] Y. Q. Liu, H. X. Li, and T. L. Huang, *Shandong Mining Series and Mining Prediction of Gold, Iron and Coal Deposits*, pp. 1–288, Geological Publishing House, Beijing, 2004.

[32] P. J. Lu and W. Yao B, "Questions on the construction of luxi spin rolls," *Ournal of Shandong University of Science and Technology (Natural Science)*, vol. 2, pp. 92–99, 1987.

[33] S. X. Hu, Y. Y. Zhao, B. Lu, and B Xu, "Tectonic setting and gold mineralization of the Jiaobei terrane," *Contributions to Geology and Mineral Resources Research*, vol. 1, pp. 1–10, 1993.

[34] S. W. Yang, "A discussion on the Jiaodong group strata, the source-bed of gold and the stratabound features of gold ore deposits in northwest part of Jiaodong peninsula," *Contributions to Geology and Mineral Resources Research*, vol. 3, pp. 39–49, 1986.

[35] G. X. Lu, Q. C. Kong, and J. Deng, "Study and estimate of depths of the formation of the Linglong and jiaojia gold deposits," *Shandong. Geological Review*, vol. 6, pp. 550–559, 1996.

[36] M. C. Song, Y. X. Song, K. Shen, H. L Jiang, and S. Y Li, "Geochemical fatures of deeply-seated gold deposit and discussions on some associated problems in jiaojia gold ore field, Shandong peninsula, China," *Geochimica*, vol. 42, no. 3, pp. 274–289, 2013.

[37] F. C. Li and L. J. Wang, "Stress measurements in north China," *ACTA GEOPHYSICA SINICA*, vol. 22, no. 1, pp. 1–8, 1979.

[38] S. G. Zhao and J. M. Ding, "Near - surface and deep in-situ stress measurements in the middle segment of tancheng lujiang fault zone," *Journal of Seismology*, vol. 2, pp. 32–36, 1984.

[39] H. C. Zhu and Z. Y. Tao, "In-situl stress distribution in different rocks," *Acta Seismologica Sinica (Chinese edition)*, vol. 1, pp. 49–63, 1994.

[40] H. P. Xie, F. Gao, and Y. Ju, "Research and development of rock mechanics in deep ground engineering," *Chinese Journal of Rock Mechanics and Engineering*, vol. 34, no. 11, pp. 2161–2178, 2015.

[41] Y. H. Wang, X. F. Cui, X. P. Hu, and F. R Xie, "Study on the stress state in upper crust of China mainland based on in-situ stress measurements," *Chinese Journal of Geophysics*, vol. 55, no. 9, pp. 3016–3027, 2012.

[42] B. Lu, S. X. Hu, and S. Z. Zhou, "Terrane tectonics and tectonic setting of gold deposits in the Shandong peninsula," *Geological Review*, vol. 1, pp. 7–14, 1995.

Hindawi
Advances in Civil Engineering
Volume 2022, Article ID 2405174, 9 pages
https://doi.org/10.1155/2022/2405174

Research Article

Fully Mechanized Mining Technology and Practice of Water Conservation with Large Gravity Filling of Aeolian Sand-Like Paste

Pengliang Liu [1,2]

[1]*CCTEG Coal Mining Research Institute, Beijing 100013, China*
[2]*Coal Mining and Design Department, Tiandi Science and Technology Co., Ltd., Beijing 100013, China*

Correspondence should be addressed to Pengliang Liu; 274966405@qq.com

Received 7 April 2022; Revised 26 May 2022; Accepted 31 May 2022; Published 14 July 2022

Academic Editor: Lijie Guo

Aiming at the serious problem of Salawusu formation aquifer damage caused by caving mining in Yuyang coal mine, the technique of mechanized backfill mining with Aeolian sand-like paste was invented. Aeolian sand was used as aggregate and alkali-activated fly ash as cementing agent in the backfill material. Slurry ratio was studied where the water-sand ratio was 1 : 1.3 and the mass concentration was 72%, while slurry initial fluidity could reach 210 m. The author proposed the local resistance loss calculation method of slurry pipeline transportation, and the field gravity transport test results showed that resistance loss of unit length elbow was 4.26 times as big as loss of resistance along path; thus the pipeline diameter with 14.9 gravity of self-flowing was determined, and the pipeline flow design precision was improved by more than 10%. The backfill capacity could reach 360 m^3/h and the running energy consumption was lower because of adopting backfill station model with double pulping system and underground equipment pool. The author also put forward whole backfill space sealing in which cloth consumption was only 40% of bag backfill. Industrial test showed that the backfill mining technique met requirements of water resources protection, primarily because the filling rate was 98.5% in goaf, strata behavior appeared slightly, roof water leaching was less than 2 m^3/d, and surface subsidence value was only 38 mm. There were great breakthroughs in cost and production efficiency in this technology compared with similar technologies.

1. Introduction

Yuyang coal mine of Shaanxi Zhongneng Coalfield Co., Ltd. is one of the large-scale mines in Yuheng Mining Area (north area) of Jurassic Coalfield in Northwest China, with an annual output of 3 million tons. The coal seam occurrence and mining conditions are superior. The main mining 3# coal is 3.0~3.6 m thick, with an average inclination of 1° and a buried depth of 190~230 m. The mine is located in the southern margin of Maowusu Desert, belonging to arid and semiarid climate area, with poor water resources and fragile ecological environment. The coal seam is covered with about 40 m thick water bearing Aeolian sand layer, especially the relatively stable sand gravel aquifer of Salawusu formation at the bottom of 5~25 m, which directly covers the outcrop of coal measure strata. The water-conducting fault zone of caving mining is easy to communicate with the aquifer above the work face, which poses a great threat to the safe mining of coal seam and the fragile ecological environment of Mu Us Desert.

Compared with strip mining, thickness limiting mining, and other water conservation mining methods [1, 2] that reduce the degree of overburden damage at the cost of reducing resource recovery, the backfill mining achieves the effect of controlling mining damage without losing coal resources by backfilling solid or cemented filling materials to the goaf, which is an ideal environment-friendly mining method. In recent years, the backfill mining technology with waste gangue and power plant fly ash as the main filling materials has been rapidly developed and applied in coal mining under buildings (structures) and near water in mining areas in central and eastern China [3–12], which has achieved remarkable economic and environmental benefits and had a demonstration effect. In view of the urgent

demand of water conservation mining in Northwest Mining Area and the characteristics of extensive occurrence of aeolian sand on the surface, it is imperative to use local materials and use Aeolian sand as filling material to carry out filling mining. Yan et al. put forward a roadway pillar top coal caving filling mining method [13]; Cui et al. tested the basic properties of Aeolian sand and the properties of cemented filling materials with aeolian sand as aggregate [14]; Cao et al. used the orthogonal test to study the slump and compressive strength in 7 d and 28 d for paste filling materials with Aeolian sand; and the optimal proportion of filling materials was analyzed by SEM [15]. The above results promoted the development of Aeolian sand filling mining technology; however, the slurry preparation, transportation system, and filling coal mining technology suitable for the characteristics of Aeolian sand filling materials have not been formed, and the engineering practice is lacking. In addition, the benefits of filling coal mining are related to the popularization and application value of this technology. It is of great significance to improve the filling mining production capacity and reduce the cost from the perspective of materials, systems, and processes.

After three years, the author and his team have developed high fluidity Aeolian sand-like paste filling materials, established a 14.9-large line artesian flow system, adopted the mode of double pulping system and low energy consumption filling station, put forward a new way of overall sealing of the filling space of the working face, and formed a relatively perfect high-efficiency and low-cost Aeolian sand-like paste filling coal mining technology. The successful trial mining has been carried out in no. 2307 fully mechanized mining filling face of Yuyang coal mine, which meets the requirements of protecting the overlying aquifer and provides a reference for promoting the application of filling and water conservation mining technology in Northwest Mining Area.

2. Overview of Test Mine and Working Face

The mine field area of Yuyang coal mine is 13.0 km^2. The surface is desert beach and semifixed dune landform, with little topographic fluctuation, as shown in Figure 1. The average thickness of Cenozoic Aeolian sand layer in the mine field is about 43 m, which is composed of pore phreatic water of Salawusu formation of Upper Pleistocene and pore fissure phreatic water aquifer of Lishi loess of Middle Pleistocene. The pumping data during mine exploration and the production practice of adjacent mines show that the pore aquifer of Salawusu formation is composed of medium and coarse sand, with high sand content and pure texture, unit water inflow $q = 1.375\sim2.596$ L/s.m, and permeability coefficient $k = 14.234\sim27.463$ m/d, belonging to medium ~ strong aquifer, which is an important barrier for desert ecological environment protection. Under this aquifer, a water resisting layer composed of loess of Lishi formation of Quaternary Middle Pleistocene and laterite of Baode jingle formation of Neogene Pliocene is developed. Bedrock aquifers mainly include bedrock weathered zone aquifers and coal measure sandstone aquifers, of which the roof sandstone and medium sandstone aquifers overlying the coal seam belong to weak water bearing sandstone fissure aquifers. Under the condition of traditional high-strength caving mining, the overburden aquiclude is easy to be damaged, the pore phreatic water of Salawusu formation leaks, and the water inflow of the working face has reached 790 m^3/h.

Figure 1: Aeolian sand landscape in Yuyang coal mine.

No. 2307 fully mechanized mining filling test face is located in the southwest of the mine, untapped area in the south, boundary coal pillar in the west, and return air roadway in the south in the east. The strike of the working face is 1149 m long and 150 m wide (excluding two lanes), the average mining thickness is 3.5 m, and the dip angle is 0.28°. The coal seam floor elevation is +966~+971m, the ground elevation is +1160~+1169m, and the buried depth is 190~198 m.There are scattered houses on the surface. In order to monitor the surface movement and deformation, one strike observation line is set above the cut hole, including 3 control points, A1, A2, and A3, with spacing of 50 m. There are 29 observation points: 1#~29#, the point spacing is 20 m, and the total length of the survey line is 690 m, as shown in Figure 2, which meets the observation requirements of mining impact. Observation shall be carried out once a month from the mining of the working face.

3. Characteristics of Aeolian Sand-Like Paste Filling Material

3.1. Filling Material Composition

3.1.1. Aeolian Sand. 32 sand samples were collected from Aeolian sand layers at different positions on the surface of Yuyang coal mine. Through microscopic observation (Figure 3), the main mineral components are quartz, feldspar, mica, and so forth. X-ray diffraction analysis shows that the chemical components are SiO_2, Al_2O_3, Cao, Fe_2O_3, and MgO, and the main components SiO_2 and Al_2O_3 account for 65.75% and 12.83%, respectively. The screening test shows that the particle size of Aeolian sand is mostly concentrated between 0.075 and 0.6 mm, with an average of 0.249 mm and a maximum of no more than 1.0 mm. It belongs to ultrafine sand, with nonuniformity coefficient $C_u = 2.49$ and curvature coefficient $C_C = 1.03$. The bulk density is 1.503~1.543 g/cm^3, and the porosity is 40.2%~42.5%. The apparent density is 2.571~2.599 g/cm^3 [16, 17].

3.1.2. Cementitious Material. Alkali-activated cementitious material is a new type of inorganic nonmetallic cementitious material developed in recent years. It takes pozzolanic or

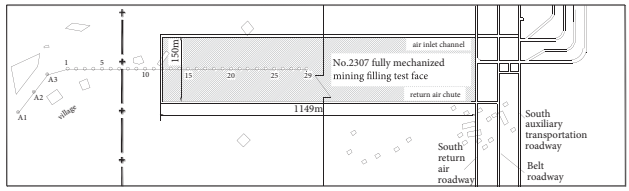

Figure 2: No. 2307 fully mechanized backfill mining face and surface movement deformation observation point.

Figure 3: The fluidity test of Aeolian sand-like paste [12].

potential hydraulic active materials (e.g., slag, fly ash, etc.) as the main material, which is activated by adding alkaline activator to produce hydraulic cementitious performance. Making full use of industrial waste, this material has low cost, and its strength, acid and alkali resistance, and carbonation resistance are better than those of Portland cement [18]. The filling material is a cementitious material with fly ash as the main material and lime, gypsum, and cement as alkaline activator.

The fly ash is grade III fly ash from Guohua Jinjie Power Plant. Its main components are SiO_2, Al_2O_3, Fe_2O_3, FeO, Cao, and TiO_2, with an average apparent density of 2.18 g·cm^{-3}. Calcium quicklime is used as quicklime, with reference to the standard of building quicklime (JC/T479-1992). Gypsum shall meet the requirements of reference building materials and grade 1.6 specified in GB9776-2008. The cement is 32.5# ordinary Portland cement.

3.1.3. Water. Mine water can be used to prepare filling materials.

3.2. Filling Material Ratio Experiment. The rheological parameters (fluidity, viscosity, and yield stress) of filling slurry, final setting time, bleeding rate, and strength of filling body are the main performance indexes of cemented filling material. The orthogonal test method of two factors and four levels is used to test the performance of filling materials with different ratios. The mass concentrations are 69%, 72%, and 75%, and the water-sand ratios are 1 : 0.7, 1 : 1, and 1 : 1.3. The experimental results are shown in Table 1. The measurement of slurry fluidity is shown in Figure 3.

Compared with the current mine cemented filling materials [19–21], the Aeolian sand-like paste filling materials show the characteristics of strong fluidity and high strength as a whole. From the perspective of meeting the performance indexes and making full use of Aeolian sand as much as possible, the scheme with water-sand ratio of 1 : 1.3 and mass concentration of 72% is finally selected.

4. Feasibility Analysis and Determination of Inner Diameter of Pipeline for Gravity Transportation of Large Pipeline

4.1. Analysis of Local Resistance Loss in Slurry Pipeline Transportation. The filling station of Yuyang coal mine is located in the industrial square. The slurry conveying pipeline reaches the farthest cutting position along the vertical drilling, filling pipeline channel, south return air roadway, and no. 2307 work face return air roadway. The length $L = 2652$ m, the height difference between the starting point and the end point $h = 178$ m (Figure 4), and the filling multiple line is $n = L/h = 14.9$, which has exceeded the maximum gravity multiple line of the current mine by 11.76 [22]. There are two kinds of filling slurry transportation: pumping and self-flow. In view of the strong fluidity of Aeolian sand-like paste slurry, the feasibility of self-flow transportation mode is studied.

According to Bernoulli equation of fluid pipeline transportation, the energy equation of filling slurry gravity transportation is

$$\rho \mathrm{gH} = \frac{\rho v^2}{2} + I, \tag{1}$$

where ρ is the slurry density, kg/m^3; G is gravity acceleration, 9.81 m/s^2; v is the outlet slurry flow rate, m/s; I is the total resistance loss of pipeline, Pa.

Equation (1) shows that if the slurry can be transported by gravity, the potential energy of the height difference between the starting point and the ending point of the pipeline should overcome its resistance loss in the process of pipeline transportation and make the outlet slurry meet certain flow requirements. It can be seen that determining the resistance loss in the conveying process is very important to analyze the feasibility of gravity conveying.

The pipeline resistance loss includes the resistance loss i_s along the straight pipe section and the local resistance loss I_b mainly at the position of 90° elbow.

(1) The resistance loss i_s is the product of the total length L_s of the straight pipe section and the resistance loss i_s per unit length. i_s is usually calculated by the following formula:

$$\mathrm{i_s} = \frac{16}{3\mathrm{D}}\tau_0 + \eta\frac{32\mathrm{v}}{\mathrm{D}^2}, \tag{2}$$

Table 1: Experimental results of backfill material proportioning.

Number	Concentration/%	Water-sand ratio	Viscosity coefficient/(Pa·s)	Yield stress/Pa	Initial mobility/mm	Final setting time/h	Bleeding rate/%	Strength at different ages/MPa			
								12 h	3 d	7 d	28 d
1	69	1 : 0.7	0.096	2.31	266	6.2	0.9	0.21	2.15	3.30	4.92
2	72	1 : 1	0.256	4.85	206	6.2	1.0	0.19	2.20	3.31	4.77
3	75	1 : 1.3	0.848	8.78	190	5.8	1.3	0.25	2.56	3.44	5.02
4	69	1 : 1	0.110	2.43	247	6.5	1.2	0.19	1.98	3.12	4.67
5	72	1 : 1.3	0.261	5.04	210	6.0	1.2	0.20	2.11	3.23	4.80
6	69	1 : 1.3	0.124	2.61	240	6.3	1.5	0.18	1.92	3.02	4.55
7	75	1 : 0.7	0.243	4.52	208	6.0	0.5	0.24	2.41	3.53	4.98
8	72	1 : 0.7	0.238	4.37	214	6.1	0.6	0.17	2.26	3.34	4.87
9	75	1 : 1	0.264	4.96	193	6.1	0.8	0.21	2.32	3.48	4.90

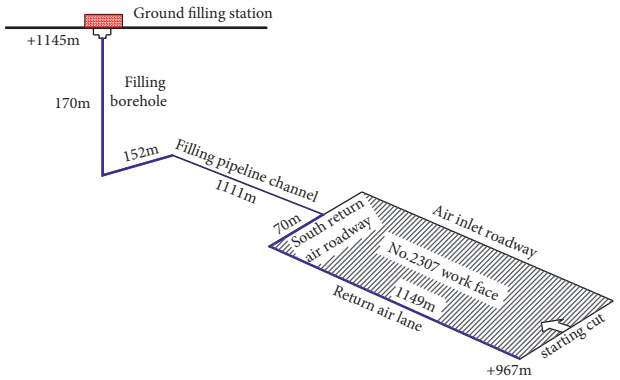

Figure 4: The backfill pipeline route from filling station to no. 2307 work face.

(2) where τ_0 is the yield stress of slurry, Pa; D is the inner diameter of the pipeline, m; η is the slurry viscosity, Pa·s.

(3) Due to the complex flow law of slurry in the elbow section of the pipeline, the local loss of the pipeline in the literature is considered as a whole and is calculated according to 10%~20% of the total resistance loss along the pipeline [23, 24]; that is, formula (2) is expressed as

$$\rho g H = \frac{\rho v^2}{2} + (1.1 \sim 1.2)\left(\frac{16}{3D}\tau_0 + \eta\frac{32v}{D^2}\right)L. \quad (3)$$

The laying route of filling pipeline in each mine is different, and the number of elbows is inconsistent or even quite different. Using simple estimation will cause great error. As a part of the pipeline, the inner diameter and slurry parameters of the elbow are the same as those of the straight pipe. Therefore, the resistance loss of the elbow section also adopts the unit length as the calculation unit, and the local resistance loss I_b per unit length is expressed by multiple K of the resistance loss i_s along the unit length; that is,

$$i_b = k i_s = k\left(\frac{16}{3D}\tau_0 + \eta\frac{32v}{D^2}\right). \quad (4)$$

Substituting (3) and (4), straight pipe length L_s and elbow cumulative length L_b into (2), the following is obtained:

$$\rho g H = \frac{\rho v^2}{2} + \left(\frac{16}{3D}\tau_0 + \eta\frac{32v}{D^2}\right)L_s + \left(\frac{16}{3D}\tau_0 + \eta\frac{32v}{D^2}\right)kL_b, \quad (5)$$

where $L_b = n\pi R/2$; n is the number of elbows; and R is the radius of curvature of the elbow, m.

Compared with formulas (3) and (5) including the elbow parameters of specific pipeline and the multiple relationship between the local resistance loss per unit length and the resistance loss along the way, the local resistance loss can be determined by obtaining the value of K through test.

4.2. Field Gravity Conveying Test. Theoretical analysis, numerical simulation, and loop experiment play an important role in the study of filling slurry pipeline transportation law [25, 26]. However, due to the complexity of slurry transportation process and large similarity of simulation, the results often deviate from the reality. Using the idle pipeline of the mine to carry out the slurry transportation test in the field according to the fill-times-line and length similar to the design can provide more accurate test parameters for studying the slurry transportation law.

The purpose of the field artesian conveying test of Aeolian sand-like paste body is to determine the value of K, so as to provide a basis for the feasibility analysis and pipe diameter selection of 14.9 fill-times-line artesian conveying in Yuyang coal mine. The test was carried out in a mine site, and a simple pulping station was set on the ground, and the filling materials used were completely consistent with the actual filling. The transmission pipeline uses idle drainage pipe, and the model is $\Phi 133 \times 6$ seamless steel pipe, with an inner diameter of 121 mm and a total length of 2480 m, which is composed of 145 m vertical pipe and 2335 m underground pipe. The filling gravity is 13.1. There was a large slope in the underground roadway, so some lines show certain fluctuation. In order to occupy the production roadway as little as possible and set more elbows, coil mode is adopted locally. There were 22 elbows (all 90°) in the pipeline.

Multiple tests can reduce the data error. After the full-length pipeline transportation test, the slurry transportation

tunnel coil (a)

slurry discharged from pipeline (b)

Figure 5: Experimental scene of large gravity flow. (a) Tunnel coil. (b) Slurry discharged from pipeline.

test was carried out twice again by dismantling the pipeline, reducing the total length, and changing the corresponding number of gravity lines and bends. The coiled pipe in the roadway and the slurry discharged from the test are shown in Figure 5. From Table 2 for thepipeline parameters and flow velocity of the three tests, the following can be seen:

(1) The Aeolian sand-like paste slurry realizes the self-flow transportation under the conditions of gradient 8.5, 10.5, and 13.1, and the flow decreases with the increase of filling gravity. The flow can reach 70.4 m^3/h under the condition of gradient 13.1. It can be predicted that the 14.9 gradient self-flow transportation of Yuyang coal mine is feasible, and the flow requirements can be realized through the adjustment of pipe diameter.

(2) Substitute the relevant data of three conveying tests into equation (5) to obtain $K_1 = 4.4$, $K_2 = 4.2$, and $K_3 = 4.2$, and the average value $K = 4.3$, that is, the local resistance loss of unit length elbow is 4.26 times that of straight pipe. The calculated resistance losses of straight pipe section and elbow section in the three transportation tests are shown in Table 3. The ratio of resistance loss of elbow section to straight pipe section is 4.8%, 3.9%, and 3.6%, respectively, which does not reach 10%~20% in the traditional estimation method, indicating that the calculation of local resistance loss and total resistance loss of the latter is too large, so the kinetic energy of outlet slurry (flow rate) is low. Under the same flow requirements, the designed pipe diameter will be too large.

4.3. Determination of Inner Diameter of Conveying Pipeline in Yuyang Coal Mine. The number of elbows (n) in the filling slurry conveying pipeline of Yuyang coal mine is 5, the radius of curvature is 1.5 m, and the cumulative length of the elbow section is $L_b = n(\pi R)/2 = 12$ m, and then the length of the straight pipe section is $L_S = l - l_b = 2338$ m. Substituting pipeline parameters and rheological parameters of Aeolian sand-like paste slurry and $K = 4.26$ into (5), the slurry flow rate and flow corresponding to the inner diameter of several groups of common pipelines are obtained, as shown in Table 4. According to the flow design requirements of 180 m^3/h single pipeline, 16 Mn seamless steel pipe pipeline with inner diameter of 156 mm and wall thickness of 10 m is selected. After the completion of the system, the measured actual flow rate at the pipeline outlet is 2.66 m/s and the flow is 184 m^3/h, with a design error of only 1.7%, meeting the production requirements. Using the traditional estimation method, the overall local resistance loss is considered as the minimum 10% of the resistance loss along the way. The inner diameter of the pipeline $d = 0.16$ m under the condition of flow of 180 m^3/h is obtained through (3), which is substituted into (5), and, combined with the relationship between the actual flow and pipe diameter of Yuyang coal mine, the estimated flow is more than 202 m^3/h, and the error rate is 12%.

The pipeline transportation test and practice show that the flow design accuracy is more than 10% higher than that of the traditional estimation method because of obtaining the local resistance loss of the pipeline accurately, with the local resistance loss considering the specific length of the elbow section and obtaining the multiple relationship between the local resistance loss per unit length and the resistance loss along the way through the test.

5. Low Energy Consumption Filling Station Mode of Double Pulping System

The preparation system of Aeolian sand-like paste filling slurry is composed of primary slurry tank, auxiliary material tank (storing activator), cement tank, slurry forming tank, Aeolian sand screening and conveying system, and fly ash silo. The pulping process is as follows: start the mixing motor, and inject fly ash to make the primary slurry after injecting quantitative water into the primary slurry tank; the raw materials of Aeolian sand are removed by eccentric synchronous horizontal screen (the size of screen mesh is 25 mm), and the finished sand is transported and measured by belt conveyor and electronic belt scale; the primary slurry,

Table 2: Experimental results of large gravity self flow.

Serial number	Elevation difference between starting point and ending point of pipeline (H)/m	Total length of pipeline (L)/m	Self-flow gravity (N)	Elbow of pipe			Outlet velocity (v)/(m/s)	Flow (Q)/(m^3/h)
				Number (n)	Mean radius of curvature (r)/m	Cumulative length (L_b)/m		
1	190	2480	13.1	22	1.0	35	1.70	70.4
2	220	2300	10.5	18	1.0	28	2.24	92.7
3	150	1274	8.5	9	1.0	14	2.85	118.0

Table 3: Comparison of local resistance loss in the pipeline between this method and the traditional method.

Serial number	Resistance loss along the whole pipeline/MPa	Resistance loss of elbow section/MPa	Ratio of local resistance loss to along path resistance loss/%	
			This method	Traditional estimation method
1	3.0	0.2	4.8	
2	3.5	0.2	3.9	10~20
3	2.4	0.1	3.6	

Table 4: Corresponding value of pipe diameter, flow velocity, and flow.

Serial number	Pipe inner diameter/m	Current speed/m/s	Flow/m^3/s
1	0.065	0.3	31.6
2	0.109	1.2	88.8
3	0.156	2.6	181.0
4	0.165	3.0	203.4

auxiliary materials, cement, and Aeolian sand are transported to the slurry tank according to the set proportion for uniform mixing. Automatic control is adopted for quantitative material conveying and liquid level monitoring in slurry preparation process.

The pulping capacity of filling stations at home and abroad is only 60~150 m^3/h, and a single system is often used, which has become one of the factors restricting the production capacity of backfill mining. In view of this, the filling station adopts two sets of 180 m^3/h pulping systems for centralized layout and simultaneous operation. The plan is shown in Figure 6. The prepared slurry is transported to the work face through two pipelines, and the maximum filling capacity can reach 360 m^3/h.

Due to the higher height of the storage tank, the process of upward water supply, ash striking, and material conveying causes great energy consumption waste and increases the operation cost. Therefore, the filling station is designed in the way of underground equipment pool, as shown in Figure 5: the primary slurry tank, auxiliary material tank, and cement tank are placed 10 m below the ground, and the top of the tank is parallel to the ground to realize horizontal ash striking; the storage, screening, and conveying system of Aeolian sand is arranged from the ground to 10 m below, and the Aeolian sand is naturally transported downward during screening; the slurry tank is placed 15 m below the ground and is in the center of the equipment pool. The slurry tank's top is flush with the bottom of the above equipment, where the primary slurry and various materials are transported horizontally. This style can achieve obvious effect of reducing energy consumption.

6. A New Way of Overall Sealing of Filling Space in Working Face

The cemented filling coal face adopts the short step "coal mining-filling-solidification" cycle process to move forward. How to construct the filling space fast with excellent results after each cycle of coal mining is one of the ways to improve the filling efficiency. At present, the style of filling slurry into the bags sewn by high-strength fiber cloth hung behind the support is often used, which solves the problem of building a closed space in the goaf with complex geological environment. However, there are some problems, such as unsafe working environment, large number of hanging bags, and large cloth consumption.

A new way of overall sealing of filling space is put forward: after coal mining, the fiber cloth is laid along the whole area of the top and bottom plate behind the support, and the upper and lower layers of fiber cloth are squeezed by the mechanical force at the support position, so that the filling space can be mined behind. The empty area forms a confined space, as shown in Figure 7. The relevant structures and functions of the support are as follows: an operation room is set at the rear, a fixed baffle and a lifting baffle are set at the side of the goaf, the fixed baffle is integrated with the base of the hydraulic support, the lifting baffle is slidably connected with the fixed baffle, and a flexible pad is set at the top. The specific operation of the overall sealing of the filling space is as follows: starting from the cutting of the working face, lay the fiber cloth along the full length of the top plate, the cutting coal wall, and the bottom plate behind the support, and then pull the two remaining edges of the fiber cloth to the support operation room, and then raise the lifting baffle, clamp the top and bottom cloth between the lifting baffle and the top beam, and sew or seal the fiber cloth at both ends of the working face, which forms a closed space filling. The Aeolian sand-like paste slurry is filled into the rear space through the pipeline until it is full. During the solidification of the filling body, the workers continue to connect the fiber cloth between the support operations to

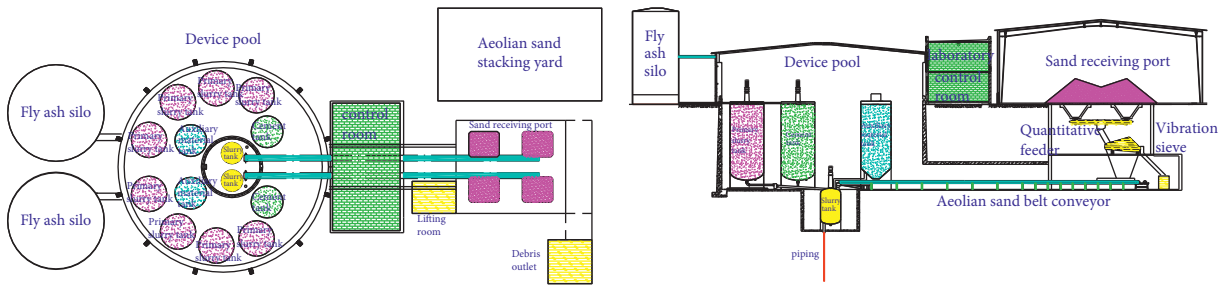

Figure 6: Layout and scene of backfill station in Yuyang coal mine. (a) Plane sketch. (b) Section diagram.

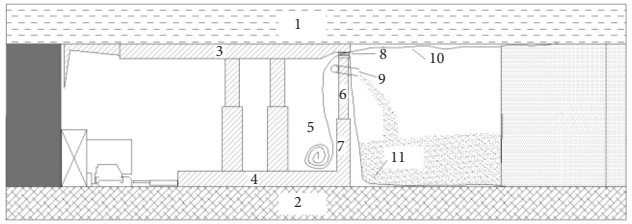

1—roof ; 2—floor ; 3—support top beam ; 4—bracket base ; 5—operation room ; 6—lifting baffle ; 7—fixed baffle ; 8—flexible pad ; 9—filling pipe outlet ; 10—roof cloth ; 11—floor cloth

Figure 7: Whole backfill space sealing in mining face.

prepare for the next cycle. When the solidification strength of the filling body meets the requirements, lower the lifting baffle, move the support forward, and take off the fiber cloth from the filling body for the next cycle of coal mining and filling operation.

The advantages of the new method of overall sealing of the filling space are that workers work in the support operation room during the whole process, and the safety is guaranteed; the mechanical force of the support is used to realize the sealing of fiber cloth, which reduces the labor intensity of workers and improves the operation efficiency; the cloth consumption is greatly reduced, taking no. 2307 work face as an example; if bag filling is adopted, the bag size of 10 m (length) × 3 m (width) × 3.5 m (height) is considered, and 6000 bags need to be hung in the whole goaf, and the total amount of cloth is 900000 m^2; the fabric consumption of this method is about 360000 m^2, reducing 540000 m^2, which is only 40% of that of bag hanging method.

7. Practice of Mechanized Filling Coal Mining with Aeolian Sand-Like Paste Body

7.1. Operation of Filling Coal Mining System. In October 2012, the mechanized filling and mining system of Aeolian sand-like paste body in Yuyang coal mine was completed, and the industrial test of filling and mining in no. 2307 work face was carried out at the end of November. As of middle of December 2013, the work face had been advanced 310 m in total, and 213000 t coal has been output, and the total filling slurry was about 170000 m^3; 110000 tons of Aeolian sand, 83000 tons of fly ash, 12000 tons of activator, and 85000 tons of mine water were consumed. Later, due to the closure of the mine, the filling mining could not be continued.

In the early stage of the industrial test, the running in degree of the system was insufficient, the workers were not skilled in the filling process, there were many on-site implementation problems, and the production efficiency was low. In the later stage, it gradually played a high level.

7.2. Water Retaining Mining Effect. A total of 72 coal mining and filling cycles were carried out in the work face. After each cycle, the filling and roof connection should be observed and recorded along the full length of the work face. Due to the low bleeding rate of filling body and strict on-site management, the statistical results showed that the average filling rate of goaf was as high as 98.5%.

There were 88 fully mechanized mining filling supports in the work face, and one pressure measuring station was set every 10 supports. The measured data from December 11, 2012, to December 11, 2013, showed that the pressure in the middle of the working face was relatively large and gradually decreased towards the head and tail, but the roof pressure was small as a whole, the change trend was gentle with the advancement of the work face, and there was no obvious periodic pressure on the roof. The working resistance time (P-T) curve of the middle 45# support of the working face is shown in Figure 8.

The final surface subsidence curve is shown in Figure 9. The maximum subsidence is 38 mm. It is located at 22# measuring point and 196 m from the cutting hole. The buildings on surface are not affected.

Based on the above measured data, a similar material model is established to analyze the damage degree of overlying strata in caving mining and Aeolian sand-like paste filling mining of no. 2307 work face: the "three zones" of caving mining have obvious characteristics, the height of water-conducting fault zone is 145m, running through the aquiclude, and the phreatic water of Salawusu formation is damaged; the filling mining roof did not collapse, and only a small amount of separation is generated in the lower roof, which does not damage the water resisting layer. The measured roof water leaching of the working face is less than 2 m^3/d. It shows that the overburden damage of Aeolian sand-like paste filling mining is slight, and the effect of protecting water resources is realized.

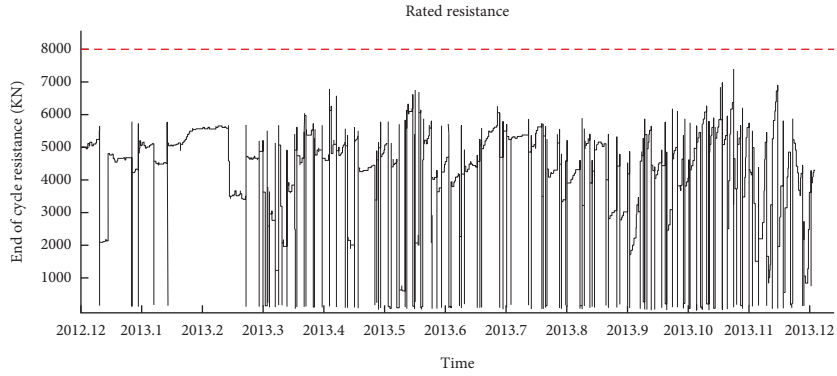

Figure 8: P-T curve of 45# hydraulic support in middle of mining face [12].

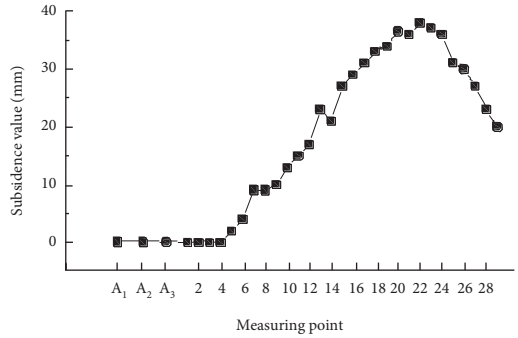

Figure 9: Relative position of surface subsidence curve.

Table 5: Cost composition per ton of coal with Aeolian sand-like paste filling (unit: yuan).

Filling material (including sealing cloth)	Depreciation fee of fixed assets	Operation cost of filling system	Labor cost	Other	Total
55.2	8.2	1.2	7.1	9.8	81.5

7.3. Productivity and Cost. At present, the production capacity of cemented filling coal mining single face is 200000~300000 t/a, and the filling cost per ton of coal is 110~140 yuan, according to the author's investigation and statistics. In contrast, by adopting the large capacity filling system and the overall sealing mode of the filling space of the working face, the coal mining filling cycle with a step distance of 6.4 m is completed every two days, the monthly push progress is 88 m, and the production capacity reaches 600000 t/a, which is nearly doubled. Due to the local use of Aeolian sand and the optimization of many measures, such as simple pulping process, low energy consumption of filling station, gravity transportation, and small consumption of closed cloth at the work face, the filling cost per ton of coal is about 81.5 yuan (its composition is shown in Table 5), which is reduced by 35%.

8. Conclusion

The following conclusions can be drawn from this study:

(1) The developed paste-like filling material of Aeolian sand takes Aeolian sand as aggregate and alkali-activated fly ash as cementation material, which has the characteristics of strong slurry fluidity and relatively high strength of filling body. The test determines that the ratio of water to sand is 1 : 1.3 and the mass concentration is 72%.

(2) The calculation method of local resistance loss of slurry pipeline transportation is put forward. Through the field gravity transportation simulation test, it is concluded that the resistance loss of elbow per unit length is 4.26 times of the resistance loss along the way. The inner diameter of 14.9-fold gravity transportation pipeline is selected to improve the flow design accuracy by more than 10%.

(3) The low energy consumption layout mode of double pulping system in the filling station is adopted, and a new way of overall sealing the filling space of the working face is adopted, which improves the filling efficiency and reduces the cost.

(4) The monitoring of gob filling rate, working resistance of working face support, roof water leaching, and surface subsidence shows that the Aeolian sand-like paste backfill mining causes slight damage to the overburden, and the overlying aquifer has been effectively protected, and a great breakthrough has been made in the production efficiency and cost of this technology.

(5) In view of the good mechanical properties of Aeolian sand-like paste backfill and the control effect of rock stratum movement, the proportion of filling materials should be optimized and the feasibility of partial filling mining should be studied to further improve the economic benefits and promote the wider application prospect of this technology in water retaining mining in Northwest Mining Area in China.

Data Availability

The data used to support the findings of this study are available from the corresponding author upon request.

Conflicts of Interest

The author declares no conflicts of interest.

Acknowledgments

This work was supported by the Tiandi Technology "other internal R&D projects of the company" "science and technology innovation fund" of mining design division (TDKC-2022MS-04).

References

[1] Q. X. Huang, "Research on roof control of water conservation mining in shallow seam," *Journal of China Coal Society*, vol. 42, no. 1, pp. 50–55, 2017.

[2] X. P. Shao, Z. W. Ding, X. Q. Yuchi, and J. Zhang, "Study on long time effect and replacement mining method for coal pillar in strip mining," *Coal Engineering*, vol. 47, no. 8, pp. 57–59, 2015.

[3] Q. L. Chang, X. Yao, S. Ge, Y. Xu, and Y. Sun, "Control of water inrush from longwall floor aquifers using a division paste backfilling method," *Geofluids*, vol. 2021, pp. 1–10, 2021.

[4] Q. L. Chang, C. l. Yuan, Y. Z. Wang, B. Zhang, and H. Q. Zhou, "Semi-convex mechanical analysis on stability of step coal wall in fully mechanized mining with paste filling," *Journal of China University of Mining & Technology*, vol. 51, no. 01, pp. 46–55, 2022.

[5] P. L. Liu, H. X. Zhang, F. Cui, K. H. Sun, and W. M. Sun, "Technology and practice of mechanized backfill mining for water protection with aeoliansand paste-like," *Journal of China Coal Society*, vol. 42, no. 1, pp. 118–126, 2017.

[6] Q. Lu, Y. C. Wu, and M. X. Xu, "Research progress of fly ash activation and its application in the porous catalytic materials," *Clean Coal Technology*, vol. 27, no. 3, pp. 1–12, 2021.

[7] J. M. Liu, *Study and Application of Mechanical Properties of Gangue Paste Material*, China University of mining and technology, Xuzhou, 2020.

[8] Y. D. Wang, J. Y. He, and Q. Gao, "Study on Application of waste rock coarse aggregate filling slurry pipeline gravity filling technology," *Journal of Xuzhou Institute of Technology(Natural Sciences Edition)*, vol. 34, no. 2, pp. 86–92, 2019.

[9] B. N. Hu, P. L. Liu, and F. Cui, "Review and development status of filling coal mining technology in China," *Coal Science and Technology*, vol. 48, no. 9, pp. 39–47, 2020.

[10] S. M. Sui, "Study on the overlying rock movement and surface subsidence control of solid backfilling mining," Fuxin: Liaoning University of engineering and technology, 2018.

[11] Y. C. Huang, T. Y. Lin, S. Q. Lu, G. P. Chen, and Z. Zhang, "Research and application of the test method on high density gangue backfill slurry's rheological parameters," *China mining Magazine*, vol. 25, no. 2, pp. 102–104, 2016.

[12] P. L. Liu, "Technologies and practices of mechanized backfill mining for water protection with aeolian sand paste-like," *PPPaste 2017 & 20th International Seminar on Paste and Thickened Tailings*, vol. 13, pp. 284–293, 2017.

[13] S. H. Yan, Q. M. Liu, H. X. Zhang, and H. X. Wang, "Backfill mining technology for gateway and pillar top coal caving mining under aquifer of shallow thin bedrock," *Coal Science and Technology*, vol. 36, no. 1, pp. 1–3, 2008.

[14] F. Cui and H. X. Zhang, "Feasibility analysis of aeolian-sand for underground stowing," *Coal Mining Technology*, vol. 14, no. 3, pp. 42-43, 2009.

[15] X. F. Cao, Y. C. Tang, N. D. Deng, Y. Zhou, H. Shang, and Y. Wang, "Development of paste filling materials based on aeolian sand," *Mining Research and Development*, vol. 40, no. 1, pp. 43–48, 2020.

[16] K. H. Sun, "Experimental research on aeolian sand paste-like stowing material for mine," *Coal Technology*, vol. 33, no. 5, pp. 262–265, 2014.

[17] K. H. Sun, P. L. Liu, W. M. Sun, and K. Zhu, "Research and application on aeolian sand paste-like stowing material for mine," *Metal Mine*, vol. 478, no. 4, pp. 172–176, 2016.

[18] X. D. Wang, "Relationship between engineering performance and mix proportion of fly ash for cemented and high concentration backfill material with wind blown sand as aggregate," *Journal of Engineering Geology*, vol. 24, no. 1, pp. 78–86, 2016.

[19] J. H. Jiang, *Study on Preparation,structures and Properties of Mine Backfill Materials from Mud Solidification*, p. 7, Hunan University of Science and Technology, Xiangtan, 2012.

[20] Y. Z. Lu, *Study on the Movement Law of Overlying Strata under the Control of Coal Gangue Paste Filling Method*, vol. 24, p. 33, Central South University, Changsha, 2006.

[21] Y. Fu, Y. Xie, D. K. Liu, Z. Li, and X. J. Zou, "New technology test of self flowing filling slurry pipeline," *Nonferrous Metals*, vol. 55, no. 5, pp. 8–11, 2003.

[22] J. W. Zhang, W. Ni, W. Hu, and X. Y. Huang, "Research on the fluidity of backfilling material with preparation of steel slag gel system," *Metal Mine*, vol. 443, no. 5, pp. 153–156, 2013.

[23] X. Zhou and P. X. Wang, "Research on the gravity-flowed convey cemented filling technology with great times line pipeline," *Metal Mine*, vol. 422, no. 8, pp. 25–28, 2011.

[24] M. F. Mao, B. L. He, W. K. Zhang, J. L. You, and Y. K. Zhao, "Analysis of the influence of filling times line on slurry pipeline gravity transportaion," *Mining and Metallurgy*, vol. 23, no. 2, pp. 15–18, 2014.

[25] D. Q. Gan, F. Gao, Y. Q. Wu, and C. Chen, "Study on concentration and pipe diameter matching of high concentration filling slurry," *Industrial Minerals & Processing*, vol. 25, no. 4, pp. 52–55, 2016.

[26] M. H. Tian, X. M. Wang, G. Q. Zhang, Q. Zhang, and S. Li, "Self-flowing transportation of the large capacity super fine tailing slurry in overlength pipelines," *Science and Technology Review*, vol. 33, no. 12, pp. 56–60, 2015.

Hindawi
Advances in Civil Engineering
Volume 2022, Article ID 6067529, 6 pages
https://doi.org/10.1155/2022/6067529

Research Article

Study and Application of Full Tailing Deep Concentration and Rapid Dewatering Technology

Liang Peng,[1,2,3] Bokun Zheng,[2,3] TengLong Huang,[2,3] Xin Zhu ,[2,3] Yang Liu,[2,3] and Fan Hu[2,3]

[1]*School of Resources and Safety Engineering, Central South University, Changsha, Hunan 410083, China*
[2]*Changsha Institute of Mining Research Co., Ltd, Changsha, Hunan 410012, China*
[3]*National Engineering Research Center for Metal Mining, Changsha, Hunan 410012, China*

Correspondence should be addressed to Xin Zhu; 1056986271@qq.com

Received 7 April 2022; Revised 8 June 2022; Accepted 27 June 2022; Published 12 July 2022

Academic Editor: Qianqian Wang

The problem of unstable full tailing sand concentration and dewatering in some mine filling systems has led to substandard bottom flow concentration of tailing sand concentration equipment, wide fluctuation ranges of filling concentration, substandard return water concentration at filling stations, and high flocculant addition cost. Through flocculation and sedimentation tests, the effect of the flocculant and sedimentation law and the effect of slurry concentration on sedimentation rate were studied, and the field application of the flocculant addition point model was verified. The results showed that (1) when the dose of the flocculant was added, the *F*1-type polyacrylamide as the flocculant made the best settling effect of the whole tailing sand in the test, as judged by comparing the falling rate of the clarified layer and the clarification degree of the supernatant. (2) With the increasing flocculant concentration, the settling speed of tailing sand gradually becomes slower; the range of the best settling concentration was 8%–18% of tailing sand concentration; and the concentration of tailing sand corresponding to the maximum solid flux was 10%–14%. (3) Relying on the site conditions of a domestic copper mine, the feed concentration was diluted from 20%–25% to 10%–12%, and the overflow water clarification test was less than 300 ppm, which verified the flocculant test and the correctness of the flocculant addition point model. The type and dosage of the flocculant as well as the feed concentration of the tailing slurry all have an effect on the flocculation and settling effect. The results of the study can provide some implications for the efficient flocculation and settlement of tailings in other mines.

1. Introduction

In recent years, due to the gradual emphasis on environmental protection and safety in production, more and more metal mines have sought the transformation of mining methods in response to the national call to improve the safety of underground mining. Filling mining method has unique advantages such as protecting the surface environment, reducing the impact of goaf collapse, and improving the recovery rate of ore. It has been widely promoted and applied [1–8].

In the field of mine filling, most metal mines or some nonmetallic mines have started to use whole tailing sand from mine processing plants for filling underground mining areas, and many scholars have conducted indepth studies on tailing sand filling [9–11]. Wang et al. [12] conducted a study on the uniaxial compressive strength of the tailing sand filler specimens at low temperature and explored the strength evolution and consolidation mechanism of the tailing sand cemented fillers at low temperature. Hou et al. [13] studied the effect of maintenance age on the basic mechanical properties of tailing sand cemented fillers and established a segmental damage intrinsic model based on the damage mechanics theory considering the maintenance age. Zhao et al. [14] investigated the early mechanical properties and damage characteristics of the tailing sand cemented fillers with different fibers and obtained a damage intrinsic model under the action of different fibers. The early mechanical

properties and damage characteristics of the tailing sand cemented fill with different fibers were investigated, and a damage instantiation model was obtained for the filler under the action of different fibers. Wu et al. [15] studied the proportioning parameters of different filling materials in the Fankou Pb-Zn mine and analyzed the variation pattern of the tailing sand slurry fluidity and pipeline conveying resistance characteristics under different conditions. In order to improve the dewatering efficiency of the tailing sand and to increase the bottom flow concentration of the slurry, flocculant was added to the thickener. Adding flocculant to the thickener can significantly improve the settling efficiency of the tailing sand slurry and can increase the bottom flow concentration at the same time [16–22]. Li et al. [23] made technical changes to the sand bin and added a flocculant dosing device, which effectively solved the problems of unclear overflow water and low filling concentration and achieved high-quality filling of the whole tailing sand. Based on FBRM (focused beam reflectance measurement) and PVM (particle video microscope) research means, Li et al. [24] studied the distribution of floc chord length, the change of floc number, and the dynamic evolution of average floc chord length and then analyzed the fragmentation mechanism of the floc structure. Wang et al. [25] carried out a measuring cylinder settling experiment, small land semi-industrial deep cone dynamic dense test, and concluded that the nonionic flocculant with a molecular weight of 12 million was most favorable for tailing sand settling.

Flocculants can solve the problems of low concentration of tailing sand slurry and nonclarification of overflow water to a certain extent, but the problems of unstable dewatering of full tailing sand concentration and the consequent substandard bottom flow concentration, the wide fluctuation range of filling concentration, and the high cost of flocculant addition in tailing sand concentration equipment are still difficult to solve, and few relevant research results have been reported. In this context, this study aimed to investigate the effect of flocculant and settling law, the effect of slurry concentration on settling rate, and the field application of the flocculant addition point model by conducting flocculation and settling test to obtain the optimal flocculant type, the best flocculation slurry concentration, and successful practice experience, which provide a reference basis for high-quality mine tailing sand filling.

2. Study on the Role of Flocculants and the Optimal Flocculant Preference

2.1. Density and Grain Size Determination of Whole Tailing Sand. The flocculation and sedimentation test study were carried out with the whole tailing sand of a domestic production copper mine, and the solid density was first determined. The solid density of the whole tailing sand was tested at a temperature of 20°C, and the solid density of the tailing sand sample was 2.805 g/cm^3. The results are presented in Table 1.

Malvin MS3000 laser diffraction particle size analyzer was used to analyze the particle size of the whole tailing sand, and the test results are shown in Figure 1.

Table 1: Determination of density of the sample at 20°C.

Sample	Density (g/cm^3)
1	2.801
2	2.806
3	2.808

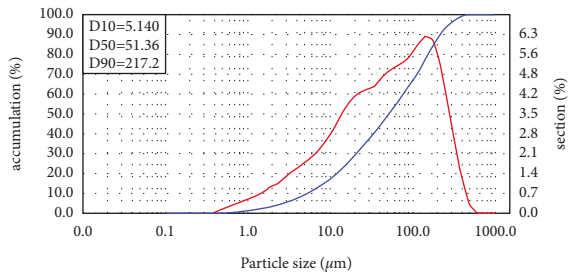

Figure 1: Differential and cumulative distribution curves of whole tail sand particle size.

Compared with the total tailings in the references [16–23], the density of the total tailings in this copper mine and the particle size of the total tailings was smaller, as a result of which there may be differences in the flocculation settlement effect.

2.2. Flocculant Preference Test. The settlement effect of the tailings is embodied in the speed of settlement. The settlement speed of tailings was calculated by observing the height of the clarification layer changing with time, and then the settlement effect of each type, different concentration, and flocculant ratio of tailings mortar were compared. The most suitable flocculant type, the best settlement concentration, and the corresponding flocculant addition were selected.

In order to select the most suitable flocculant for tailing sand, it is necessary to observe and study the settling effect of each type of polyacrylamide flocculant on the test tailing sand through selection tests to determine the flocculant type to be selected for subsequent tests and actual projects. The flocculation and sedimentation effect of the tailing sand is mainly judged by comparing the rate of fall of the clarified layer and the degree of clarification of the supernatant.

Eight different types of flocculants from a flocculant manufacturer, *F*1, *F*2, *F*3, *F*4, *F*5, *F*6, *F*7, and *F*8, were selected for this test, of which *F*1, *F*2, *F*3, and *F*4 were cationic type and *F*5, *F*6, *F*7, and *F*8 were anionic type, as shown in Figure 2. The flocculants were prepared into 1000 ppm concentration.

The tailing slurry with 15% mass concentration was prepared in 1 L cylinder as a control group to observe natural settling. Eight groups of tailing sand slurry with 15% mass concentration were prepared, and different types of flocculant solutions were added to each group of tailing sand slurry at 15 g/t. The hole stirrer was placed at the bottom of the measuring cylinder and was lifted twice quickly and then once slowly to ensure that the settling conditions of each group of tailing sand were the same except for the different types of flocculants. While the

stirrer left the liquid surface, the timing was started, and the heights of the clarified layers at 30 s, 60 s, 120 s, and 180 s were recorded as shown in Table 2, and the effect of settling of tailing sand was observed.

According to the test observation, the tailing sand was fine, and the natural settling speed was slow; therefore, it was not possible to observe an obvious clarification layer, but the effect was significant after adding the flocculant. It can be determined that it is feasible and effective to improve the settling effect of the tailing sand by adding flocculant.

The settling of tailing sand is divided into two stages,fast settling and compression settling. When the tailing slurry starts to settle down, it enters the fast settling stage, and the duration is generally 30 s to 2 min. With the same dosage of flocculant added, the higher the concentration, the slower the settling speed of the fast settling stage, and the longer the duration of the fast settling stage. In the fast settling stage, the sediment layer and the liquid surface of the clarified layer can be observed at the bottom. When the liquid surface of the clarified layer coincides with the liquid surface of the sediment layer and the settling speed is lower than 30 mm/min, it enters the compression settling stage.

In this test, the rapid settling phase was completed within 60 s, so the settling speed within 60 scan reflects the superiority of its settling effect. The bar graph of flocculation and sedimentation for each group is shown in Figure 3.

It can be seen in Figure 4 that, in the *F*1, *F*8, *F*2, and *F*4 flocculant group ,the settling speed is faster than in other groups, and it is observed that the clarification of the supernatant is best in the *F*1 group, slightly worse in *F*2 and *F*4 groups, and the worst in the *F*8 group; therefore, when the added flocculant dose is certain, *F*1-type polyacrylamide as flocculant makes the best settling effect of test full tailing sand.

Compared with the flocculation effect in [16–23], the flocculation sedimentation effect of the cationic flocculant was better than that of the anionic flocculant, indicating that the properties of the tailings were more suitable for the cationic flocculant. The flocculation settling velocity was slower than the tailings in the references [16–23], which was related to the smaller density of the total tailings.

3. Study on the Effect of Slurry Concentration on Flocculation and Sedimentation Rate

The concentration of tailings produced by the concentrator and the amount of flocculant added also have an important impact on the settlement of tailings. In general, the lower the concentration of tailings produced by the concentrator, the faster the settling velocity after entering the sand bin. Within a certain range, the larger the flocculant dosage is, the faster the sedimentation rate is. The concentration of the tailing sand output of the processing plant is generally determined according to the beneficiation process, and the tailing sand treatment as a downstream process does not require the beneficiation process to change to achieve the best results for itself, especially when such changes require a certain cost. Flocculation does not get better with increasing amounts

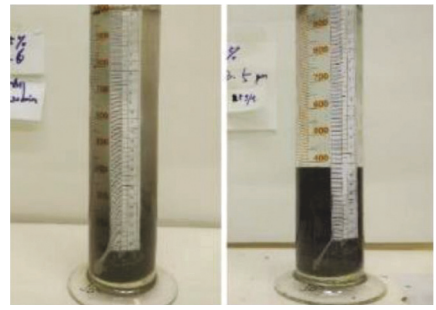

Figure 2: Comparison of natural settling and flocculation settling.

of flocculant. On the one hand, the increase of flocculant addition means the increase of cost. On the other hand, the study also found that, after an increase of the flocculant amount, the settlement of tailings would not change significantly or may even become worse.

The laboratory test aims to study the effect of flocculant settling when different concentrations of tailing slurry are added with different amounts of flocculant and to determine the best amount of flocculant to be added for each concentration of tailing sand to provide a basis for the modification of the filling system.

According to the results of the flocculant selection test, weigh the corresponding tailing sand and water volume and prepare 8%, 10%, 12%, 15%, 20%, and 25% tailing sand slurry, respectively. The total volume should be ensured to be 1 L after the completion of the preparation, and the flocculant addition amounts are 5 g/t, 10 g/t, 15 g/t, 20 g/t, and 25 g/t, respectively. The corresponding flocculant solution amounts are added into the tailing sand slurry with a pipette. The hole stirrer was put to the bottom of the measuring cylinder and lifted twice quickly and then once slowly to ensure that the settling conditions of each group of tailing sand were the same except for the different amounts of flocculants added.

While the stirrer was left on the liquid surface, the time was started, the height of the clarified layer at 10 s, 20 s, 30 s, 45 s, 60 s, 90 s, 120 s, 180 s, and 240 s was recorded, and the clarity of the supernatant during settling was observed and judged qualitatively.

For example, at 8% tailing sand concentration, the settling effect is already obvious at 5 g/t flocculant, so there is no need to test the settling effect at a higher flocculant addition for this concentration of tailing sand; for example, at 12% tailing sand with 5 g/t flocculant, the settling effect is not good, so there is no need to test the settling effect at a higher flocculant addition. Therefore, there was no need to test 5 g/t of flocculant when the concentration of tailing sand was higher. In the end, 19 sets of tests were conducted, and 18 sets of data were measured, among which the clarified layer was not observed for the tailing sand slurry with a concentration of 15% and a flocculant addition of 10 g/t.

The best settling effect of 8% tailing slurry was achieved at 5 g/t flocculant addition, 10% tailing slurry at 10 g/t flocculant addition, 12%, 15%, and 20% tailing slurry at 15 g/t flocculant

Table 2: Recording the height of the clarification layer for the flocculant test (unit: mm).

Type Time (s)	*F*1	*F*2	*F*3	*F*4	*F*5	*F*6	*F*7	*F*8
30	70	42	71	50	70	60	68	74
60	121	83	119	95	110	107	120	117
120	150	139	148	143	154	156	164	163
180	170	153	171	163	170	172	178	173
Degree of clarification	Good	Average	Good	Poor	Poor	Average	Poor	Average

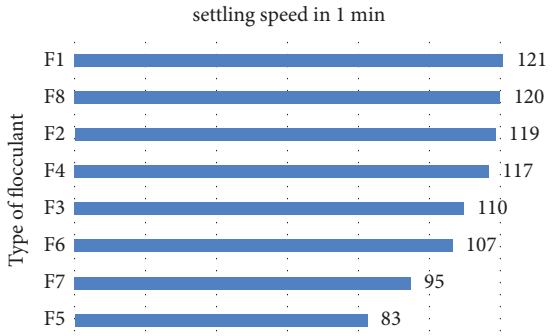

Figure 3: Comparison of flocculation and sedimentation speed (unit: mm/min).

addition, and 25% tailing slurry at 20 g/t flocculant addition. The best settling data for different concentrations were compared, and the curves shown in Figure 4 were obtained.

Its settling velocity was obtained by calculation as shown in Figure 5.

Through the test data, it can be intuitively seen that, with the increasing concentration, the settling speed of each group of tailing sand gradually becomes slower, when the concentration is 8%, and only 5 g/t of flocculant is added. The settling height is 188 mm in 30 s, which completes the process of rapid settling and turns into compression settling, and its settling speed is 376 mm/min; while when the concentration of tailing sand is 25% and the amount of flocculant added is 20 g/t, the settling speed is only 11 mm/min, which is 1/34 of the settling speed of 8% tailing sand slurry, so it can be seen that the size of the initial concentration has a great influence on the speed of settling. On the other hand, the amount of flocculant consumed during the settling of low concentration tailing slurry is also less, and the cost is lower. Therefore, according to the test results, the secondary dilution of the tailing sand of the processing plant can be designed to reduce its concentration to a reasonable range during the use of the subsequent filling system.

Compared with the tailings in the references [16–23], the initial concentration of tailings slurry in this copper mine was higher, and the maximum concentration was about 25%. At the same time, the optimal flocculant dosage was 20 g/t, and the dosage was large. In references [16–23], the tailing slurry concentration was about 5%~18%, the flocculant dosage was about 7~16 g/t, the the dosage was small, and the flocculant cost was low. Therefore, the dilution of tailing slurry can improve the flocculation effect and reduce the dosage of flocculant and can reduce the cost.

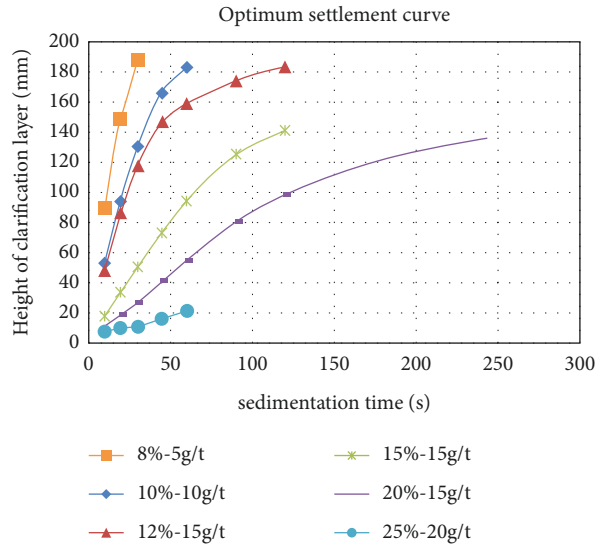

Figure 4: Settlement curve.

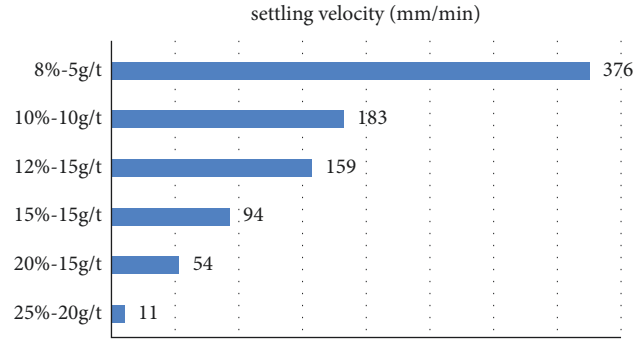

Figure 5: Settlement curve.

4. Coagulant Addition Point Model and Application Validation

4.1. Optimal Dilution Concentration and Solid Flux of the Concentrator. Secondary dilution concentration is the key research direction of flocculation and sedimentation, and many studies mainly focus on the optimal dilution concentration of the study target mines, lacking general and generic studies of similar mines. The design tailing concentration, experimental optimum dilution concentration, and actual postdilution concentration vary from mine to mine.

According to the definition of solid flux, the physical amount of a certain solid passed vertically through a unit

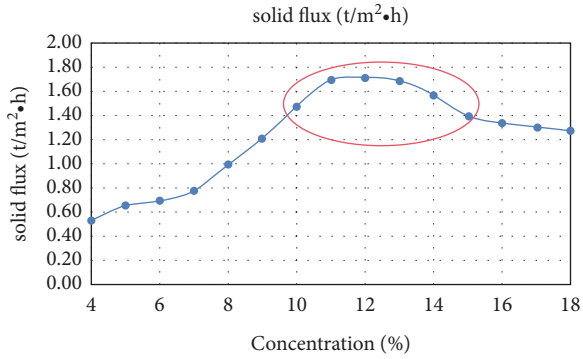

Figure 6: Solid flux-feed concentration curve.

area per unit time. A maximum value exists because the lower the concentration of the slurry, the faster the settling speed, but, at the same time, the lower the mass per unit volume of the slurry. The larger the solid flux, the greater the concentration processing efficiency and the faster the concentration rate.

Combining the relationship between the feed concentration and settling velocity mentioned in Section 3, the solid flux of the slurry at different feed concentrations was calculated and the variation curve of solid flux vs. feed concentration was plotted as shown in Figure 6.

Since the settling rate of full tailings is affected by the mass concentration of tailings slurry, regarding tailing settling experiments and related flocculation and settling studies, the range of optimal settling concentration is generally 8% to 18% of tailings concentration. It can be seen from Figure 7 that the maximum solid flux corresponds to 10% to 14% of tailings concentration. Therefore, to take into account the treatment efficiency and dilution cost,based on the study of the rapid dewatering flocculant addition system of the thickener, the mathematical model of solid flux and the best dilution concentration of incoming tailings from common nonferrous metal ores are suggested to be 10%–16%.

4.2. Center Feed Barrel Flocculant Addition Point Model and Application Validation. Based on the site conditions of a domestic copper mine, a small feed bucket device was designed to flocculate and settle the tailing sand slurry for secondary dilution according to the feed concentration range. The mine tailing sand solid density is 2.8 t/m^3, about 20%–25% mass concentration of low concentration tailing sand slurry into the top center of the thickener small feed bucket device, to seek the best performance of flocculant concentration and secondary dilution concentration, to develop a highly efficient dynamic concentration and dewatering test program suitable for the site concentration device, and to optimize the location and number of flocculant addition point.

A model of the center feed bucket flocculant addition point is shown schematically in Figure 7.

The flocculant preparation concentration was diluted to about 0.1% in the central feed barrel for multipoint addition, and the location and depth of the addition point were

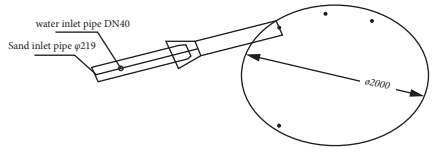

Figure 7: Schematic diagram of the flocculant addition point model for the central feed drum.

Figure 8: Overflow effect diagram.

optimized and adjusted according to the site conditions. The feed was diluted from 20%–25% to 10%–12% based on the self-dilution and the appropriate addition of external water according to the fluctuation of the feed volume to achieve the best flocculation and sedimentation effect and also to ensure a large solid flux site The results show that the overflow water clarification test is less than 300 ppm, and the overflow effect graph is shown in Figure 8.

5. Conclusion

By carrying out flocculation and settlement tests on filled tailings, the effect of flocculants and settlement laws and the effect of concentration on settlement rate and field application verification were studied, and the following conclusions were obtained:

(1) When a certain dose of flocculant was added, it was judged that *F*1-type polyacrylamide as a flocculant made the best settling effect of the whole tailing sand in the test by observing and comparing the falling rate of the clarified layer and the clarification degree of the supernatant.

(2) With the increasing concentration, the settling speed of the tailing sand gradually becomes slower, and the optimal settling concentration ranges from 8% to 18% for the tailing sand and 10% to 14% for the maximum solid flux. Subsequent secondary dilution of the tailings sand is required to improve the settling speed and solid flux.

(3) Relying on the site conditions of a domestic copper mine, the feed concentration was diluted from 20%–25% to 10%–12%, and the overflow water clarification test was less than 300 ppm, which verified the correctness of the flocculant test and the addition point model.

The type and dosage of flocculant as well as the feed concentration of the tailings slurry all have an effect on the

flocculation and settling effect. The results of the study can provide some implications for the efficient flocculation and settlement of tailings in other mines.

Data Availability

The data used to support the findings of this study are included within the article.

Conflicts of Interest

The authors declare that they have no conflicts of interest.

Acknowledgments

This work was supported and financed by the National Key Research and Development Program of the 13th Five-Year Plan (nos. 2018YFC0604603 and 2018YFC0604606), all of which are greatly appreciated.

References

[1] W. Zhiyuan, Z. Wenru, and L. Qianyong, "Research and practice on safe and efficient mining of ore bodies under complex conditions," *Mining Research and Development*, vol. 38, no. 5, pp. 10–12, 2018.

[2] Z. Yongfeng, Z. Xuongtian, and M. Hongfu, "Research on efficient mining methods for slowly inclined medium-thick ore bodies," *Metal Mining*, vol. 6, pp. 19–23, 2016.

[3] Z. Tongtong, W. Yongyan, and Y. Zhuoqun, "Effect of loading rate on the strength characteristics of layered fillers," *Science Technology and Engineering*, vol. 21, no. 34, pp. 14535–14541, 2021.

[4] X. Wenbin, L. Bin, and W. Yubin, "Experimental design and analysis of permeability characteristics of all-tailed sand colluvial fill," *Mining Research and Development*, vol. 41, no. 12, pp. 99–103, 2021.

[5] C. Jie, C. Yunkai, and H. Qingheng, "Study on the rheological properties of high sand filling materials[J]," *Mining Research and Development*, vol. 41, no. 12, pp. 109–113, 2021.

[6] Z. Aiqing, L. Jinyun, W. Aixiang, and Z. Y. Wang, "Experimental study on the mechanism of whole tailing sand vibratory dewatering based on bulk dynamics," *Mining Research and Development*, vol. 41, no. 12, pp. 119–123, 2021.

[7] W. Fan, H. Bin, and H. Yafei, "Calculation and application study of friction loss of paste-filled slurry pipe transport," *Journal of Mining and Safety Engineering*, vol. 38, no. 6, pp. 1158–1106, 2021.

[8] Z. Meidao, R. Yunzhang, and X. Wenfeng, "Orthogonal test for optimization of all-tailed sand paste filling ratio," *Gold Science and Technology*, vol. 29, no. 5, pp. 740–748, 2021.

[9] R. Zhuen, W. Aixiang, and W. Yiming, "Multi-objective optimization of key performance indicators for all-solid waste paste," *Journal of Engineering Science*, pp. 1–9, 2020.

[10] C. Gezhong, L. Cuiping, and R. Zhuen, "Effect of flocculation conditions on floc structure and solid-liquid separation efficiency in paste filling," *Chinese Journal of Nonferrous Metals*, pp. 1–20, 2020.

[11] C. Chong, L. Wu, and Z. Yalei, "Research and application of upward-downward nested paste-filled mining technology," *Mining Research and Development*, vol. 39, no. 7, pp. 24–27, 2019.

[12] W. Binwen, G. Su, and D. Pingbo, "Experimental study on consolidation characteristics of tailing sand colluvial fillings in alpine regions," *Chinese Journal of Nonferrous Metals*, pp. 1–12, 2014.

[13] H. Yongqaing, Y. Shenghua, and C. Yong, "Uniaxial compressive stress-strain relationship and its damage intrinsic model for tailing sand cemented fillers," *Materials Guide*, no. 7, pp. 1–15, 2022.

[14] Z. Kang, S. Yufeng, and Y. Xiang, "Early mechanical properties and damage intrinsic modeling of tailing sand colluvial fill under the action of different fibers," *Journal of Rock Mechanics and Engineering*, vol. 41, no. 2, pp. 282–291, 2022.

[15] W. Junhui, X. Youwei, and L. Xiaojing, "Experimental study on the characteristics of high-concentration tailing sand filling materials in Van Kou lead-zinc mine," *Mining Research and Development*, vol. 41, no. 7, pp. 135–139, 2021.

[16] J. Xiaodong, Z. Gengjie, and S. Laifa, "Effect of flocculants on the performance of colloidal filler of ultrafine tailings," *Metal Mining*, vol. 10, pp. 61–66, 2021.

[17] S. Can, W. Xiaojun, and W. Xinmin, "Study on the law and mechanism of APAM single consumption on flocculation of particles of different grain size in full tailing sand flocculation and sedimentation," *Mining Research and Development*, vol. 40, no. 5, pp. 67–74, 2020.

[18] Z. Liyi, Y. Peng, and L. Wensheng, "Experimental study on the influencing factors of flocculation and sedimentation and densities of all-tailed sand," *Mining Research and Development*, vol. 41, no. 8, pp. 59–64, 2021.

[19] L. Qi, C. Youhua, and L. Dongrui, "Prediction of technical parameters of full tailing sand densities based on static settlement test," *Gold Science and Technology*, vol. 29, no. 2, pp. 266–274, 2021.

[20] Y. Zilong, T. Yuye, and F. Jianxin, "Optimal flocculant selection and floc NMR analysis of all-tailed sand," *Mining Research and Development*, vol. 41, no. 4, pp. 136–140, 2021.

[21] Z. Gengjie, Z. Wangcheng, and H. cheng, "Study on the application of flocculants in vacuum filtration and dewatering of gold tailings," *Metal Mining*, vol. 4, pp. 45–52, 2021.

[22] W. Zhenjiang, Y. Xiaobing, and L. Litao, "Selection and optimization of flocculation and settling parameters for all-tailed mortar based on RSM-BBD," *Chinese Journal of Nonferrous Metals*, vol. 30, no. 6, pp. 1437–1445, 2020.

[23] L. Chengwei, Z. Xin, and P. Liang, "Design and application study of a full tailing sand filling system technology for an iron ore mine," *Mining Research and Development*, vol. 42, no. 3, pp. 158–142, 2022.

[24] L. Cuiping, C. Zhongge, and R. Zhuen, "Dynamic evolution law of floc structure during the whole process of tailing sand densification," *Chinese Journal of Nonferrous Metals*, pp. 1–18, 2022.

[25] W. Hongjiang, W. Xiaolin, and Z. Xi, "Dynamic flocculation concentration test of ultrafine whole tailing sand with deep cone," *Journal of Engineering Science*, vol. 44, no. 2, pp. 163–169, 2022.

Hindawi
Advances in Civil Engineering
Volume 2022, Article ID 8463754, 10 pages
https://doi.org/10.1155/2022/8463754

Research Article

Experimental Study on Dynamic Characteristics of Annular Coal Mine Sandstone after Different Temperatures

Qi Ping,[1,2,3] **Yulin Wu**,[2,3] **Qi Gao**,[2,3] **Shuo Wang**,[2,3] **Kaifan Shen**,[2,3] **Chen Wang**,[2,3] **and Xiangyang Li**[2,3]

[1]*State Key Laboratory of Mining Response and Disaster Prevention and Control in Deep Coal Mine, Anhui University of Science and Technology, Huainan, Anhui 232001, China*
[2]*Research Center of Mine Underground Engineering, Ministry of Education, Anhui University of Science and Technology, Huainan, Anhui 232001, China*
[3]*School of Civil Engineering and Architecture, Anhui University of Science and Technology, Huainan, Anhui 232001, China*

Correspondence should be addressed to Qi Ping; ahpingqi@163.com

Received 28 March 2022; Revised 21 April 2022; Accepted 22 April 2022; Published 9 May 2022

Academic Editor: Lijie Guo

The rock mass is the main carrier of underground engineering. Many rock engineering involves rock mass excavation, and the temperature of deep rock mass increases with the depth rising. The study on the dynamic mechanical properties of annular coal mine sandstone under different temperatures has important guiding significance for mine excavation and rock engineering design and construction. To research the effect of high temperatures on the physical and dynamic mechanical characteristics of annular coal mine sandstone specimens, the physical parameters of the samples after the heating temperature from 25°C to 500°C were tested, and the dynamic splitting tests under the same loading condition were conducted by using SHPB test equipment. The findings indicate that with the temperature rising, the volume of samples increases, the mass and density decrease, and the change rate of the physical parameters of the annular sample is a little greater than that of the intact sample; as the temperature goes up, the dynamic tensile strength increases first and then decreases, there is a quadratic polynomial relationship with temperature; both the dynamic strain and the average strain rate decrease first and then increase as the temperature grows, showing a quadratic polynomial relationship with temperature; the damage degree of the annular and intact samples become worse as the temperature improved, and the fragments of specimen increase obviously after 200°C.

1. Introduction

At present, underground space has been continuously expanded and developed. Shallow mineral resources have been unable to meet human needs, and deep mining has become an inevitable trend of mining development. The underground high temperature and strong disturbance aggravate the possibility of frequent disasters in deep engineering and the difficulty of prediction, and the geological environment of many rock engineering involves the mechanical properties of rock after high temperature. Rock mass excavation is often needed in tunnels, mine tunnels, and underground chambers. With the mining depth increasing, the temperature of deep rock mass will also increase, which can reach dozens or even several hundred degrees. When rock engineering is subjected to fire, explosion, and complex geothermal geological conditions, the mechanical characteristics of rock after different temperatures should be considered. Therefore, the research on the dynamic mechanical properties of annular coal mine sandstone after different temperatures has important guiding significance for the safety production and disaster prevention of rock engineering.

Scholars at home and abroad have conducted a lot of experimental research studies on the mechanical properties of rock under and after high temperature. In static mechanics, You [1] used marble samples with different inner diameters to conduct conventional triaxial compression tests

when the inner pore pressure was 0 and analyzed the influence of nonuniform stress distribution in the sample on the carrying capacity and deformation characteristics of the test piece. Xiao et al. [2] carried out uniaxial acoustic emission experiments on rock test pieces with holes and analyzed the relationship between the mechanical properties of rock samples and the position and diameter of holes. Yang [3] analyzed the crack propagation process of marble under different stresses by conducting a uniaxial compression test on samples with a single hole. Lian [4] performed uniaxial and triaxial compression experiments on granite test pieces with different apertures to analyze the intensity, deformation, and damage characteristics of granite test pieces under different confining pressure conditions. Wu et al. [5] conducted loading and unloading tests on thick-walled cylindrical limestone samples under different internal pressures and analyzed the failure mechanism of the samples under pressure relief conditions in holes. Zhu et al. [6] studied the influence of pore core distance and dip angle on sandstone intensity, deformation characteristics, and fracture evolution process by carrying out a uniaxial compression experiment on plate test pieces with prefabricated double circular holes. Du et al. [7] implemented uniaxial compression experiments on slab sandstone samples with prefabricated oval holes and discovered that the strength and deformation parameters of sandstone test pieces with holes were reduced compared with intact sandstone. The crack propagation process is described from the macroscopic point of view, without in-depth analysis from the microscopic point of view. Zhang et al. [8] performed uniaxial compression experiments on the marble of different numbers and diameters of holes and found that the peak strength of samples gradually decreased with the numbers and diameters of holes increasing. Su et al. [9] researched the relationship between mechanical characteristics and temperature by carrying out a uniaxial compression experiment on fine sandstone samples after high temperatures from 400°C to 1000°C. Du et al. [10] investigated the variation law of mechanical properties of granite with temperature by conducting a uniaxial compression experiment on granite cylindrical test pieces at room temperature and after high temperature treatment from 200°C to 800°C. The test pieces used in the experiment are not from the same rock, and the mineral composition inside the rock is different, which may cause the deviation and dispersion of the results. Zhang [11] carried out 5-stage uniaxial compression experiments under different loading rates on limestone samples at 200°C. Zhu et al. [12] performed a uniaxial compression experiment on test pieces from room temperature to 800°C and analyzed the deformation, intensity, and damage properties of fractured sandstone. Zhao [13] conducted uniaxial compression experiments on brittle rocks with circular holes and studied the fracture evolution process of brittle rocks with prefabricated circular holes. Chen [14] implemented uniaxial compression experiments on dry and saturated rock samples, respectively, and investigated the influence of saturated water on mechanical parameters of complete disc and ring rock samples.

In terms of dynamic mechanics, Sha [15] simulated the destruction process of rock ring samples to analyze the influence of the ratio of inner and outer diameter and loading rate of rock ring samples on the failure form of the sample. You [16] conducted a Brazilian splitting test on intact and annular specimens with different inner diameters of four rocks, to investigate the effect of water saturation on the intensity of rocks. Huang [17] carried out Brazilian splitting tests on intact and porous granite disc test pieces at normal temperature and after high temperature treatment from 150°C to 900°C, to research the relationship between mechanical properties and temperature. Zhang et al. [18, 19] performed Brazilian splitting tests on complete disc and annular sandstone samples with different pore sizes, the influence of the ratio of inner and outer pore sizes on the mechanical properties and damage characteristics of rock samples were studied. The effect of temperature change on rock mechanical properties is not involved. Wang et al. [20] carried out a radial compression test of annular granite under temperature-humidity cycling conditions by cooling the ring granite after being treated at a high temperature from 100°C to 700°C and immersing it in water temperature from 10°C to 70°C for maintenance. Ping et al. [21] used SHPB test equipment to carry out impact compression experiments on limestone specimens after temperature treatment from 25°C to 800°C under the same loading conditions, and the influence law of temperature on dynamic mechanical parameters was analyzed. Chen [22] conducted Brazilian splitting experiments on sandstone samples after different high temperatures and analyzed the damage evolution mechanism of sandstone under different temperatures. Xu and Liu [23] researched the changing rules of dynamic mechanical parameters by conducting impact compression tests on marble after different temperature treatments from 25°C to 1000°C. Ping et al. [24] conducted impact compression experiments on the coal mine roadway sandstone treated with water bath at different temperatures and analyzed the effects of water bath at different temperatures on the physical and dynamic mechanical characteristics of the rock. Du et al. [25] operated impact compression experiments on red sandstone samples and studied the relationship between dry wet cycle and mechanical characteristics of samples. Li et al. [26] conducted static and dynamic splitting experiments on marble annular samples of different inner diameters and analyzed the relation between the intensity and the ratio of internal diameter to external diameter under different loading rates.

The above-mentioned scholars have done a large number of experimental researches in exploring the static mechanical characteristics of rocks with holes and the static and dynamic mechanical characteristics of intact rocks after high temperatures, but the dynamic characteristics of rocks with holes after different heating temperatures need to be further studied. To analyze the effect of different heating temperatures on the physical and dynamic properties of annular sandstone, the physical parameters of annular and intact samples at normal temperature and after temperature treatment from 100°C to 500°C were measured before and after different temperatures. Under the same loading conditions, dynamic splitting tests of sandstone samples after different heating

temperatures were conducted by using SHPB test equipment.

2. Specimen Preparation and SHPB Test Device

2.1. Specimen Processing. The sandstone used in this test comes from Dingji Coal Mine in Huainan City. To strengthen the contrast of experiments, all samples are taken from the same stone. Based on the experiment procedure [27, 28], the intact sample with a diameter of 50 mm and a height of 25 mm and the annular sample with an external diameter of 50 mm, a height of 25 mm, and an inner diameter of 10 mm are processed from the same rock block.

2.2. Specimen Heating. Sandstone specimens are heated at high temperatures in a box-type resistor furnace. Firstly, there is a certain gap between the test pieces, and the annular and intact sandstone test pieces are evenly placed in the furnace. Close the furnace door and heat until the specified temperature is reached. Temperature setting points are 100°C, 200°C, 300°C, 400°C, and 500°C, respectively, and a group of normal temperature specimens are added for a comparative test, a totally 6 kinds of temperature gradients. In order to heat the specimens evenly and have the same temperature field inside and outside, the specimens are heated to a set temperature and kept at a constant temperature for 3 h. Finally, close the heating system and let the heated sandstone samples cool naturally to normal temperature in the furnace, open the furnace door and take out the samples, and record the quality, diameter, height, and aperture of samples.

2.3. SHPB Test Equipment. The SHPB test equipment of the State Key Laboratory of Mining Response and Disaster Prevention and Control of Deep Coal Mine is used to conduct dynamic splitting tests on annular and intact sandstone samples after experiencing different temperatures.

This experimental equipment consists of an incident rod, transmission rod, absorber rod, oscilloscope recorder, and super dynamic strain gauge. During the test, a spindle-type bullet is used and the bullet is pushed into the same location in the launching chamber tube every time, and impact pressure is adjusted to 0.3 Mpa each time, the sandstone samples are subjected to dynamic splitting tests under the same loading conditions, the sample holds as shown in Figure 1.

Figure 1: The clamping state of specimens.

3. Basic Physical Characteristics of Samples after Different Heating Temperatures

3.1. The Change of Sample Color. The color changes of annular sandstone samples after different treating temperatures are shown in Figure 2.

Figure 2 shows that the color of the specimen does not change significantly if the heating temperature is below 200°C. When the temperature reaches 300°C, the color of the sandstone surface begins to change, from gray-black to light reddish-brown. As the temperature goes up, the color gradually changes to dark reddish-brown, tapping the specimen gently makes a crisp sound.

3.2. The Basic Physical Parameters of Samples. The size and mass of annular and intact sandstone specimens at normal temperature and after different temperatures are measured one by one. The basic physical parameters are shown in Tables 1 and 2.

3.3. Specimen Volume, Mass, and Density Change. The change of volume expansion rate of a specimen with temperature is shown in Figure 3.

Figure 3 shows that the volume expansion rates of both specimens increase as the temperature improved. The volume of the two specimens is not significantly affected by temperature, and the volume expansion rate is relatively small in the range of 100°C~200°C, which may be due to the expansion of mineral grains in the sandstone when they are heated, occupying the initial micropores and microcracks inside samples, therefore, the volume increase rate is relatively small. The volume increase rate of the two specimens grows relatively fast if the temperature exceeds 200°C. As the temperature rises, the original micropores and cracks in the sample exceed the thermal stress limit of the structure, and new micropores and microcracks begin to emerge in the sandstone, resulting in a relatively large volume increase rate of samples. Besides, the volume increase rate of the annular test piece is a little higher than that of the intact test piece.

The relation between volume expansion rate and temperature is a quadratic polynomial, as shown in the following formula:

$$\begin{cases} V_{T1} = 1.0414 \times 10^{-6} T^2 + 0.0018T - 0.0230 \left(R^2 = 0.9877\right), \\ V_{T2} = 1.5020 \times 10^{-6} T^2 + 0.0012T - 0.0154 \left(R^2 = 0.9837\right), \end{cases} \tag{1}$$

where V_{T1} and V_{T2} are the volume expansion rate of annular and intact specimens, respectively, and T is the treating temperature.

The change of mass loss rate of samples with temperature is shown in Figure 4.

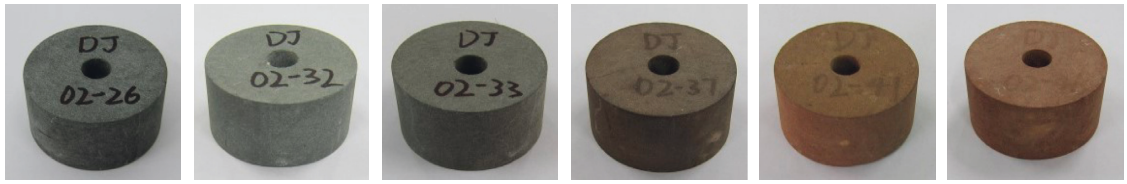

Figure 2: Color change of annular samples with the heating temperature: (a) 25°C, (b) 100°C, (c) 200°C, (d) 300°C, (e) 400°C, and (f) 500°C.

Table 1: Basic physical parameters of annular samples.

Temperature/°C	Specimen number	Before heating				After heating			
		Aperture (mm)	Diameter (mm)	Height (mm)	Quality (g)	Aperture (mm)	Diameter (mm)	Height (mm)	Quality (g)
25	DJ02-25	9.97	50.01	24.97	119.59	Unheated			
	DJ02-26	10.02	50.09	24.88	118.98				
100	DJ02-29	10.03	50.04	24.99	119.88	9.98	50.08	25.02	117.97
	DJ02-30	9.91	50.09	25.02	119.42	9.90	50.11	25.05	117.69
200	DJ02-35	10.05	50.03	25.03	119.95	9.98	50.01	25.12	116.53
	DJ02-36	9.94	50.09	24.99	118.75	9.85	50.11	25.05	115.30
300	DJ02-38	9.94	50.09	25.01	119.78	9.81	50.13	25.11	115.73
	DJ02-39	10.02	50.12	25.00	121.49	9.91	50.12	25.10	117.53
400	DJ02-41	10.02	50.14	24.96	120.67	9.86	50.21	25.08	116.23
	DJ02-42	9.95	50.08	25.03	118.08	9.79	50.18	25.13	114.07
500	DJ02-46	10.04	50.08	25.00	119.99	9.80	50.20	25.10	114.72
	DJ02-47	9.93	50.07	24.98	119.39	9.74	50.17	25.13	113.98

Table 2: Basic physical parameters of intact samples.

Temperature/°C	Specimen number	Before heating			After heating		
		Diameter (mm)	Height (mm)	Quality (g)	Diameter (mm)	Height (mm)	Quality (g)
25	DJ02-01	50.04	24.95	125.81	Unheated		
	DJ02-02	50.05	24.92	122.17			
100	DJ02-07	50.08	24.92	125.82	50.07	24.96	124.15
	DJ02-08	50.08	24.91	125.48	50.11	24.92	123.70
200	DJ02-09	50.06	24.91	125.21	50.05	24.96	120.68
	DJ02-10	50.03	24.95	125.38	50.06	24.97	121.88
300	DJ02-13	50.10	24.91	124.61	50.14	25.01	120.43
	DJ02-16	50.08	25.08	126.94	50.10	25.18	122.93
400	DJ02-18	50.08	25.00	125.76	50.15	25.13	121.41
	DJ02-19	50.10	25.05	125.14	50.19	25.14	120.62
500	DJ02-21	50.07	24.90	121.30	50.18	25.03	116.63
	DJ02-22	50.04	24.94	125.05	50.14	25.11	119.84

Figure 4 shows that the mass loss rate of both specimens rises as the temperature goes up, and the mass loss rate of specimens increases greatly when the temperature rises from normal temperature to 300°C. When the temperature exceeds 300°C, the increase in mass loss rate is relatively small. Analysis reasons: when the temperature is low, the free water and bound water in the specimen evaporate and escape, and when the temperature continues to rise, the cracks in the specimen increase, the structure deteriorates, and the separation of granular debris, leading to the mass loss of samples.

The mass loss rate of the test piece has a quadratic polynomial relationship with the heating temperature, as shown in the following formula:

$$\begin{cases} M_{T1} = -1.7842 \times 10^{-5} T^2 + 0.0179T - 0.2756 \left(R^2 = 0.9794\right), \\ M_{T2} = -2.0265 \times 10^{-5} T^2 + 0.0182T - 0.3291 \left(R^2 = 0.9813\right), \end{cases} \quad (2)$$

where M_{T1} and M_{T2} are the mass loss rate of annular and intact specimens, respectively, and T is the heating temperature.

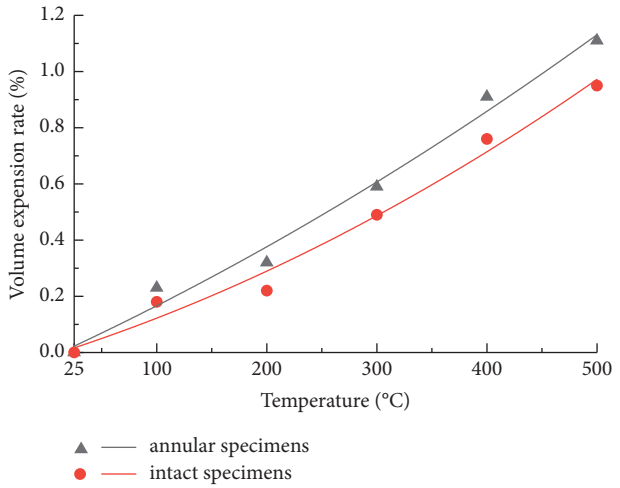

Figure 3: Volume expansion rate of samples after different temperatures.

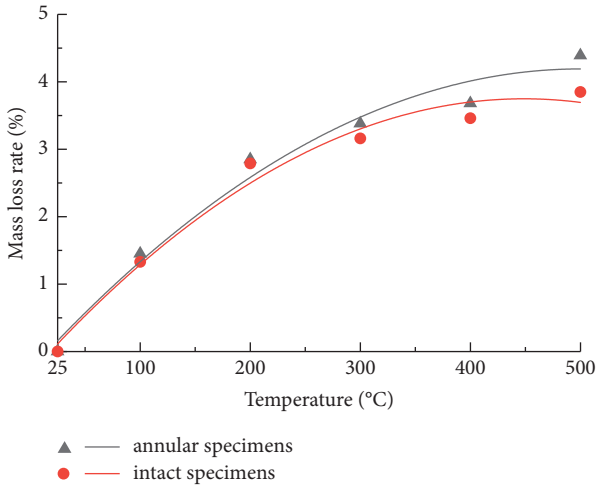

Figure 4: Variation in the mass of samples with heating temperature.

The change of density reduction rate of the specimen with temperature is shown in Figure 5.

Figure 5 shows that the density reduction rate of the annular specimen is slightly greater than that of the intact specimen, and the density reduction rate of both specimens increases as the temperature grows. The density reduction rate of the two kinds of specimens increases greatly when the temperature changes from room temperature to 300°C, and if the temperature exceeds 300°C, the density reduction rate of the two kinds of specimens increases relatively small. The decrease of specimen density is caused by the mass and volume changes of the specimen under the effect of temperature. As the temperature goes up, the mass of the specimen decreases and the volume increases, resulting in a decrease in the density of the specimen.

The decrease rate of specimen density increases as a quadratic function of temperature, as shown in the following formula:

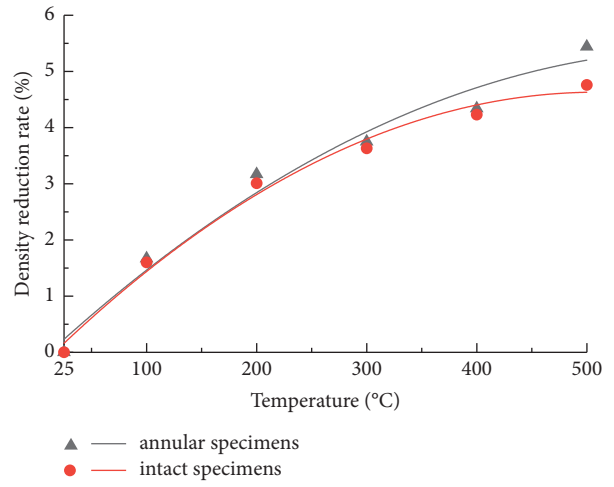

Figure 5: Density reduction rate of sandstone specimens after different temperatures.

$$\begin{cases} \rho_{T1} = -1.4844 \times 10^{-5} T^2 + 0.0183T - 0.2155 \left(R^2 = 0.9774\right), \\ \rho_{T2} = -1.9059 \times 10^{-5} T^2 + 0.0194T - 0.3138 \left(R^2 = 0.9894\right), \end{cases} \tag{3}$$

where ρ_{T1} and ρ_{T2} are the density reduction rates of annular and intact specimens, respectively, and T is the treating temperature.

3.4. Mineral Composition and Microstructure of Sample. X-ray diffraction and scanning electron microscope experiments were performed on SHPB impact test sandstone fragments at normal temperature and after high temperature. The typical XRD patterns and SEM pictures of sandstone after different temperatures are shown in Figures 6 and 7.

Figure 6 shows that the components of sandstone are mainly Quartz-SiO_2, Kaolinite-$Al_4(OH)_8(Si_4O_{10})$, Albite-$Na(AlSi_3O_8)$, and illite-$K(Al_4Si_2O_9(OH)_3)$ at normal temperature, accounting for 29.5%, 31.2%, 14.0%, and 25.3%, respectively. Microcline-$K(AlSi_3O_8)$ is formed when the temperature rises to 200°C. The composition of sandstone at 500°C is basically the same as that at normal temperature, but the content is different.

Figure 7 shows that there are micropores and microcracks in the sandstone at normal temperature. When the heating temperature rises from normal temperature to 200°C, the mineral grains in the sandstone expand when they are heated, occupying the primary micropores and microcracks inside test pieces, so the compactness and internal structure of the test piece are enhanced. When the temperature reaches 300°C, the primary micropores and microcracks in the sandstone test piece surpass the thermal stress limit of the structure, and the test piece begins to generate new microcracks. As the temperature keeps rising, the primary cracks and new cracks in the sandstone expand and connect, and the higher the temperature is, the more obvious the cracks

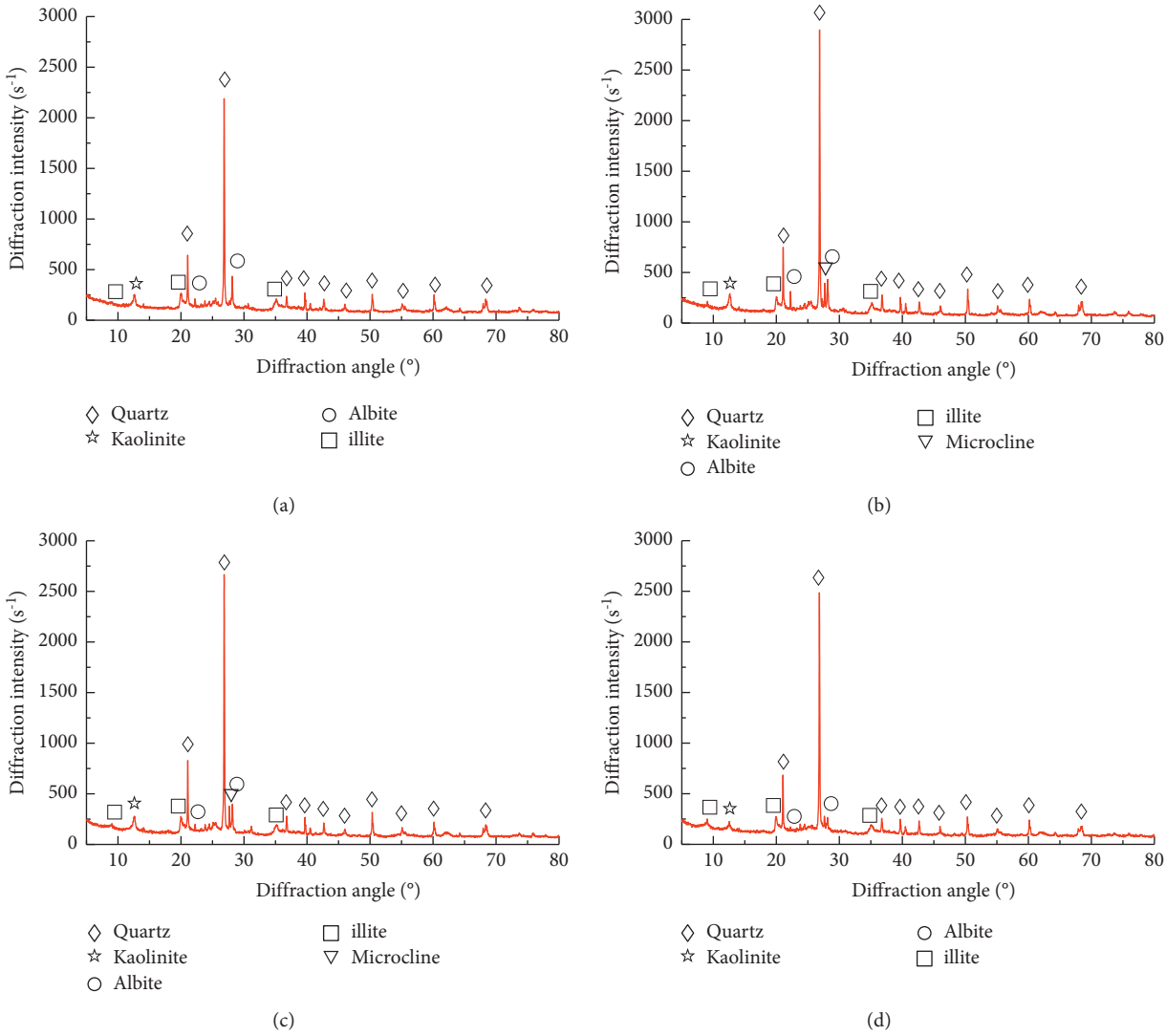

Figure 6: Typical XRD pattern after different temperatures: (a) 25°C, (b) 200°C, (c) 300°C, and (d) 500°C.

appear, and the macroscopic dynamic mechanical properties deteriorate as the temperature goes up.

4. Dynamic Splitting Mechanical Characteristics of Samples after Different Temperatures

4.1. Dynamic Stress-Strain Curve of Specimen. The dynamic stress-strain curves of annular and complete sandstone samples after different heating temperatures under the same loading conditions are shown in the given figures.

Figures 8 and 9 show that the dynamic stress-strain curves of annular and intact specimens are basically the same, but with slightly different shapes. Dynamic stress-strain curves of both annular and intact test pieces increase first and then decrease with the rise of dynamic strain. With the temperature increasing, the slope of curves increases firstly, after that, it reduces at the rising stage of both specimens. At the same temperature, the dynamic stress-strain curve of the annular sample is significantly lower than that of the intact sample.

4.2. The Variation Rules in Dynamic Tensile Strength. The relation between the dynamic tensile strength and the heating temperature of sandstone samples is shown in Figure 10.

Figure 10 shows that the dynamic tensile strength of both specimens increases first and then decreases with the temperature growth. The dynamic tensile strength of the two specimens reaches the maximum value at 200°C. Analysis reasons: after the specimen is heated, the internal mineral particles expand and fill the initial micropores and microcracks inside the sample, the compactness and internal structure of the sample are enhanced, so the tensile strength of the specimen is improved. As the treating temperature keeps rising, new microcracks occur in the

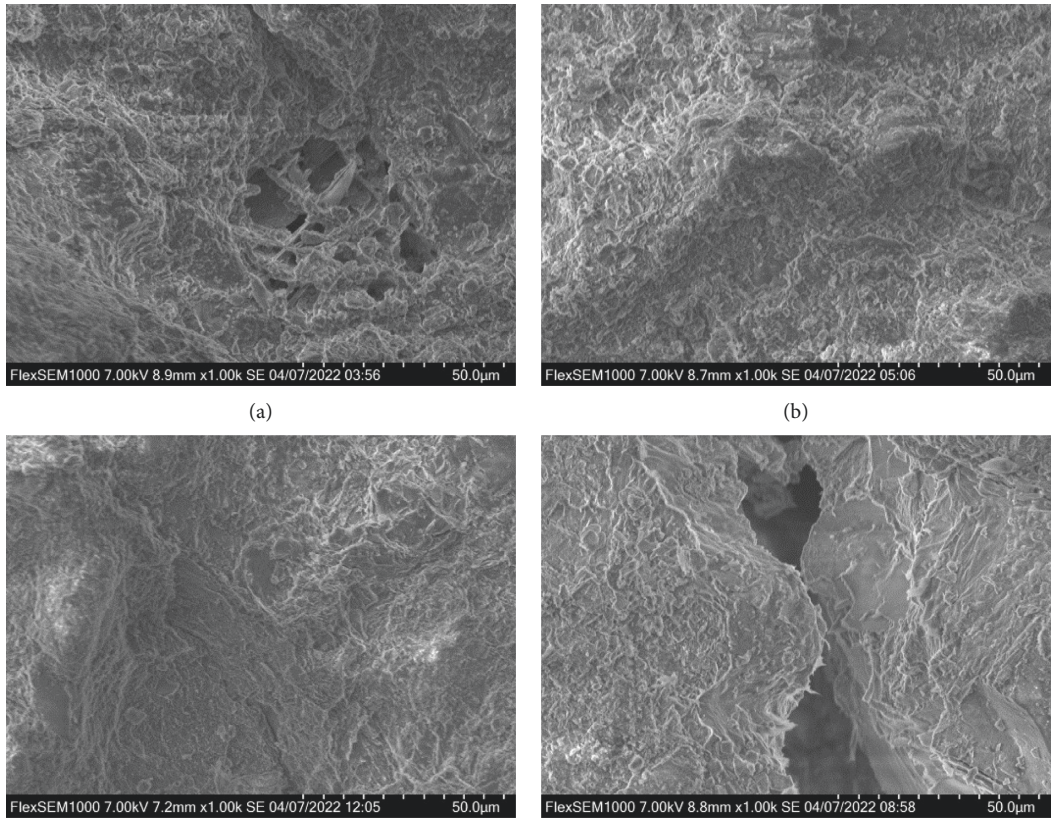

Figure 7: SEM images of sandstone after different temperatures (×1000): (a) 25°C, (b) 200°C, (c) 300°C, and (d) 500°C.

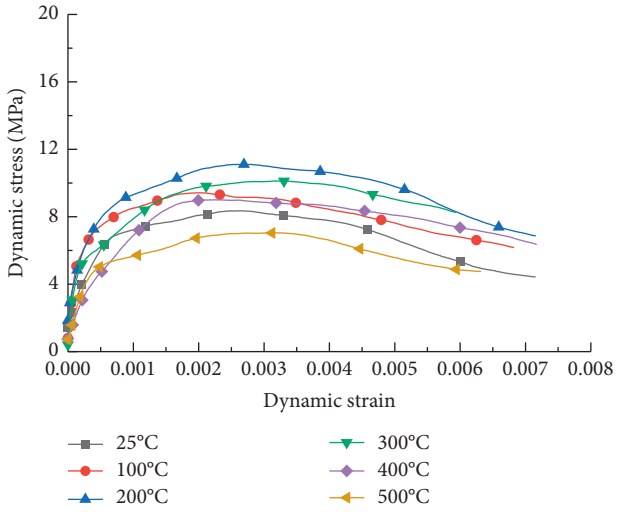

Figure 8: Dynamic splitting stress-strain curves of annular sandstone samples.

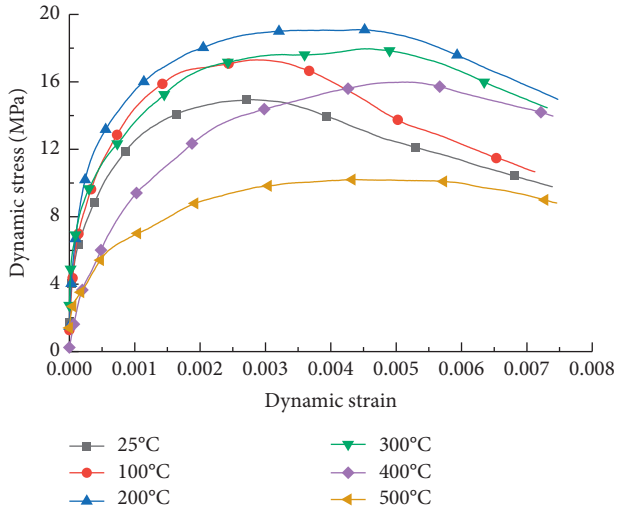

Figure 9: Dynamic splitting stress-strain curves of intact sandstone samples.

sample, the carrying capacity decreases, the microcracks increase, the structure further weakens, and the tensile strength of the test piece gradually decreases. The tensile strength of the annular test piece is lower than that of the intact test piece at the same temperature, indicating that the prefabricated holes reduce the bearing capacity of the sandstone specimens. There is a quadratic polynomial relationship between tensile strength and temperature, as shown in the following formula:

$$\begin{cases} \sigma_{T1} = -4.2202 \times 10^{-5} T^2 + 0.0192T + 8.9024 \left(R^2 = 0.9913\right), \\ \sigma_{T2} = -1.0502 \times 10^{-4} T^2 + 0.0447T + 14.7710 \left(R^2 = 0.9739\right), \end{cases} \tag{4}$$

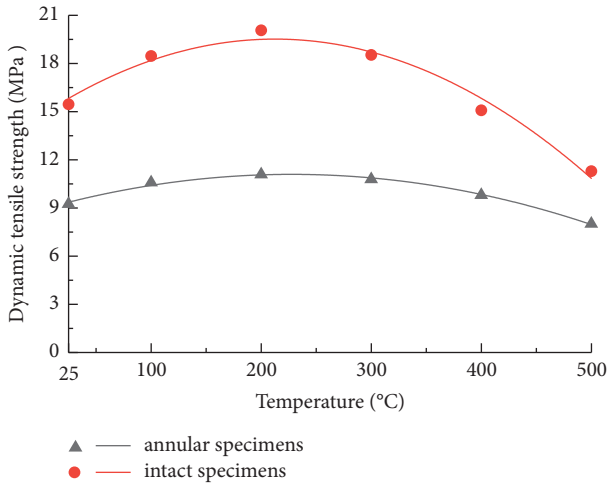

Figure 10: Dynamic tensile strength of samples after different temperatures.

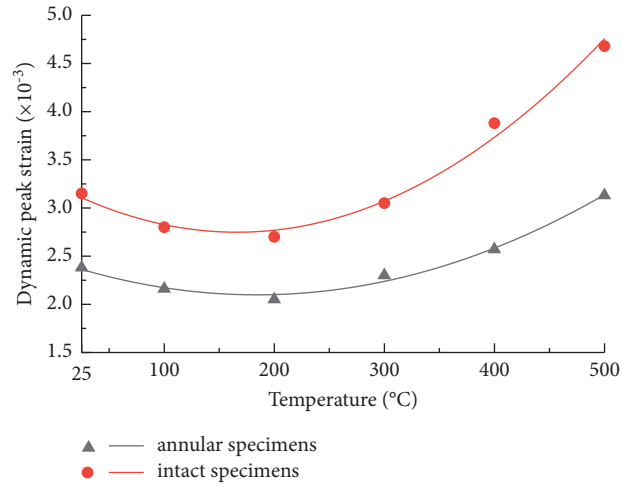

Figure 11: Dynamic peak strain of samples after different temperatures.

where σ_{T1} and σ_{T2} are the dynamic tensile strength of annular and intact test pieces, respectively, and T is the heating temperature.

4.3. The Variation in Peak Strain of Samples. The relation between the dynamic strain of samples and the heating temperature is shown in Figure 11.

Figure 11 shows that the peak strain of both specimens decreases firstly, after that, it increases as the temperature improved. The peak strain of the annular sample is smaller than that of the intact sample at the same temperature. Cause analysis: in the range of normal temperature to 200°C, mineral particles expand when heated, some primary microfractures are closed, and the number and area of defects are reduced to a certain extent, which makes the dynamic strain of sandstone samples show a decreasing trend. As the acting temperature continues to rise, new micropores and microcracks are generated in the sample and gradually expand and increase, resulting in the increase of dynamic strain. At 200°C, the dynamic peak strain of annular and intact samples reaches the minimum, which is 2.05×10^{-3} and 2.7×10^{-3}, respectively. The dynamic strains of annular and intact samples are 3.13×10^{-3} and 4.68×10^{-3} at 500°C, respectively, which are 32% and 49% higher than those at room temperature.

The dynamic peak strain of the specimen is a quadratic function of temperature, as shown in the following formula:

$$\begin{cases} \varepsilon_{T1} = 1.0421 \times 10^{-5} T^2 - 0.0038T + 2.4517 \left(R^2 = 0.9905\right), \\ \varepsilon_{T2} = 1.8008 \times 10^{-5} T^2 - 0.0060T + 3.2450 \left(R^2 = 0.9879\right), \end{cases} \tag{5}$$

Where ε_{T1} and ε_{T2} are the peak strain of the annular and intact samples, respectively, and T is the heating temperature.

4.4. The Variation Law of Average Strain Rate. The relation between the average strain rate of the test piece and the treating temperature is shown in Figure 12.

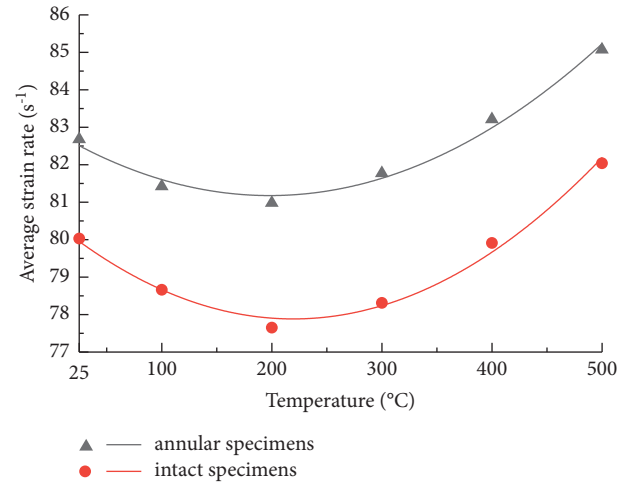

Figure 12: Average strain rate of sandstone specimens after different temperatures.

Figure 12 shows that the average strain rates of both samples decrease first and then increase as the temperature improved. The mean strain rate of the annular test piece is larger than that of the intact test piece under the same temperature condition. Average strain rates of both annular and intact specimens reach the lowest values at 200°C, 80.98s^{-1}, and 77.65s^{-1}, respectively. Analysis reasons: the average strain rate varies with temperature when the same impact pressure is used in the test. In the range of normal temperature to 200°C, the strength of the test piece rises with the temperature increasing and the average strain rate also increases. When the temperature surpasses 200°C, the strength of the test piece decreases as the temperature rises and the average strain rate also decreases. There is a quadratic polynomial relation between the average strain rate and temperature, as shown in the following formula:

Figure 13: Failure modes of annular and intact sandstone specimens after different temperatures: (a) 25°C, (b) 100°C, (c) 200°C, (d) 300°C, (e) 400°C, and (f) 500°C.

$$\begin{cases} \dot{\varepsilon}_{T1} = 4.4412 \times 10^{-5} T^2 - 0.0176T + 82.9182 \left(R^2 = 0.9826\right), \\ \dot{\varepsilon}_{T2} = 5.4698 \times 10^{-5} T^2 - 0.0240T + 80.5175 \left(R^2 = 0.9873\right), \end{cases} \tag{6}$$

where $\dot{\varepsilon}_{T1}$ and $\dot{\varepsilon}_{T2}$ are the average strain rate of the annular and the intact specimen, respectively, and T is the heating temperature.

4.5. Failure Mode of Specimens. The impact failure mode of annular and intact samples after experiencing different temperatures is shown in Figure 13.

As can be seen from Figure 13, The failure degree of the two specimens does not change significantly when the temperature rises from 25°C to 200°C. If the temperature exceeds 200°C, the damage degree of the two specimens becomes more and more serious as the temperature improved, and the fragments of the specimens gradually increase. Analysis reasons: when the temperature rises from normal temperature to 200°C, the sandstone mineral particles expand and fill the primary microcracks in the specimen, leading to the sample becoming denser and improving the intensity of the sample, thus reducing the failure degree of the sample. When the heating temperature surpasses 200°C, the expansion stress in the sample becomes larger and begins to produce new fractures. The primary fractures and new fractures in the sandstone expand and connect, resulting in structural deterioration and reducing the intensity of the specimen, thus aggravating the damage degree of the sample.

5. Conclusion

(1) The total porosity of the sandstone test piece increases as the temperature improved. The micropores and small cracks in sandstone gradually increase with the temperature rising. When the temperature surpasses 200°C, the cracks develop more fully and the primary cracks and new cracks in sandstone expand and connect, forming larger cracks, leading to structural deterioration.

(2) With the temperature rising, the volume of annular and intact specimens increases, while the mass and density decrease. In the range of room temperature to 500°C, the volume increase rate, mass loss rate, and density reduction rate of the two kinds of specimens increase with the rise of temperature and the change rate of physical parameters of the annular sample is slightly higher than that of the intact sample.

(3) The dynamic tensile strength of annular and intact samples increases firstly, after that, it decreases as the temperature improved and achieves the maximum at 200°C. The tensile strength of the annular sample is obviously lower than that of the intact sample at the same temperature.

(4) As the temperature improved, the peak strain and average strain rate of annular and intact samples decrease first and then increase. The peak strain of the annular sample is smaller than that of the intact sample, and the average strain rate is larger than that of the intact sample at the same temperature.

(5) As the temperature goes up, the damage degree of the annular and intact samples increases and the damage degree of the annular sample is slightly smaller than that of the intact sample. After 200°C, the fragments of the two specimens increase obviously.

Data Availability

The data used to support the study are included in the paper.

Conflicts of Interest

The authors declare that there are no conflicts of interest in publishing this paper.

Acknowledgments

This research received financial supports from the National Natural Science Foundation of China (Grant Nos. 52074005 and 52074006), Anhui Provincial Natural Science Foundation (Grant No. 1808085ME134), Anhui Postdoctoral Science Foundation (Grant No. 2015B058), Anhui University of Science and Technology Graduate Innovation Fund Project (Grant No. 2021CX2032), and the National

College Student Innovation and Entrepreneurship Training Program (Grant No. 202010361022). Thanks are due to the Engineering Research Center of Underground Mine Construction, Ministry of Education, and Anhui University of Science and Technology, State Key Laboratory of Mining Response and Disaster Prevention and Control in Deep Coal Mine, for providing the experiment conditions.

References

[1] M. Q. You, C. D. Su, and Y. Gou, "Experimental study on strength and deformation properties of hollow cylindrical specimens of marbles," *Chinese Journal of Rock Mechanics and Engineering*, vol. 26, no. 12, pp. 2420–2429, 2007.

[2] F. Xiao, R. Li, L. Xing et al., "Research on the impact of different force directions on the mechanical properties and damage evolution law of sandstone with different hole diameters," *Advances in Civil Engineering*, vol. 2021, no. 6, pp. 1–14, 2021.

[3] S. Q. Yang, C. H. Lu, and T. Qu, "Investigations of crack expansion in marble having a single pre-existing hole: experiment and simulations," *Journal of China University of Mining and Technology*, vol. 38, no. 6, pp. 774–781, 2009.

[4] S. L. Lian, *Study on Mechanical Properties of Thick-Walled cylinder Granite*, Hunan University of Science and Technology, Hunan, China, 2019.

[5] Q. H. Wu, X. B. Li, F. J. Zhao, and L Chen, "Failure characteristics of hollow cylindrical specimens of limestone under hole pressure unloading," *Chinese Journal of Rock Mechanics and Engineering*, vol. 36, no. 6, pp. 1424–1433, 2017.

[6] T. T. Zhu, H. W. Jing, H. J. Su, and M.-R Du, "Mechanical behavior of sandstone containing double circular cavities under uniaxial compression," *Chinese Journal of Geotechnical Engineering*, vol. 37, no. 6, pp. 1047–1056, 2015.

[7] M. R. Du, H. W. Jing, H. J. Su, and T Zhu, "Experimental study of strength and failure characteristics of sandstone containing prefabricated elliptical hole," *Journal of China University of Mining & Technology*, vol. 45, no. 6, pp. 1164–1171, 2016.

[8] C. Zhang, J. X. Tang, J. Y. Teng, and L Chen-lin, "Experimental study of influences of pore number and pore size on mechanical properties of marble," *Rock and Soil Mechanics*, vol. 38, no. S2, pp. 41–50, 2017.

[9] C. D. Su, S. J. Wei, B. D. Qin, and Y. S Yang, "Experimental study of influence mechanism of high temperature on mechanical properties of fine-grained sandstone," *Rock and Soil Mechanics*, vol. 38, no. 3, pp. 623–630, 2017.

[10] S. J. Du, H. Liu, H. T. Zhi, and H Chen, "Testing study on mechanical properties of post-high-temperature granite," *Chinese Journal of Rock Mechanics and Engineering*, vol. 23, no. 14, pp. 2359–2364, 2004.

[11] L. Y. Zhang and X. B. Mao, "Experimental study of the mechanical effects of loading rates on limestone at high temperature," *Rock and Soil Mechanics*, vol. 31, no. 11, pp. 3511–3515, 2010.

[12] T. Zhu, H. Jing, H. Su, and Q. M. G. Yin, "Physical and mechanical properties of sandstone containing a single fissure after exposure to high temperatures," *International Journal of Mining Science and Technology*, vol. 26, no. 2, pp. 319–325, 2016.

[13] X.-d. Zhao, H.-x. Zhang, and W.-c. Zhu, "Fracture evolution around pre-existing cylindrical cavities in brittle rocks under uniaxial compression," *Transactions of Nonferrous Metals Society of China*, vol. 24, no. 3, pp. 806–815, 2014.

[14] X. L. Chen, *Experimental Study on Rock Mechanical Properties under Dry and Saturated States*, Henan Polytechnic University, Henan China, 2011.

[15] R. D. Sha, *Numerical Simulation on Failure Mechanism of Rocks Containing Holes under Dynamic Loads*, Dalian University of Technology, China, 2019.

[16] M. Q. You, X. L. Chen, and C. D. Su, "Brazilian splitting strengths of discs and rings of rocks in dry and saturated conditions," *Chinese Journal of Rock Mechanics and Engineering*, vol. 30, no. 3, pp. 464–472, 2011.

[17] Y. H. Huang and S. Q. Yang, "The tensile mechanical behavior of granite containing pre-existing holes after high temperature treatment," *Journal of China University of Mining and Technology*, vol. 46, no. 4, pp. 783–791, 2017.

[18] S. P. Zhang, *Experimental Study on Mechanical Properties of Specimens Containing Fillings*, Hunan University of Science and Technology, Henan China, 2019.

[19] Q. H. Wu, F. J. Zhao, X. B. Li, S. M Wang, B Wang, and Z. H Zhou, "Mechanical properties of ring specimens of sandstone subjected to diametral compression," *Rock and Soil Mechanics*, vol. 39, no. 11, pp. 3969–3976, 2018.

[20] C. Wang, H. B. Wang, Z. Q. Xiong, W Cheng, C Luping, and Z Shuaifei, "Experimental study on mechanical characteristics of radial compression of circular granite under the condition of temperature-humidity cycling," *Chinese Journal of Rock Mechanics and Engineering*, vol. 39, no. S2, pp. 3260–3270, 2020.

[21] Q. Ping, H. P. Su, and D. D. Ma, "Experimental study on physical and dynamic mechanical properties of limestone after different high temperature treatment," *Rock and Soil Mechanics*, vol. 42, no. 4, pp. 932–942, 2021.

[22] Y. B. Chen, Y. Wang, and H. Luo, "Study on Brazil split test of sandstones under different temperatures," *Mining Research and Development*, vol. 38, no. 08, pp. 45–50, 2018.

[23] J. Y. Xu and S. Liu, "Effect of impact velocity on dynamic mechanical behaviors of marble after high temperatures," *Chinese Journal of Geotechnical Engineering*, vol. 35, no. 5, pp. 879–883, 2013.

[24] Q. Ping, D. Qi, Q. Diao, and C. Q. Y. Zhang, "Experimental study on physical and dynamic mechanical properties of temperature-water coupled sandstone," *Shock and Vibration*, vol. 2021, pp. 1–12, 2021.

[25] B. Du, H. Bai, M. Zhai, and S. He, "Experimental study on dynamic compression characteristics of red sandstone under wetting-drying cycles," *Advances in Civil Engineering*, vol. 2020, no. 2, pp. 1–10, Article ID 6688202, 2020.

[26] D.-y. Li, T. Wang, T.-j. Cheng, and X.-l. Sun, "Static and dynamic tensile failure characteristics of rock based on splitting test of circular ring," *Transactions of Nonferrous Metals Society of China*, vol. 26, no. 7, pp. 1912–1918, 2016.

[27] "National standards compilation group of the people's Republic of China," *Methods for Determining of Physical and Mechanical Properties of Coal and Rock*, Standards Press of China, Beijing, China, 2010.

[28] "Chinese Society for Rock Mechanics and Engineering. T/CSRME 001-2019 Technical specification for testing method of rock dynamic properties [EB/OL]," 2019, http://www.ttbz.org.cn/Home/Show/10253.

Hindawi
Advances in Civil Engineering
Volume 2022, Article ID 1026129, 10 pages
https://doi.org/10.1155/2022/1026129

Research Article

Copper Adsorption Using Hydroxyapatite Derived from Bovine Bone

Lingchang Kong,[1] Xin Liu,[1] Guocheng Lv,[1] Tianming Liu,[2] Peijun Zhang,[1] Yuxin Li,[1] Bin Chen,[3] and Libing Liao[1]

[1]*Beijing Key Laboratory of Materials Utilization of Nonmetallic Minerals and Solid Wastes, National Laboratory of Mineral Materials, School of Material Sciences and Technology, China University of Geosciences, Beijing 100083, China*
[2]*School of Science, China University of Geosciences, Beijing 100083, China*
[3]*Institute of Environment Engineering, Beijing General Research Institute of Mining & Metallurgy, Beijing 100160, China*

Correspondence should be addressed to Xin Liu; xliu@cugb.edu.cn and Libing Liao; clayl@cugb.edu.cn

Received 20 March 2022; Accepted 11 April 2022; Published 6 May 2022

Academic Editor: Tingting Zhang

Mining and smelting effluent have resulted in heavy metal-contaminated groundwater. Copper-polluted groundwater poses a severe threat to human health and the ecological environment. Permeable reactive barrier (PRB) has been rapidly developed as the in situ remediation technology to control toxic copper migration. Low cost, seepage stability, and great longevity are considered within PRB reactive media. In this paper, hydroxyapatite derived from bovine bone was proven to be a suitable adsorbent owing to cost-effectiveness, great adsorption capacity, and longevity. Batch experiments were carried out to determine the copper adsorption behavior as a function of copper concentration and contact time. Adsorption isotherm was represented by the Langmuir isotherm model, and the adsorption capacity of 25.7 mg/g was superior to most of the adsorbents. A kinetic study was accurately fitted by the pseudo-second-order kinetic model interpreted as a chemical reaction. In addition, the column study confirmed hydroxyapatite has excellent hydraulic performance with no clogging phenomenon happened. At $C/C_0 = 0.5$, the number of pore volume (PV) reached 450. The batch and column experiments also revealed that the overall adsorption process followed up the monolayer chemisorption. Furthermore, systematic analyses demonstrated that surface adsorption was responsible for the copper removal by hydroxyapatite based on experimental analysis and density functional theory (DFT) calculations. This work provides an alternative strategy as filling material for in situ remediation of copper-contaminated groundwater and enriches relevant theoretical references.

1. Introduction

Groundwater is essential for human life and industrial production as a vital water resource [1]. Nowadays, mining and smelting effluent have resulted in more and more heavy metal-contaminated groundwater [2, 3]. Among the toxic heavy metals, copper has posed a severe threat to human health and the natural ecosystem because of accumulation and degradation resistance [4]. The copper concentration is in the range of 1.2 mg/L–200 mg/L under acid mine drainage and polluted groundwater [5, 6]. The copper concentration even reached 1000 mg/L in industrial wastewater [7]. However, the maximum copper concentration of direct discharge is 0.1–0.5 mg/L in different wastewater discharge standards [8, 9]. Hence, efficient remediation of heavy metal polluted groundwater has attracted extensive attention worldwide [10]. Various technologies aim to address this problem, including ex situ remediation using a pump-and-treat (P&T) system or in situ remediation through the permeable reactive barrier (PRB) [11, 12]. P&T technology has been widely used for controlling contaminant migration, but the complicated management, lack of long-term operation, and secondary pollution have remained unsolved [13]. In contrast, PRB technology has been proven to be a

promising strategy due to its cost-effectiveness and sustainability [14]. Thus, PRB was rapidly developed as the green technology for remediating polluted groundwater. The contaminant was immobilized by the reactive media in the filling well through precipitation, adsorption, or reduction into a low-toxicity pollutant [15]. Therefore, the research on filling material for PRB is crucial for heavy metal polluted groundwater [16].

High porosity, effect-cost, seepage stability, and longevity of filling media have been increasingly considered for practical application at pilot or field-scale [17]. Zero-valent iron material is widely applied to PRB due to its outstanding reductivity and adsorption performance [18], but easy oxidation and blocking inhibit its application. Nowadays, studies on natural waste resources as PRB reactive material have developed into hot points. Compared with the expensive synthetic methods, hydroxyapatite derived from animal bone, such as fish bone, chicken bone, and bovine bone, has been developed as an adsorbent for heavy metal polluted water or soil because of its porous structure and excellent adsorption capacity [19–29]. The previous finding suggested that hydroxyapatite could serve for heavy metal-contaminated groundwater, such as uranium, lead, manganese, and copper [30–33]. However, study has not involved in the laboratory column experiment, especially copper flow and transport on hydroxyapatite. Laboratory column experiment could simulate the groundwater condition to explore the flow and pollutant transport model in porous media [34].

Crystallinity plays an important role in the adsorption performance of heavy metals by hydroxyapatite [35]. The previous finding revealed that crystallinity or morphology can be affected by sintering temperature, especially for animal bone [36]. Under low temperatures (<~ 600°C), because organic components in the animal bone cannot be completely thermal decomposed, hydroxyapatite derived from the animal bone has low crystallinity with poor mechanical strength; however, it has higher adsorption capacity (e.g., 99.98 mg/g at 400°C) [37, 38]. Under high temperatures (>~ 600°C), hydroxyapatite has higher crystallinity with excellent mechanical strength; however, it has lower adsorption capacity [39]. Hydroxyapatite would transform into oxy-hydroxyapatite through dehydroxylation and even decomposed into calcium phosphate with higher sintering temperatures (>1000°C) [40, 41]. The systematic effect of mechanical strength, pore structure, and adsorption capacity should be comprehensively taken into account in determining the suitable temperature. Therefore, it is essential to investigate the effect of interaction between crystallinity and calcination temperature on copper removal by hydroxyapatite [42].

It was believed that hydroxyapatite has a significant effect on remediation of heavy metal polluted water or soil, and the removal mechanism has been extensively studied [43]. The previous studies demonstrated that surface adsorption was mainly attributable to favorable interaction with the functional group on the surface of hydroxyapatite, such as hydroxyl and phosphate [44, 45]. However, the comprehensive explanation of adsorption sites not be fully revealed completely through traditional analyses [46–48]. Hence, the detailed model with a specific binding site is the key to interpret adsorption process. Simulation calculation was extensively used to study the adsorption behavior on the surface of hydroxyapatite as supplementary approach [49–51].

In this paper, batch and column experiments were designed to investigate the adsorption performance of copper by hydroxyapatite derived from the bovine bone. The adsorption mechanism was studied in-depth through the experimental analysis methods, such as X-ray diffraction (XRD) combined with Rietveld refinement [52, 53], X-ray photoelectron spectroscopy (XPS), high-resolution transmission electron microscope (HRTEM), and DFT calculations. This work provides the primary reference for evaluating the copper removal mechanism on hydroxyapatite as reactive media within PRB for groundwater remediation.

2. Materials and Methods

2.1. Reagents. Copper nitrate ($Cu(NO_3)_2{\cdot}2H_2O$) used in these experiments was supplied by West Long Chemical Co., Ltd. Copper standard solution was purchased from Guobiao (Beijing) Testing & Certification Co., Ltd. The bones of bovine were bought from Weihai, China.

2.2. Batch Experiments. The adsorption performance was studied by batch equilibrium experiments. The initial concentration range of copper was 0–500 mg/L. 0.2 g hydroxyapatite was added into 30 mL copper solution for 72 h. The equilibrated suspensions were centrifuged for 5 min at 8000 rpm. Langmuir adsorption isotherm was utilized to simulate the adsorption behavior [54]. For adsorption kinetic, 0.2 g hydroxyapatite was added into a 30 mL copper solution for different reaction times. The pseudo-second-order kinetic model was used to fit the copper uptake kinetics on hydroxyapatite [55]. The above experiments for each condition were conducted in triplicates.

2.3. Column Experiment. The experiment used a glass column (length: 15.5 cm; inner diameter: 3.6 cm) equipped with sampling ports at the top. The column was packed with 20 g hydroxyapatite in the middle of the column together with quartz at the top and base of the column. In the column experiment, the 20 mg/L copper solution was pumped upward through the column at a constant flow rate of 0.612 mL/min to simulate a flow rate of 1 m/d for the groundwater environment. Detailed information regarding the column is presented in Table SI.1. The groundwater model software (FEFLOW 6.0) was carried out to simulate the results from the column experiment. The mathematical model was described as the one-dimensional of copper solution undergoing equilibrium sorption in porous hydroxyapatite column based on the adsorption mechanism.

2.4. Characterization of Hydroxyapatite before/after Adsorbing Copper. The thermogravimetric behavior of bovine bone was investigated through thermogravimetric-differential scanning calorimetry (Diamond TG-DSC, PE) at a heating rate of 10°C/min under an air atmosphere. The

element content of hydroxyapatite was measured by X-ray Fluorescence Spectrometer (XRF, ZSX PrimusII). Nitrogen isotherms were investigated using ratio surface and porosity analyzer (BET, Autosorb-iQ). Surface areas were recorded through Brunnauer–Emmett–Teller (BET) equation fitting. Phase analysis was analyzed by powder X-ray diffractometer (XRD, SmartLab) from 5° to 120° with a step of 0.02, speed of 2°/min with Cu Kα radiation at 40 kV and 200 mA. Rietveld refinement of solids was conducted using FullProf software. Inductively coupled plasma atomic emission spectrometry (ICP-OES, ICAP 7600) was used for the determination of copper concentration. Surface chemical composition was measured through XPS (Thermo Scientific Escalab 250Xi+) equipped with an Al Kα X-ray as the excitation source, and the spectra binding energy was calibrated with the C 1s peak at 284.8 eV. Morphology and element distribution were speculated by a high-resolution transmission electron microscope (HRTEM, TalosF200X). The adsorption energy was calculated through the Materials Studio software package with the CASTEP module and ultrasoft pseudopotentials, where the energy cut-off was 520 eV, and the energy change was less than 1×10^{-6} eV. The optimized structure was adopted to make a (001) surface adsorption model with 14 Å thick bulk hydroxyapatite and a 24 Å thick vacuum layer. The vacuum distance (24 Å) is enough to avoid interaction between periodic configurations. DFT calculations were conducted under the Monkhorst–Pack k-mesh of $3 \times 3 \times 2$ in the Brillouin zone. The adsorption energy is as follows:

$$E\text{ads} = E(\text{Total}) - E(\text{HAP}) - E(\text{Cu}), \quad (1)$$

where E(Total) is the total energy of the hydroxyapatite adsorbing copper, E(HAP) is the energy of bulk hydroxyapatite, and E(Cu) is the energy of the isolated copper atom.

3. Results and Discussion

3.1. Effect of Calcination on the Hydroxyapatite. Calcination temperature is a critical factor in determining the crystallinity, grain size, and pore structure of hydroxyapatite. To investigate the effect of calcination temperature on the bovine bone, comprehensive analyses are employed to discuss the hydroxyapatite formation from bovine bone. The thermogravimetric analysis is essential for investigating the hydroxyapatite extraction process from bovine bone (Figure 1(a)). A slight weight loss of 8% is attributed to the evaporation of adsorbed water at low temperatures (<120°C). The DSC curve shows a low endothermic peak correspondingly. The decomposition of organic matter causes a weight loss of 36.7% at 120–540°C. This reaction is followed by broad endothermic peaks correspondingly. A slight weight loss of 2.4% at 540–900°C can occur due to the dehydroxylation of hydroxyapatite promoted by heat.

To control the crystallinity and porosity, a series of characterizations systematically depict the crystallization process of the hydroxyapatite phase during the heat sintering. XRD analysis confirms that all powders under different sintering temperatures are hydroxyapatite ($Ca_{10}(PO_4)_6(OH)_2$, JCPDS 84-1998). The crystallinity increases with increasing temperature due to the broad diffraction peaks transform into sharp diffraction peaks (Figure 1(b)). These results agree with previous reports [39, 41, 56]. In the process of heat treatment, the crystal phase of hydroxyapatite gradually emerges as the calcination temperature increases between 500°C and 600°C. The organic matter is decomposed into carbon dioxide through carbonation and decarboxylation. The nitrogen adsorption isotherms of hydroxyapatite under different temperatures belong to V-type adsorption isotherms, indicating that hydroxyapatite has a pore structure with the coexistence of micropores and mesopores (Figure 1(c)). The specific surface area, specific volume, and pore diameter also decrease with the increase in calcination temperature (Figure 1(d)). Specific surface area is 11.43 m^2/g under 600°C. XRF analysis confirms that hydroxyapatite under 600°C mainly consists of three components, containing calcium, oxygen, phosphorus (Table SI.2). Hence, 600°C is the suitable sintering temperature for hydroxyapatite derived from bovine bone.

3.2. Batch Experiment. The adsorption amount as the function of copper concentration is shown in Figure 2(a). The adsorption capacity of 25.7 mg/g is superior to most of the adsorbents (Table 1) [53–64]. The copper adsorption isotherm agrees well with the Langmuir model interpreting as homogeneous monolayer adsorption. The detailed parameters are shown in Table SI.3. The R^2 value of the copper fitting model reaches 0.9993 (Figure 2(b)). The effect of contact time on the copper uptake is investigated to explore the reaction kinetic, which is shown in Figure 2(c). The adsorption process of copper by hydroxyapatite is fitting well with the pseudo-second-order kinetic model indicating the chemisorption. It can be found that the adsorption capacity of copper increases rapidly in the first 10 h. However, only a slight increase in adsorption capacity is observed after 10 h. It declares that its adsorption process consists of two parts: adsorption by available surface and further transformation from the solid-liquid interface to the pore of hydroxyapatite. The parameter values obtained through the pseudo-second-order kinetics model fitting are shown in Table SI.3. The R^2 value of copper fitting models is 0.9868 correspondingly (Figure 2(d)). It can be concluded that copper removal by hydroxyapatite is mainly rate-limited chemisorption.

3.3. Column Experiment. The removal behavior of copper by hydroxyapatite is further evaluated by performing a column study. The breakthrough curve of copper for a column packed with hydroxyapatite is shown in Figure 3(a). At $C/C_0 = 0.5$, the number of pore volume (PV) is 450, suggesting excellent column durability [65]. Hydroxyapatite has a stable hydraulic performance to copper because no clogging phenomenon happened in the column. Based on the simulation model, the breakthrough curve of different copper concentrations has been further predicted through FEFLOW software (Figure 3(b)). The breakthrough time decreases with the increase in input copper concentration. The half-life of the reaction reaches 43 d when the input concentration of copper is 15 mg/L. The above results confirm that

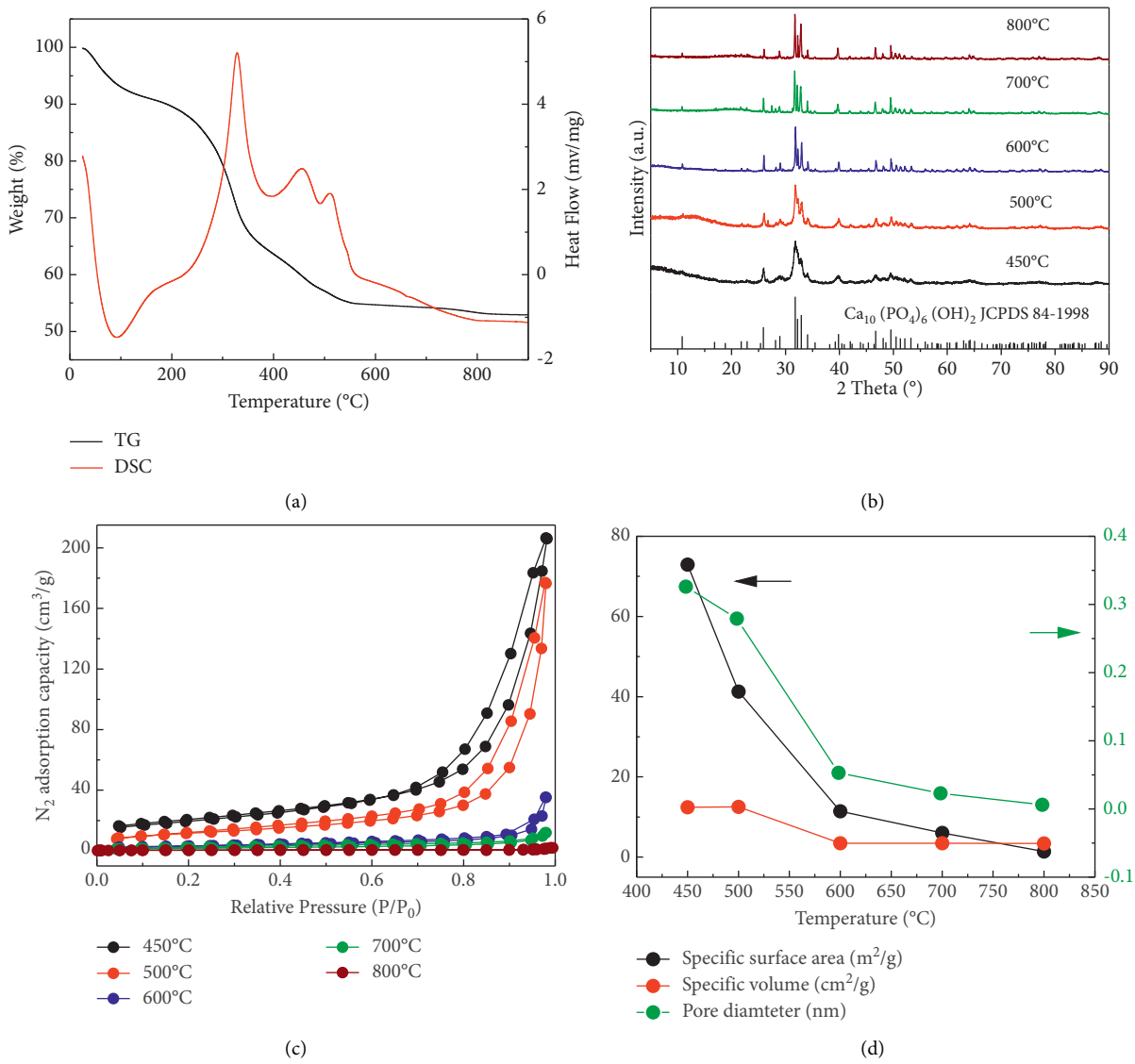

Figure 1: (a) TG-DSC curve of bovine bone. (b) XRD patterns of hydroxyapatite under different calcination temperatures. (c) N_2 adsorption isotherms of hydroxyapatite under different calcination temperatures. (d) Surface parameters of hydroxyapatite under different calcination temperatures.

hydroxyapatite derived from bovine bone is highly effective in in situ remediation of copper-contaminated groundwater as a suitable filling material within PRB. This dynamic column study provides a good prospect for removing copper in field application.

3.4. Adsorption Mechanism. XRD combined with Rietveld refinement is used to analyze the product after adsorption shown in Figure 4(a). The result represents that the product after adsorbing copper belongs to hydroxyapatite phase ($Ca_{10}(PO_4)_6(OH)_2$) according to JCPDS 84-1998. Rietveld refinement defines that the calcium site and phosphate site were fully occupied. The fitting coefficients are R_p of 9.61% and R_{wp} of 13.5%. The functional groups of hydroxyapatites before/after adsorbing copper are identified through FTIR analysis, and corresponding results are presented in Figure 4(b). It can be seen that characteristic peak of hydroxyapatite before/after adsorbing copper is approximately identical. The hydroxyl stretching vibration band at 3560 cm^{-1} is presented. The characteristic peaks at 1030 cm^{-1}, 609 cm^{-1}, and 545 cm^{-1} are attributed to asymmetric stretching of PO_4^{3-}. Besides, the carbonate group is observed at 1407 cm^{-1}, which indicates slight substitution of carbonate group into phosphate group in the hydroxyapatite lattice.

XPS analysis (Figure 5) is consistent with the XRD data. The fitted Cu 2p spectra (Figure 5(a)) show two peaks of Cu $2p_{1/2}$ and Cu $2p_{3/2}$ at the binding energy of 953.25 eV and 933.5 eV, respectively [66]. The spin-orbit splitting E(Cu $2p_{1/2}$) − E(Cu $2p_{3/2}$) of 19.73 eV is associated with the Cu^{2+}. The XPS characterization is corresponding to the presence of copper ions adsorbed on the surface of hydroxyapatite. The XPS spectra of Ca 2p, P 2p, and O 1s are characteristic of phosphorus, calcium, and oxygen ions in hydroxyapatite before/after adsorbing

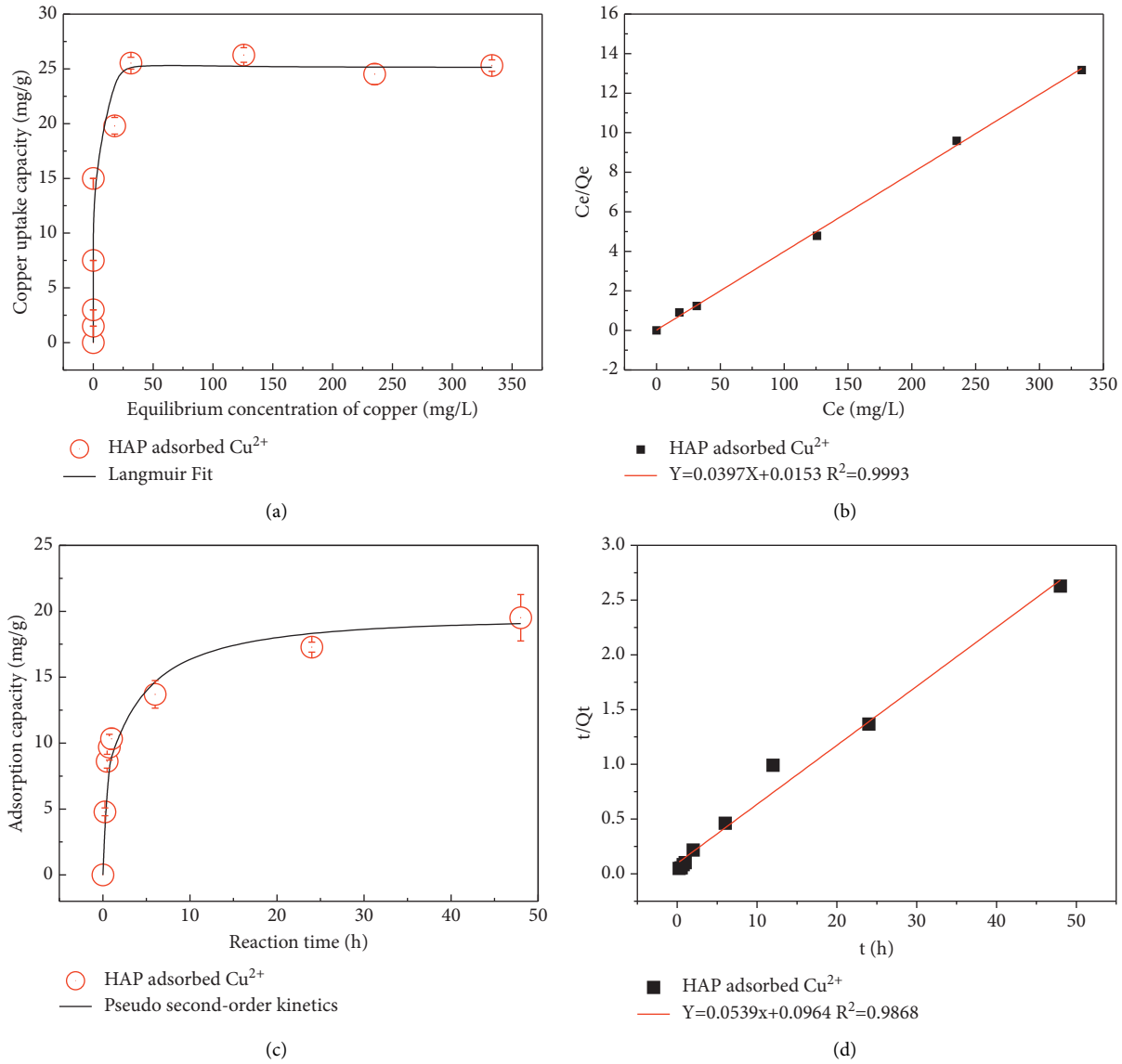

Figure 2: (a) Adsorption equilibrium isotherm of copper on hydroxyapatite. Langmuir model fitting. (b) Linear plot of Langmuir model for adsorption isotherm. (c) Adsorption kinetic of copper on hydroxyapatite. Pseudo-second-order kinetic model fitting (adsorbent dosage: 0.2 g; copper concentration: 500 mg/L; solid/solution ratio: 6.7 g/L at 25 ± 2°C). (d) Linear plot of pseudo-second-order kinetic model for adsorption kinetics.

Table 1: Adsorption capacity of copper by various absorbent.

Adsorbent	Q_m(mg/g)	References
Raw pomegranate peel	30.12	Ben-Ali et al. 2017 [57]
Pine fruit	14.1	Najim et al. 2009 [58]
Fe_5C_2@SiO_2	37.73	Ahmadpoor et al. 2019 [59]
Bioball	5.60	Çelebi 2021[60]
Chicken feather	7.84	Solis-Moreno et al. 2021 [61]
Chicken bone charcoal	15.057	Niu et al. 2021 [62]
Activated carbon	13.05	Imamoglu and Tekir 2008 [63]
Rice shell	2.954	Aydin et al. 2008 [64]
Hydroxyapatite	25.7	Present study

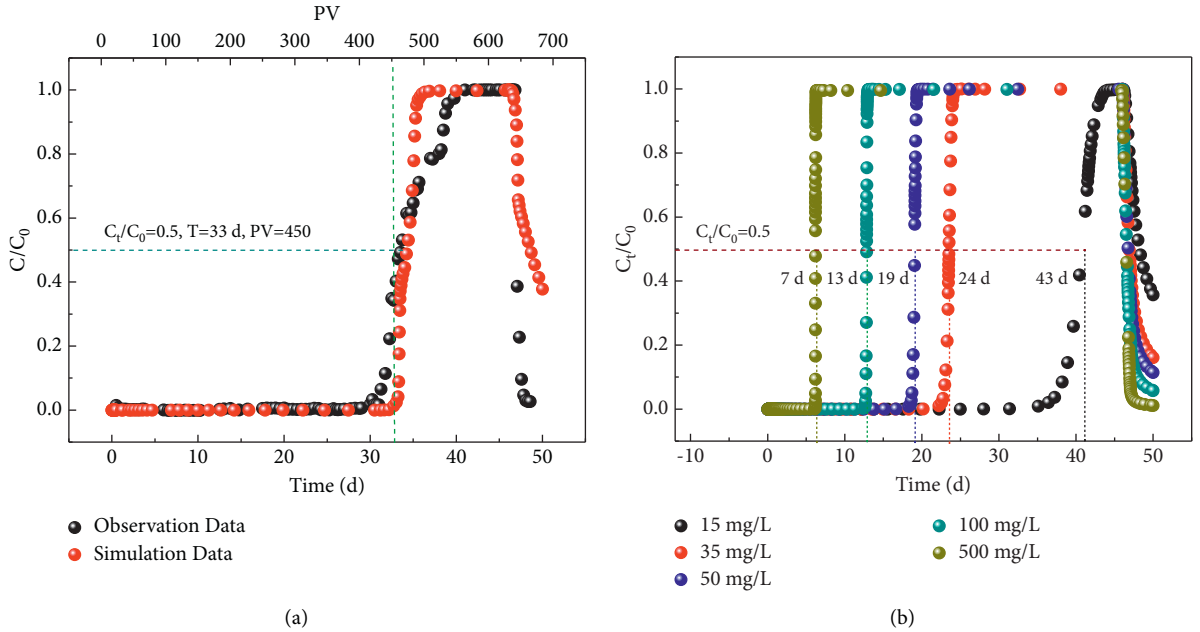

Figure 3: (a) Experimental and fitting breakthrough curve of copper for a column packed with hydroxyapatite. The input concentration of copper is 20 mg/L. Adsorbent mass is 20 g. (b) Predicting breakthrough curve of copper for a column packed with hydroxyapatite for different copper concentrations.

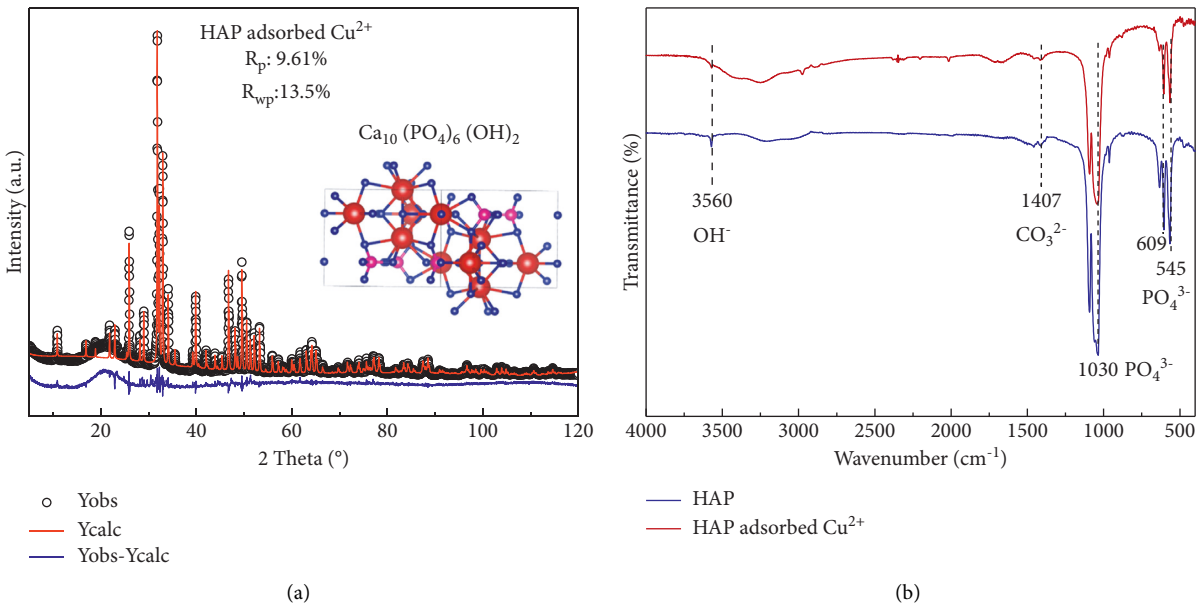

Figure 4: (a) X-ray diffraction patterns with Rietveld refinement of hydroxyapatite adsorbing copper. (b) FTIR spectra before/after adsorbing copper by hydroxyapatite.

copper (Figures 5(c) and 5(d)). The P 2p peaks at 133.8 eV and 132.9 eV are assigned to P of hydroxyapatite ($Ca_{10}(PO_4)_6(OH)_2$). The Ca 2p spectra are composed by two peaks Ca $2p_{1/2}$ and Ca $2p_{3/2}$, in which the energy separation value of $E(\text{Ca } 2p_{1/2}) - E(\text{Ca } 2p_{3/2})$ is 3.57 eV on representing of Ca^{2+} ions. The binding energy of O 1s consists of two peaks at 531.58 eV and 530.85 eV associated with the presence of O-P and O-H groups in hydroxyapatite, respectively. The XPS results also show the similar surface chemical status of hydroxyapatite before/after adsorbing copper.

Morphology characterization further confirms that copper is adsorbed on the surface of nanorod hydroxyapatite in Figure 6. HRTEM images with annular dark field (HADDF-HRTEM) of hydroxyapatite adsorbing copper show complete nanorods. The corresponding EDX elemental mappings also show the core/shell structure formation. Copper is mostly located in the outside area of the nanorod structure. Furthermore, calcium, oxygen, and phosphorus are uniformly distributed on the internal area of the nanostructure. The above results confirm that surface

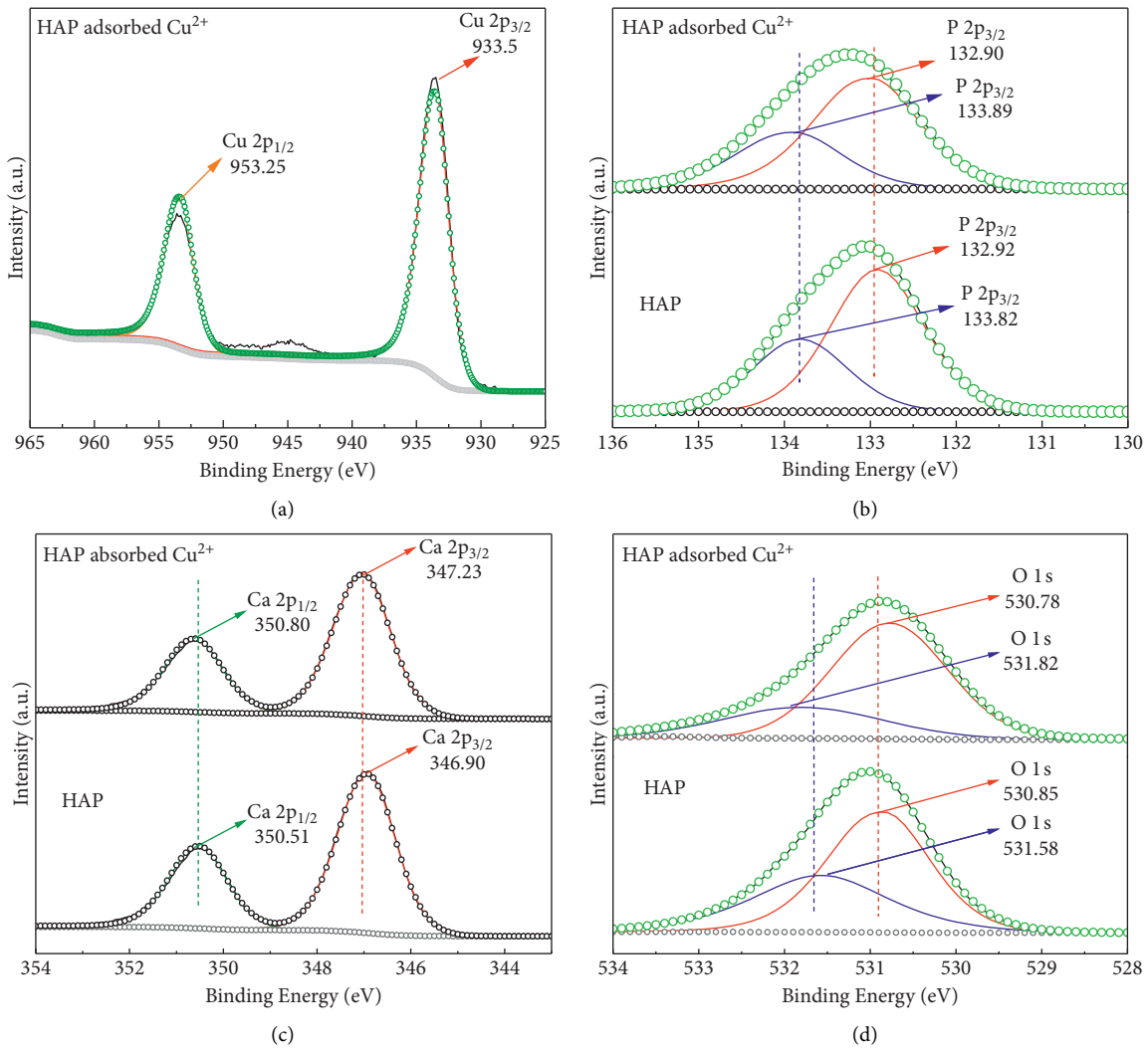

Figure 5: XPS spectra before/after adsorbing copper by hydroxyapatite. (a) Cu 2p XPS spectra. (b) P 2p XPS spectra. (c) Ca 2p XPS spectra. (d) O 1s XPS spectra.

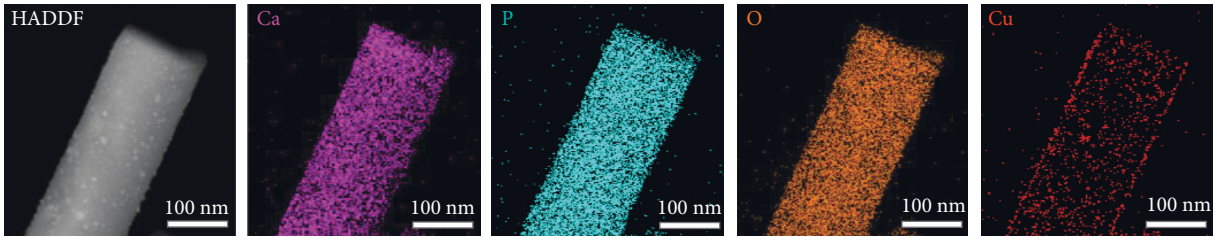

Figure 6: HADDF-STEM image and EDX elemental mappings of hydroxyapatite after adsorbing copper.

chemisorption is the copper uptake mechanism on hydroxyapatite.

DFT calculation is conducted to further study the adsorption site in Figure 7. (001) and (100) are typical planes in hydroxyapatite, in which hydroxyapatite has electronegativity in (001) and electropositivity in (100). Bivalent cation is easier to be adsorbed on hydroxyapatite (001) surface through electrostatic attraction. Hence, (001) plane is considered as a dominant plane. Hydroxyapatite has acidic-basic sites, where acidic groups (≡POH, ≡PO^-, and ≡CaOH) could complex with heavy metal on the surface. The calculation result shows that copper prefers to be adsorbed to the Ca(I) site through bonding to three oxygens of phosphate group stably in the hydroxyapatite (001). The calculation adsorption energy before/after adsorbing copper is −1.15 eV, indicating strong copper adsorption on the surface. Hence, a surface chemisorption model has proposed that copper bounds to the oxygen of phosphate through complexation with a Cu-O distance of ~2.15 Å. The DFT calculations provide new insights into the copper adsorption mechanism on hydroxyapatite as adsorbent.

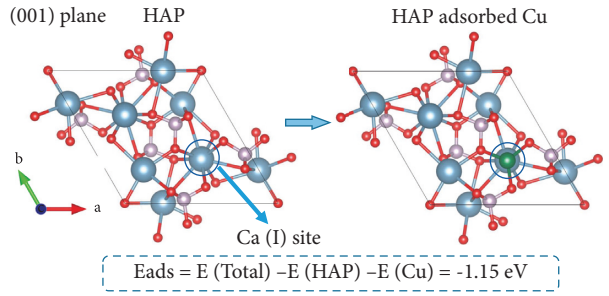

Figure 7: DFT calculation of copper adsorption energy on hydroxyapatite. Copper adsorption on the pristine hydroxyapatite (001). Oxygen, calcium, phosphorus, hydrogen, and copper are in red, blue, pink, yellow, and green, respectively.

4. Conclusion

Copper-contaminated groundwater is directly associated with human health and the ecological environment. In this paper, cost-effective hydroxyapatite derived from bovine bone was proven as a suitable adsorbent for in situ remediation of copper-contaminated groundwater within PRB. Calcination temperature has a significant effect on the crystallinity and porosity, and 600°C is confirmed as suitable temperature for hydroxyapatite derived from the bovine bone. Hydroxyapatite has a porous structure, and its specific surface area is 11.43 m^2/g. Hydroxyapatite is proven as an excellent adsorbent owing to cost-effectiveness, great adsorption capacity, and longevity. Adsorption isotherm is represented by the Langmuir isotherm model, and adsorption capacity of 25.7 mg/g is superior to most of the adsorbents. The kinetic study is accurately fitted by the pseudo-second-order kinetic model interpreted with chemical reaction. In addition, column study confirms that hydroxyapatite has excellent hydraulic performance with no clogging phenomenon happened. At $C/C_0 = 0.5$, the number of pore volume (PV) reaches 450, suggesting stable durability. The model predicates that breakthrough time decreases with the increase in input copper concentration through FEFLOW software. The batch and column experiments also reveal that the overall adsorption process follows up the monolayer chemisorption. XRD combined with Rietveld refinement demonstrated that copper has not incorporated into the calcium sites in hydroxyapatite. Other characterizations such as XPS analysis, EDX mapping images, and FTIR further confirm that copper is adsorbed on the surface of hydroxyapatite. DFT calculation shows that copper was attracted to oxygen atoms to form complexes based on the phosphate group in the (001) plane. The adsorption energy is −1.15 eV with a Cu-O distance of ~2.15 Å. This work provides an alternative strategy as filling material for in situ remediation of copper-contaminated groundwater and enriches relevant theoretical references.

Data Availability

The data used to support the findings of this study are available from the corresponding author upon request.

Conflicts of Interest

The authors declare that there are no conflicts of interest regarding the publication of this paper.

Acknowledgments

The authors are grateful for the funding support from the National Natural Science Foundation of China (41831288).

Supplementary Materials

The supporting information is available free of charge. Additional tables are displayed in the supplementary materials file, including parameters for the column experiment, mass fraction of hydroxyapatite, and detailed parameters of copper adsorption. The data used and generated in this paper are openly available. (*Supplementary Materials*)

References

[1] N. Moosdorf and T. Oehler, "Societal use of fresh submarine groundwater discharge: An overlooked water resource," *Earth-Science Reviews*, vol. 171, pp. 338–348, 2017.

[2] X. Gong, Z. Chen, and Z. Luo, "Spatial distribution, temporal variation, and sources of heavy metal pollution in groundwater of a century-old nonferrous metal mining and smelting area in China," *Environmental Monitoring and Assessment*, vol. 186, no. 12, pp. 9101–9116, 2014.

[3] Y. Fan, T. Zhu, M. Li, J. He, and R. Huang, "Heavy Metal contamination in soil and Brown Rice and human health Risk Assessment near three Mining Areas in Central China," *Journal Of Healthcare Engineering*, vol. 2017, Article ID 4124302, 9 pages, 2017.

[4] E. M. Alissa and G. A. Ferns, "Heavy metal poisoning and cardiovascular disease," *Journal of Toxicology*, vol. 2011, Article ID 870125, 21 pages, 2011.

[5] R. W. Gaikwad, S. A. Misal, and D. V. Gupta, "Removal of metal from acid mine drainage (AMD) by using natural zeolite of Nizarneshwar Hills of Western India," *Arabian Journal of Geosciences*, vol. 4, no. 1-2, pp. 85–89, 2009.

[6] I. Panfili, M. L. Bartucca, E. Ballerini, and D. Del Buono, "Combination of aquatic species and safeners improves the remediation of copper polluted water," *Science of the Total Environment*, vol. 601-602, pp. 1263–1270, 2017.

[7] H. Sun, L. Sun, Y. Zhao et al., "A combined hydrate-based method for removing heavy metals from simulated wastewater with high concentrations," *Journal of Environmental Chemical Engineering*, vol. 9, no. 6, Article ID 106633, 2021.

[8] General Administration of Quality Supervision, *Inspection and Quarantine of the People's Republic of China, GB 25467-2010 Emission Standard of Pollutants for Copper, Nickel, Cobalt Industry*, China Environmental Science Press, Beijing, China, 2013.

[9] ISO, *Soil Quality, Extraction of Trace Elements Soluble in Aqua Regia*, ISO 11466, Geneva, Switzerland, 1995.

[10] N. Makombe and R. D. Gwisai, "Soil remediation Practices for Hydrocarbon and heavy Metal Reclamation in Mining polluted soils," *The Scientific World Journal*, vol. 2018, Article ID 5130430, 7 pages, 2018.

[11] F. Feizi, A. K. Sarmah, and R. Rangsivek, "Adsorption of pharmaceuticals in a fixed-bed column using tyre-based activated carbon: experimental investigations and numerical

modelling," *Journal of Hazardous Materials*, vol. 417, Article ID 126010, 2021.

[12] B. Thangagiri, A. Sakthivel, K. Jeyasubramanian, S. Seenivasan, J. Dhaveethu Raja, and K. Yun, "Removal of hexavalent chromium by biochar derived from Azadirachta indica leaves: batch and column studies," *Chemosphere*, vol. 286, no. Pt 1, Article ID 131598, 2022.

[13] Y. Zha, T.-C. J. Yeh, W. A. Illman, C. M. W. Tso, C.-H. M. Carrera, and Y.-L. Wang, "Exploitation of pump-and-treat remediation systems for characterization of hydraulic heterogeneity," *Journal of Hydrology*, vol. 573, pp. 324–340, 2019.

[14] J. Song, G. Huang, D. Han, Q. Hou, L. Gan, and M. Zhang, "A review of reactive media within permeable reactive barriers for the removal of heavy metal(loid)s in groundwater: Current status and future prospects," *Journal of Cleaner Production*, vol. 319, 2021.

[15] J. Lee, A. J. Graettinger, J. Moylan, and H. W. Reeves, "Directed site exploration for permeable reactive barrier design," *Journal of Hazardous Materials*, vol. 162, no. 1, pp. 222–229, 2009.

[16] H. Zhou, Z. Liu, X. Li, and J. Xu, "Remediation of lead (II)-contaminated soil using electrokinetics assisted by permeable reactive barrier with different filling materials," *Journal of Hazardous Materials*, vol. 408, Article ID 124885, 2021.

[17] B. Yu, Z. Chen, and J. Wu, "Experimental investigation on seepage stability of filling Material of Karst Collapse Pillar in Mining Engineering," *Advances in Civil Engineering*, vol. 2018, Article ID 3986490, 10 pages, 2018.

[18] F. Zhu, X. Tan, W. Zhao et al., "Efficiency assessment of ZVI-based media as fillers in permeable reactive barrier for multiple heavy metal-contaminated groundwater remediation," *Journal of Hazardous Materials*, vol. 424, 2022.

[19] J. Oliva, J. De Pablo, J.-L. Cortina, and C. Ayora, "Removal of cadmium, copper, nickel, cobalt and mercury from water by Apatite II: column experiments," *Journal of Hazardous Materials*, vol. 194, pp. 312–323, 2011.

[20] C. Rojas-Mayorga, D. Mendoza-Castillo, A. Bonilla-Petriciolet, and J. Silvestre-Albero, "Tailoring the adsorption behavior of bone char for heavy metal removal from aqueous solution," *Adsorption Science and Technology*, vol. 34, no. 6, pp. 368–387, 2016.

[21] C. Xue, L. Zhu, S. Lei et al., "Lead competition alters the zinc adsorption mechanism on animal-derived biochar," *Science of the Total Environment*, vol. 713, Article ID 136395, 2020.

[22] Y.-Y. Wang, Y.-X. Liu, H.-H. Lu, R.-Q. Yang, and S.-M. Yang, "Competitive adsorption of Pb(II), Cu(II), and Zn(II) ions onto hydroxyapatite-biochar nanocomposite in aqueous solutions," *Journal of Solid State Chemistry*, vol. 261, pp. 53–61, 2018.

[23] S. Lei, Y. Shi, Y. Qiu, L. Che, and C. Xue, "Performance and mechanisms of emerging animal-derived biochars for immobilization of heavy metals," *Science of the Total Environment*, vol. 646, pp. 1281–1289, 2019.

[24] D. Smoleń, T. Chudoba, S. Gierlotka et al., "Hydroxyapatite Nanopowder synthesis with a Programmed Resorption rate," *Journal of Nanomaterials*, vol. 2012, Article ID 841971, 9 pages, 2012.

[25] J. M. Hughes and J. F. Rakovan, "Structurally Robust, chemically Diverse: Apatite and Apatite Supergroup Minerals," *Elements*, vol. 11, no. 3, pp. 165–170, 2015.

[26] Y. Wang, R. Li, W. Liu, L. Cheng, Q. Jiang, and Y. Zhang, "Exploratory of immobilization remediation of hydroxyapatite (HAP) on lead-contaminated soils," *Environmental Science and Pollution Research*, vol. 26, no. 26, pp. 26674–26684, 2019.

[27] A. M. Mohammad, T. A. Salah Eldin, M. A. Hassan, and B. E. El-Anadouli, "Efficient treatment of lead-containing wastewater by hydroxyapatite/chitosan nanostructures," *Arabian Journal of Chemistry*, vol. 10, no. 5, pp. 683–690, 2017.

[28] L. Dong, Z. Zhu, Y. Qiu, and J. Zhao, "Removal of lead from aqueous solution by hydroxyapatite/magnetite composite adsorbent," *Chemical Engineering Journal*, vol. 165, no. 3, pp. 827–834, 2010.

[29] F. Safatian, Z. Doago, M. Torabbeigi, H. Rahmani Shams, and N. Ahadi, "Lead ion removal from water by hydroxyapatite nanostructures synthesized from egg sells with microwave irradiation," *Applied Water Science*, vol. 9, no. 4, p. 108, 2019.

[30] W. Zhang, H. Liu, X. Fan, Z. Zhuo, and Y. Guo, "Removal of uranium from aqueous solution by a permeable reactive barrier loaded with hydroxyapatite-coated quartz sand: Implication for groundwater remediation," *Geochemistry*, vol. 80, no. 4, 2020.

[31] S. A. Chattanathan, T. P. Clement, S. R. Kanel, M. O. Barnett, and N. Chatakondi, "Remediation of uranium-contaminated groundwater by sorption onto hydroxyapatite derived from Catfish bones," *Water, Air, & Soil Pollution*, vol. 224, no. 2, p. 1429, 2013.

[32] C. C. Fuller, J. R. Bargar, J. A. Davis, and M. J. Piana, "Mechanisms of uranium interactions with hydroxyapatite: Implications for groundwater remediation," *Environmental Science & Technology*, vol. 36, no. 2, pp. 158–165, 2002.

[33] Y. Liu, R. Zhang, Z. Sun et al., "Remediation of artificially contaminated soil and groundwater with copper using hydroxyapatite/calcium silicate hydrate recovered from phosphorus-rich wastewater," *Environmental Pollution*, vol. 272, Article ID 115978, 2021.

[34] P. R. Rad and A. Fazlali, "Optimization of permeable reactive barrier dimensions and location in groundwater remediation contaminated by landfill pollution," *Journal of Water Process Engineering*, vol. 35, 2020.

[35] C. Stotzel, F. A. Muller, F. Reinert, F. Niederdraenk, J. Barralet, and U. Gbureck, "Ion adsorption behaviour of hydroxyapatite with different crystallinities," *Colloids and Surfaces B: Biointerfaces*, vol. 74, no. 1, pp. 91–95, 2009.

[36] Y. X. Pang and X. Bao, "Influence of temperature, ripening time and calcination on the morphology and crystallinity of hydroxyapatite nanoparticles," *Journal of the European Ceramic Society*, vol. 23, no. 10, pp. 1697–1704, 2003.

[37] P. T. Ngueagni, E. D. Woumfo, P. S. Kumar et al., "Adsorption of Cu(II) ions by modified horn core: effect of temperature on adsorbent preparation and extended application in river water," *Journal of Molecular Liquids*, vol. 298, 2020.

[38] M. Wang, Y. Liu, Y. Yao, L. Han, and X. Liu, "Comparative evaluation of bone chars derived from bovine parts: Physicochemical properties and copper sorption behavior," *Science of the Total Environment*, vol. 700, Article ID 134470, 2020.

[39] P. P. Biswas, B. Liang, G. Turner-Walker et al., "Systematic changes of bone hydroxyapatite along a charring temperature gradient: An integrative study with dissolution behavior," *Science of the Total Environment*, vol. 766, Article ID 142601, 2021.

[40] S. Patel, J. Han, W. Qiu, and W. Gao, "Synthesis and characterisation of mesoporous bone char obtained by pyrolysis of animal bones, for environmental application," *Journal of Environmental Chemical Engineering*, vol. 3, no. 4, pp. 2368–2377, 2015.

[41] A. M. Sofronia, R. Baies, E. M. Anghel, C. A. Marinescu, and S. Tanasescu, "Thermal and structural characterization of synthetic and natural nanocrystalline hydroxyapatite," *Materials Science and Engineering: C*, vol. 43, pp. 153–163, 2014.

[42] W. P. Wijesinghe, M. M. Mantilaka, E. V. Premalal et al., "Facile synthesis of both needle-like and spherical hydroxyapatite nanoparticles: effect of synthetic temperature and calcination on morphology, crystallite size and crystallinity," *Materials Science and Engineering: C*, vol. 42, pp. 83–90, 2014.

[43] Z. Li, M.-M. Zhou, and W. Lin, "The research of Nanoparticle and Microparticle hydroxyapatite Amendment in Multiple heavy Metals contaminated soil remediation," *Journal of Nanomaterials*, vol. 2014, Article ID 168418, 8 pages, 2014.

[44] R. Agha Beygli, N. Mohaghegh, and E. Rahimi, "Metal ion adsorption from wastewater by g-C_3N_4 modified with hydroxyapatite: a case study from Sarcheshmeh Acid Mine Drainage," *Research on Chemical Intermediates*, vol. 45, no. 4, pp. 2255–2268, 2019.

[45] Y. Chen, M. Li, Y. Li et al., "Hydroxyapatite modified sludge-based biochar for the adsorption of Cu^{2+} and Cd^{2+}: Adsorption behavior and mechanisms," *Bioresource Technology*, vol. 321, Article ID 124413, 2021.

[46] D. N. Thanh, P. Novák, J. Vejpravova, H. N. Vu, J. Lederer, and T. Munshi, "Removal of copper and nickel from water using nanocomposite of magnetic hydroxyapatite nanorods," *Journal of Magnetism and Magnetic Materials*, vol. 456, pp. 451–460, 2018.

[47] E.-S. Bogya, R. Barabás, A. Csavdári, V. Dejeu, and I. Baldea, "Hydroxyapatite modified with silica used for sorption of copper(II)," *Chemical Papers*, vol. 63, no. 5, 2009.

[48] Y. Zhan, J. Lin, and J. Li, "Preparation and characterization of surfactant-modified hydroxyapatite/zeolite composite and its adsorption behavior toward humic acid and copper(II)," *Environmental Science and Pollution Research*, vol. 20, no. 4, pp. 2512–2526, 2013.

[49] P. Li, X. Li, and S. Dai, "Adsorption of gold cyanide on quartz," *Colloids and Surfaces A: Physicochemical and Engineering Aspects*, vol. 590, 2020.

[50] X.-Y. Liu, J.-W. Cao, X.-L. Qin et al., "A Computational Validation of water Molecules Adsorption on an NaCl surface," *Crystals*, vol. 11, no. 6, p. 610, 2021.

[51] M.-H. Ri, Y.-M. Jang, U.-S. Ri, C. J. Yu, K. I. Kim, and S. U. Kim, "Ab initio investigation of Adsorption characteristics of Bisphosphonates on hydroxyapatite (001) surface," *Journal of Materials Science*, vol. 53, no. 6, pp. 4252–4261, 2017.

[52] A. Fahami, B. Nasiri-Tabrizi, G. W. Beall, and W. J. Basirun, "Structural insights of mechanically induced aluminum-doped hydroxyapatite nanoparticles by Rietveld refinement," *Chinese Journal of Chemical Engineering*, vol. 25, no. 2, pp. 238–247, 2017.

[53] S. Lala, M. Ghosh, P. K. Das, D. Das, T. Kar, and S. Pradhan, "Magnesium substitution in carbonated hydroxyapatite: structural and microstructural characterization by Rietveld's refinement," *Materials Chemistry and Physics*, vol. 170, pp. 319–329, 2016.

[54] S. L. Iconaru, M. Motelica-Heino, R. Guegan, M. Beuran, A. Costescu, and D. Predoi, "Adsorption of Pb (II) ions onto hydroxyapatite Nanopowders in Aqueous solutions," *Materials*, vol. 11, pp. 2204–11, 2018.

[55] Y. Long, J. Jiang, J. Hu, X. Hu, Q. Yang, and S. Zhou, "Removal of Pb(II) from aqueous solution by hydroxyapatite/carbon composite: preparation and adsorption behavior," *Colloids and Surfaces A: Physicochemical and Engineering Aspects*, vol. 577, pp. 471–479, 2019.

[56] M. Younesi, S. Javadpour, and M. E. Bahrololoom, "Effect of heat treatment temperature on chemical compositions of extracted hydroxyapatite from bovine bone Ash," *Journal of Materials Engineering and Performance*, vol. 20, no. 8, pp. 1484–1490, 2011.

[57] S. Ben-Ali, I. Jaouali, S. Souissi-Najar, and A. Ouederni, "Characterization and adsorption capacity of raw pomegranate peel biosorbent for copper removal," *Journal of Cleaner Production*, vol. 142, pp. 3809–3821, 2017.

[58] T. S. Najim, N. J. Elais, and A. A. Dawood, "Adsorption of copper and iron using low cost Material as Adsorbent," *E-Journal of Chemistry*, vol. 6, no. 1, pp. 161–168, 2009.

[59] F. Ahmadpoor, S. A. Shojaosadati, and S. Z. Mousavi, "Magnetic silica coated iron carbide/alginate beads: synthesis and application for adsorption of Cu (II) from aqueous solutions," *International Journal of Biological Macromolecules*, vol. 128, pp. 941–947, 2019.

[60] H. Çelebi, "Use of Bioballs as an Adsorbent for the removal of copper," *Journal of the Chemical Society of Pakistan*, vol. 43, no. 2, p. 114, 2021.

[61] C. A. Solis-Moreno, E. Cervantes-Gonzalez, and M. Z. Saavedra-Leos, "Use and treatment of chicken feathers as a natural adsorbent for the removal of copper in aqueous solution," *Journal of Environmental Health Science and Engineering*, vol. 19, no. 1, pp. 707–720, 2021.

[62] C. Niu, S. Li, G. Zhou, Y. Wang, X. Dong, and X. Cao, "Preparation and characterization of magnetic modified bone charcoal for removing Cu^{2+} ions from industrial and mining wastewater," *Journal of Environmental Management*, vol. 297, Article ID 113221, 2021.

[63] M. Imamoglu and O. Tekir, "Removal of copper (II) and lead (II) ions from aqueous solutions by adsorption on activated carbon from a new precursor hazelnut husks," *Desalination*, vol. 228, no. 1–3, pp. 108–113, 2008.

[64] H. Aydin, Y. Bulut, and C. Yerlikaya, "Removal of copper (II) from aqueous solution by adsorption onto low-cost adsorbents," *Journal of Environmental Management*, vol. 87, no. 1, pp. 37–45, 2008.

[65] G. Du, Z. Li, L. Liao et al., "Cr(VI) retention and transport through Fe(III)-coated natural zeolite," *Journal of Hazardous Materials*, vol. 221-222, pp. 118–123, 2012.

[66] A. Amedlous, O. Amadine, Y. Essamlali, H. Maati, N. Semlal, and M. Zahouily, "Copper loaded hydroxyapatite nanoparticles as eco-friendly Fenton-like catalyst to effectively Remove organic Dyes," *Journal of Environmental Chemical Engineering*, vol. 9, no. 4, 2021.

Hindawi
Advances in Civil Engineering
Volume 2022, Article ID 8375918, 10 pages
https://doi.org/10.1155/2022/8375918

Research Article

Effect of Biomass Improvement Method on Reclaimed Soil of Mining Wasteland

Yanfei Xu,[1,2] Shikai An,[1,2] Yongchun Chen,[1,2] Chao Yuan,[3] and Pengfei Tao[1,2]

[1]*National Engineering Laboratory for Protection of Coal Mine Eco-Environment, Ping an Mining Engineering Technology Research Institute Co., Ltd., Huainan 232001, China*
[2]*Coal Mining National Engineering Technology Research Institute, Huainan, Anhui 232001, China*
[3]*School of Resource & Environment and Safety Engineering, Hunan University of Science and Technology, Xiangtan, Hunan 411201, China*

Correspondence should be addressed to Chao Yuan; yuanchaozh1@126.com

Received 20 December 2021; Revised 30 March 2022; Accepted 6 April 2022; Published 2 May 2022

Academic Editor: Lijie Guo

Aiming at the problem of soil improvement for mining wasteland reclamation, this article takes the coal mining subsidence reclamation area of a coal mine in the east of China as the research object. Compost improvement and green manure improvement experiments were carried out to study the impact of different biomass improvement methods on the quality of reclaimed soil. 10 soil physical and chemical indicators including water content, total nitrogen, ammonia nitrogen, nitrate nitrogen, available phosphorus, available potassium, total phosphorus, organic matter, pH, and conductivity were selected to evaluate the effect of soil improvement. After 5 months of soil improvement, the results showed that planting alfalfa and Mexican corn in the reclaimed area can increase soil available phosphorus, available potassium, total phosphorus, and organic matter content. Cattail, a common aquatic plant in the coal mining subsidence area in the east, is used to make organic compost. When the compost is applied to reclaimed soil, the content of available phosphorus, available potassium, and total phosphorus in the soil can be significantly increased. Using white vanilla clover as green manure for reclaiming soil can significantly increase the content of nitrate nitrogen, available phosphorus, available potassium, and total phosphorus in the soil. Biomass improvement technology can improve the fertility level of coal mine reclamation soil in a short time. It is conducive to promoting the restoration of soil fertility of mining wasteland and realizing the sustainable development and utilization of plant resources and land resources.

1. Introduction

With abundant coal resources, China is one of the major coal mining countries in the world. The continuous exploitation of coal resources contributes to the gradual closure of many coal mines [1]. According to "Strategic Studies of High-Efficient and Energy-Effective Coal Extractions in China," a key consulting project of the Chinese Academy of Engineering, the number of abandoned coal mines in China can reach 15 000 by 2030. The increasing abandoned coal mines finally generate a lot of mining wasteland. Ecological restoration of mining wasteland is one of the important topics in the development and utilization of abandoned coal mines [2].

Soil serves as a material basis for human survival. It is basic for crop growth, food, and animal production, thus being the material basis for human survival and development. In the study of remediation and utilization of abandoned coal mines, soil reconstruction and soil quality improvement and capacity increase have been the research hotspots [3, 4]. The existing research results show that the soil quality of mining wasteland deteriorates to varying degrees because of the exploitation of coal resources in the long time series, which leads to the changes in soil moisture, structure, fertility, and material composition in mining areas. For example, Wei et al. found that the soil water content in mining subsidence areas is generally smaller than that in nonsubsidence areas [5]. Huang and Luo found that the contents of organic matter, nitrogen, and phosphorus in the mining area soil were only 20%~30%, compared with those in the vegetation-covered soil [6]. A good many

research results show that the structure, fertility, pH value, and other aspects of the reconstructed soil in the mining area are greatly different from those in the ordinary farmland, and the soil productivity is difficult to reach the same level as the previous or cultivated soil [7–9]. The recovery of damaged land in mining areas is very slow, and in the process of land remediation and utilization of mining wasteland, how to improve the reclaimed soil, enhance the quality of mining soil, and restore land productivity is one of the key issues in land reclamation of mining wasteland [10–14].

Huainan Coalfield has a coal mining history of more than 100 years. It is one of 14 important large-scale coal bases and six coal-electricity bases in China. Located in the northern central part of Anhui Province, it is the coalfield with the best coal resources and the largest coal reserves in the eastern and southern regions of China at present. The coal resources provide a strong support for the rapid social and economic development of Huainan [15–17]. However, coal mining has led to the formation of large-scale subsidence areas. At present, the subsidence area of Huainan Coalfield is about 240 km^2 (calculated according to the subsidence line of 0.1 m). Huainan Coalfield is a Middle-Eastern plain area with coal, grain, and population highly concentrated. About 50% of the subsidence areas have become waterlogged areas and cannot be cultivated at all, while in the other 50%, affected by seasonal rain, some areas may not be cultivated [18, 19]. Coal mining has caused a series of problems concerning village relocation, compensation, resettlement, land-lost farmers' employment, social security, and so on. In order to restore cultivated land, integrate land resources, alleviate the contradiction between man and land, and restore the function of the regional ecosystem, many efforts in land reclamation have been made in the subsidence areas, which is of great significance to realize the sustainable development of Huainan Coalfield [20]. After land reclamation in the subsidence areas, the soil structure and properties have changed greatly compared with the original soil [21]. Land reclamation and reconstruction of soil in the subsidence areas often destroy the original structure and layer profile of soil due to mechanical crushing in the process. The physicochemical properties and fertility level of the reconstructed soil have changed greatly. The structure, fertility, and pH value of the reconstructed soil are still quite different from those of the ordinary farmland, so the productivity of the soil was difficult to reach the same level as the previous or cultivated soil [22]. And Huainan Coalfield is located in areas with high groundwater levels, and the depth of the subsidence area is generally more than 1.5 m, which forms the water area. Due to the function of soil capillaries and evaporation, salt accumulation in the surface soil leads to land salinization, and therefore, crops gain poor growth and low yields. Land productivity has been affected severely. It has brought a great harmful impact on the ecological environment of the region and threatened the regional ecological security [23].

Aiming at the problem of poor soil quality in the reclamation of mining wasteland, compost improvement and green manure improvement experiments were carried out to study the impact of different biomass improvement methods on the quality of reclaimed soil in this paper.

2. Materials and Methods

2.1. Methods of Land Reclamation. In order to study the effect of biomass improvement on the reclaimed soil quality of mining wastelands, the reclamation area of Xinzhuangzi coal mine in Huainan Coalfield is selected to study. The geographical location of the study area is shown in Figure 1. The control area of Xinzhuangzi Coal Mine Geological Environment Treatment Project is 22.87 hm^2. The method of reclamation of coal mining subsidence areas is to fill coal gangue. Firstly, coal gangue is filled in waterlogged subsidence areas, and then, loess is covered on the surface of coal gangue. The gangue is filled in layers, and 0.4 m is filled each time. The large particle size of gangue is backfilled to the bottom of the subsidence area, then the small particle size of gangue is backfilled, and next, a small amount of loess is added into the gangue to improve the water retention property. Each layer of the gangue filled in layers is rolled for more than 8 times. After the coal gangue filling, 1.0 m of thick loess covers the surface. The land structure of the gangue-filled reclamation area is shown in Figure 2. The land reclamation process is shown in Figure 3. After the topsoil layer is covered with soil, woody plants such as Metasequoia, Ligustrum lucidum, and peach trees are planted. After the planting for a period, soil hardening occurred, and the survival rate of Metasequoia was low. In study areas, field investigation, sampling and indoor analysis, and determination of samples were finished to clarify the types and spatial distribution of surface soil degradation and to figure out the main factors affecting the survival and development of plant communities in degraded soil [24]. The physical and chemical indicators of the reclaimed soil and the control farmland soil showed that the pH of the reclaimed soil was higher than that of the control farmland, being weak alkali. The four indicators, organic matter, available phosphorus, total potassium, and total phosphorus, were lower than the control farmland. The physical and chemical indicators of the reclaimed soil and the control farmland soil are shown in Table 1.

2.2. Soil Improvement Method. In order to improve the soil quality of the reclamation area, compost improvement and green manure improvement experiments were carried out in the study area, and then, the fertility index of the improved soil was measured and analyzed to study the impact of different biomass improvement methods on the quality of reclaimed soil.

2.2.1. Experimental Design of Compost Improvement

(1) Compost Preparation. The aquatic plant Cattail in the coal mining reclamation area is the main ingredient of organic compost. The compost can be divided into 4 types according to different auxiliary materials added in the composting process. Nutrient content in each type of compost is shown in Table 2.

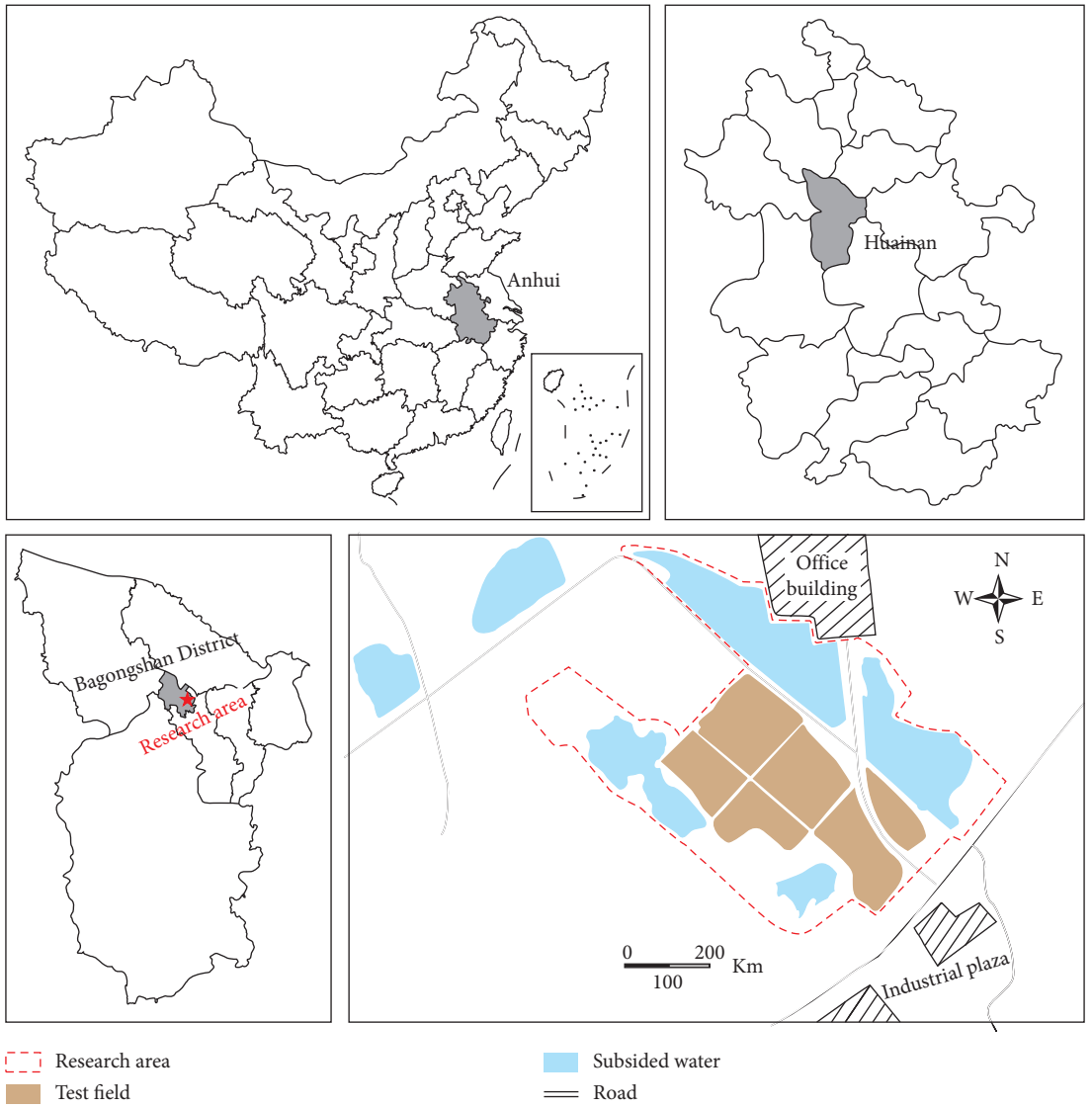

Figure 1: Geographical location of the study area.

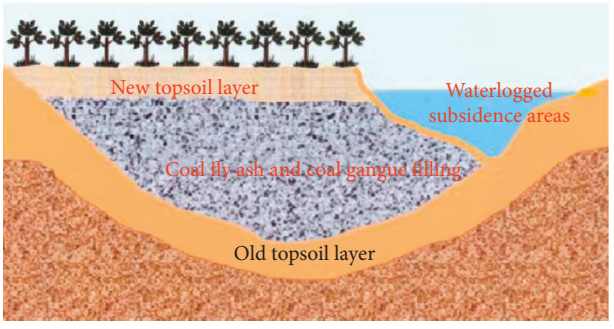

Figure 2: Diagram of filling the reclamation area of mining subsidence land.

(2) Test Scheme of Compost Improvement. Different types of compost are randomized into 11 groups for the compost improvement test, of which 8 treatment groups and 3 control groups are designed. The experimental design is shown in Table 3. Each treatment group covers an area of 200 m^2 and 0.9 kg/m^2 of organic compost being used in the experiment. The other three control groups are without fertilizer application. Alfalfa and Mexican corn are sown in each group after soil tillage. Alfalfa and Mexican corn are both salt-tolerant and barren tolerant and are suitable for growing on the reclaimed soil of mining wasteland. At the same time, they have the function of improving soil and are widely planted as forage grass in the local area. Therefore, we choose these two plants as experimental vegetation for soil improvement.

2.2.2. Experimental Design of Green Manure Improvement. White vanilla clover, a nitrogen-fixing leguminous plant growing in winter and early spring, is used as green manure. After soil tillage, white vanilla clover is planted in topsoil to increase the content of phosphorus and organic matter and improve the soil structure and boost fertility and water retention capacity. Different types of green manure are randomized into 3 groups for the green manure

(a) (b) (c)

Figure 3: Land reclamation process of mining wasteland. (a) Original condition of mining subsidence area. (b) Filling coal fly ash and coal gangue. (c) Covering the surface soil.

Table 1: Physical and chemical indicators of the reclaimed soil and the control farmland soil.

Soil type	pH	Bulk density (g/cm^3)	Organic matter (g/kg)	Available phosphorus (mg/kg)	Total potassium (g/kg)	Total phosphorus (g/kg)
The reclaimed soil	8.06	1.35	12.80	11.84	21.21	0.22
The control farmland soil	7.58	1.28	13.51	13.92	22.67	0.31

Table 2: Contents of nitrogen and phosphorus in organic fertilizers.

Type of organic fertilizer	Total *N* (%)	Available *N* (%)	Total *P* (%)	Available *P* (%)
NO.1	2.04	0.252	0.787	0.046
NO.2	1.71	0.231	0.949	0.226
NO.3	1.43	0.078	0.377	0.176
NO.4	1.67	0.171	0.761	0.121

Table 3: Experimental design for compost improvement in the reclamation area.

Type	Grasses	Type of organic fertilizer	Group name	Experimental area (m^2)	Amount of compost (kg/m^2)	Depth of improvement (cm)
Ecological restoration experiment in covering soil layer with trees and leguminous grass planted, plus compost improvement	Alfalfa	NO.1	Z1	200	0.9	20
		NO.2	Z2	200		
		NO.3	Z3	200		
		NO.4	Z4	200		
Ecological restoration experiment in covering soil layer with trees and gramineous grass planted, plus compost improvement	Mexican corn	NO.1	M1	200	0.9	20
		NO.2	M2	200		
		NO.3	M3	200		
		NO.4	M4	200		
Control group 1	Alfalfa	Nontreated	DZ	70	0	20
	Mexican corn	Nontreated	DM	70		
Control group 2	—	Nontreated	CK	800	0	0

improvement test, of which 2 treatment groups and 1 control group are designed. The experimental design is shown in Table 4.

2.3. Sample Collection and Processing. As for the collection of soil samples, stratified sampling shall be done according to soil profiles. During land reclamation, after filling gangue in a waterlogged area, 1.0 m of thick loess covers the surface. As the 1-meter-thick loess is homogeneous, samples should be collected in layers according to the technical specification for soil environmental monitoring in the environmental protection industry standard of the People's Republic of China. A sampling layer is divided every 20 cm from the surface, and samples are taken in the middle of each sampling layer to study the vertical distribution characteristics of soil nutrients in the soil. Therefore, in this paper, samples were collected from three soil layers at depths of 0–20 cm, 20–40 cm, and 40–60 cm, respectively. The arrangement of sampling points is shown in Figure 4. When sampling, mark off the sampling section within the depth range of sampling and take out soil samples layer by layer from top to bottom. Put soil samples in a bag, stick a label prepared before, and then

Table 4: Experimental design for green manure improvement in the reclamation area.

Type	Name	Group name	Experimental area (m^2)	Green plants	Depth of improvement (cm)
Ecological restoration experiment in covering soil layer with trees and leguminous grass planted, plus green manure improvement	Alfalfa	LZ	5.300	White vanilla clover	20
Ecological restoration experiment in covering soil layer with trees and gramineous grass planted, plus green manure improvement	Mexican corn	LM	5.300	White vanilla clover	20
Control group	—	CK	2.000	Nontreated	20

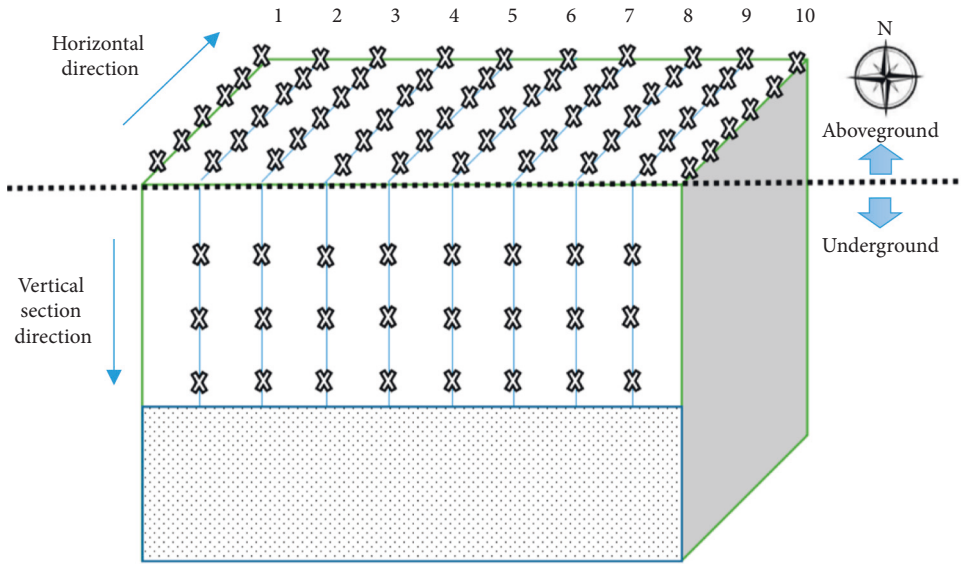

Figure 4: Distribution of sampling points.

bring them back to the laboratory. The samples were poured on a clean and dry plastic film or on a porcelain plate for natural air drying. The air-dried soil samples were ground, sieved (2 mm and 0.25 mm), placed in a dryer, and stored at room temperature, in a shade, cool, dry, and sealed environment [25]. The collection and processing process of soil samples is shown in Figure 5.

2.4. Soil Sample Testing. In order to ensure the accuracy of the test data, the unified test method of China is adopted for testing. The test standards and specifications used include soil technical analysis standard, soil environmental quality standard, and agricultural industry standard of the People's Republic of China. The measurement methods and standards of each index are shown in Table 5.

3. Results and Analysis

After 5 months of using compost and green manure to improve the reclaimed soil and planting grasses, the topsoil of the study area is sampled, and 10 soil physical and chemical indicators including water content, total nitrogen, ammonia nitrogen, nitrate nitrogen, available phosphorus, available potassium, total phosphorus, organic matter, pH, and conductivity are selected to evaluate the effect of soil improvement and to analyze the soil improvement effect.

3.1. Analysis of the Soil Improvement Effect by Growing Grasses. The fertility test data of control group 1 and control group 2 are compared to analyze the improvement effect on soil with grasses planted. As shown in Figure 6, compared with the control group CK, the available phosphorus increased by 60% and 55% in the reclamation areas of DZ and DM, respectively, the available potassium increased by 19% and 10%, the total phosphorus increased by 33% and 70%, and the organic matter increased by 40% and 8%.

There are no significant increases in water content, total nitrogen, ammonia nitrogen, nitrate nitrogen, pH, and conductivity of the topsoil. The results show that planting alfalfa and Mexican corn in reclaimed soil has little effect on the six soil indexes, so the six soil indexes are not analyzed. The results show that planting alfalfa and Mexican corn in the reclamation area can increase the contents of available P, available K, total P, and organic matter. And the content of available P in the topsoil is significantly increased. For organic matter, available phosphorus, total potassium, and total phosphorus contents are lower than the control group,

(a) (b) (c)

Figure 5: The collection and processing of soil samples. (a) Soil improvement test site. (b) Soil samples were collected with a ring knife. (c) Air-dry soil samples.

Table 5: Soil sample testing methods and standards.

Test indicators	Test methods	Reference standards
Soil moisture content	Drying method	T 0103-1993
pH	Potential method	GB7859-1987
Bulk density	Ring knife method	NY/T 1121.4-2006
Available nitrogen	Alkali-diffusion method	GB/T7849-1987
Available phosphorus	Ammonium fluoride-hydrochloric acid extraction	GB7853-1987
Available potassium	Ammonium acetate extraction-flame photometric method	GB7856-1987
Organic matter	Heavy acid oxidation-external heating method	NY/T1121.6-2006
Total nitrogen	CHN elemental analyzer	
Total phosphorus	Sodium hydroxide solution-molybdenum-antimony resistance colorimetric method	GB9837-1988
Total potassium	Acid solution-flame photometry	NY/T 87-1988

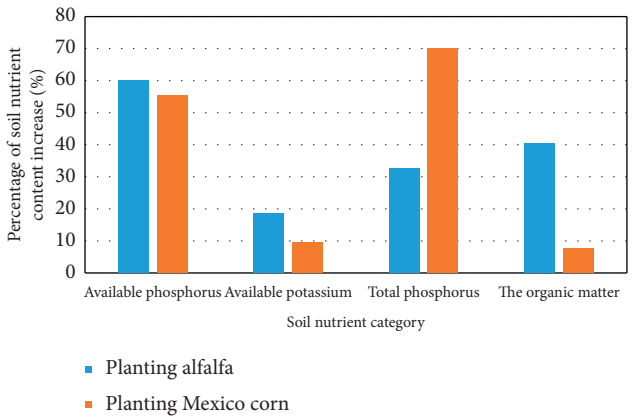

Figure 6: Physical and chemical indicators of the selected soils.

and we can conclude that planting alfalfa and Mexican corn in the reclamation area can effectively improve the soil quality.

3.2. Analysis of Soil Improvement Effect by Applying Compost. According to Table 4, compost No.1 to No.4 are, respectively, applied in treatment groups, and alfalfa is planted in groups called Z1 to Z4, while Mexican corn is planted in groups called M1 to M4. The above 10 indexes are measured, respectively, and three indexes of available phosphorus, available potassium, and total phosphorus do have obvious increases. In order to study the influence of different experimental designs on the indexes of available phosphorus, available potassium, and total phosphorus in reclaimed soil, Figure 7 is created to show the changes in available phosphorus, available potassium, and total phosphorus in groups Z1 to Z4 and M1 to M4.

(1) Growing Alfalfa after Applying Compost. As can be seen from the first three box plots of Figure 7, compared with the control group DZ, in the soil of the groups Z1 to Z4, the contents of available phosphorus increased to 123% from 45%, the contents of available potassium increased to 25% from 20%, and the contents of total phosphorus increased to 66% from 58% after applying four kinds of compost, respectively. A box plot uses its length to depict the distribution of a group of numeric data. According to the length of the first three box plots in Figure 7, the box of available phosphorus in Z1to Z4 is the longest, indicating that the content of available phosphorus changes most obviously in the soil after composting, and planting alfalfa after composting with alfalfa as the main raw material in reclaimed soil of the subsidence area can significantly improve the content of soil available phosphorus.

(2) Growing Mexican Corn after Applying Compost. In accordance with the last three box plots in Figure 7, compared with the group DM, after applying four kinds of compost, respectively, the contents of available phosphorus in M1to M4 increased to 114% from 22%, the contents of available potassium increased to 38% from 18%, and the contents of total phosphorus increased to 62% from 19%. According to the last three boxes in Figure 7, the available phosphorus,

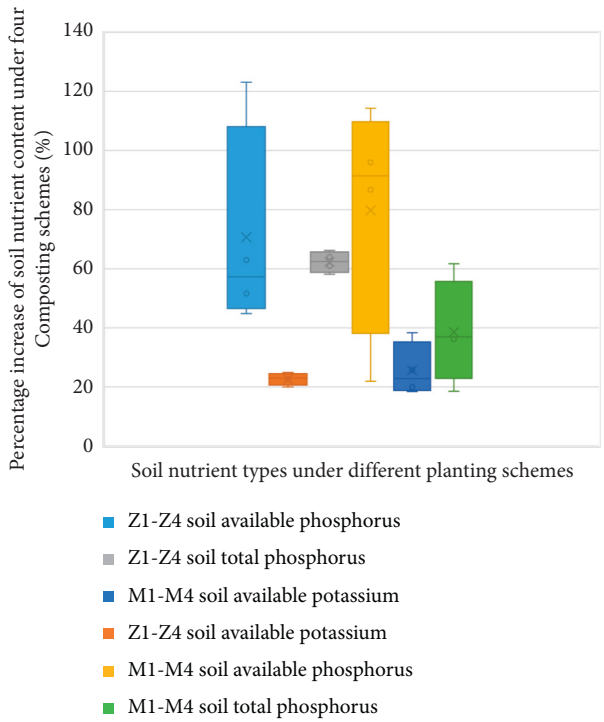

Figure 7: Nutrients changes in the soil with alfalfa and Mexican corn planted after compost improvement.

available potassium, and total phosphorus in the soil of M1–M4 are all longer, indicating that the contents of available phosphorus, available potassium, and total phosphorus have obvious changes after applying compost, and planting Mexican corn after applying compost with Cattail as the main raw material in the reclaimed soil of the subsidence area can obviously improve the contents of soil available phosphorus, available potassium, and total phosphorus.

(3) Optimization of Compost Improvement Method. The percentage increases in contents of available phosphorus, available potassium, and total phosphorus in the soil of Z1 to Z4 and of M1 to M4, as well as of DZ and DM, are shown in Figure 8. It can be seen from the figure that the groups with a faster increase in available phosphorus are Z1, M1, M2, and M3 with values of 123%, 114%, and 96%, respectively; the group with a faster increase in available potassium is M1 with the values of 38%; the groups with a faster increase in total phosphorus are Z3, Z4, and M1 with the value of 64%, 66%, and 62%.

At the same time, potassium, as a necessary element for plant growth, should be taken into consideration. Potassium plays an important role in biophysical and biochemical aspects, which is closely related to product transportation, energy conversion, and enzyme catalytic reaction in plants, and can obviously improve crop quality. In conclusion, the group with the best improvement effect of composting treatment is M1, in which planting Mexican corn after applying organic compost No. 1 has the best improvement effect on surface soil fertility in reclamation area.

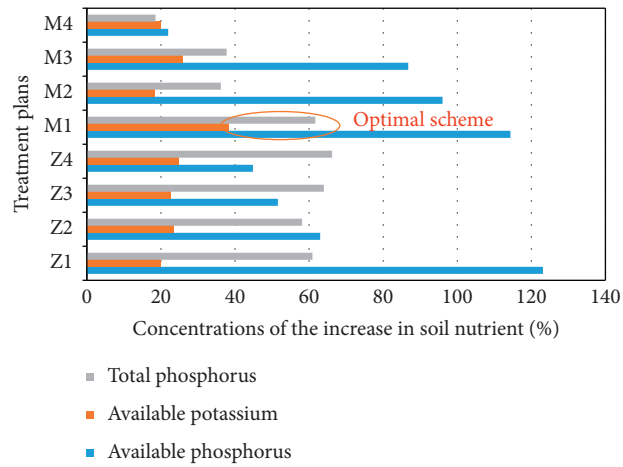

Figure 8: Fertility level of different treatment plans for compost improvement.

3.3. Effect of Green Manure Improvement on Soil Fertility. According to Table 4, the experiment on green manure improvement effect on treatment groups has been designed and conducted, and above 10 fertility indexes have been measured to draw the following conclusions.

After the nitrogen-fixing legume white vanilla clover is used as green manure to improve the soil in the reclamation area, compared with the control group CK, the contents of nitrate nitrogen, available phosphorus, available potassium, and total phosphorus in the surface soil of the group LZ increase by 155%, 58%, 30%, and 61%, respectively, while those of the group LM increase by 13%, 34%, 20%, and 29%. The test results are shown in Figure 9. In both groups LZ and LM, the rest of the fertility indexes are without obvious improvement. The results indicated that Melilotus Baixiang as green manure could significantly increase the contents of nitrate nitrogen, available phosphorus, available potassium, and total phosphorus in the surface soil of the reclamation area.

3.4. Effect of Biomass Improvement Scheme on Soil Nutrients. Through the above study, it is found that the three methods including growing grasses, applying compost, and green manure improvement on the reclaimed soil in the mining wasteland can improve the soil. Due to the barren soil in the mining waste area, the soil has a greater demand for available nutrients such as available phosphorus and available potassium. Therefore, the soil improvement schemes with more increase in available nutrients are selected to study the influence of soil improvement program on soil physical and chemical indexes. Therefore, six soil improvement schemes DZ, DM, Z1, M1, LZ, and LM are selected. Compared with the control scheme CK, the increased percentage of 10 soil physical and chemical indicators including water content, total nitrogen, ammonia nitrogen, nitrate nitrogen, available phosphorus, available potassium, total phosphorus, organic matter, pH, and conductivity is calculated. The calculation results are shown in Figure 10.

After the reclaimed soil of the mining wasteland is improved, the improvement effect is shown in Figure 10. LZ

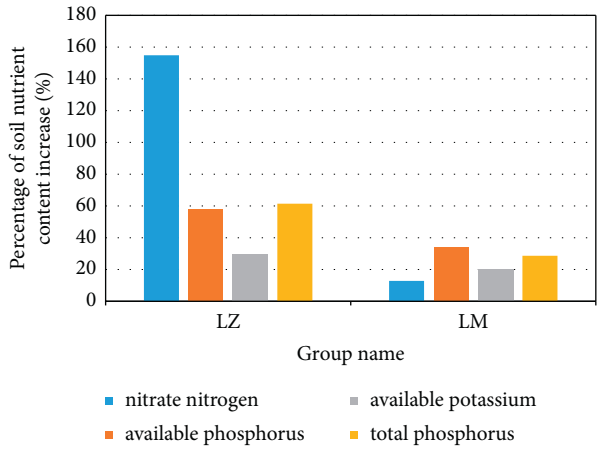

Figure 9: Fertility level of different treatment plans for green manure improvement.

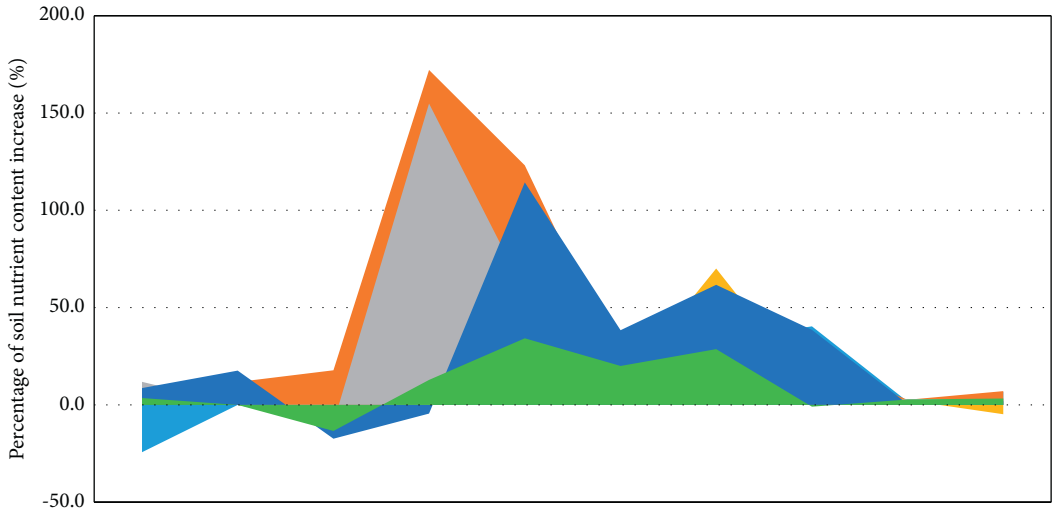

	Water content	Total nitrogen	Ammonia nitrogen	Nitrate nitrogen	Available phosphorus	Available potassium	Total phosphorus	Organic matter	pH	Conductivity
DZ	-24.3	0.0	-9.8	12.8	60.1	18.6	32.7	40.4	1.7	6.7
Z1	3.3	11.8	17.8	172.1	123.1	20.0	60.9	22.7	2.7	7.1
LZ	11.8	0.0	-9.2	154.9	58.2	29.6	61.5	0.7	3.0	3.0
DM	7.8	0.0	-7.5	0.0	55.2	9.5	70.1	7.8	2.4	-4.8
M1	8.6	17.6	-17.4	-4.4	114.3	38.4	61.7	38.6	0.5	1.9
LM	3.5	0.0	-13.4	12.8	34.2	20.0	28.7	-0.9	2.8	3.3

Physical and chemical indicators of reclaimed soil

Figure 10: Effect of biomass improvement scheme on physical and chemical indexes of soil.

has the largest effect on water content, and pH, M1 has the largest effect on total nitrogen and available potassium. Z1 has the largest increasing effect on ammonia nitrogen, glutamic nitrogen, and available phosphorus in the soil, while DM has the largest increasing effect on total phosphorus in the soil. DZ has the greatest effect on improving organic matter and conductivity in soil. This is helpful in the selection of soil improvement schemes.

4. Discussion

The reclaimed soil of mining wasteland belonged to the artificial reconstruction soil, the soil structure had been completely changed, it was different from the original soil, and it was realized as the soil quality deteriorates and productivity decreases, and the main reason was that the physical and chemical properties of reclaimed soil had

changed greatly [8]. Biomass improvement methods applied to reclaimed soil could effectively restore the soil productivity of land [10]. In this study, the soil quality of reclaimed soil was effectively improved by planting alfalfa and Mexican corn. Cattail, an aquatic plant, was used as raw material to make organic compost and applied to reclaimed soil of mining wasteland. After planting Mexican corn, the content of available phosphorus, available potassium, and total potassium in the soil was significantly increased. White vanilla clover was made into green fertilizer and applied to reclaimed soil of mining wasteland, which significantly increased the contents of nitrate nitrogen, available phosphorus, available potassium, and total phosphorus in the surface soil of the reclamation area. Biomass improvement technology could improve the fertility level of coal mine reclamation soil in a short time. It is conducive to promoting the restoration of soil fertility of mining wasteland and realizing the sustainable development and utilization of plant resources and land resources. In general, these biomass improvement methods on reclaimed soil can provide a reference for land reclamation of mining wasteland.

5. Conclusion

(1) After planting alfalfa and Mexican corn in the reclaimed soil, the contents of available phosphorus in the soil increase by 60% and 55%, respectively, the contents of available potassium increase by 19% and 10%, the contents of total phosphorus increase by33% and 70%, and the contents of organic matter increase by 40% and 8%. Thus, we can conclude that planting alfalfa and Mexican corn in the reclaimed soil can effectively improve soil quality.

(2) Cattail, a common aquatic plant, is the main raw material to make organic compost. After the compost is applied to reclaimed soil, planting alfalfa could significantly improve the soil's available phosphorus content, while planting Mexican corn could significantly improve the contents of the soil's available phosphorus, available potassium, and total phosphorus. The results show that the experimental design of the group M1 has the best effect on soil improvement, which means the improvement effect on the soil of the reclamation area with Mexico corn planted after applying organic compost No.1 is the best.

(3) The surface soil is ploughed with nitrogen-fixing legume white vanilla clover as green manure. After soil improvement, alfalfa and Mexican corn are planted, respectively, and then, the contents of nitrate nitrogen in the soil increase by 155% and 13%, the contents of available phosphorus increase by 58% and 34%, the contents of available potassium increase by 30% and 20%, and the contents of total phosphorus increase by 61% and 29%. White vanilla clover could be used as good green manure to improve the reclaimed soil in mining wasteland.

Data Availability

Data are available from the corresponding author upon request.

Conflicts of Interest

The authors declare that there are no conflicts of interest regarding the publication of this paper.

Acknowledgments

The authors also gratefully acknowledge the financial support of the Huainan Science and Technology Plan Project (2021A261), National Key Research and Development Plan (2016YFC0501105), and the Natural Science Foundation of Hunan Province (2021JJ40211).

References

[1] S. Z. Li, "Present status and Outlook on land damage and reclamation technology of mining subsidence area in China," *Coal Science and Technology*, vol. 42, no. 1, pp. 93–97, 2014.

[2] L. Yuan, Y. D. Jiang, K. Wang, Y. X. Zhao, X. J. Hao, and C. Xu, "Precision exploitation and utilization of closed/abandoned mine resources in China," *Journal of China Coal Society*, vol. 43, no. 1, pp. 11–20, 2018.

[3] C. Yuan, L. Cao, L. Fan, and J. Guo, "Theoretical analysis on distribution Pattern of plastic Zone in surrounding Rock of high-Gas-coal Roadway," *Advances in Civil Engineering*, vol. 2021, Article ID 6684243, 17 pages, 2021.

[4] Z. P. Xiao, C. L. Liao, X. H. Shan et al., "Effects of land Consolidation on soil fertility and spatial Variability," *Hunan Agricultural Sciences*, vol. 2020, no. 7, pp. 47–53, 2020.

[5] J. S. Wei, J. J. He, Y. Gao, X. He, and L. N. Lu, "Response of spatial and Temporal characteristics of soil moisture to mining subsidence in loess Hilly region," *Bulletin of Soil and Water Conservation*, vol. 28, no. 5, pp. 66–69, 2008.

[6] M. H. Huang and Y. M. Luo, "Land remediation and ecological restoration of mined land," *Acta Pedologica Sinica*, vol. 40, no. 2, pp. 161–169, 2003.

[7] Y. C. Chen, S. K. An, Y. H. Zhong, and C. Xu, "Investigation and evaluation of soil Fertilities in coal mining subsidence areas," *Journal of Anhui University of Science and Technology*, vol. 39, no. 3, pp. 7–15, 2019.

[8] C. Yuan, Y. Guo, W. Wang, L. Cao, L. Fan, and C. Huang, "Study on "Triaxial Loading-Unloading-Uniaxial Loading" and Microscopic damage test of sandstone," *Frontiers of Earth Science*, vol. 8, p. 11, 2020.

[9] Y. H. Zheng, Z. G. Zhang, Y. C. Chen et al., "Study on effect and evaluation of tree species on reclamation soil fertility quality in coal mining area," *Coal Science and Technology*, vol. 48, no. 4, pp. 156–168, 2020.

[10] J. P. Du, J. G. Shao, S. J. Tan, and F. Cao, "The research of land reclamation in coal mining area: Prospects and progress," *Journal of Chongqing Normal University (Natural Science)*, vol. 35, no. 1, pp. 131–140, 2018.

[11] L. J. Shi, X. Y. Wang, and Z. H. Hu, "Effects of different land Use Ways on soil basic properties and fertility," *Journal of Anhui Agricultural Sciences*, vol. 45, no. 6, pp. 106–108, 2017.

[12] C. Yuan, L. Cao, W. Wang, L. Fan, and C. Huang, "Case study on Rock support technology for Roadways based on

characteristics of plastic area," *KSCE Journal of Civil Engineering*, vol. 25, no. 2, pp. 705–723, 2021.

[13] S. D. Wang, Y. Liu, X. C. Wang, and C. Wu, "Suitability evaluation of mining-land reclamation based on improved decision tree model," *Science of Soil and Water Conservation*, vol. 14, no. 6, pp. 35–43, 2016.

[14] B. G. Hu and W. Y. Guo, "Mining subsidence area status, syntheses Governance model and Governance Recommendation," *Journal of Mining and Strata Control Engineering*, vol. 23, no. 2, pp. 1–4, 2018.

[15] Y. R. Song, J. M. Wang, X. F. Li, K. N. Wu, and Z. K. Bai, "Simulation of moisture Transfer Law with different soil reconstruction Models in coal mining subsided area with high ground-water level," *Journal of Soil and Water Conservation*, vol. 30, no. 2, pp. 143–148, 2016.

[16] S. Wang, M. Chen, X. Y. Chen, Q. H. Chen, B. L. Liu, and Z. Y. Hu, "Water Redistribution and Gas-Heat Diffusion of reconstruction soil filled with gangue," *Journal of Soil and Water Conservation*, vol. 31, no. 4, pp. 93–97, 2017.

[17] C. Yuan, L. Fan, J. F. Cui, and W. J. Wang, "Numerical simulation of the supporting effect of anchor rods on layered and nonlayered roof rocks," *Advances in Civil Engineering*, vol. 2020, Article ID 4841658, 14 pages, 2020.

[18] M. Chen, X. Y. Chen, H. R. Gui, G. J. Liu, B. L. Liu, and Z. Y. Hu, "Temperature variation and its response to topsoil thickness from reconstruction soil profile filled with coal gangue," *Journal of China Coal Society*, vol. 42, no. 12, pp. 3270–3279, 2017.

[19] L. G. Xu, Q. G. Li, X. M. Zhu, and S. G. Liu, "Hyperspectral Inversion of Heavy metal content in coal gangue filling reclamation land," *Spectroscopy and Spectral Analysis*, vol. 37, no. 12, pp. 3839–3844, 2017.

[20] W. G. Hou, C. S. Jiang, Q. W. Xiong, and J. X. Chen, "Evaluation of soil quality based on GIS," *Geomatics and Information Science of Wuhan University*, vol. 28, no. 1, pp. 60–64, 2003.

[21] C. X. Huang, J. S. Zhang, and X. M. Li, "Application of range Grey Clustering method on the soil quality Assessment," *Environmental Science Survey*, vol. 28, no. 4, pp. 61–64, 2009.

[22] B. G. Ma, J. Wang, J. R. Liu, Y. L. Wu, and J. Z. Hao, "Experimental study on water infiltration of soil weathering coal gangue," *Journal of China Coal Society*, vol. 39, no. 12, pp. 2501–2506, 2014.

[23] Z. Q. Hu, L. H. Duo, and X. T. Wang, "Principle and Method of reclaiming subsidence land with inter-layers of filling materials," *Journal of China Coal Society*, vol. 43, no. 1, pp. 198–206, 2018.

[24] H. J. Wei, Y. C. Li, N. Wang, L. G. Zheng, H. Cheng, and C. Xu, "Relationship between physical properties and organic-material Complexes of reclaimed soil back-filled with coal gangue under Various vegetation restoration Models," *Bulletin of Soil and Water Conservation*, vol. 35, no. 6, pp. 207–212, 2015.

[25] Y. H. Zheng, Z. G. Zhang, D. X. Yao, and X. Y. Chen, "Study on influence of gangue on reclaimed soil properties," *Journal of Anhui University of Science and Technology*, vol. 33, no. 4, pp. 7–11, 2013.

Hindawi
Advances in Civil Engineering
Volume 2022, Article ID 3675169, 10 pages
https://doi.org/10.1155/2022/3675169

Research Article

Groundwater Risk Assessment of a Rock Cave Type Landfill with Nontraditional Solid Waste

Chenchen Huo,[1] Lijie Guo ,[2,3] Weifang Wu,[1] Runsheng Yang,[1] Yue Zhao ,[2,3] Mingxin Lei,[1] Linfeng Shi,[1] and Baomin Yu[1]

[1]*The Fourth Research and Design Engineering Corporation, CNNC, Shijiazhuang 050021, China*
[2]*Beijing General Research Institute of Mining and Metallurgy, Beijing 100160, China*
[3]*National Centre for International Research on Green Metal Mining, Beijing 102628, China*

Correspondence should be addressed to Lijie Guo; guolijie@bgrimm.com

Received 4 December 2021; Accepted 25 March 2022; Published 27 April 2022

Academic Editor: Bang Yeon Lee

Rock cave landfill has the characteristics of superior geological conditions and strong risk controllability. In this study, taking the first rock cave type nontraditional solid waste landfill in a uranium mine in China as an example, combined with the hydrogeological conditions and engineering characteristics of the mining area, the solute transport model of underground water in a rock cave type nontraditional solid waste landfill was constructed, and the characteristic pollutants were identified, and the pollution migration law of total chromium in the impervious barrier with damaged holes was simulated and characterized. The results show that the leakage of pollutants will affect the groundwater environment when the impervious barrier of the landfill is damaged. The pollution plume exceeding the standard is mainly concentrated in the groundwater aquifer within the landfill area, which is less likely to spread to the off-site environment. The vertical high concentration pollution plume is primarily distributed in the landfill layer. According to the characteristics of rock cave landfills, it is suggested that hazardous solid waste should be separated from surrounding rock. The research results can provide technical guidance for groundwater environment prediction and prevention measures for the same type of project.

1. Introduction

With the continuous advancement of urbanization and industrialization, hazardous waste (HW) production in China continues to overgrow. Industrial nontraditional solid waste is the main source of HW for most cities and regions of China [1, 2]. According to the annual report of environmental statistics 2016–2019, the production and comprehensive utilization and disposal of industrial nontraditional solid waste increased year by year, from 52.195 million tons and 43.172 million tons in 2016 to 81.26 million tons and 75.393 million tons in 2019, up 55.7% and 74.6%, respectively (National Statistical Bulletin on Ecological Environment of 2016–2019, 2020). Industrial nontraditional solid waste has the characteristics of corrosivity, toxicity, flammability, reactivity, and infectivity. It has a wide range of sources and complex components [3–5]. HW has become a critical environmental issue throughout the world [6–8]. Improper disposal of nontraditional solid waste will pose a potential hazard to the atmospheric environment, soil environment, and water resources [9]. The disposal technique for nontraditional solid waste includes comprehensive utilization, incineration, and safe landfill, among which the safe landfill of nontraditional solid waste is the final disposal method of hazardous waste [10].

At present, nontraditional solid waste landfills in China are generally disposed of with surface landfills, and rock cave nontraditional solid waste landfills are the first in China. The rock cave type nontraditional solid waste landfill site has complete and hard surrounding rock as the external natural barrier for nontraditional solid waste disposal. The waste disposal will be less affected by rainfall, temperature, and humidity changes, which reduces the possibility of leachate generation and is convenient for all-round monitoring and

maintenance of the landfill chamber. The environmental risk of nontraditional solid waste landfills was mainly reflected in the leakage of the impervious layer [11]. The groundwater pollution caused by the leakage of leachate caused by the damage to the impermeable layer has become the primary problem of environmental risk of nontraditional solid waste landfills and its surrounding areas [12–14]. However, risk assessment and characterization of groundwater contamination due to rock cave landfills with the seepage of the impervious layer in China have not been studied.

Numerical models are effective means to solve many environmental problems. Models that predict groundwater dynamics can calculate the migration path and concentration trend of pollutants in the environment by generalizing hydrogeological and boundary conditions. Sathe and Mahanta [15] applied MODFLOW to reveal the distribution of arsenic in the aquifer. Tomiyama and others [16] used a numerical model to elucidate the groundwater flow patterns in the abandoned mine area. Huan and others [17] calculated the groundwater nitrate pollution risk based on the modeling method.

The objective of this study was to characterize the spatiotemporal trend of groundwater pollution arising from the condition of damage and continuous leakage of the impervious layer of the first rock cave type nontraditional solid waste landfill of a uranium mine in China. This study provides a basis for the implementation of groundwater environmental protection engineering measures in the landfill site.

2. Research Areas

2.1. Nontraditional Solid Waste. The rock cave type nontraditional solid waste landfill of a uranium mine is filled with HW18 (fly ash and incineration residue) according to the National Catalogue of Hazardous Wastes (NCHWs, hazardous waste list in China). The landfill scale of the underground landfill is 20000 tons per year of fly ash solidified body and 20775 tons per year of incineration residue solidified body. The production service life is 11 years, of which the first year is the capital construction period.

2.2. Physical Geography. The research areas were located in the low mountains and hills in Quzhou City, Zhejiang Province. The central location of the site is 28°50′40″ N and 118°58′36″ E. The altitude of the research areas is 160m ~ 600m, and the terrain of this area is high in the south and low in the north. The terrain of this area fluctuates wildly and is covered with well-developed plants. This area belongs to a subtropical monsoon climate with a humid climate and abundant rainfall. The annual average rainfall is 1763.7 mm, the annual evaporation is 986.5 mm, the yearly average temperature is 17.3°C, the maximum temperature is 40.5°C, and the minimum temperature is -10.4°C.

2.3. The Landscape of Research Areas. To establish the hydrogeological conceptual model for the research areas, field investigation and exploratory drilling were used to obtain the structural information about the aquifer. The hydrogeological information for the site is shown in Figure 1.

The strata in the site area are mainly Quaternary strata and volcanic rocks and pyroclastic rocks of the Upper Jurassic Moshanshi Formation. Quaternary strata are mainly artificial fill and residual slope deposits with small thicknesses. Volcanic rocks and pyroclastic rocks are mainly rhyolite and have a small amount of green layer. The geostructure of the site is located at the junction of the Yangtze Huaihe platform and the South China fold system. The regional structure is mainly NE trending faults, including Jiangshan-Shaoxing deep fault and Datangdi fault. The site mainly develops NNE formation and NWW formation faults (Figure 2), with a fault extension length of 280m ~ 2200m and a width of 1m ~ 20m. Breccia and fracture zones are mostly developed in the fault and filled with siliceous, fault gouge, or kaolin.

2.4. Hydrogeology. The east and west boundary of the research areas are Tongzikeng and Xiaoqiuyuan Rivers, respectively, and the surface water flows from south to north. Groundwater in the site can be divided into Quaternary pore phreatic water, bedrock weathering fissure phreatic water, bedrock fissure water, and structural fissure water. The Quaternary pore phreatic water is the pore water of alluvium and eluvium and the pore water of diluvium. The pore water of alluvium and eluvium is mainly distributed in bands along the Xiaoqiuyuan River. The pore water of diluvium is widely distributed in and around the site, and the thickness of diluvium is 0.5m–5.0 m.

Bedrock weathered fissure phreatic water mainly occurs in strongly weathered bedrock, exposed at the foot of the mountain, low-lying places, and scarps. It is often mixed with pore phreatic water of Quaternary eluvium and diluvium to form a phreatic aquifer with a unified groundwater level. The slightly (non)weathered bedrock is a good impermeable layer.

Bedrock fissure water is mainly distributed in the structural fracture zone or joint fissure dense zone of rock mass caused by multiple tectonic movements, with uneven water distribution and flow of 0.05 L/s ~ 0.62 L/s. Structural fissure water occurs in the structural fissure water-bearing zone. The main structural fissure water-bearing zones in the site are F1, F4, F6, Bailey, and Dachayuan fault-bearing zones, mostly water-blocking faults.

Atmospheric precipitation is the main recharge source of phreatic water in the site area. The phreatic water runoff path is short and has the characteristics of local recharge and discharge. The groundwater flows follow the nature of the terrain to the bottom of the valley and are mainly exposed to the surface in descending springs.

3. Methodology

3.1. Hydrogeological Conceptual Model. Based on the regional hydrogeological conditions in the landfill site and the distribution of sensitive areas, the simulation range is determined as

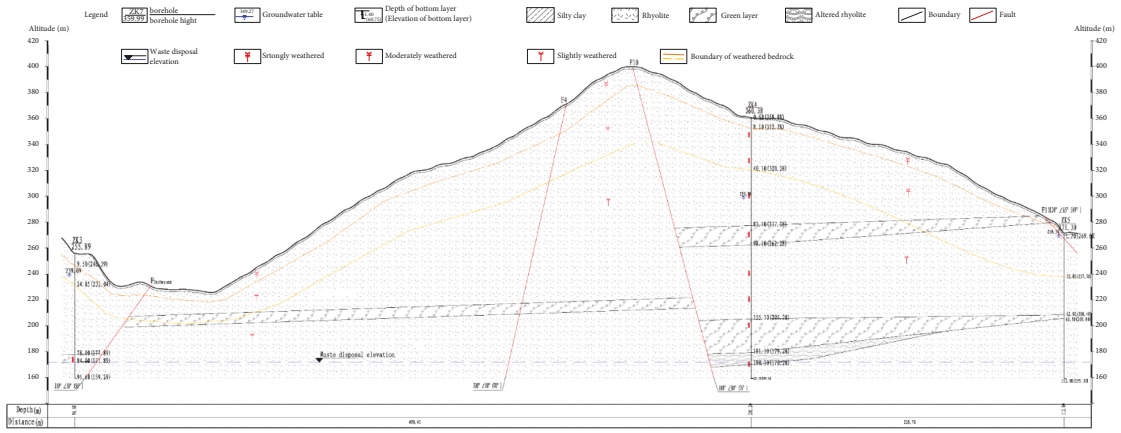

Figure 1: The exploration profiles of the site.

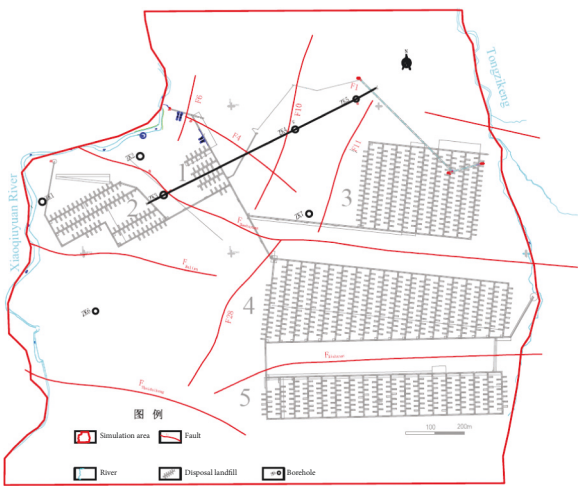

Figure 2: Map of simulation range.

follows: the west is bounded by Xiaoqiuyuan River, the east is bounded by Tongzikeng stream, and the north and south are artificially delineated. The north range is about 300m away from the center of the F1 fault, and the south range is about 310m away from the Shuiduikeng fault. The total area of the simulation area is about 2.4 km^2, which constitutes a relatively complete hydrogeological unit (Figure 2).

According to the information collected from exploratory boreholes and field investigation, the Quaternary eluvium and diluvium are mainly distributed on the two wings of ridge and hillside, with small thickness. Volcanic rocks and pyroclastic rocks are mostly strongly weathered, moderately weathered, and slightly (non)weathered rhyolites. As the rock cave landfill is underground, the design elevation of the landfill area is 170m ~ 185m, and the design elevation is mainly slightly (non)weathered rhyolite. Therefore, to better study the vertical variation of leachate concentration of nontraditional solid waste, the structure stratum can be vertically divided into three layers. The first layer is from the quaternary system to the top plate of the landfill area (185m elevation), the second layer is the location of the landfill layer, 170m ~ 185m, and the third layer is from the bottom plate of the landfill layer to 110m elevations.

The groundwater in the aquifers is conceptualized to be unsteady three dimensional. The aquifers are considered heterogeneous and anisotropic.

The study area is hilly, and the terrain is generally high in the south and low in the north. The groundwater flow direction is consistent with the terrain. Therefore, the southern boundary of the study area is generalized as the second type of constant flow supply boundary, the northern boundary is generalized as the second type of constant flow discharge boundary, and the east and west sides are generalized as the common head boundary. Moreover, the upper boundary is the precipitation supply and evaporation discharge boundary of water, and the lower boundary takes the bedrock as the bottom relative water barrier boundary.

3.2. Boundary Conditions and Pollution Source Settings. Boundary conditions reflect the water and material exchange process and intensity between the model and external system, and reasonable boundary conditions ensure a true reflection of the physical model [18]. The boundary of the model is characterized by local topography and adjacent water bodies. Therefore, the boundary settings were as follows. As the terrain is generally high in the south and low in the north, the south side of the simulation area was set as the second type of constant flow supply boundary. The north side was the discharge boundary of the simulation area. The east and west river are generalized as the common head boundary. The precipitation supply and evaporation discharge boundary is the upper boundary, and the lower boundary takes the bedrock as the bottom relative water barrier boundary. The model domain (including the boundary conditions and positions of the observation wells) is shown in Figure 2.

The landfill site comprises a landfill chamber, landfill roadway, development and transportation roadway, leachate collection tank, groundwater, and an excavation water inflow storage tank, which are successively divided into zone 1 ~ zone 5 (Figure 2). According to the "Standard for pollution control on the hazardous waste landfill" [19], the landfill adopts a rigid antiseepage structure composed of reinforced concrete shell and flexible artificial lining. From bottom to top, it is rock base, antiseepage reinforced concrete,

concrete slope making layer, observation layer, composite geonet, protective layer geotextile, HDPE antiseepage layer, protective layer geotextile, leachate diversion layer pebble, etc. The intact impervious membrane can play a good role in preventing the pollutants in the leachate. However, in the process of nontraditional solid waste disposal and the operation conditions of the landfill, the impervious layer will inevitably be damaged by puncture, tension crack, and aging, resulting in round hole type and crack type damage. The waterproof effect of the damaged impervious structure on the pollutants will be significantly weakened, which is prone to groundwater pollution risk [20].

According to the investigation results of landfill vulnerability density in China and relevant cases [21], it is determined that the vulnerability density of the impervious layer is 30 holes per 4047 m^2, and each hole is a circular hole with a diameter of 10 cm. The leachate flows into the groundwater through the damaged hole is calculated with

$$Q = K * J * A, \tag{1}$$

where Q is the seepage flow at the damaged hole in unit time (m^3/d); K represents the values of hydraulic conductivity of geotextile (m/d); A is the leakage area of the hole(m^2); J is the vertical upward hydraulic gradient.

The hydraulic conductivity of geotextile is 1×10^{-4}~10^{-3} cm/s. To estimate the extreme conditions, the hydraulic conductivity is defined as 1×10^{-3} cm/s, $J = 1.0$. The leakage area is calculated according to the hole with a diameter of 10 cm, and the single hole leachate flow is Q single hole = 0.0067 m^3/d. According to the area of the landfill chamber and landfill roadway in each landfill area, the area where the impervious layer may be damaged is estimated. The leachate flow in each area is as follows: Q Zone 1 = 0.16 m^3/d, Q Zone 2 = 0.62 m^3/d, zone Q Zone 3 = 1.53 m^3/d, Q Zone 4 = 3.21 m^3/d, and Q Zone 5 = 1.37 m^3/d, which are added into the model in the form of the point source.

The solid waste in the landfill site is enriched with $Cr6^+$, Total Cr, Hg, Cd, As, Pb, Ni, and other heavy metal elements. The identification of prediction factors is shown in Table 1. Control limits for entering landfill areas are taken from "Standard for pollution control on the hazardous waste landfill"

3.3. Mathematical Model of Flow and Mass Transport. A commercial professional software developed by Canadian Waterloo Hydrogeologic Inc—Visual MODFLOW—was used in this study to estimate groundwater pollution transportation. The software establishes the groundwater flow model by using the application module for three-dimensional finite-difference numerical simulation [23, 24]. According to the above hydrogeological conceptual model, the groundwater seepage mathematical model in the study area is established in

$$\begin{cases} \dfrac{\partial}{\partial \mathbf{x}}\left(\mathbf{K}\dfrac{\partial \mathbf{H}}{\partial \mathbf{x}}\right) + \dfrac{\partial}{\partial \mathbf{y}}\left(\mathbf{K}\dfrac{\partial \mathbf{H}}{\partial \mathbf{y}}\right) + \dfrac{\partial}{\partial \mathbf{z}}\left(\mathbf{K}\dfrac{\partial \mathbf{H}}{\partial \mathbf{z}}\right) + W = \mu\dfrac{\partial \mathbf{H}}{\partial \mathbf{t}} & (\mathbf{x}, \mathbf{y}, \mathbf{z}) \epsilon \Omega, t > 0, \\ H(\mathbf{x}, \mathbf{y}, \mathbf{z}, \mathbf{t}) = \mathbf{H}_0(\mathbf{x}, \mathbf{y}, \mathbf{z}) & (\mathbf{x}, \mathbf{y}, \mathbf{z}) \epsilon \Omega, \\ -KM\dfrac{\partial \mathbf{H}}{\partial \mathbf{n}}|\Gamma_2 = q & t > 0, \end{cases} \tag{2}$$

where H_0 is the initial head (m); H is the underground water level elevation (m); K represents the values of hydraulic conductivity (m/d); μ is specific yield; M is the aquifer thickness (m); x, y, and z are the coordinate variables (m); W is vertical water exchange intensity (m^3/d·m^2); q is the unit width seepage flow on the second type of boundary (m^2/d); n is normal direction outside the second type of boundary; Γ_2 is the second type of boundary; and O is the range of calculation area.

Based on the MT3DMS solute transport module, the pollutant transport law of the characteristic pollutant was simulated and predicted under the condition of continuous leakage. In this study, the adsorption and chemical reaction terms are not considered. Only the convection dispersion effect is considered, and the pollutant transport simulation is carried out based on the groundwater flow numerical model. The solute transport equation used in this simulation is

$$\begin{cases} n\dfrac{\partial \mathbf{C}}{\partial \mathbf{t}} = \dfrac{\partial}{\partial \mathbf{x_i}}\left(\mathbf{n}\mathbf{D_{ij}}\dfrac{\partial \mathbf{C}}{\partial \mathbf{x_i}}\right) - \dfrac{\partial}{\partial \mathbf{x_i}}(\mathbf{n}\mathbf{v_i}\mathbf{C}) + \mathbf{q_s}\mathbf{C_s}\ (\mathbf{x}, \mathbf{y}, \mathbf{z}) \in \Omega,\ i, j = 1, 2, 3,\ t > 0, \\ C(\mathbf{x}, \mathbf{y}, \mathbf{z}, 0) = \mathbf{C}_0(\mathbf{x}, \mathbf{y}, \mathbf{z}) \qquad (\mathbf{x}, \mathbf{y}, \mathbf{z}) \in \Omega, t = 0, \end{cases} \tag{3}$$

Table 1: Predictor identification.

Item	Cr6+	Total Cr	Hg	Cd	As	*P*b	Ni
Control limit for entering landfill area (mg/L)	6	15	0.12	0.6	2	1.2	2
Class III standard	0.05	0.05	0.001	0.005	0.01	0.01	0.02
Standard index	120	300	120	120	200	120	100

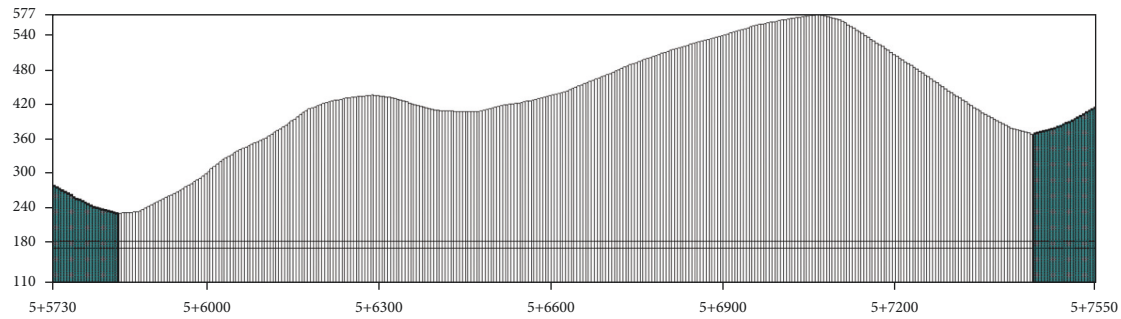

Figure 3: Vertical section of the grid.

where n is the medium porosity; C is the mass fraction of component ($mg \cdot L^{-1}$); t is the time; Dij is the hydrodynamic dispersion coefficient tensor ($m^2 \cdot d^{-1}$); Vi is the groundwater seepage velocity tensor ($m \cdot d^{-1}$); O is the calculation area; C_0 is the initial mass fraction distribution ($mg \cdot L^{-1}$); qs is the volume flow of source and sink of unit volume aquifer; Cs is the mass fraction of components in source and sink water ($mg \cdot L^{-1}$).

3.4. Model Construction and Calibration. Rectangular grids of 5m × 5m were used to subdivide the modelled area. The whole simulation area is divided into 324 rows along the north-south direction and 364 columns along the east-west direction. There are 97455 effective cells, representing the actual area of 2.4 km2. Vertically, the whole simulation area is divided into three layers, and the calculation area is divided into 292365 active units in space. Figure 3 shows the vertical section of the grid. The 1 : 2000 topographic map in the study area is digitised to form elevation data. After elevation points are extracted, and abnormal points are eliminated, the original elevation data of the simulation area are obtained. On this basis, the Kriging spatial interpolation method is further used to generate the digital elevation model [25], which meets the accuracy requirements of establishing the groundwater flow numerical model (Figure 4).

The main factors controlling the accuracy of the model predictions were hydrogeological parameters and solute transport parameters, which were obtained by in situ hydrogeological experiments and similar lithology investigation data. The values of various parameters for the reasonable-fit model are shown in Table 2, including the values of hydraulic conductivities (K) and the water yield of each layer.

The model was calibrated to enhance simulation reliability. A manual trial-and-error calibration method was used to achieve the calibration. The predicted output flow field was compared with the measured water level data to verify the rationality of the model [26–28]. The smaller the value of the standard error of the estimate, the closer the model predictions were to the actual observation values, and the higher the model accuracy. Seven hydrogeological boreholes in the area are used for identification and correction. The results are shown in Figure 5. Figure 6 shows that the correlation coefficient of water level fitting is 0.998, proving that the fitting effect is good. After the model identification, the initial groundwater flow field in the study area is obtained, as shown in Figure 7.

4. Results and Discussion

According to the design life of the landfill, the characteristic pollutant transport of the landfill in 20 years is simulated. Figure 8 and Figure 9 show the migration and diffusion of total chromium in the landfill's groundwater after the first, fifth, tenth, and twentieth years. Table 3 lists the simulation results of pollution plume migration distance and pollution area of total chromium at the above time points.

After the first year, five years, ten years, and twenty years, the predicted maximum concentration of total chromium was 0.2 mg/l, 0.45 mg/l, 0.6 mg/l, and 0.8 mg/l, respectively, under the condition of continuous leakage of pollutants, and no prevention measures were taken, exceeding the requirements of class III standard limit in groundwater quality standard. The maximum concentration was mainly distributed in the landfill site. On the plane, the pollution plume moves along the flow direction of groundwater as a whole. After the first year, the pollution plume in each landfill area is basically centered on the point source, and the diffusion area is small. From the 5th year to the 20th year, the pollution plume takes the point source as the center, the horizontal migration distance increases, and the area of the pollution plume increases. After 20 years, the pollution plume of the landfills in zone 3, zone 4, and zone 5 passes through the Dachayuan fault and Xishansi fault in the site, and other faults are less affected by pollution. After 20 years

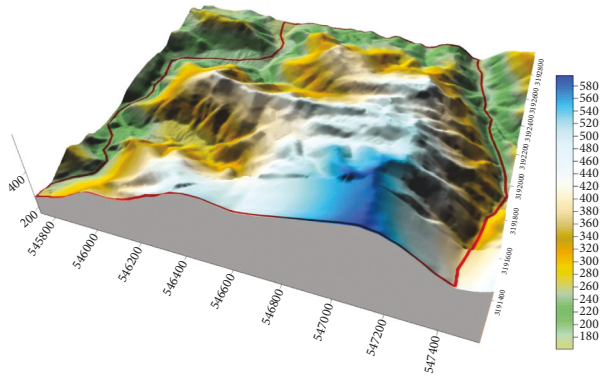

Figure 4: Digital elevation model of the study area.

Table 2: Hydrogeological parameters of the validated groundwater flow model.

Number	Lithology	Kxx/(m/d)	Kyy/(m/d)	Kzz/(m/d)	μ
1	Quaternary	0.2~1	0.2~1	0.2~1	0.2
2	Strongly weathered bedrock	0.1~0.2	0.1~0.2	0.1~0.2	0.1
3	Moderate weathered bedrock	0.02	0.02	0.02	0.05
4	Slightly nonweathered bedrock	0.002~0.02	0.002~0.02	0.002~0.02	0.05
5	Fault	0.0055~0.012	0.0055~0.012	0.0055~0.012	0.05

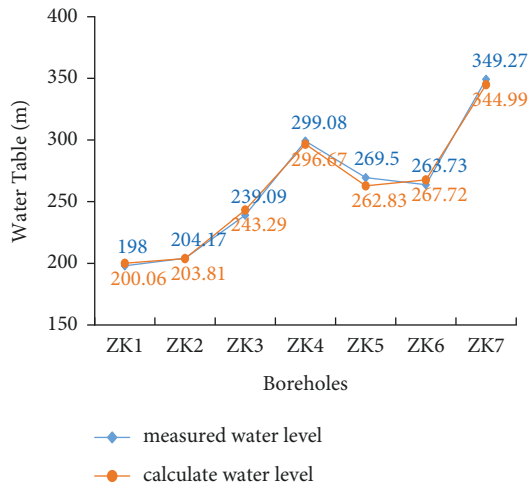

Figure 5: Comparison between calculated water level and measured water level.

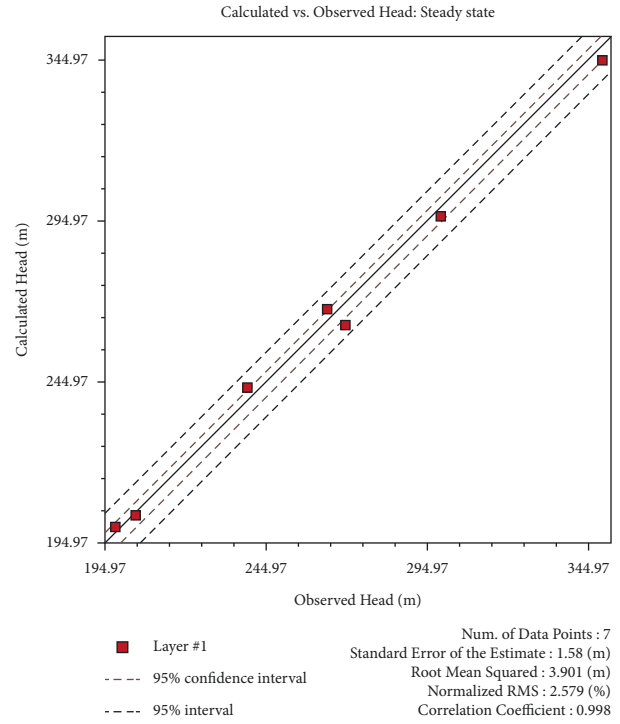

Figure 6: Fitting diagram of calculated water level and measured water level.

of continuous leakage, the areas of groundwater quality exceeding the standard in each landfill area are 0.03m2, 0.07m2, 0.16m2, 0.27m2, and 0.18m2, respectively, and the maximum migration distances from the pollution plume center are 158.48 m, 180.82 m, 253.57 m, 396.20 m, and 419.97 m. During the simulation period, the excessive range of total chromium pollution plume is mainly concentrated in the underground aquifer within the landfill area, the excessive range does not migrate to the surface water, and the leachate has little impact on the groundwater environment around the site.

Vertically, no top waterproof layer is set for nontraditional solid waste in the model, and the leachate is in direct contact with the top and sidewalls of the surrounding rock. Due to convection and dispersion, the damage to the impervious layer will cause pollutants to have a specific impact on the upper and lower aquifers of the landfill layer. Due to the small permeability coefficient of the surrounding rock, the pollutant concentration in the upper and lower aquifers of the landfill layer is low, and the high concentration pollution plume is still mainly distributed in the landfill layer.

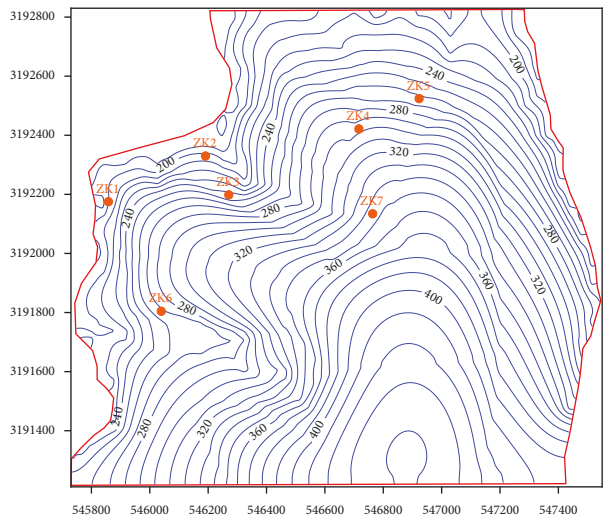

Figure 7: Initial flow field in the simulation area.

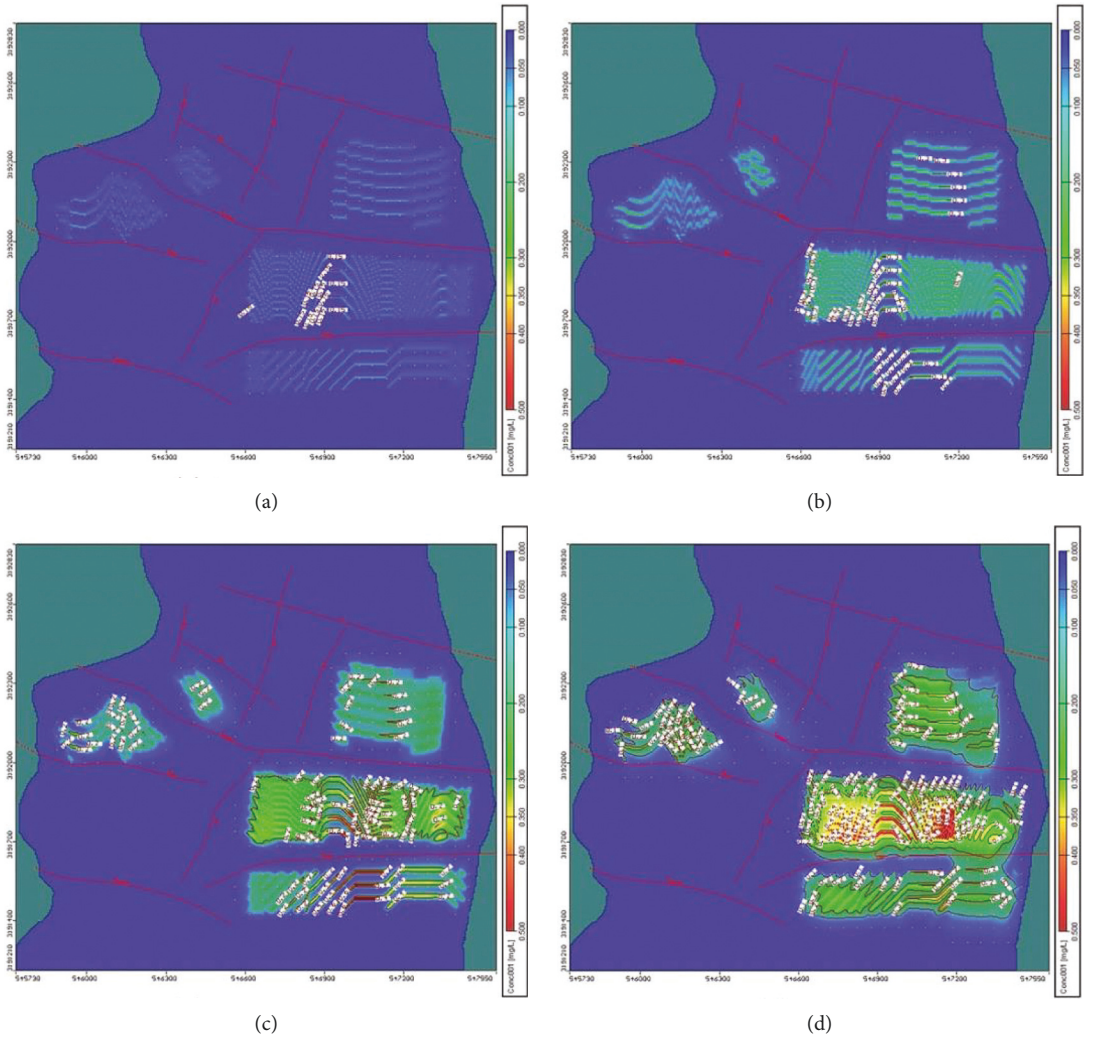

Figure 8: Total chromium pollution plume of disposal layer in the study area.

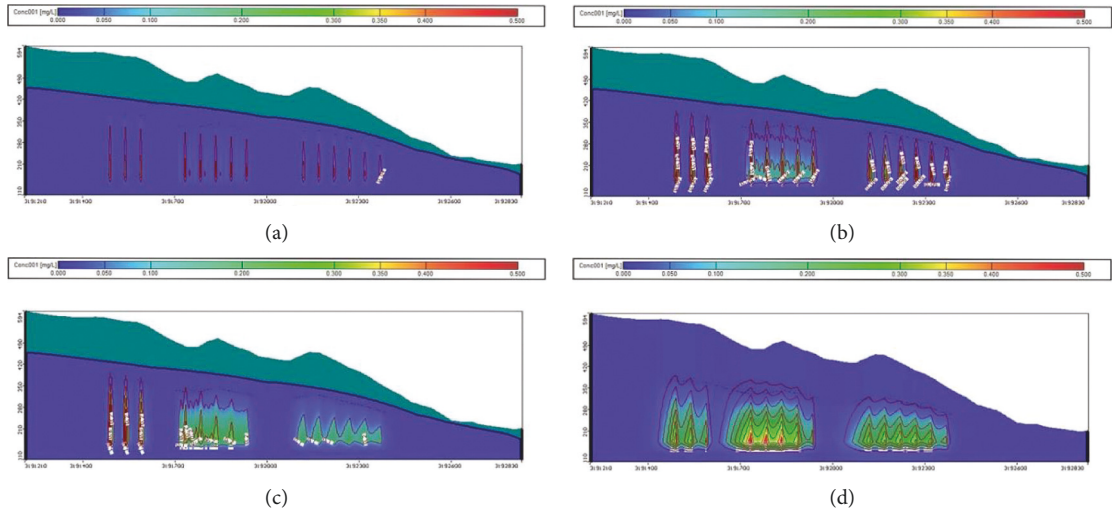

Figure 9: Total chromium pollution plume profile in the study area.

Table 3: Prediction results of total chromium pollution plume in groundwater.

	Zone 1		Zone 2		Zone 3		Zone 4		Zone 5	
	Maximum horizontal migration distance (m)	Polluted area (m2)	Maximum horizontal migration distance (m)	Polluted area (m2)	Maximum horizontal migration distance (m)	Polluted area (m2)	Maximum horizontal migration distance (m)	Polluted area (m2)	Maximum horizontal migration distance (m)	Polluted area (m2)
1 year	0.00	0.00	158.33	0.01	200.00	0.07	366.67	0.10	166.67	0.04
5 year	95.42	0.02	130.17	0.04	213.33	0.12	395.00	0.22	387.50	0.13
10 year	120.50	0.03	137.67	0.065	222.50	0.13	404.17	0.22	416.67	0.14
20 year	158.48	0.03	180.82	0.07	253.57	0.16	396.20	0.27	419.97	0.18

Note. The maximum horizontal migration distance is the maximum horizontal distance from the center of the pollution plume [19]. Taking the maximum value of the standard index, the prediction factor of this simulation is total Cr. According to the landfill scheme, the aquifer with an elevation of 170m ~ 185m is set as the polluted layer. The concentration of leakage pollutants is 15 mg/L. The final migration boundary concentration of pollutants refers to the class III standard limit in the "Standard for groundwater quality" [22].

5. Conclusions and Recommendations

This paper establishes a hydrogeological numerical model for the first cave type nontraditional solid waste landfill in a uranium mine in China, revealing the risk of groundwater pollution under continuous leachate leakage. The results justify the following conclusions.

In the case of continuous leakage of hole pollutant leachate in the impervious layer and no prevention measures are taken, the diffusion range of total chromium pollution gradually expands with time in the simulation period. Due to the slight leakage of pollutants and the small permeability coefficient of the aquifer, combined with the project layout scheme, the excessive range of pollution plume is mainly concentrated in the underground aquifer within the landfill area, the migration distance is short, and the possibility of diffusion to the off-site environment is slight. Therefore, it has little impact on the groundwater environment around the site. Vertically, the high concentration pollution plume is mainly distributed in the landfill layer and has little effect on the upper and lower aquifers of the landfill layer.

During the construction and landfill of the nontraditional solid waste landfill, the construction and landfill shall be carried out in strict accordance with relevant standards and guidelines to ensure the integrity of the impervious layer and reduce the risk of groundwater pollution caused by the damage of the impermeable layer. The rock cave type nontraditional solid waste landfill is still the first case in China. This study proves that it is feasible to use the rock cave type to safely landfill industrial hazardous waste, which has a particular reference significance for the implementation of similar projects in the future.

According to the characteristics of the rock cave type nontraditional solid waste landfill, to reduce the possibility of the impact of pollutants on the groundwater environment, it is recommended to set up space isolation between the solid waste and the chamber wall, such as HDPE waterproof layer on the top and a particular gap between the protective pool and the chamber wall. The patrol inspection and leachate monitoring of the landfill site are strengthened during the landfill and operation period. [29].

Data Availability

Data are available from the corresponding author upon request.

Conflicts of Interest

CH, WW, RY, ML, LS, and BY were employed by the Fourth Research and Design Engineering Corporation. The remaining authors declare that the research was conducted in the absence of any commercial or financial relationships that could be construed as a potential conflict of interest.

Authors' Contributions

CH, LG, and WW contributed to conceptualisation; CH and RY contributed to data curation; CH and ML contributed to formal analysis; LG contributed to funding acquisition; CH and WW contributed to the investigation; CH, WW, LS, and BY contributed to methodology; CH, WW, and BY contributed to numerical modeling; CH contributed to visualisation; CH contributed to writing the original draft; LG, WW, RY, YZ, ML, LS, and BY contributed to review and editing.

Acknowledgments

The authors would also like to thank the Zhejiang Quzhou Industry Corporation of China for their technical support. Financial support from the National Key Research and Development Program of China (2018YFE0123000) is gratefully acknowledged.

References

[1] H. Duan, Q. Huang, Q. Wang, B. Zhou, and J. Li, "Hazardous waste generation and management in China: a review," *Journal of Hazardous Materials*, vol. 158, no. 2-3, pp. 221–227, 2008.

[2] P. Kang, H. Zhang, and H. Duan, "Characterising the implications of waste dumping surrounding the Yangtze River economic belt in China," *Journal of Hazardous Materials*, vol. 383, pp. 121–207, 2020.

[3] A. Augustsson, T. Uddh Söderberg, J. Jarsjö et al., "The risk of overestimating the risk-metal leaching to groundwater near contaminated glass waste deposits and exposure via drinking water," *The Science of the Total Environment*, vol. 566-567, pp. 1420–1431, 2016.

[4] Y. Chen, L. Xu, S. N. Tan, X. Sun, Y. Deng, and W. Yang, "Solidification and multi-cytotoxicity evaluation of thermally treated MSWI fly ash," *Journal of Hazardous Materials*, vol. 388, Article ID 122041, 2020.

[5] M. Guarienti, A. Gianoncelli, E. Bontempi et al., "Biosafe inertization of municipal solid waste incinerator residues by COSMOS technology," *Journal of Hazardous Materials*, vol. 279, pp. 311–321, 2014.

[6] G. Salihoglu, "Industrial hazardous waste management in Turkey: current state of the field and primary challenges," *Journal of Hazardous Materials*, vol. 177, no. 1-3, pp. 42–56, 2010.

[7] K. Orloff and H. Falk, "An international perspective on hazardous waste practices," *International Journal of Hygiene and Environmental Health*, vol. 206, no. 4-5, pp. 291–302, 2003.

[8] L. Fazzo, F. Minichilli, M. Santoro et al., "Hazardous waste and health impact: a systematic review of the scientific literature," *Environmental Health*, vol. 16, no. 1, p. 107, 2017.

[9] V. Misra and S. D. Pandey, "Hazardous waste, impact on health and environment for development of better waste management strategies in future in India," *Environment International*, vol. 31, no. 3, pp. 417–431, 2005.

[10] R. Malviya and R. Chaudhary, "Factors affecting hazardous waste solidification/stabilization: a review," *Journal of Hazardous Materials*, vol. 137, no. 1, pp. 267–276, 2006.

[11] G. Hamer, "Solid waste treatment and disposal: effects on public health and environmental safety," *Biotechnology Advances*, vol. 22, no. 1-2, pp. 71–79, 2003.

[12] T. M. Alslaibi, Y. K. Mogheir, and S. Afifi, "Assessment of groundwater quality due to municipal solid waste landfills leachate," *Journal of Environmental Science and Technology*, vol. 4, no. 4, pp. 419–436, 2011.

[13] S. Banu and T. Berrin, "Parametric fate and transport profiling for selective groundwater monitoring at closed landfills: a case study," *Waste Management Series*, vol. 38, pp. 263–270, 2015.

[14] G. X. Chen, L. Wang, G. C. Wang, and J. H. Liu, "Modeling the transportation of pollutants in shallow groundwater in the landfill site near a medium city," *Hydrogeology & Engineering Geology*, vol. 6, pp. 112–116, 2008.

[15] S. S. Sathe and C. Mahanta, "Groundwater flow and arsenic contamination transport modeling for a multi aquifer terrain: assessment and mitigation strategies," *Journal of Environmental Management*, vol. 231, pp. 166–181, 2019.

[16] S. Tomiyama, T. Igarashi, C. B. Tabelin, P. Tangviroon, and H. Ii, "Modeling of the groundwater flow system in excavated areas of an abandoned mine," *Journal of Contaminant Hydrology*, vol. 230, 2020.

[17] H. Huan, L. Hu, and Y. Yang, "Groundwater nitrate pollution risk assessment of the groundwater source field based on the integrated numerical simulations in the unsaturated zone and saturated aquifer," *Environment International*, vol. 137, Article ID 105532, 2020.

[18] F. Lachaal and S. Gana, "Groundwater flow modeling for impact assessment of port dredging works on coastal hydrogeology in the area of Al-Wakrah (Qatar)," *Modeling Earth Syst. Environ*, vol. 2, 2016.

[19] GB 18598, *Taking the Maximum Value of the Standard index, the Prediction Factor of This Simulation Is Total Chromium*, (In Chinese), Beijing, China, 2019.

[20] L. Zhou, D. An, Y. Yang, B. Xi, and Y. Wang, "Predicting leakage and contaminant transport through composite liners in hazardous waste landfill," *Acta Scientiae Circumstantiae*, vol. 37, no. 6, pp. 2210–2217, 2017, (In Chinese).

[21] Y. Xu, C. Neng, and Y. Liu, "Statistical analysis on density of accidental-hole in landfill liner system," *Chinese Journal of Environmental Engineering*, vol. 9, pp. 4558–4564, 2015.

[22] Gb/T 14848, *Standard for Groundwater Quality*, National Standard Of The People's Republic Of China, Beijing, China, 2017.

[23] S. F. R. Khadri and C. Pande, "Ground water flow modeling for calibrating steady state using MODFLOW software: a case study of Mahesh River basin, India," *Modeling Earth Syst. Environ*, vol. 2, 2016.

[24] W. Li, Y. Y. Zhang, Y. Y. Zhang, X. Li, and C. Shen, "Research on the deep foundation pit dewatering design by three-dimensional numerical simulation," *Urban. Geotech. Investig. Surv*, vol. 1, pp. 189–192, 2019.

[25] T. M. Milillo and J. A. Gardella, "Spatial analysis of time of flight-secondary ion mass spectrometric images by ordinary kriging and inverse distance weighted interpolation techniques," *Analytical Chemistry*, vol. 80, pp. 4896–4905, 2008.

[26] S. Okhravi, S. Eslamian, and N. Fathianpour, "Assessing the effects of flow distribution on the internal hydraulic behavior of a constructed horizontal subsurface flow wetland using a

numerical model and a tracer study," *Ecohydrology and Hydrobiology*, vol. 18, p. 307, 2018.

[27] S. Guo, H. Wu, Y. Tian, H. Chen, Y. Wang, and J. Yang, "Migration and fate of characteristic pollutants migration from an abandoned tannery in soil and groundwater by experiment and numerical simulation," *Chemosphere*, vol. 271, Article ID 129552, 2021.

[28] X. Bai, K. Song, J. Liu, A. K. Mohamed, C. Mou, and D. Liu, "Health risk assessment of groundwater contaminated by oil pollutants based on numerical modeling," *International Journal of Environmental Research and Public Health*, vol. 16, no. 18, p. 3245, 2019.

[29] Ministry of Ecology and Environment of the People's Republic of China, "National statistical bulletin on ecological environment of 2016-2019," 2020, https://www.mee.gov.cn/hjzl/sthjzk/sthjtjnb/.

Hindawi
Advances in Civil Engineering
Volume 2022, Article ID 1112514, 15 pages
https://doi.org/10.1155/2022/1112514

Research Article

Research on Surrounding Rock Stability Affected by Surrounding Rock Pressure and Rock Fracture under Blasting Vibration Load Action

Qingjie Qi, Shuai Huang, and Yingjie Liu

China Coal Research Institute, Beijing 100013, China

Correspondence should be addressed to Qingjie Qi; qiqingjie@126.com

Received 31 December 2021; Accepted 21 March 2022; Published 23 April 2022

Academic Editor: Lijie Guo

The influence mechanisms of factors, such as high confining pressure and *in situ* stress caused by deep mining on the stability of surrounding rock of roadways, are complex. Particularly, the motion and energy release of the rock mass medium can be caused by vibration transmission induced by blasting excavation in the underground mining. Based on this, by taking a metal mine with the buried depth of 498 m as a research object, influences of different excavation distances on roof deformation and stress of roadway surrounding rock during the excavation were studied by using a three-dimensional numerical model. Moreover, the weak position of the roof of surrounding rock was determined. Finally, influences of fractured rock mass on propagation of blasting vibration waves in surrounding rock and energy distribution characteristics were analyzed. The research shows that rock mass around the excavated roadway moves towards the excavated space in different advance stages of a working face. The displacement fields on the top of a lateral tunnel present a heart-shaped distribution along the working face and the maximum displacement appears to the roof at the junction of the lateral tunnel and a horizontal roadway along veins. As the advance distance of the working face increases, compression-shear failure mostly occurs in the roadway surrounding rock, and tensile failure and combined tensile and shear failure occur at the unsupported roof and floor of the roadway. With the rise of the confining pressure, the total energy in frequency bands increases and its increase amplitude also rises. Furthermore, energy in a frequency domain of response signals to blasting vibration is transmitted from a secondary frequency band to a primary frequency band and is increasingly concentrated. With the increase of the damage degree of the roadway, signal energy in the frequency domain is transmitted from the primary to the secondary frequency band and signal energy is distributed more dispersedly. The test results are basically consistent with numerical simulation results. This study could provide technical guidance for the stability evaluation of surrounding rock of underground engineering structures.

1. Introduction

As the core of energy resource industry, mining industry has laid a foundation for national economic development and social progress. However, due to many uncertainties in mining as well as the high difficulty in and low level of management, the safety of mines are more complex than other industries. Based on statistics of mine accidents over the years, the annual death toll due to all kinds of mine engineering accidents accounts for more than 60% of the total casualties of workers in industrial and mining enterprises in China and the accident rate is much higher than that in other industries. In recent years, the mining depth of metal mines has been larger than 1,000 meters. However, factors, such as high confining pressure and *in situ* stress, lead to the state of stress instability of roadway surrounding rock, which increases difficulties in support and easily causes rib spalling and roof caving in surrounding rock. The safety of surrounding rock is a comprehensive factor reflecting integrity, deformation characteristics, strength, and stress states [1–3], and there are many influence factors and complex influence mechanisms. Therefore, it is of great significance to clarify influences of the confining pressure and different types of surrounding rock under blasting vibration on the stability of surrounding rock (Figure 1).

Figure 1: A collapse in a goaf.

In underground mining, the vibration triggered by blasting excavation can exert many influences on the surrounding rock stability. The impacts of the blasting load on rock mass can be regarded as motion and energy release of the rock mass medium in the propagation of blasting stress waves in rock mass. The failure of rock mass under the blasting load is directly related to the stability and safety of rock mass and involves the corresponding engineering support and reinforcement measures. Therefore, many researchers in the world have studied failure theory and rock mass models influenced by blasting and made a great progress. Zhai et al. [4] calculated the dynamic response of a cylindrical cavern under the load in a limited time of period based on the superposition method. Sinhg [5] explored damages of adjacent blasting to underground coal mines. Guo [6] analyzed vibration effects under different blasting modes and their propagation in surrounding rock. Liu and Wang [7] analyzed the dynamic response of the cavern under blasting loads with different waveforms. The causes of failure of surrounding rock by blasting can be summarized into three basic viewpoints: ① failure due to the expansion pressure produced by explosive gas [8], ② failure due to reflection of stress waves induced by shock waves [9], and ③ joint action of expansion pressure produced by explosive gas and stress waves caused by shock waves. Among the three viewpoints, the first two theories only unilaterally emphasize damage effects of the blasting load on rock mass from a certain aspect. However, the third theory simultaneously considers the action of expansion pressure produced by explosive gas and stress waves, which is often used to analyze practical blasting problems. Nevertheless, the above theories are all based on blasting characteristics of homogeneous materials. The heterogeneity and anisotropy caused by joints or fractures in rock mass can significantly affect the propagation of explosive gas and stress waves in rock mass, which obviously influences blasting response characteristics of rock mass. The failure theories of rock mass caused by blasting established based on characteristics of internal structures of rock mass include the elastoplastic theory (Harries model [10] and Favreau model [11]), fracture theory (nucleation and growth to fragmentation (NAG-FRAG) model [12] and BCM model [11]), and damage theory [13]. The effects of discontinuous structural planes, such as joints, fractures, and beddings, in actual rock mass on blasting characteristics are mainly manifested as local stress concentration, enhancement of stress waves, and energy attenuation. How to consider influences of discontinuity of rock mass on blasting vibration effects is also the research focus of failure of rock mass induced by blasting at present. Li [14] proposed that corresponding blasting parameters should be selected in actual engineering according to geological characteristics of the surrounding rock, so as to obtain good blasting effects. Cui et al. [15] explored interactions of fracture and joint types with blasting vibration waves. Moreover, they proposed that the breaking orientation of jointed surrounding rock is smaller than that of surrounding rock without joints, while phenomena, such as excessive fragmentation and uneven blocks, exist in local surrounding rock. Liang et al. [16] believed that discontinuous structural planes including joints can weaken the structure of rock mass. The structure of rock mass shows more complex characteristics of stress fields under the blasting load, while the presence of the structural plane obviously increases the attenuation rate of stress waves. Rossmanith and Uenishi [17] explored propagation of blasting waves at joints with different strengths and concluded that the joint stiffness of the rock mass medium can filter high-frequency components of blasting vibration waves. Scholars in the world have deeply explored spectral characteristics of blasting vibration signals under different blasting parameters. For instance, effects of factors, such as distance from blasting center, decked charging quantity, and total charging quantity on spectral characteristics of blasting vibration signals, were studied. Nevertheless, there are few studies on influences of fractures in surrounding rock on blasting waves' propagation in the rock and energy distribution in surrounding rock in response to blasting vibration of the roadway in an underground structure. Some scholars [18–22] have researched response signals of various engineering structures to vibration loads based on the wavelet transform analysis. They also have made many achievements in the optimization of blasting parameters and identification of blasting process and safety criteria of blasting vibration. However, due to high complexity and uncertainty of underground structure of rock

mass and blasting vibration load, it is necessary to carry out systematical and in-depth research.

Based on this, influences of different excavation distances on roof deformation and surrounding rock stress during roadway excavation were studied based on the three-dimensional (3D) numerical model. The weak position of the roof was determined. Finally, influences of fractured rock mass on blasting waves' propagation in surrounding rock and energy distribution characteristics were analyzed. In addition, the analysis results were verified to be reasonable through a laboratory test.

2. Analysis of Roof Stability of the Roadway

2.1. Calculation Model and Parameters. A metal mine was used in this study, and the gold mine is located in a low and gentle hilly area in the west of Jiaodong Peninsula and has better geological conditions compared with other gold mines, hard rock and low permeability. The project is controlled in a length of about 3,000 m and has a thickness ranging from more than one hundred meters to hundreds of meters. The project shows a strike angle of about 45° and is inclined to the southeast, with a dip angle of about 42° and obvious lithologic zoning. The main fracture surface is distributed along the contact zone between Archaean Jiaodong Group and rock mass in Linglong gold mine, with the thickness from tens of centimeters to several meters. Altered and quartz diorite porphyrite are widely developed in the footwall of the main fracture surface, and the main industrial orebodies were distributed in pyrite sericite and beresitized granitic cataclasite. The aim of this study is to master internal stress, deformation, and failure characteristics of surrounding rock caused by mining of the working face and dynamic response of rock mass in the mining process. To this end, a horizontal working face with the buried depth of 498 m of No. VII orebody in the gold mine was taken as the research object. Based on this, effects of blasting excavation-induced disturbance on the stability of surrounding rock were simulated by using a 3D calculation model. The planar distribution at the buried depth of 498 m is shown in Figure 2.

A calculation model was established by selecting the strike of the working face, a haulage way, and the vertical direction separately as the X, Z, and Y directions. In order to truly reflect surrounding rock environment, the dimensions of the 3D model were finally determined as $70\,\text{m} \times 30\,\text{m} \times 21\,\text{m}$ by comprehensively considering distribution characteristics of orebodies and surrounding rock and excavation-induced disturbance, as shown in Figure 3. The model had 65,321 elements and 73,821 nodes in total. Horizontal constraints were applied to the periphery of the model and vertical constraints were imposed to the bottom of the model. The Mohr–Coulomb model was used for the constitutive relationship. To obtain the stability of surrounding rock at different positions, five monitoring surfaces were set in a horizontal roadway along veins, and eight monitoring points were set on the cross section of the roadway.

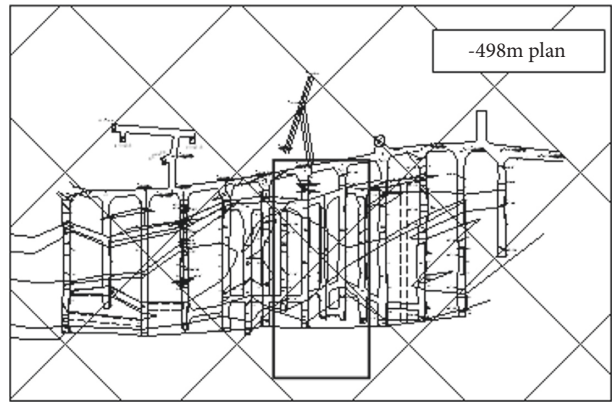

Figure 2: Planar graph at the buried depth of 498 m of the orebody.

The initial supporting elastic modulus E is 31.5 GPa, Poisson's ratio is 0.2, and bulk density is $2500\,\text{kg/m}^3$. The analysis parameters of the rock used in the calculation model were from geological survey report, as listed in Table 1.

The MAT_HIGH_EXPLOSIVE_BURN high-performance explosive materials in ANSYS/LS-DYNA program were used for simulation and the calculation took $5 \times 10^5\,\mu\text{s}$. The parameters of explosives are listed in Table 2. Lagrange algorithm was used for rock mass, and Arbitrary Lagrangian Eulerian (ALE) algorithm was utilized for explosives.

2.2. Analysis of Effects of Mining on the Surrounding Rock Stability. Before analyzing influences of blasting vibration on the roadway rock stability, change laws of displacement in the mining process were firstly analyzed, as demonstrated in Figure 4.

As shown in Figure 4, rock around the excavated roadway moves to the excavation space with the working face advance. The displacement fields on the lateral tunnel top are distributed in a heart shape along the working face, and the maximum displacement (6.3 mm) is found on the roof at the junction of the lateral tunnel and the horizontal roadway along veins. The displacement of surrounding rock of the floor reaches the maximum at the junction of the lateral tunnel and the horizontal roadway along veins, while displacement fields change unobvious along the excavation direction. Because the roof is unsupported due to roadway excavation, its displacement fields change more severely compared with those on the floor.

To further clarify the displacement variation of the roof of the horizontal roadway along vines, vertical displacements of the roof at different monitoring points were calculated under the advance distances of the working face of 5, 20, and 45 m. The change curves of the displacement are shown in Figure 5.

As shown in Figure 5, with the increasing of the excavation distance, the vertical displacement of surrounding rock tends to rise. The horizontal roadway along veins within 3 m from the lateral tunnel is significantly affected where the vertical displacement changes most obviously so that the vertical displacement increases by 62% at most. When the distance from the horizontal roadway along veins to the

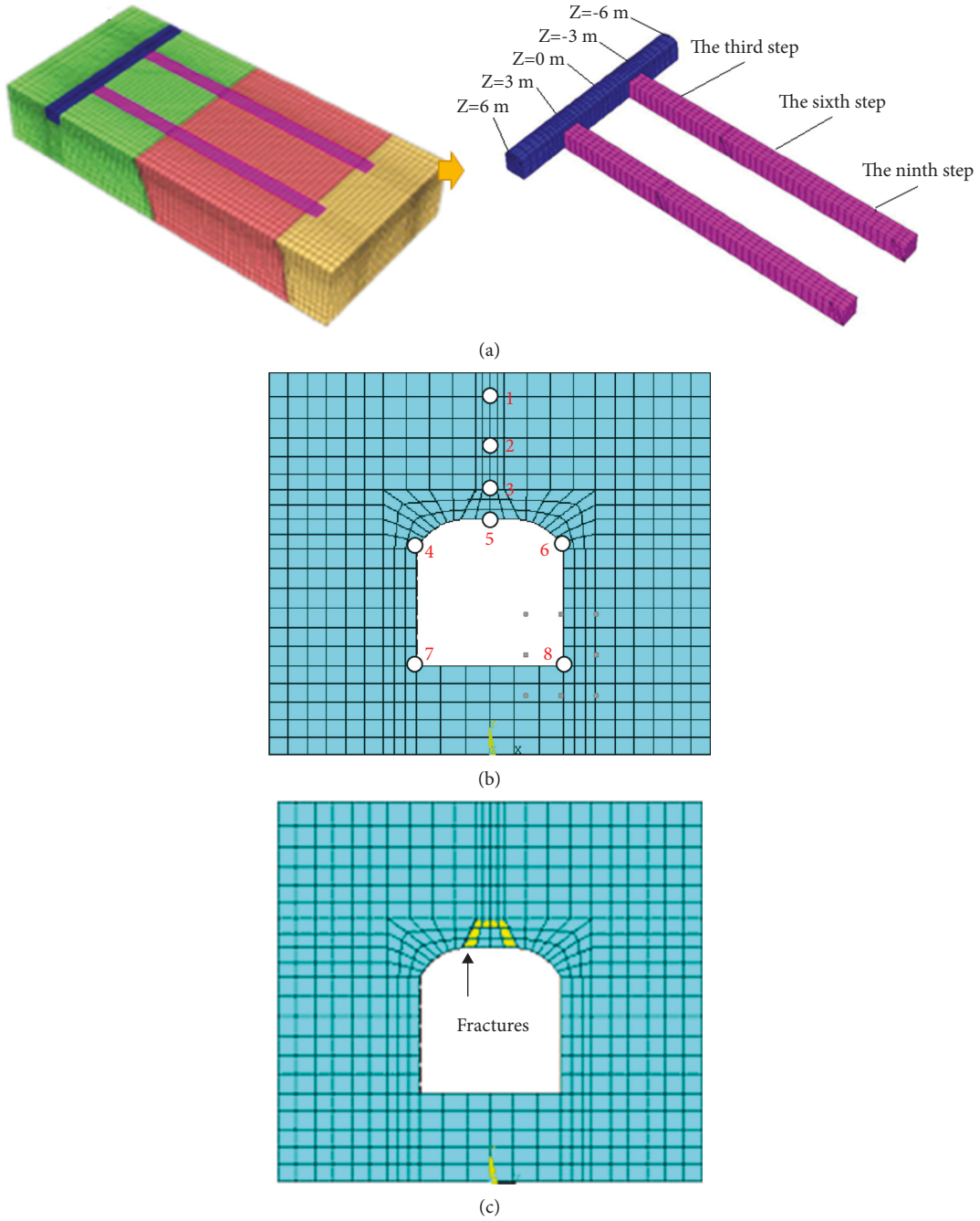

Figure 3: Establishment of the simulation model. (a) 3D model. (b) Intact rock. (c) Fractured rock.

Table 1: Rock parameters in the calculation model.

Rock	Tensile strength (MPa)	Elastic modulus (GPa)	Poisson's ratio	Cohesion (MPa)	Angle of internal friction (°)	Density (kg·m^{-3})
Hanging wall	7.1	17	0.27	4.3	27	2640
Ore body	8.0	23	0.22	6.2	34	2870
Footwall	7.2	21	0.25	5.5	31	2640

Table 2: Parameters of explosive materials.

Density (kg/m^3)	Blasting velocity (m/s)	A (GPa)	B/	R_1/	R_2 (GPa)	RCJ (GPa)	E_0 (GPa)
1250	5600	248	0.21	4.5	0.88	3.58	4.25

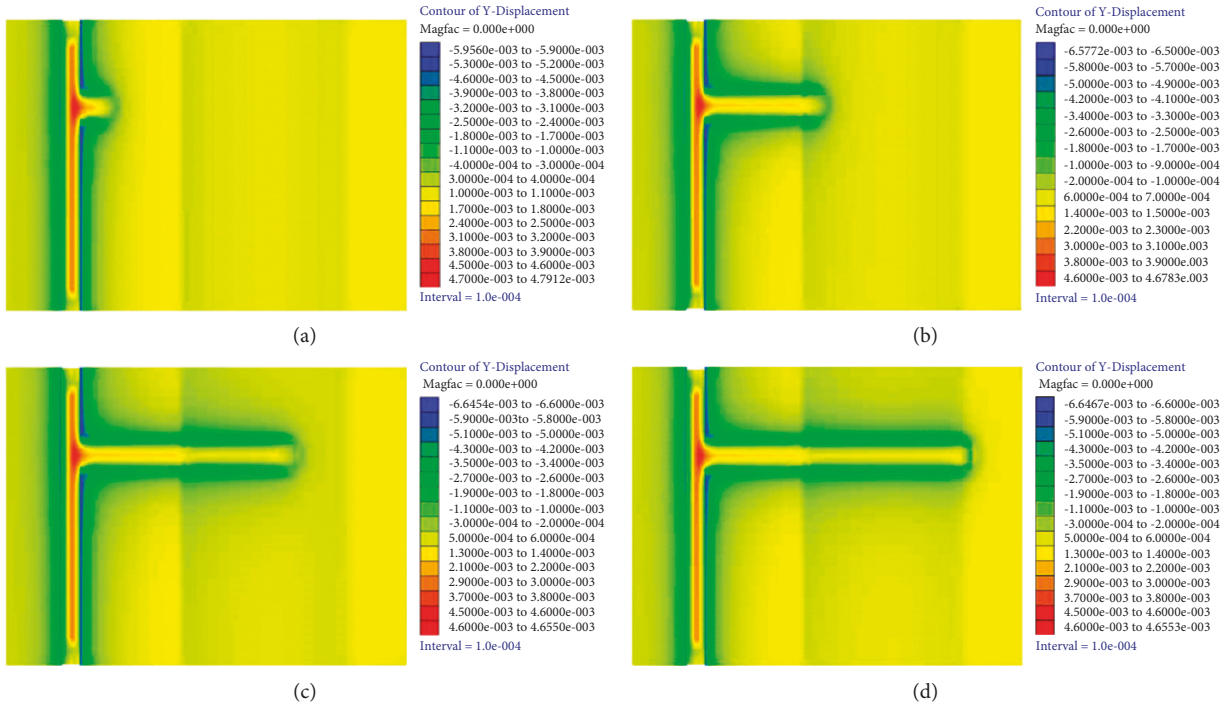

Figure 4: Displacement fields of the lateral tunnel. (a) Excavation 5 m. (b) Excavation 20 m. (c) Excavation 35 m. (d) Excavation 45 m.

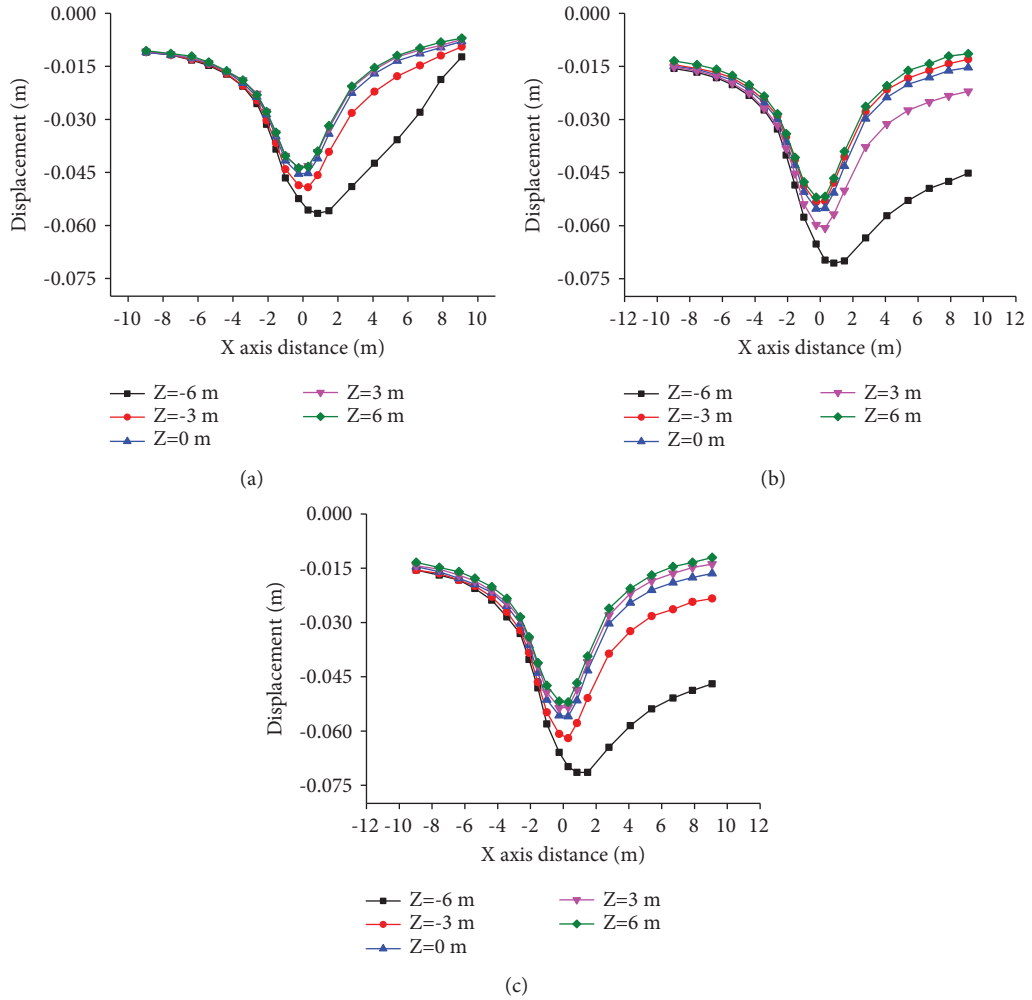

Figure 5: Vertical displacements of the roof at the monitoring sections under different distances. (a) Excavation 5 m. (b) Excavation 20 m. (c) Excavation 45 m.

lateral tunnel is larger than 3 m, the vertical displacement along veins changes insignificantly and the maximum displacement increases by 30%. On the whole, with the increasing of the excavation distance, the deformation of surrounding rock of the roadway increases, while its increase amplitude tends to decrease. Particularly, when the working face advances 5 m beyond the monitoring position, its deformation gradually tends to be stable. After exceeding 20 m, it can be considered that there is no influence.

The 3D simulation results for failure of the roadway surrounding rock during the excavation of the working face are demonstrated in Figure 6.

As displayed in Figure 6, damage of rock mass gradually accumulates as the advance depth of the working face increases. Due to low shear-bearing capacity of rock mass, surrounding rock mainly shows compression-shear failure, while tensile failure and tensile-shear failure mainly occur in surrounding rock of the roof and floor of the roadway in different excavation distance. With the excavation of the roadway, strain energy accumulates at the junction of the horizontal roadway along veins and the lateral tunnel so that the failure zone continuously develops. As the working face advances, overburden failure leads to continuous shear failure of overburden strata, which releases energy accumulated in rock mass and reduces the probability of dynamic disasters. When the excavation distance is 45 m, the subsequent failure zone in the roadway surrounding rock gradually changes into the elastic state.

2.3. Analysis of Influences of Fracture on Propagation Characteristics of Stress Waves in Surrounding Rock. To investigate different behaviors of stable roof and unstable roof of surrounding rock in blasting vibration, this study firstly simulated intact roof of surrounding rock and roof with the fracture when the detonation point was at the top of the model. The propagation of explosive waves lasted for 600 μs, as shown in Figures 7 and 8.

As illustrated in Figure 7, blasting waves propagate around in a ring from the explosion center in the initial blasting stage. In the following 80 μs, the vibration-induced stress waves propagate downward to both sides of the roadway bypassing the section of the roadway to form tensile stress zones on both sides till waves reach two side boundaries and bottom boundary. At 170 μs, a wide range of tensile stress concentration occurs directly above the roof. In the following time, the interaction between stress waves and reflected waves results in an alternation of compressive stress and tensile stress within the model until reaching stability. Similar to blasting vibration-induced stress waves' propagation in the stable roof, the simulated blasting starts from the roof at 0 s, and a wave front rapidly propagates from the blasting point to the whole model in the first 60 μs. This process is identical with that of the stable roof within 60 μs.

As displayed in Figure 8, when blasting-induced stress waves propagate to the fracture in the unstable roof, there are differences. Because of changes in physical parameters of the medium, stress waves do not propagate as the wave front of concentric circles, and at the fracture, the waves produce a concave surface pointing to the detonation point and then continuously develop. Moreover, reflected waves weaken when encountering the roof of the roadway. In the following 80 μs, vibration-induced stress waves propagate downward to both sides of the roadway bypassing the section of the tunnel, forming tensile stress zones on both sides, till the waves reach two side boundaries and bottom boundary. However, the tensile stress zones seen at 170 μs on both sides are much larger than those before, and the compressive stress concentration zone is formed above the fracture. In the subsequent time, stress waves interact with reflected waves to lead to the alternation of compressive stress and tensile stress in the model. When there is a fracture in the range of 200~450 μs, compressive stress and tensile stress waves alternate at regular intervals. This is because blasting vibration waves and waves reflected by the roof of the roadway are superimposed and act alternately. At about 450 μs, the fracture begins to fail, that is, internal fractures propagate. From 450 μs to 600 μs, fractures in the fracture constantly propagate and the structure finally fails. Based on this, the unit fractures in the unstable roof gradually propagate with the alternation of tensile and compressive stress till complete failure of the fracture at 600 μs.

3. Effects of the Confining Pressure on Energy Distribution of Response Signals of the Tunnel to Vibration

3.1. Energy Analysis of Response to Blasting Vibration. Based on wavelet transform and energy principle, the energy of response signals in surrounding rock of the roadway is decomposed into different frequency bands in a frequency domain. To investigate the energy distribution of each frequency band under different confining pressures, the energy ratio p_j in frequency bands is defined as follows:

$$p_i = \frac{E_i}{E_0} \, (i = 0, 1, 2, 3 \cdots, k-1), \tag{1}$$

where E_i and E_0 represent the energy in the ith frequency band in wavelet energy spectrum and total energy in the wavelet frequency band, respectively.

In the damped vibration system with multiple degrees of freedom, the rock mass medium was divided into structures with different frequency responses by fractures or cracks in rock mass. Therefore, the response signals of surrounding rock of the roadway to blasting vibration are composed of multiple frequency bands with different energies in different frequency ranges. After response signals of the roadway surrounding rock to blasting under different confining pressures are decomposed by 7-level wavelet transform, the results and energy in frequency bands are obtained. Based on this, the frequency band with the maximum energy is defined as a primary frequency band, while the rest frequency bands are defined as secondary frequency bands. Therefore, the primary frequency band of response signals is the frequency band 4, namely, 15.7~31.3 Hz.

Proportions of primary and secondary frequency bands in the increase amplitude of total energy in frequency bands

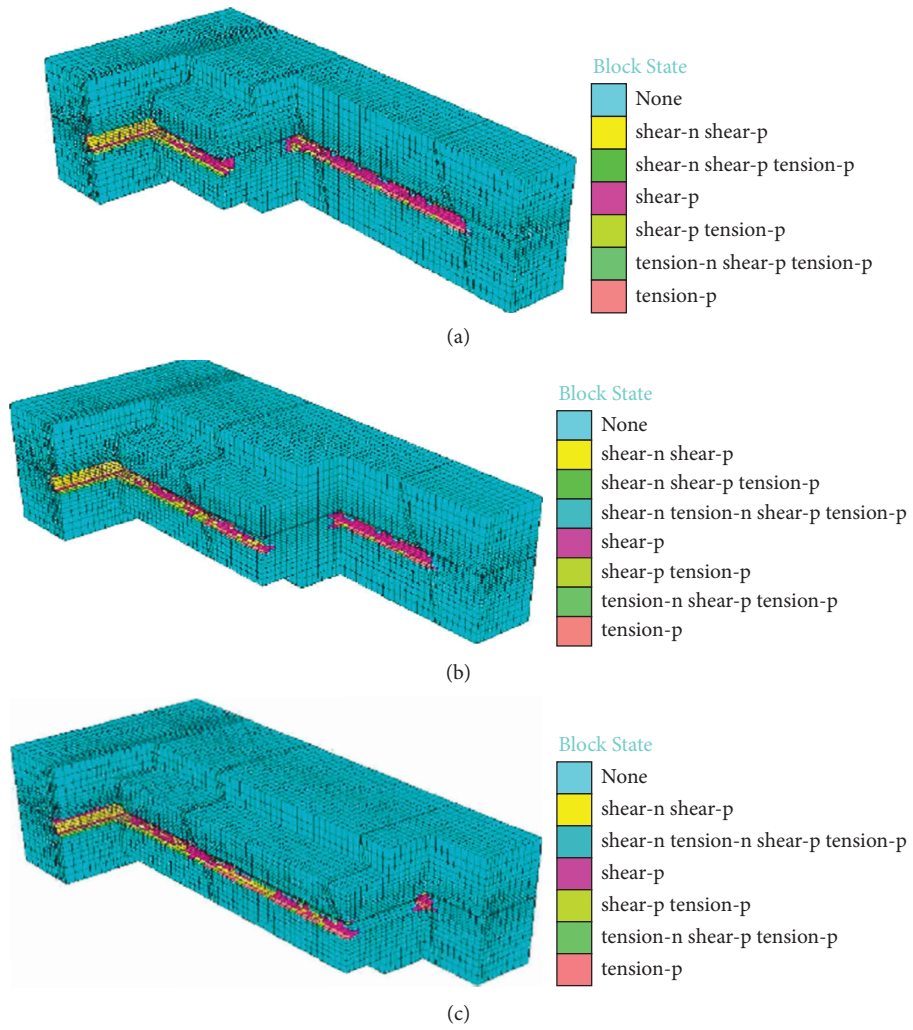

Figure 6: Damage models of surrounding rock in process of excavation. (a) Excavation for 15 m. (b) Excavation for 30 m. (c) Excavation for 45 m.

at eight monitoring points are extracted every time when the confining pressure increases by 4 MPa (the buried depth of the roadway increases by 160 m), as shown in Tables 3 and 4.

As illustrated in Tables 3 and 4, the increase amplitude of the energy in the primary frequency band is dominated in that of total energy in frequency bands caused by the increasing of the confining pressure. The increase amplitude of energy in the primary frequency band at monitoring point 2 accounts for about 63% of the increase amplitude of total energy, while those at monitoring points 5 and 6 occupy about 52%. Moreover, the increase amplitude of energy in the primary frequency band at monitoring point 8 accounts for around 42%. In the meanwhile, with the confining pressure increasing, the proportion of the increase amplitude of energy in the primary frequency band in that of total energy in frequency bands rises correspondingly. As the distance from blasting center increases, the energy ratio in the primary frequency band reduces. When the confining pressure is 20 MPa, the energy ratios in primary frequency bands at monitoring points 2, 5, 6, and 8 are 63.11%, 53.54%, 52.21%, and 42.32%, respectively. This indicates that a larger distance from the blasting center leads to wider energy distribution in the frequency domain of response signals in surrounding rock of the roadway, more uniform energy distribution, and larger influence range of blasting vibration effects.

Figure 9 shows vibration response signals of the roadway surrounding rock under the confining pressure of 1 MPa.

As demonstrated in Figure 9, the vibration velocity in the horizontal direction attenuates rapidly, while that in the vertical direction decays slowly after 0.2 s. The reason is that the reflection boundary is not applied on the model, so the horizontal blasting vibration waves are not reflected when propagating to the boundary; the vertical blasting vibration waves are reflected when propagating to the bottom of the model. In the meanwhile, the second and third wave peaks appear at 0.06 s and 0.085 s as well as 0.2 s and 0.3 s in time histories in the horizontal and vertical directions at monitoring points 5, 6, and 8. This implies that reflection existing when blasting vibration waves propagate to the roadway walls.

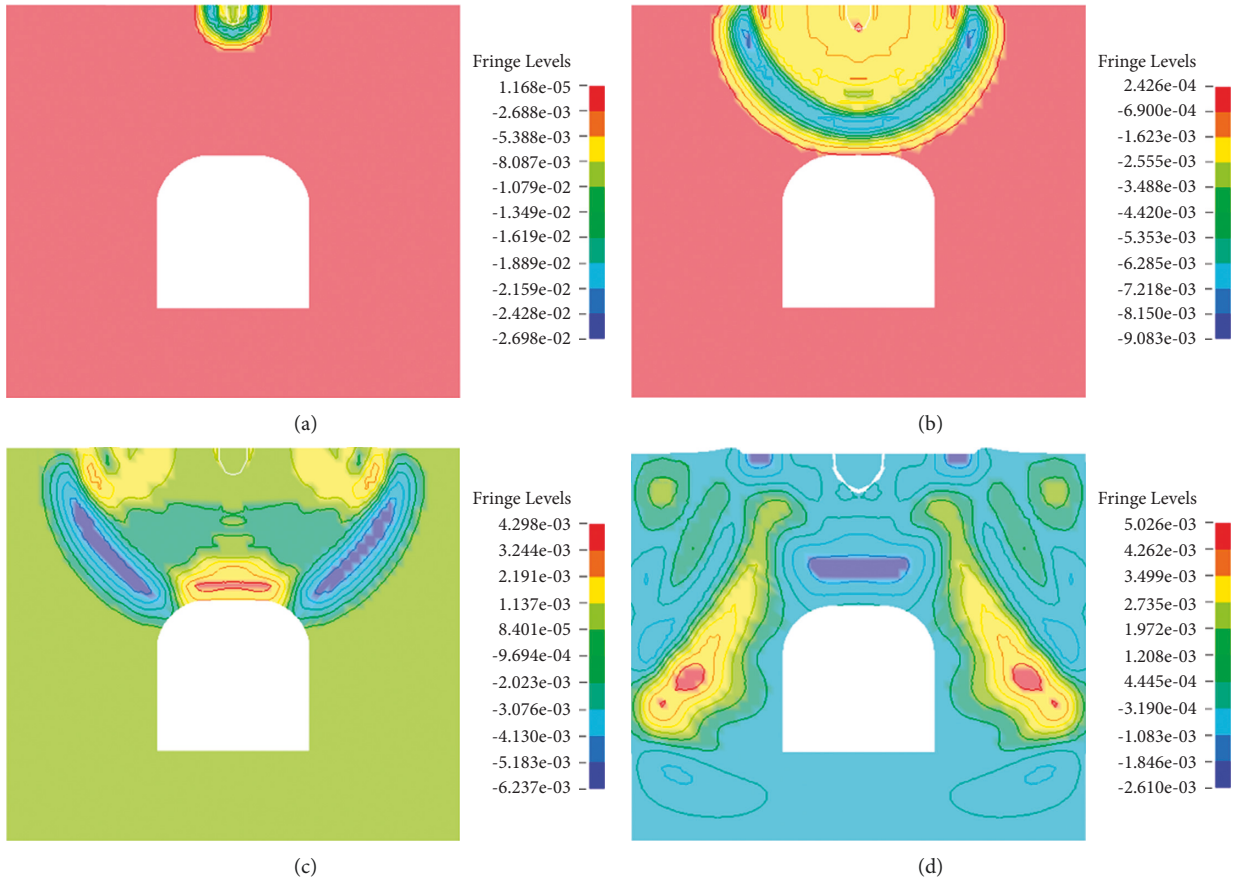

FIGURE 7: Blasting waves' propagation in intact surrounding rock. (a) Stress propagation within 30 μs. (b) Stress propagation within 120 μs. (c) Stress propagation within 400 μs. (d) Stress propagation within 660 μs.

The surrounding rock stress state directly affects the propagation and attenuation of blasting vibration waves. Figure 10 demonstrates the horizontal and vertical peak vibration displacements at various monitoring points under different confining pressures.

Figure 10 shows that the displacements tend to rise with the confining pressure increasing from 1 to 11 MPa. Taking the horizontal displacement as an example, the differences of the displacements at different monitoring points separately are 13.1%, 46.5%, 30.02%, 6.5%, 38.1%, 19.4%, 17.7%, and 67.9% under the confining pressure of 1 MPa. Under the confining pressure of 20 MPa, the differences are 422.7%, 383.7%, 559.9%, 362.1%, 558.9%, 269.3%, 125.2%, and 55.1%, respectively.

In Figure 11, as the confining pressure rises from 1 to 11 MPa, the horizontal stresses and vertical stresses of different monitoring points increase. In addition, under the confining pressure of 1 MPa, the differences of peak stresses in horizontal and vertical directions at different monitoring points separately are 13.5%, 46.2%, 28.5%, 7.0%, 35.5%, 17.1%, 15.8%, and 65.7%. The differences are 418.5%, 378.2%, 571.5%, 349.2%, 548.8%, 272.5%, 122.9%, and 53.5% under the confining pressure of 20 MPa.

The total energies in wavelet frequency bands at various monitoring points in surrounding rock of the roadway under different confining pressures are compared in Figure 12.

As displayed in Figure 12, the total energies in frequency bands in the horizontal direction at each monitoring point are smaller than those in the vertical direction under different confining pressures. By taking the monitoring point 5 as an example, the total energy in frequency bands in the horizontal direction is 3.35×10^4 J, while that in the vertical direction is 1.69×10^5 J under the confining pressure of 20 MPa. In the meanwhile, the total energy in frequency bands in the horizontal direction is maximum at monitoring point 8, while the minimum value is found at monitoring point 1. The opposite phenomenon is found in the vertical direction. This is because these monitoring point have different distances to the blasting center. The larger the distance from blasting center is, the greater the total energy in wavelet frequency bands of response signals. With the confining pressure increasing, the total energy in frequency bands rises and its increase amplitude also increases. Similarly, by taking the monitoring point 5 as an example, the increase amplitudes of total energy in frequency bands in the horizontal direction separately are 2,112, 3,989, 5,898, 7,798, and 9,587 J, while those in the vertical direction are 10,809, 22,415, 33,890, 45,700, and 56,910 J, respectively.

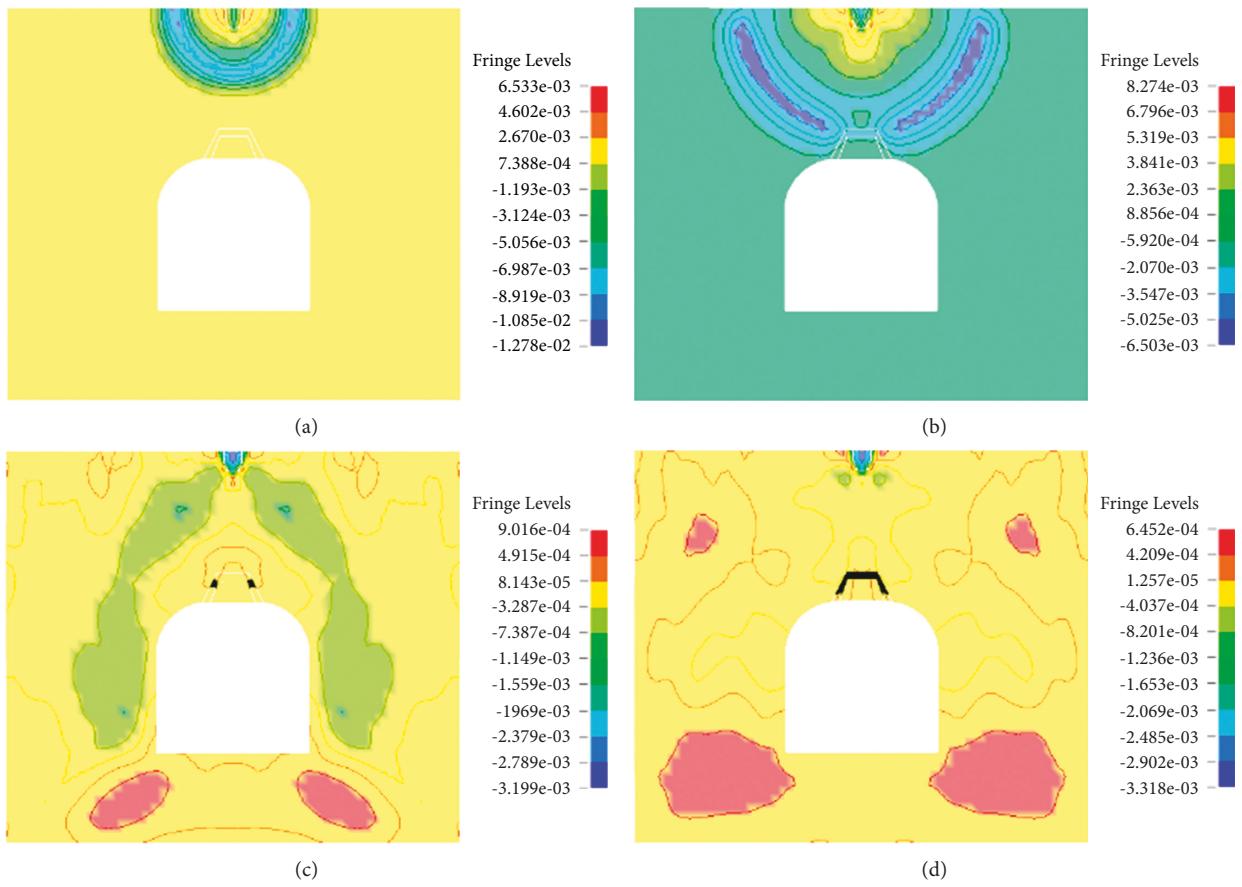

Figure 8: Stress waves' propagation in rock mass with the fracture. (a) Stress propagation within 30 μs. (b) Stress propagation within 120 μs. (c) Stress propagation within 400 μs. (d) Stress propagation within 660 μs.

Table 3: Proportions of primary and secondary frequency bands in the increase amplitude of total energy in frequency bands at monitoring points 1~4 (%).

Variation of confining pressure	Monitoring point 1		Monitoring point 2		Monitoring point 3		Monitoring point 4	
	Primary	Secondary	Primary	Secondary	Primary	Secondary	Primary	Secondary
1~4 MPa	63.25	34.75	62.30	35.70	60.20	37.80	58.15	39.85
4~8 MPa	63.06	34.94	62.81	35.19	60.65	37.35	58.89	39.11
8~12 MPa	63.02	34.98	62.97	35.03	60.75	37.25	59.01	38.99
12~16 MPa	63.04	34.96	63.04	34.96	60.90	37.10	59.27	38.73
16~20 MPa	63.00	35.00	63.11	34.89	60.90	37.10	59.28	38.72

Table 4: Proportions of primary and secondary frequency bands in the increase amplitude of total energy in frequency bands at monitoring points 5~8 (%).

Variation of confining pressure	Monitoring point 5		Monitoring point 6		Monitoring point 7		Monitoring point 8	
	Primary	Secondary	Primary	Secondary	Primary	Secondary	Primary	Secondary
1~4 MPa	52.06	45.94	51.23	46.77	42.06	55.94	41.33	56.67
4~8 MPa	52.95	45.05	51.86	46.14	42.78	55.22	42.05	55.95
8~12 MPa	53.29	44.71	52.07	45.93	42.75	55.25	42.06	55.94
12~16 MPa	53.40	44.60	52.20	45.80	43.03	54.97	42.31	55.69
16~20 MPa	53.54	44.46	52.21	45.79	43.07	54.93	42.32	55.68

4. Model Test

The general roadway in actual mining engineering is simplified here. The engineering conditions are shown as follows. The roadway spans 2 m and mining width is 2.5 m. There is no pillar and the roof is supported by anchor bolts. End-anchored bolts are mainly used for anchorage. The arranged grids are 1 m × 0.8 m and the anchorage length is

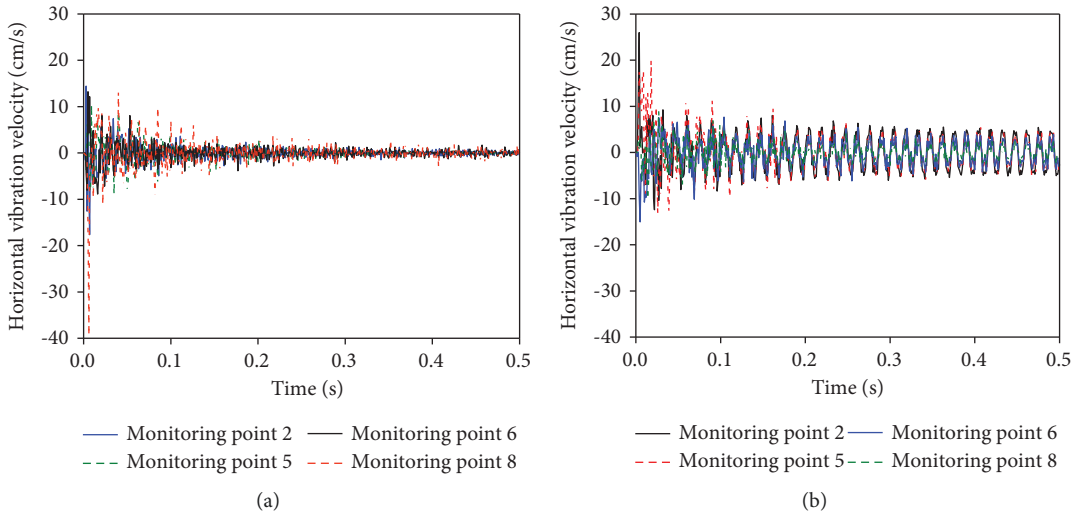

Figure 9: Vibration velocity under the confining pressure of 1 MPa. (a) Horizontal velocity. (b) Vertical velocity.

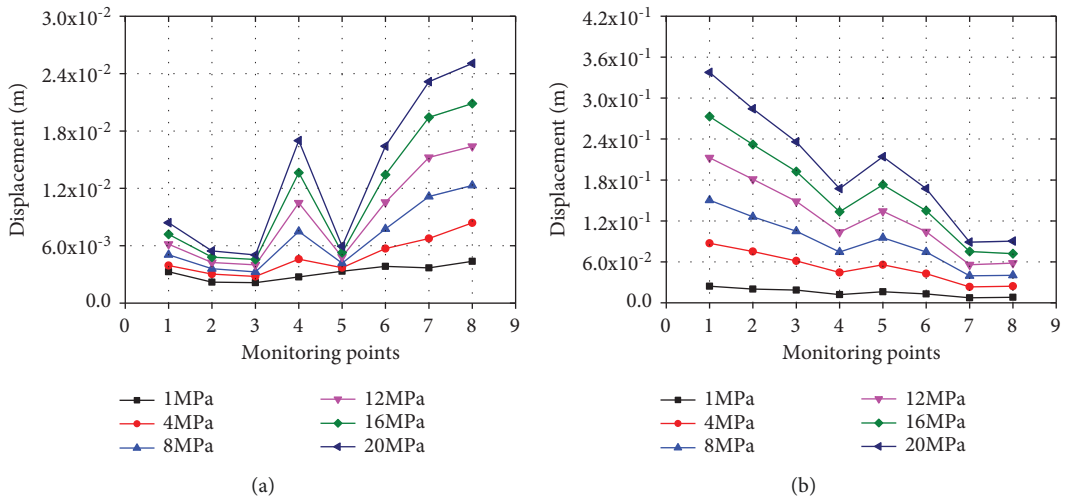

Figure 10: Surrounding rock displacements of the roadway at different monitoring points. (a) Horizontal displacement. (b) Vertical displacement.

1.8 m. Only the dead-weight stress field of the model and the overburden confining pressure are considered in the test, so a plane stress model under the dead-weight stress field is selected for the test. In actual engineering, the physical and mechanical parameters of materials and stress states of the roadway surrounding rock are complicated and cannot be completely reproduced in the model test. Therefore, to ensure that the test meets the main objective requirements [19, 23–25], certain simplification and assumptions are adopted. ① Discontinuous structural planes, such as joints and fractures, are not considered in the model of rock mass, that is, it is assumed that roadway surrounding rock is homogeneous, continuous, and isotropic. ② Influences of structure are ignored in the model of anchor bolts, which only have monitoring functions.

4.1. Calculation in the Model Test Based on Similarity Theory. In accordance with dimensional theory, the physical quantities with the same strength dimension should be expressed by the stress similarity ratio α_σ, while the similarity ratio of dimensionless quantities is a constant of 1. Therefore, similarity ratios of physical quantities of simulated materials of rock are calculated in Table 5. The similarity ratio α_σ of stress and similarity ratio α_L of geometry are control physical quantities and the similarity ratios of other physical quantities are derived according to the dimensional theory. The similarity ratios of physical quantities of simulated materials of anchor bolts are illustrated in Table 6.

According to the test purpose, the response signals under different damage degrees of surrounding rock and different confining pressures were tested, respectively.

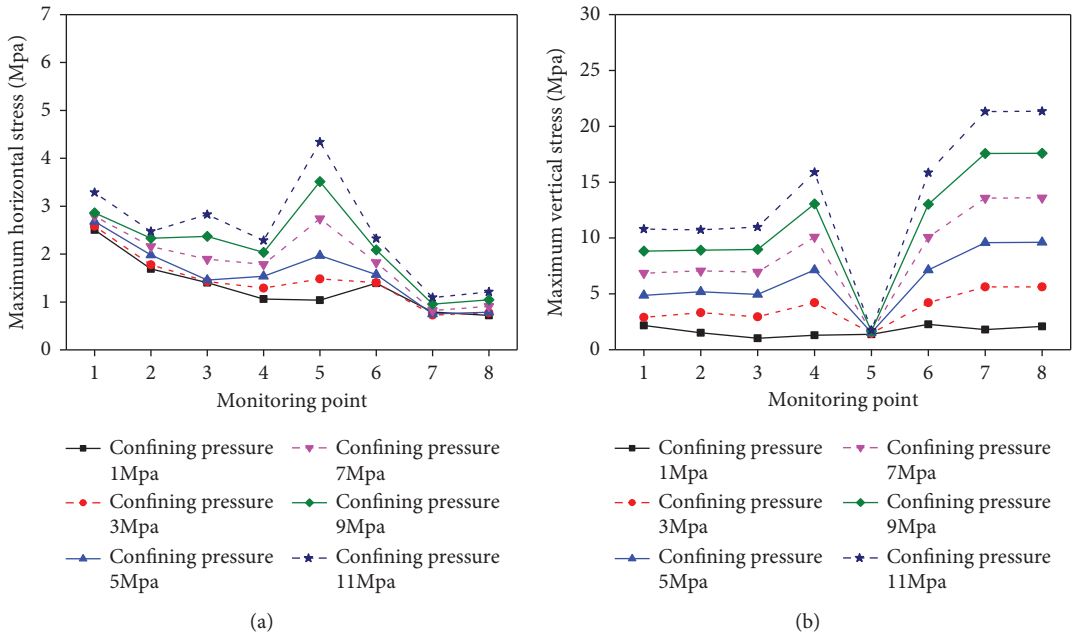

Figure 11: Surrounding rock stresses of the roadway under different confining pressures. (a) Horizontal direction. (b) Vertical direction.

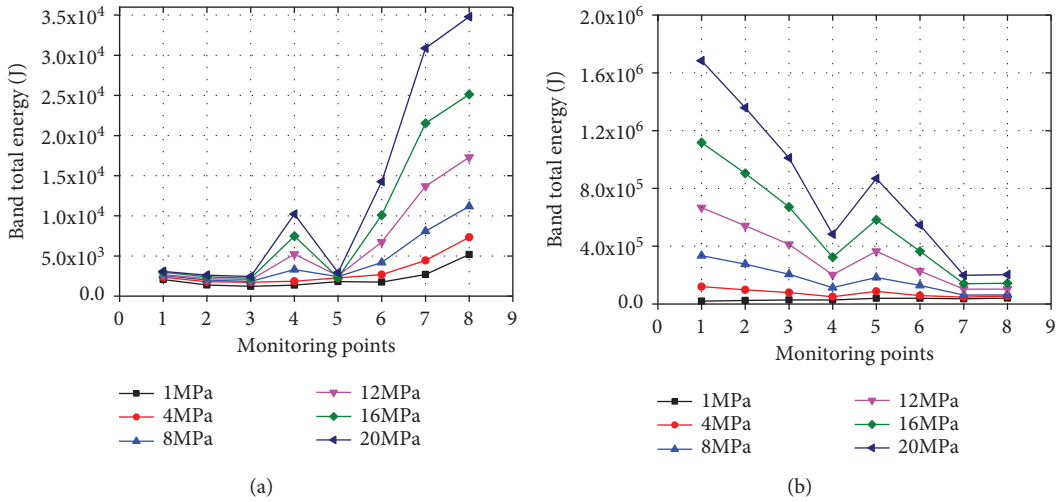

Figure 12: Total energies in wavelet frequency bands under different confining pressures. (a) Horizontal direction. (b) Vertical direction.

Table 5: Similarity ratios of physical quantities of simulated materials of rock.

Physical quantity	Stress, α_σ	Elastic modulus, α_E	Poisson's ratio, α_μ	Cohesion, α_C	Bulk density, α_γ	Surface force of boundary, α_X	Displacement, α_u	Angle of internal friction, α_φ
Similarity ratio	5	5	1	1	1	5	5	1

Table 6: Similarity ratios of physical quantities of simulated materials of anchor bolts.

Physical quantity	Stress, α_σ	Elastic modulus, α_E	Bulk density, α_γ	Geometry, α_L
Similarity ratio	5	5	1	1

(a) (b) (c)

Figure 13: Models of surrounding rock with different damage degrees. (a) Intact model. (b) Damage model. (c) Failure model.

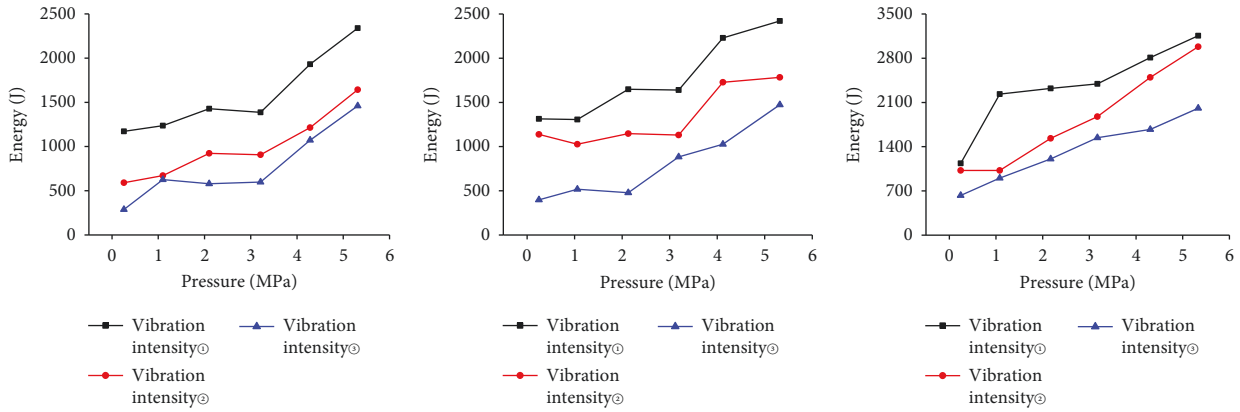

Figure 14: Total energy analysis. (a) Intact model. (b) Damage model. (c) Failure model.

4.1.1. Damage Degree of Surrounding Rock. Three damage grades of the surrounding rock are divided, namely, the intact model (undamaged block), the damage model (mortar ratio of 8 : 1 : 1 for connection), and the failure model (there is no mortar, and the damaged block is anchored only by anchor bolts), as shown in Figure 13.

The total energies in frequency bands of response signals in surrounding rock under different vibration intensities and confining pressures for models with different damage degrees were compared. With the decrease of the vibration intensity, the total energy in frequency bands reduces. When the confining pressure is 4.0 MPa, the total energies in frequency bands in the intact model under different vibration intensities are 1,872, 1,232, and 1,262 J, while those of the damage model are 2,251, 1,455, and 1,172 J, respectively. The total energies in frequency bands in the failure model separately are 2,861, 2,689, and 1,912 J. As the confining pressure rises, the total energies in frequency bands of response signals increase in different models. When the confining pressure rises from 0.2 to 4 MPa, the total energies in frequency bands in the intact model, damage model, and failure model increase by 102.65%, 141.56%, and 180.25%, respectively, under the first vibration intensity. This suggests that the energy in frequency bands of response signals of surrounding rock to vibration is more sensitive to variation of the confining pressure after fractures propagate in surrounding rock mass.

4.2. Distribution of Energy in Frequency Bands of Response Signals. First, we applied vibrations of different intensities to each of the three models, and the frequency band energy of the vibration signal of the three test models is analyzed, as shown in Figure 14.

Figure 14 shows the total energy of frequency band increases with the surrounding rock pressure increase. The total energy of frequency band intact model increases 10 times under the vibration strength 3 action. Also, we could find that total energy increases with the decreasing of the vibration strength.

After five-level wavelet decomposition, the test signals are decomposed into six frequency bands in the frequency domain. According to formula (1), energies distributed in each frequency band and the energy ratios P in each frequency band are calculated. The calculation results are shown in Figure 15.

Figure 15 shows that energy in frequency bands of response signals is distributed consistently in each model under different confining pressures. The frequency band with the maximum energy, namely, the primary frequency band, is the frequency band 3 in the range of 15.55~32.10 Hz. The results are consistent with numerical simulation results. The difference is that the energy ratio in the frequency band 6 of test signals is about 11%, while those in the frequency bands 7 and 8 in numerical simulation results are smaller than 5%. This indicates that there is more energy in the high-

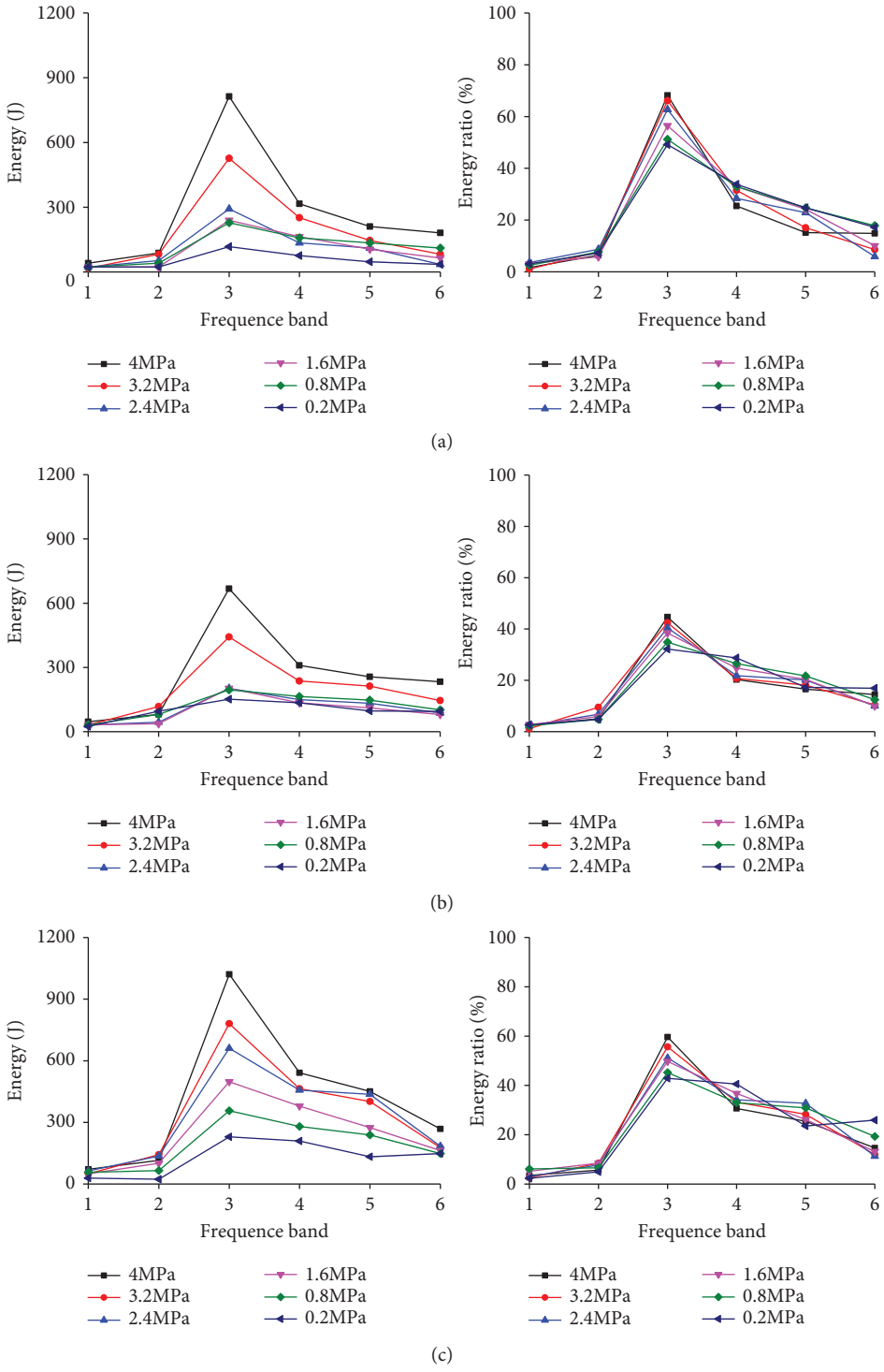

Figure 15: Energies and energy ratios in frequency bands of response signals under different confining pressures (vibration intensity of 3). (a) Intact model. (b) Damage model. (c) Failure model.

frequency part (124~252 Hz) of the test signals, resulting from inevitable existence of fine bubbles and microfractures due to uneven vibration in the pouring process of the model. Therefore, many vibration-induced stress waves are reflected and refracted in the propagation in the surrounding rock model, and the energy of noise signals are also mainly concentrated in the high-frequency range.

Similar to analysis results of numerical simulation, with the confining pressure increase, the energy ratio in the primary frequency band rises, indicating that energy is

transferred from the secondary frequency band to the primary frequency band. The energy in the frequency domain is increasingly concentrated. For example, the energy ratios in the primary frequency bands under different confining pressures in the damage model at the vibration intensity of 3 are 31.18%, 33.35%, 37.89%, 41.05%, 41.89%, and 45.01%, respectively. In actual engineering, with the increase of the mining depth, the confining pressure rises, and the energy in the primary frequency range of response signals of surrounding rock to blasting vibration increases. Under the same blasting strength, the larger the mining depth is, the greater the blasting vibration effects of the surrounding rock is and the more easily the local failure of surrounding rock is, finally leading to overall failure and collapse accidents.

5. Conclusions

(1) In different excavation distance, rock mass around the excavated roadway moves to the excavated space. The displacement fields on the top of the lateral tunnel are distributed in the heart shape along the working face and the maximum displacement of 6.3 mm is found in the roof at the junction of the lateral tunnel and horizontal roadway along veins. The vertical displacement of the roadway surrounding rock increases and changes most significantly within the mining distance of 3 m. In this case, the maximum vertical displacement rises by 62%. When the excavation distance between the horizontal roadway and the lateral roadway is larger than 3 m, the surrounding rock displacement of the roadway along veins changes unobviously and the maximum displacement only increases by 30%.

(2) With the rise of the advance distance of the working face, compression-shear failure mainly occurs in surrounding rock of the roadway, and tensile failure and combined tensile and shear failure mainly appear to the unsupported roof and floor of the roadway. In addition, as the excavated working face of the roadway advances, the strain energy of surrounding rock accumulates at the junction of the lateral tunnel and horizontal roadway along veins so that the failure zone constantly develops. When advancing to 45 m, the subsequent failure zone in surrounding rock of the roadway gradually changes into the elastic state.

(3) With the confining pressure increasing, the total energy in frequency bands rises and its amplitude also increases. The closer the natural frequency is to the primary frequency band (15.6~31.3 Hz), the greater the blasting vibration effects on underground structures (lining structures, support structures, etc.) and the larger the possibility of failure. With the distance from the blasting center increase, the energy ratio in the primary frequency band decreases. This indicates that the large the distance from the blasting center, the wider the energy distribution in the frequency domain of response signals in surrounding rock, the more uniform the energy distribution, and the larger the influence range of blasting vibration effects.

(4) The comparison between laboratory test results and numerical simulation results shows that the energy ratio in high-frequency bands of test signals is larger. This is mainly because more reflection and refraction are present in the vibration waves propagation in the model, and there are certain high-frequency noise components in signals. With the confining pressure increase, the energy tends to be concentrated. As the damage degree of the roadway rises, the energy in the frequency domain of signals is transmitted from the primary frequency band to the secondary frequency band and signal energy is distributed more dispersedly. The test results are basically consistent with numerical simulation results.

Data Availability

The data used to support the findings of this study are available from the corresponding author upon request.

Conflicts of Interest

The authors declare no conflicts of interest.

Acknowledgments

This work was financially supported by China Postdoctoral Science Foundation (2021M691391), Open Foundation of the United Laboratory of Numerical Earthquake Forecasting (Grant no. 2021LNEF04), and the National Natural Science Foundation of China (52174188).

References

[1] E. F. Salmi, M. Karakus, and M. Nazem, "Assessing the effects of rock mass gradual deterioration on the long-term stability of abandoned mine workings and the mechanisms of post-mining subsidence - a case study of Castle Fields mine," *Tunnelling and Underground Space Technology*, vol. 88, pp. 169–185, 2019.

[2] G. S. Esterhuizen, D. R. Dolinar, and J. L. Ellenberger, "Pillar strength in underground stone mines in the United States," *International Journal of Rock Mechanics and Mining Sciences*, vol. 48, no. 1, pp. 42–50, 2011.

[3] P. R. Helm, C. T. Davie, and S. Glendinning, "Numerical modelling of shallow abandoned mine working subsidence affecting transport infrastructure," *Engineering Geology*, vol. 154, pp. 6–19, 2013.

[4] C.-j. Zhai, T.-d. Xia, G.-q. Du, and Z. Ding, "Dynamic response of cylindrical cavity to anti-plane impact load by using analytical approach," *Journal of Central South University*, vol. 21, no. 1, pp. 405–415, 2014.

[5] R. K. Snihg, "Blast vibration damage to underground coal mines from adjacent open-pit blasting," *International Journal of Rock Mechanics and Mining Sciences*, vol. 39, pp. 959–973, 2002.

[6] J.-L. Guo, "Study on vibration transmission regularity of slope in different blasting," *Opencast Mining Technology*, vol. 2, pp. 7–9, 2012.
[7] G. Liu and Z. Wang, "Dynamic response and blast-resistance analysis of a tunnel subjected to blast loading," *Engineering Science Edition*, vol. 38, no. 2, pp. 204–209, 2004.
[8] Q.-L. Shi, Y. Sheng-qiang, C.-L. Jiang, and L. He, "Research on expansion energy in initial released gas prediction model based on quantification," *Theory*, vol. 42, no. 5, pp. 1–4, 2011.
[9] R. Shan, B. Huang, and X. Cheng, "Theoretical analyses of fracture regulation of homogeneous rock bar in case of random incidence of stress wave," *Chinese Journal of Rock Mechanics and Engineering*, vol. 28, no. 4, pp. 666–672, 2009.
[10] S. K. Mandal and M. M. Singh, "Evaluating extent and causes of overbreak in tunnels," *Tunnelling and Underground Space Technology*, vol. 24, no. 1, pp. 22–36, 2009.
[11] B. Sun, W. Duan, Zhengfeng, and C. Liao, "The study on theoretical model and development trend for rock blasting," *Coal Mine Blasting*, vol. 2, pp. 1–4, 2006.
[12] J. Yao, Y. Zhu, Z. Yuan, and W. Wen, "A theoretical evolving model of rock mass blasting with statistical damage," *Chinese Journal of Rock Mechanics and Engineering*, vol. 25, no. 6, pp. 1106–1110, 2006.
[13] X.-B. Yang, Y.-P. Qin, and F. Ye, "Damage constitutive relation of sandstone considering residual stress," *Journal of China Coal Society*, vol. 40, no. 12, pp. 2807–2811, 2015.
[14] X. Li, "Influence of the structural weakness planes in rock mass on the propagation of stress waves," *Explosion and Shock Waves*, vol. 4, pp. 334–342, 1993.
[15] X. Cui, S. Chen, and D. Liu, "Attenuation mechanism of stress wave propagating in crack rock mass," *Engineering Blasting*, vol. 5, no. 1, pp. 18–21, 1999.
[16] Z. Z. Liang, D. K. Xiao, C. C. Li, X. K. Wu, and B. Gong, "Numerical study on strength and failure modes of rock mass with discontinuous joints," *Chinese Journal of Geotechnical Engineering*, vol. 36, no. 11, pp. 2086–2095, 2014.
[17] H. P. Rossmanith and K. Uenishi, "Education in blasting engineering: one-dimensional block model for bench," *Blasting*, vol. 6, no. 1, pp. 36–67, 2002.
[18] R. Ma, L. Zhao, and W. Wang, "The singular spectrum analysis of blasting vibration signal based on WTMM," *Explosion and Shock Waves*, vol. 24, no. 6, pp. 529–533, 2004.
[19] S. Huang, M. Huang, Y. Lyu, and L. Xiu, "Effect of sea ice on seismic collapse-resistance performance of wind turbine tower based on a simplified calculation model," *Engineering Structures*, vol. 227, Article ID 111426, 2021.
[20] K. V. Nguyen, H. T. Tran and H. T. Tran, Multi-cracks detection of a beam-like structure based on the on-vehicle vibration signal and wavelet analysis," *Journal of Sound and Vibration*, vol. 329, no. 21, pp. 4455–4465, 2010.
[21] S. Huang, M. Huang, and Y. Lyu, "A novel approach for sand liquefaction prediction via local mean-based pseudo nearest neighbor algorithm and its engineering application," *Advanced Engineering Informatics*, vol. 41, Article ID 100918, 2019.
[22] J. Kansanaho, K. Saarinen, and T. Kaerkkaeinen, "Spline wavelet based filtering for denoising vibration signals generated by rolling element bearings," *International Journal of Comadem*, vol. 21, no. 4, pp. 25–30, 2018.
[23] S. Huang, M. Huang, and Y. Lyu, "Seismic performance analysis of a wind turbine with a monopile foundation affected by sea ice based on a simple numerical method," *Engineering Applications of Computational Fluid Mechanics*, vol. 15, no. 1, pp. 1113–1133, 2021.
[24] S. Huang, Y. Lyu, H. Sha, and L. Xiu, "Seismic performance assessment of unsaturated soil slope in different groundwater levels," *Landslides*, vol. 18, no. 8, pp. 2813–2833, 2021.
[25] S. Huang, S. Zhai, Y. Liu, C. Liu, K. Goda, and B. Mou, "Seismic behavior analysis of the bank slope considering the effect of earthquake-induced excess pore water pressure," *Frontiers of Earth Science*, vol. 9, Article ID 799612, 2021.

Hindawi
Advances in Civil Engineering
Volume 2022, Article ID 1876435, 9 pages
https://doi.org/10.1155/2022/1876435

Research Article

Design and Implementation of an Integrated Management System for Backfill Experimental Data

Yunpeng Kou,[1,2] **Yuhang Liu**,[1] **Guoqing Li**,[1] **Jie Hou**,[1] **Liming Luan**,[1,2] **and Hao Wang**[1]

[1]*School of Civil and Resource Engineering, University of Science and Technology Beijing, Beijing 100083, China*
[2]*Backfilling Engineering Laboratory of Shandong Gold Group Co., Ltd., Laizhou 261441, China*

Correspondence should be addressed to Guoqing Li; qqlee@ustb.edu.cn

Received 21 December 2021; Accepted 25 February 2022; Published 22 March 2022

Academic Editor: Lijie Guo

With the increase in environmental awareness worldwide, the filling mining method has attracted extensive attention because this method can realize safe and green mining in underground metal mines. Recycling waste tailings in stopes to control underground rock movement, and surface settlement can reduce waste environmental pollution while ensuring mining safety. Although many test data are required to support the formulation of the mine backfill scheme, the advanced management tool of backfill test data is insufficient. In this study, a new data management method that is suitable for backfill experiments is proposed. First, this study analyses the main system requirements, including experimental business process modeling, experimental process combing, and a multidimensional query of experimental data. Then, the backfill test business flow and data flow are summarized to establish the backfill test business model and experimental index system. Then, many system functions are designed, including backfill experiment management, experimental data query, backfill knowledge maintenance, and system management. Finally, a backfill test data management system is developed based on B/S architecture. Developing a data interface, having a built-in test formula and customizing a multidimensional data analysis enable the system to solve the problems in data collection, data accounting, and data analysis. After being put into use in the Backfilling Engineering Laboratory of a group in Shandong, this system improved the data-sharing rate and utilization rate and provided a convenient data management tool for the laboratory.

1. Introduction

Mining activities produce many tons of waste tailings every year. As a kind of solid waste, the stockpiling of tailings greatly damages the environment [1, 2]. Cemented paste backfill (CPB) can fill underground goafs with solid wastes, such as waste slag and tailings. This method not only reduces the discharge of solid waste but also stabilizes the mining area, thereby avoiding the collapse of the surface due to the existence of an underground empty area. Moreover, CPB can effectively protect the surrounding environment and fully accords with the current theme of green mining [3–5].

The filling mining method is more complex than others used in mining design and production organizations [6, 7]. To ensure the backfill effect of the mine, it is necessary to rely on many experimental data from laboratory tests, semi-industrial tests, and field industrial tests to select and optimize the backfill parameters in the design or transformation of the backfill system. Therefore, managing the test process and test data is particularly important [8–10].

The backfill test theme corresponds to the problem of the mine backfill industry, and the test scheme is designed for different test themes [11, 12]. However, due to different researchers and research methods, the test schemes are different [6, 13, 14]. The construction of a backfill test platform also needs to coordinate various factors, such as materials, equipment, sites, and personnel [15]. Test data types include not only structured data but also unstructured data, such as pictures and documents [16, 17]. During data acquisition, some data need to be recorded and saved manually [18–20], and some data are automatically collected and stored by the PLC (Programmable Logic Controller)

system [21, 22]. Data are easy to lose, and query steps are cumbersome.

By performing a statistical analysis of the test data, the tester obtains the backfill slurry ratio information and pipeline resistance information; both types of information provide an important basis for material consumption, pipe network layout, and equipment selection [23–25]. The above information shows that the backfill test can solve the corresponding industrial problems. Moreover, the test process and data management have many problems, such as many factors for coordinating test development and a low degree of automation in data collection, statistics, storage, and analysis.

Common process and data management tools, such as BIM [26, 27] (building information modeling), PDM [28, 29] (product data management), LIMS [30, 31] (laboratory information management systems), and TDM (test data management) are widely used in construction, pharmaceutical, petrochemical, environment, water supply, medical treatment, quarantine, customs, food and beverage, and other industries. BIM and PDM are complete information models that can integrate the information, processes, and resources of engineering projects or products at different stages in the whole life cycle into one model for easy use by all participants in engineering projects or production. LIMS is a computer software and hardware system for comprehensively managing laboratory information and quality control. Newtera TDM is a platform software designed and developed based on the "build on demand" concept. The software functions include database model, business process, business rules, permission control, web interface, electronic form, report template, statistical analysis, and user management.

However, the traditional backfill test mode can be divided into the proposed experiment, experiment preparation, the conducted experiment, experiment data processing, experiment result analysis, and the experiment summary. In addition, the standardization of the backfill test business process and data has not been reported. Currently, there is no information system for backfilling test data analysis and mining. The lack of test data integration and summary platforms leads to problems, such as low data utilization, a low degree of data sharing, and poor data security. These problems not only increase the workload of testers and affect their work efficiency but also increase the risk of data loss and disclosure. Successful testing requires testers' rich experience and rigorous working attitude. In view of the above situation, an integrated backfilling test data management system that can manage test plans, test processes, and test data.

2. System Requirements

Currently, with the construction and development of intelligent mines, digital, information, and network technologies provide a new way to reform backfill test management. Research on backfill test management is not only a key problem to be solved during technological innovation of the mine backfill process but also a new demand after fully considering the new situation, new conditions and new methods faced by mining enterprises in backfill test management. The research and development of this system can greatly promote the digital upgrading of backfill test management, improve test business processing efficiency and the data management effect, broaden the test design form, and comprehensively improve the design efficiency and practical application effect of mine backfill systems. To achieve these objectives, the system needs to meet the following requirements.

2.1. Backfill Experimental Business Modeling. The system needs to sort out the test process, propose the concept of backfill test standardization, and solve data quality problems. In many test operations, it is inevitable that the test steps are not standardized, cannot enable all key data to be completely recorded, and may even lead to test errors, thus producing difficulties for data analysis. To standardize the experimental process, the backfill experiment business process is analyzed to construct a backfill experiment business model. Besides, the experimental operation steps are also analyzed to establish a backfill experimental knowledge base.

2.2. Experimental Data Integration Management. There are many experimental data indicators, and the relationship between them is complex. To enter, convert and store many multisource heterogeneous data, it is necessary to sort and organize them. Based on this, a reliable data storage structure is designed. Developing the system should simplify personnel operation steps and improve data management efficiency. The main input data include many structured and unstructured historical data and intelligently inputted existing multisource heterogeneous experimental data. For data calculation, in view of the tedious manual calculation steps, the system should be equipped with built-in backfill experimental formula algorithms that enable automatic data conversion. For data storage, technologies such as data warehouses and fusion should be adopted to improve the system database design.

2.3. Multidimensional Query of Experimental Data. This requirement is set mainly to realize data multidimensional analysis and hierarchical authorization queries. Due to the decentralized management of historical data, it is difficult to perform a comparative analysis of experimental data. The system automatically generates analysis charts by data slicing and drilling and realizes a multidimensional data query. Hierarchical authorization data queries are realized through system settings, such as role management and permission management.

3. System Construction

3.1. Construction of the Backfill Experiment Business Model

3.1.1. Experiment Process Analysis. The backfill test needs to coordinate the test elements, such as material, site,

equipment, and personnel. By summarizing the backfill industrial problems faced by the mine, the test subject is determined, and the test scheme is designed. Mine backfill demand is the basic condition information of backfill scheme design. Before writing the report, it is necessary to consult the literature to explain the deep-seated causes of the test phenomenon. Finally, the test summary is completed from the test conclusion. The business boundary of the backfill test process begins with the design of the testing scheme and ends with the generation of test summaries and reports. The backfill test process is illustrated in Figure 1.

As shown in Figure 1, the general process of the backfill test can be sorted as follows:

Step 1. The tester proposes the backfill test subject and designs the test scheme according to the needs of the mine backfill industry or personal research direction.

Step 2. The tester designs the number, proportion and manufacturing method of test samples according to the test scheme, prepares test materials, and builds a test platform.

Step 3. The experimenter will prepare, maintain, and test the samples; collect the test data; and preliminarily check the availability and accuracy of the data. If the test data are inadequate, the samples must be prepared again.

Step 4. The experimenter discards the waste samples and processes the experimental data by converting the parameters, importing, and auditing the data.

Step 5. The tester summarizes and analyses the experimental data, determines the relevant literature, analyses the experimental phenomena, and investigates the deep-seated causes.

Step 6. The tester summarizes all the data; creates, documents, and summarizes the test conclusions; and writes the test reports.

3.1.2. Business Model Construction. Using process analysis, the experimental business model is construct to design the system forms and data analysis themes. The backfill experimental business model is shown in Figure 2.

As shown in Figure 2, the backfill test business model can be divided into the following parts:

(1) The tester proposes the test scheme, plans the test contents, confirms that the test materials and test equipment are sufficient and available, and makes pretest preparations.

(2) The tester will perform each subtest in turn according to different test purposes. The main subtests include material physicochemical property tests, settlement tests, filling strength tests, and slurry rheology tests. The system provides the operation information of test steps and automatically records the data generated by equipment.

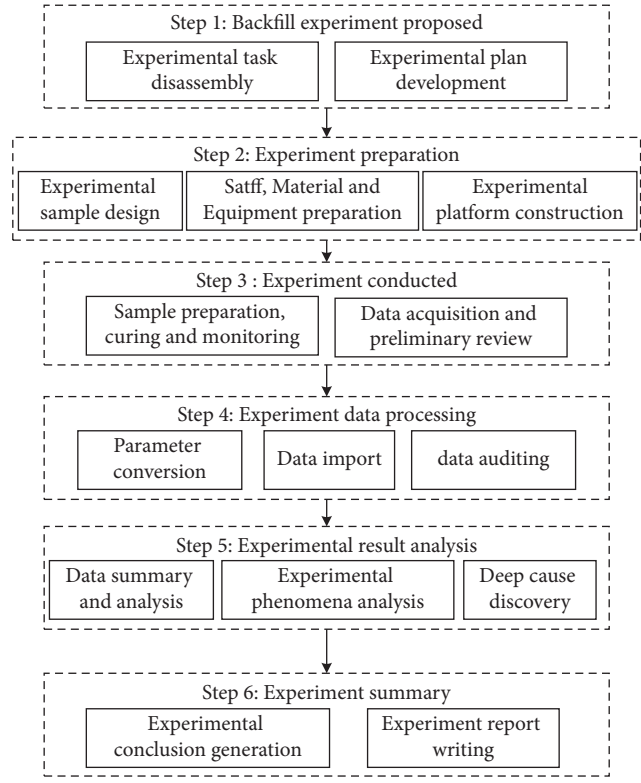

Figure 1: Flow chart of backfill experiment.

(3) The tester summarizes the data; performs the data unit conversion, test index calculation, abnormal value processing and other work; and creates the test data table after standardizing the data. Additionally, the system develops the file attachment management function to record the test pictures and documents and other information. The above structured and unstructured data form the backfill test data asset.

(4) According to the saved data, the system generates a test item data table, material physical and chemical properties table, flocculant subject analysis table, CPB strength analysis table, and slurry rheological analysis table by subject. Then, the analysis results are displayed in many ways, such as in a line chart, pie chart, and histogram.

(5) The tester summarizes the test conclusion and writes the test report according to the system accounting results and analysis chart trend.

3.2. Design of Backfill Experimental Indicator System. Backfill experimental indicators are important tools to describe, measure, and analyze backfill experiments. The backfill scheme is based on a comprehensive consideration of the relevant backfill indicators. The main body of system development is experimental data. Before carrying out the data collection, accounting, and storage work, it is necessary for us to sort out the source of the index data and its calculation method and complete the design of the index system of the backfill experiment. The design of the backfill indicator used in this article is shown in Figure 3.

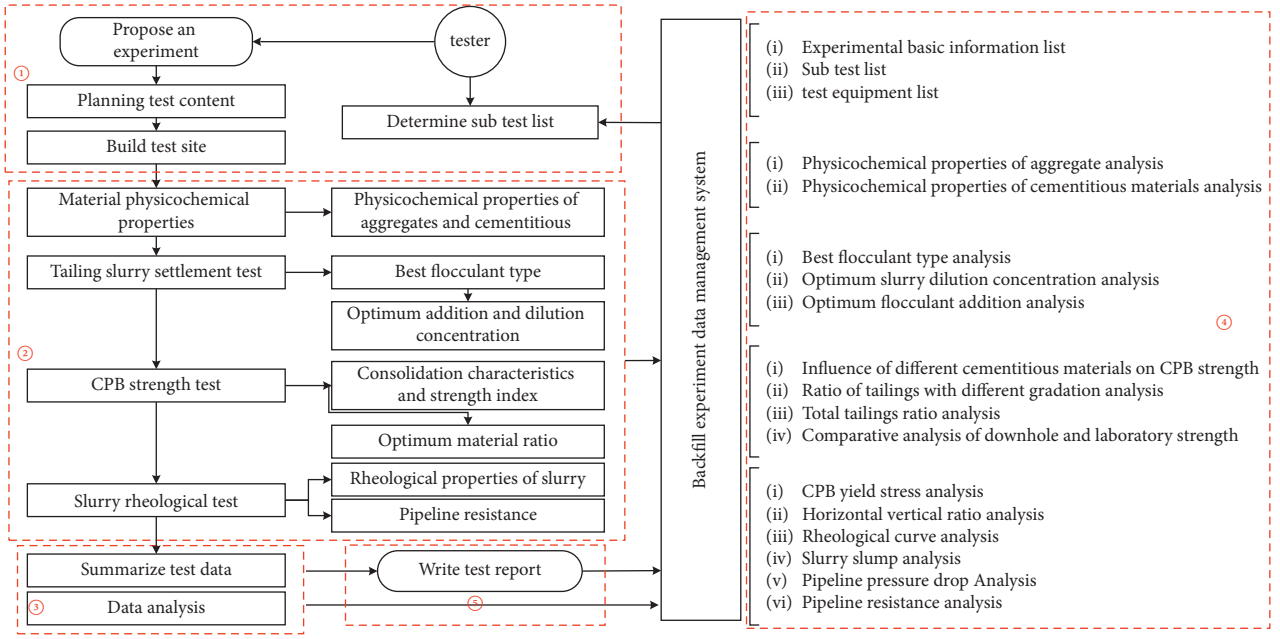

Figure 2: Backfill experiment business model.

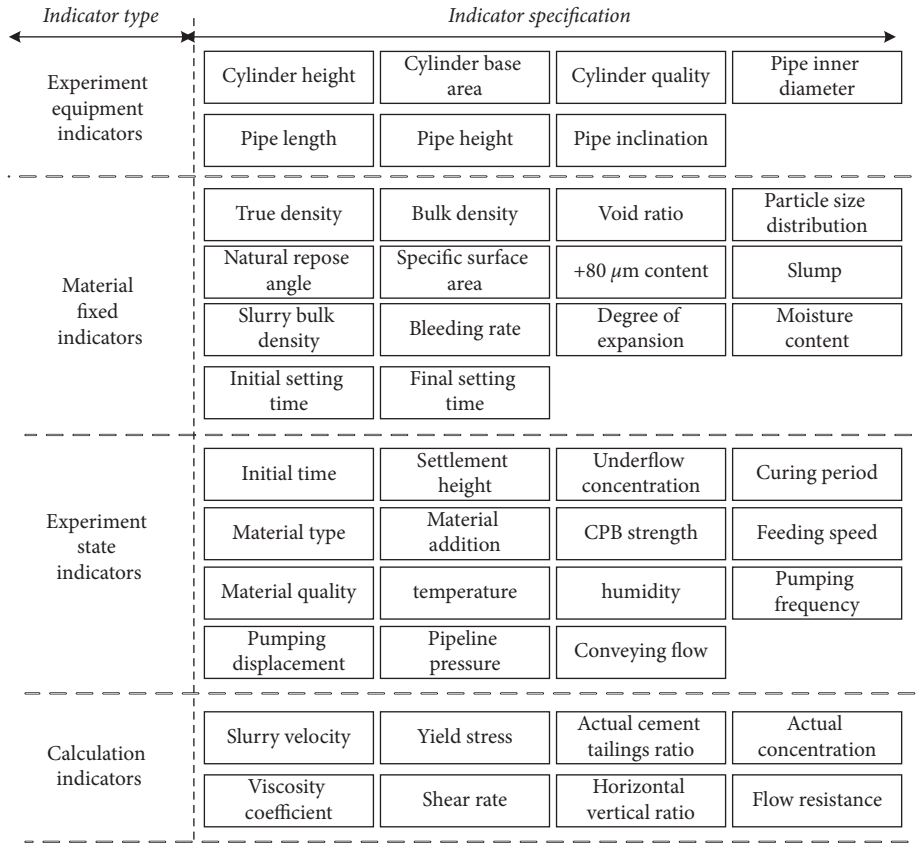

Figure 3: Backfill experiment indicator system.

According to the hierarchy of indicator data, backfill data indicators are divided into four categories: experimental equipment indicators, material fixed indicators, experimental state indicators, and calculation indicators.

(1) Test equipment indicators. Test equipment indicators are used mainly for calculating other test indicators, and generally, the specifications of enterprise test equipment are relatively fixed. The

system shall support user-defined modification of test equipment parameters.

(2) Material fixed indicators. The material fixed indicators, that is, the fixed parameter information of backfill aggregate, cementitious material, and other additives, were recorded. The material fixed index has a certain impact on the flocculation characteristics of the slurry, strength characteristics of the backfill body, and rheological characteristics, thus showing an obvious positive or negative correlation.

(3) Test status indicators. Test status indicator data have a wide range of sources and high update frequency. Additionally, these indicators are an important part of accounting data. Therefore, the requirements of this part should be considered in the system design, especially the database design.

(4) Calculation indicators. The output units present experimental results based on experimental equipment indicators, material fixed indicators, and experimental state indicators, which are automatically calculated by the built-in algorithms of the system.

Data update frequency, content, and type are the main bases for index classification. Among the update frequencies of the four types of indicators, the update frequency of equipment indicators is the lowest, and there is little change under normal circumstances. These indicators are independent variable indicators. Material fixed indicators generally fluctuate within a certain range. They will be remeasured only when new materials are used, or high accuracy is required. They are also independent variable indicators. The update frequency of the experimental state indicators is the fastest. Unlike other indicators, these indicators include both independent variable indicators (such as material type) and dependent variable indicators (such as CPB strength). All calculation indicators are dependent variable indicators.

4. System Implementation

4.1. System Function. The system functions include the system data dictionary, experiment management, data query, backfill knowledge maintenance, and system administration, as shown in Figure 4.

(1) The system data dictionary is the experimental basic data management function. It contains information on experimental project commissioning units, experimental properties, and experimental types. This part of the information will constitute the basic information of experimental projects together with experimental personnel, time, and sites.

(2) Experimental management is an experimental data collection function. It is used in developing the experimental scheme (source), processing experimental data, summarizing experimental conclusions, and generating reports. In addition, at the end of the experiment, experimental management also supports experimenters in inputting the basic information of the experiment and inputting key experimental data, supports the system in automatically collecting experimental equipment data, and checks the experimental results. This function manages the whole process of all kinds of backfill experiments, such as physical and chemical property experiments, settling experiments, CPB strength experiments, and pipeline conveying experiments.

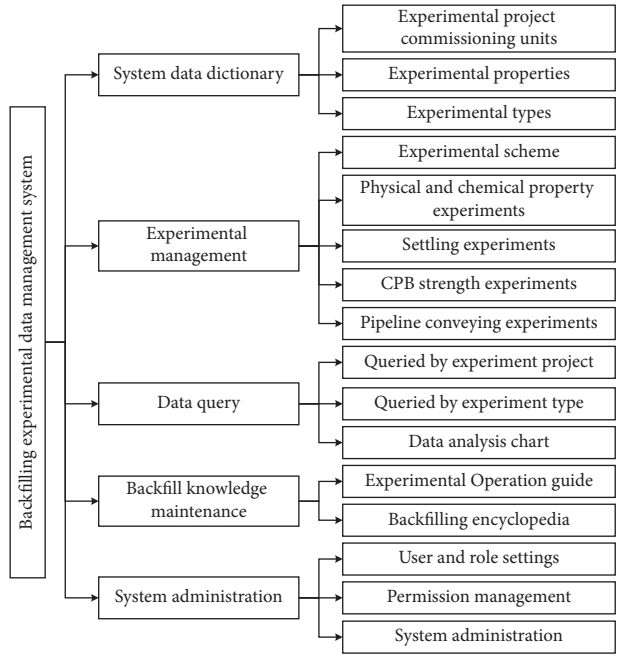

Figure 4: System function implementation.

(3) Data query is an experimental data analysis and query function. With this function, the system can automatically generate data analysis charts according to user requirements and compare and analyze the same original data in multiple dimensions to enhance data utilization. The system supports a single-channel display, multichannel display, and comparative display of data. Data can be queried by experiment project and experiment type. For the former query mode, all the data of one experiment project can be queried; this capability is convenient for the vertical control of the experimental project. For the latter query mode, all the data of the type of experiment (e.g., CPB strength experiment) can be queried; this capability is convenient for the horizontal comparison of experimental data. A fuzzy matching query function is also supported to improve the data query rate.

(4) Backfill knowledge maintenance. With this function, a knowledge base of backfill experiments are formed based on many historical and search engine data, including data on existing mainstream backfill experimental methods, experimental tools, and experimental procedures. The information volume of the knowledge base gradually increases with the service time of the system. Gradually, the knowledge

base will meet enterprises' backfill experimental knowledge needs.

(5) System administration is a function that supports system data maintenance and user and role settings involved in the above modules, making the system adapted to all types of changes in laboratory and mining operations.

4.2. System Implementation. From the perspective of informalization of backfill experimental data management, a backfill experiment data management system is established based on the following ingredients:

(i) Server platform environment: Windows server.

(ii) Development tools: PHP back-end development language and HTML + JAVASCRIPT + CSS front-end development language.

(iii) Data interface tool: Restful, a data interface tool based on the HTTP protocol.

(iv) Technologies applied in system database deployment: federal database and data fusion technologies.

(v) System structure: B/S architecture.

Currently, the system has been built and used in a group's backfill engineering laboratory in Shandong. The system's data management functions and performance meet the group's design requirements, and all the designs have been fully verified. This system effectively improves the group's data management efficiency. The interfaces of experimental data collection, query, and analysis are shown in Figures 5–7.

5. Discussion

5.1. Key Technologies

5.1.1. Data Interface Development. The development of the system is based mainly on data management. Data collection has always been the biggest problem faced by system promotion and application. For example, traditional data collection methods for backfill data are error prone. These methods have cumbersome operations and low efficiency. Data interfaces are developed to solve these problems. In this system, the Restful data interface tools are used to complete batch collections of experimental equipment data, rapidly update system data, and greatly improve data transmission efficiency.

5.1.2. Standardization and Normalization of Experimental Data. Data standardization and normalization are prerequisites for data analysis and application. If the data management approach does not match the business process, there will be many problems such as low standardization of business processes and independent and scattered data storage. Therefore, the backfill experimental data is standardized and normalized, thereby laying a solid foundation for data multidimensional query and data subject analysis.

5.1.3. Data Warehouse and Fusion Technologies of the Backfill System. Enterprises have many historical backfill experimental data. Data warehouse and data fusion technologies are introduced to effectively integrate multimine and multidimensional data. These main technologies include data warehouse logical structures, data warehouse ETL technology, and data warehouse retrieval mechanisms. These technologies are used to establish a backfill system data warehouse with high reliability, strong ductility, and good performance.

5.1.4. Native Development of the Data Management Platform. To meet the requirements of the backfill experiment process and data management, the prototype method is used to carry out the native development of the experimental data management platform. This method focuses on the interaction between users and developers and has the advantages of a short development cycle, good flexibility, and strong applicability.

5.2. Application Effects. Through the application in the filling laboratory for nearly two years, the test data management system improves the comprehensive control level of the laboratory on data; the system can thereby effectively reduce the test cost and improve the degree of data sharing and utilization. The specific application effect is shown in Table 1.

5.3. Superiority and Limitations. The primary strength of this study is that it applies project management theory and data management systems in filling experiments. Compared with the traditional filling experimental data management method, the proposed filling experimental data management system requires the isolated storage of many historical data for unified management. This study improves the traditional filling data management method, reduces the data entry and calculation workload of the experimenter, and improves the efficiency of the experimenter and the degree of data sharing. The digitization of the filling experiment is the basic work of "intelligent mining for backfill," which can carry out deeper data applications.

The limitation of the system is that it is not developed at a deeper level for the problem of data postutilization. Our next step is to establish an effective connection between existing models, such as fill strength prediction and sedimentation prediction, with the system data to form a model for sustainable improvement. Artificial intelligence is used to quickly arrive at reliable filling indicator data, thereby reducing cumbersome manual experiments. The system will accumulate many experimental data over time. Using the system data set, a correlation analysis of the backfilling data index, data mining, and knowledge discovery could be carried out.

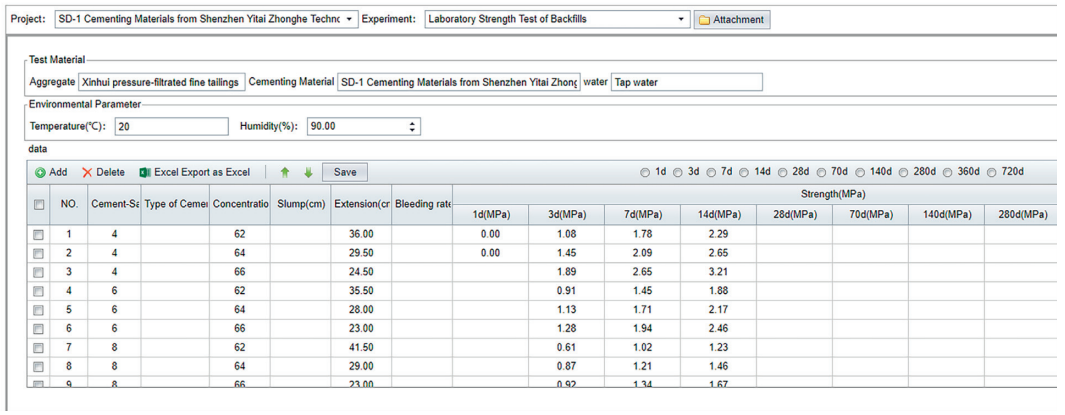

Figure 5: Input interface of backfill experiment data.

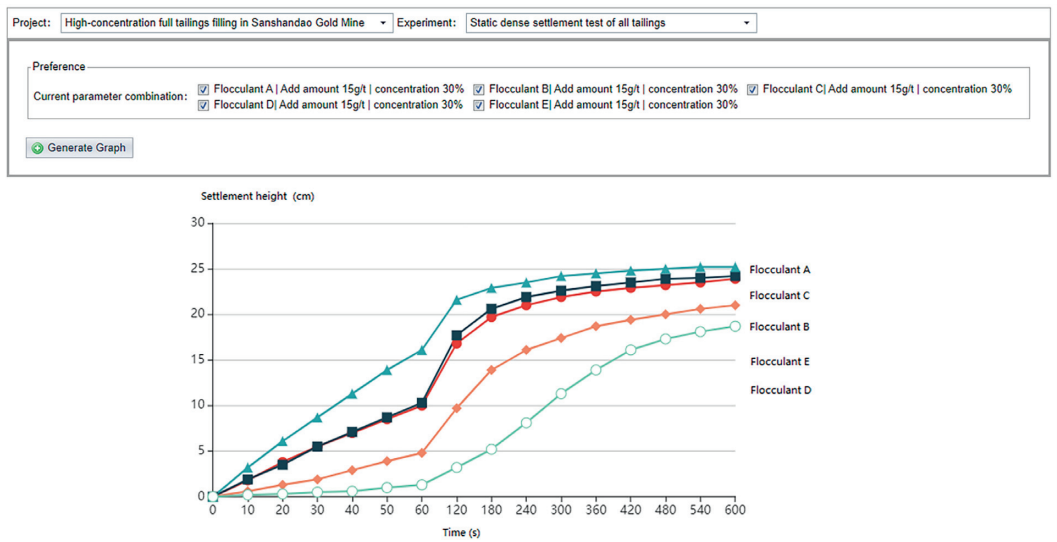

Figure 6: Analysis interface of backfill experiment data.

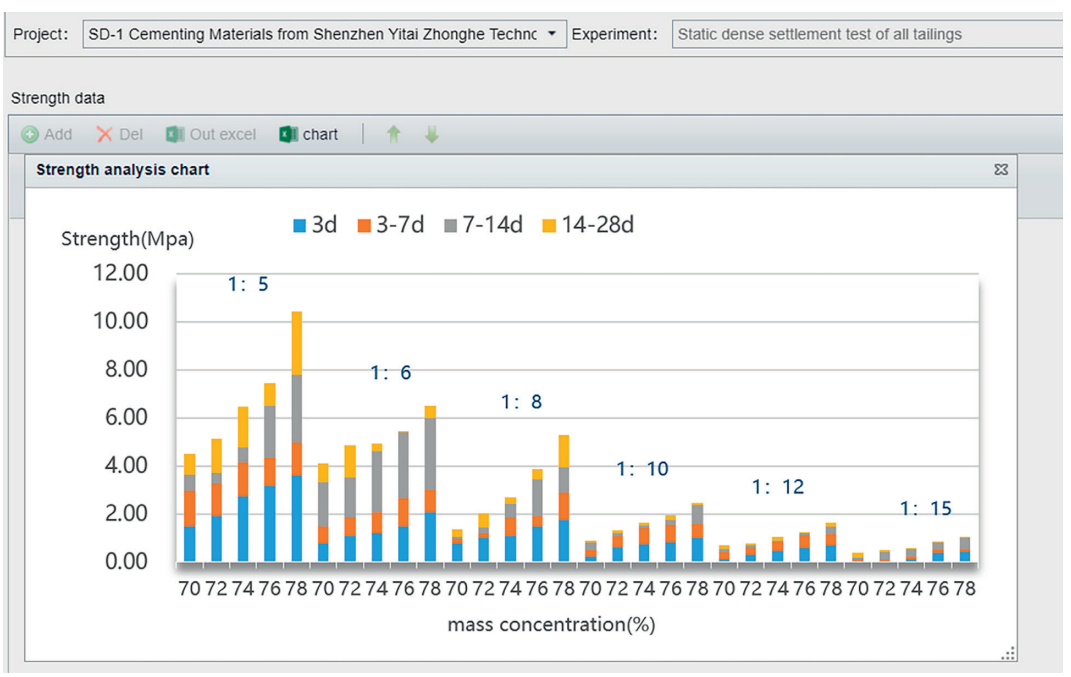

Figure 7: Strength analysis chart interface.

Table 1: Comparison of system application effects.

Items	Before system development	After system application
Test project	The administrators manually calculated material requirements and orally communicated project information to material managers and site managers.	The system automatically calculates the bill of materials and pushes relevant information to the assistant.
Sample detection	The administrators took samples according to personal memory and orally agreed to the test time and indicators with the testers.	The system pushes the sampling message and the test task to the person in charge of the test and the tester.
Data collection	The testers manually summarized machine test and manual measurement data.	The system imports machine test data in batches and integrates them with manual measurement data.
Site management	The administrators saved relevant information on personal computers and pasted it into reports.	The system saves the site information and automatically embeds it when the report is generated.
Data analysis	Administrators collected data and analyzed these data by using excel, origin, and the like	The system summarizes the data and automatically generates the analysis chart.
Test report	The administrators manually analyzed test data, summarized test conclusions, and prepared test reports.	The system automatically generates the test report according to the customized template.
Audit management	The administrator submitted the test results and other data to the leader, who signed for confirmation.	The audit business is completed in the system
Document storage	Document storage files were stored on personal computers.	Documents are recorded in the system and can be retrieved and queried at any time.

6. Conclusion

This study combs and integrates the backfill experiment data management system and proposes a data management system suitable for backfill experiment businesses. After being applied in a backfill engineering laboratory, the system manages the backfill experiment data in the laboratory. The main conclusions are as follows:

(1) The close fit between the business model and backfill experiment business process is the key to realizing data information management. Dividing the backfill experiment into six steps, this study fully considers the personality and generality of the backfill experiment and manages to establish a universal business model to ensure the ease of use of the system.

(2) Data index sorting is the premise of data management. This study classifies and arranges many complex backfill experiment indices, thereby providing an important basis for batch data collection, data processing logic design, and test data application.

(3) The backfill experiment data management system provides a new method and idea for integrating and reusing test data. Integrating and combining many historical data can effectively reduce the number and scale of similar tests. The research and development of this system can provide technical support for data reuse.

Although the backfill experiment data management system can effectively reduce the workload of experimental staff and improve the degree of data sharing, the information management of historical data needs the support of technical methods, such as character recognition and data cleaning. In addition, the knowledge discovery of experimental data needs the support of relevant intelligent algorithms. Further work can focus on building a backfill scheme optimization model. A system could integrate the monitoring data of the mine backfilling system, the parameters of the backfilling body, and the test data to optimize the backfilling scheme and the control strategy of the automatic system. Finally, the reliability and stability of the backfilling system would be greatly improved.

Data Availability

The data are generated from the field and can be available from the corresponding author upon request.

Conflicts of Interest

The authors declare that there are no conflicts of interest regarding the publication of this paper.

Acknowledgments

This work was supported by the National Key Research and Development Program of China (Grant no. 2018YFC0604405) and the General Program of National Natural Science Foundation of China (Grant no. 52074022).

References

[1] M. Edraki, T. Baumgartl, E. Manlapig, D. Bradshaw, D. M. Franks, and C. J. Moran, "Designing mine tailings for better environmental, social and economic outcomes: a review of alternative approaches," *Journal of Cleaner Production*, vol. 84, no. 1, pp. 411–420, 2014.

[2] E. Yilmaz, "Advances in reducing large volumes of environmentally harmful mine waste rocks and tailings," *Gospodarka Surowcami Mineralnymi Mineral Resources Management*, vol. 27, no. 2, pp. 89–112, 2011.

[3] A. Tariq and E. K. Yanful, "A review of binders used in cemented paste tailings for underground and surface disposal practices," *Journal of Environmental Management*, vol. 131, pp. 138–149, 2013.

[4] A. Wu, Y. Wang, B. Zhou, and J. Shen, "Effect of initial backfill temperature on the deformation behaviour of early age

cemented paste backfill that contains sodium silicate," *Advances in Materials Science and Engineering*, vol. 1–10, 2016.

[5] X. Zhao, A. Fourie, and C.-c. Qi, "Mechanics and safety issues in tailing-based backfill: a review," *International Journal of Minerals, Metallurgy and Materials*, vol. 27, no. 9, pp. 1165–1178, 2020.

[6] C. Qi and A. Fourie, "Numerical investigation of the stress distribution in backfilled stopes considering creep behaviour of rock mass," *Rock Mechanics and Rock Engineering*, vol. 52, no. 9, pp. 3353–3371, 2019.

[7] X. Zhao, X. Li, and K. Yang, "The spatiotemporal characteristics of coupling effect between roof and backfill body in dense backfill mining," *Geofluids*, vol. 2021, Article ID 6684237, 15 pages, 2021.

[8] Z. Bayer Ozturk and E. Eren Gultekin, "Preparation of ceramic wall tiling derived from blast furnace slag," *Ceramics International*, vol. 41, no. 9, pp. 12020–12026, 2015.

[9] L. Liu, P. Yang, C. Qi, B. Zhang, L. Guo, and K.-I. Song, "An experimental study on the early-age hydration kinetics of cemented paste backfill," *Construction and Building Materials*, vol. 212, pp. 283–294, 2019.

[10] S. Cao, E. Yilmaz, W. Song, E. Yilmaz, and G. Xue, "Loading rate effect on uniaxial compressive strength behavior and acoustic emission properties of cemented tailings backfill," *Construction and Building Materials*, vol. 213, pp. 313–324, 2019.

[11] J. Wang, E. Liu, and L. Li, "Characterization on the recycling of waste seashells with Portland cement towards sustainable cementitious materials," *Journal of Cleaner Production*, vol. 220, pp. 235–252, 2019.

[12] J. Xie, J. Wang, R. Rao, C. Wang, and C. Fang, "Effects of combined usage of GGBS and fly ash on workability and mechanical properties of alkali activated geopolymer concrete with recycled aggregate," *Composites Part B: Engineering*, vol. 164, pp. 179–190, 2019.

[13] X. Dong, A. Karrech, H. Basarir, M. Elchalakani, and A. Seibi, "Energy dissipation and storage in underground mining operations," *Rock Mechanics and Rock Engineering*, vol. 52, no. 1, pp. 229–245, 2019.

[14] X. Dong, A. Karrech, H. Basarir, M. Elchalakani, and C. Qi, "Analytical solution of energy redistribution in rectangular openings upon in-situ rock mass alteration," *International Journal of Rock Mechanics and Mining Sciences*, vol. 106, pp. 74–83, 2018.

[15] M. Fall, D. Adrien, J. C. Célestin, M. Pokharel, and M. Touré, "Saturated hydraulic conductivity of cemented paste backfill," *Minerals Engineering*, vol. 22, no. 15, pp. 1307–1317, 2009.

[16] J. Zhou, X. Li, and H. S. Mitri, "Classification of rockburst in underground projects: comparison of ten supervised learning methods," *Journal Ofuting in Civil Engineering*, vol. 30, no. 5, 2016.

[17] C. Qi and Q. Chen, "Evolutionary random forest algorithms for predicting the maximum failure depth of open stope hangingwalls," *IEEE Access*, vol. 6, pp. 72808–72813, 2018.

[18] Y. Lin, K. Zhou, and J. Li, "Prediction of slope stability using four supervised learning methods," *IEEE Access*, vol. 6, pp. 31169–31179, 2018.

[19] Y. Lin, K. Zhou, and J. Li, "Application of cloud model in rock burst prediction and performance comparison with three machine learning algorithms," *IEEE Access*, vol. 6, pp. 30958–30968, 2018.

[20] J. Zhou, X. Shi, K. Du, and X. Qiu, "Feasibility of random-forest approach for prediction of ground settlements induced by the construction of a shield-driven tunnel," *International Journal of Geomechanics*, vol. 17, no. 6, 2017.

[21] W. Xu, X. Tian, and P. Cao, "Assessment of hydration process and mechanical properties of cemented paste backfill by electrical resistivity measurement," *Nondestructive Testing and Evaluation*, vol. 33, no. 2, pp. 198–212, 2018.

[22] L. Liu, Z. Fang, C. Qi, B. Zhang, L. Guo, and K.-I. Song, "Experimental investigation on the relationship between pore characteristics and unconfined compressive strength of cemented paste backfill," *Construction and Building Materials*, vol. 179, pp. 254–264, 2018.

[23] J. W. Bullard, H. M. Jennings, R. A. Livingston et al., "Mechanisms of cement hydration," *Cement and Concrete Research*, vol. 41, no. 12, pp. 1208–1223, 2011.

[24] Y. Zhao, A. Taheri, M. Karakus, Z. Chen, and A. Deng, "Effects of water content, water type and temperature on the rheological behavior of slag-cement and fly ash-cement paste backfill," *International Journal of Mining Science and Technology*, vol. 30, no. 03, pp. 271–278, 2020.

[25] B. Cui, Y. Liu, G. Feng et al., "Experimental study on the effect of fly ash content in cemented paste backfill on its anti-sulfate erosion," *International Journal of Green Energy*, vol. 17, no. 12, pp. 730–741, 2020.

[26] M. Das, X. Tao, and J. C. P. Cheng, "BIM security: a critical review and recommendations using encryption strategy and blockchain," *Automation in Construction*, vol. 126, Article ID 103682, 2021.

[27] J. Zhu and P. Wu, "Towards effective BIM/GIS data integration for smart city by integrating computer graphics technique," *Remote Sensing*, vol. 13, no. 10, Article ID 101889, 2021.

[28] K. Rinos, N. Kostis, E. Varitis, and V. Vekis, "Implementation of model-based definition and product data management for the optimization of industrial collaboration and productivity," *Procedia CIRP*, vol. 100, pp. 355–360, 2021.

[29] D. Namchul, "Integration of engineering change objects in product data management databases to support engineering change analysis," *Computers in Industry*, vol. 73, pp. 69–81, 2015.

[30] P. J. Prasad and G. L. Bodhe, "Trends in laboratory information management system," *Chemometrics and Intelligent Laboratory Systems*, vol. 118, no. 9, pp. 187–192, 2012.

[31] S. Y. Cho, K. Park, J. E. Shim et al., "An integrated proteome database for two-dimensional electrophoresis data analysis and laboratory information management system," *Proteomics*, vol. 2, no. 9, pp. 1104–1113, 2015.

Hindawi
Advances in Civil Engineering
Volume 2022, Article ID 5421827, 9 pages
https://doi.org/10.1155/2022/5421827

Research Article

Study on the Solution of Sand Slabbing in the Tailing Sand Bin of Huanggang Iron Ore Mine

Xin Zhu,[1,2,3] **Bokun Zheng**,[1,2,3] **Liang Peng**,[1,2,3] **Fengfeng Wu**,[1,2,3] **Xuyan Yin**,[1,2,3] **Yang Liu**,[1,2,3] **and Xin Yang**[1,2,3]

[1]*Changsha Institute of Mining Research Co., Ltd., Changsha 410012, Hunan, China*
[2]*State Key Laboratory of Metal Mine Safety Technology, Changsha 410012, Hunan, China*
[3]*National Engineering Research Center for Metal Mining, Changsha 410012, Hunan, China*

Correspondence should be addressed to Xin Zhu; 1056986271@qq.com

Received 25 January 2022; Revised 23 February 2022; Accepted 7 March 2022; Published 21 March 2022

Academic Editor: Tingting Zhang

In order to improve the tailings utilization rate and realize full tailings' filling in Huanggang iron mine in Inner Mongolia, a flocculation settlement system was added, which resulted in silting and consolidation of tailings in sand silts. Based on this, the reason for the deposition and caking of tailings was obtained through analysis, and a set of coarse and fine tailings bin filling system was proposed. The tailings of the plant were pumped to the filling station by slurry pump. Firstly, the tailings with large particle size difference were divided into coarse tailings and fine tailings by hydrocyclone so that the fine tailings entered the No. 1 sand bin and the coarse tailings entered the No. 2 sand bin. Then, flocculant was added by automatic flocculant dosing device to flocculate and settle the coarse and fine tailings, and then, it was mixed, stirred, and filled into the well. The results showed the following. (1) The particle size difference of tailings in Huanggang Iron mine increased and resulted in unstable flocs. The coarse tailings settled to the bottom of the silo before the fine tailings, and the compression time was too long, leading to the phenomenon of silting and consolidation. (2) Flocculation and settlement of coarse and fine tailings in different sand silos can avoid deposition and compaction of tailings in sand silos. (3) According to the different requirements of the concentration and ratio of the filling slurry, the proportion of coarse sand and fine sand in the filling slurry can be controlled by controlling the flow size of the coarse sand and fine sand chamber, to achieve the design of reasonable particle size composition and concentration requirements. The research results are expected to provide technical support and theoretical guidance for the construction of full tailings cemented filling system in Huanggang iron mine.

1. Introduction

With the continuous development of society and the national requirements and promotion of green mine construction, the requirements of mine safety and environmental protection are becoming higher and higher, and the control of mining surface and environment is becoming more and more strict. The filling mining method has many advantages that other traditional mining methods do not have, such as controlling surface collapse, improving mining environment, reducing ore loss rate and dilution rate, controlling stope ground pressure, improving underground operation safety conditions, and other outstanding advantages. Therefore, more and more underground mining mines choose to adopt the filling mining method [1–8].

In the field of mine filling, most metal mines or some nonmetal mines begin to use the whole tailings produced by the mine dressing plant to fill the underground goaf, which can not only improve the utilization rate of tailings and reduce the discharge pressure on the tailings reservoir but also meet the rigid requirements of the state for the surface environment of the mining area. Therefore, many scholars have conducted in-depth studies on tailings' filling [9–12]. Based on the calculation method and results of friction loss, Fan et al. [13] studied the influence of tailing slurry mass fraction, flow rate, and pipe diameter on friction loss and

carried out industrial filling transportation for goaf. Zhuen et al. [14] studied the effects of solid mass fraction, waste rock dosage, and cementing powder consumption on the collapse degree, yield stress, uniaxial compressive strength, and bleeding rate of tailings' solid waste paste. Meidao et al. [15] used MATLAB software for data analysis and obtained the sensitivity of the influence of cement-sand ratio and slurry concentration on the strength of backfill and the prediction model of various mechanical parameters. Gezhong et al. [16] studied the change rules of equivalent diameter, fractal dimension, and sedimentation velocity of tailings flocs formed under different flocculation conditions.

It is one of the main ways of tailings filling to adopt sand silo for tailings' settlement and filling [17–20]. Jun et al. [21] proposed the calculation method of critical working pressure and working flow of high-pressure activated medium in vertical sand silo according to the basic principle of activated slurry. Ke et al. [22] studied the influence of tailings particle size composition, surface shape, and sand feeding concentration on tailings' settling velocity in sand silo. Weicheng et al. [23] proposed a sand discharging model of a sand silo and used fluid dynamics software to simulate and analyze the continuous sand discharging model. Liyi et al. [24] analyzed and studied the influence rule of ultrasonic wave on the final mass concentration of total tailings' slurry in the sand silo under different conditions. Due to the different mineral processing methods and ore properties adopted by mine concentrators, the properties of tailings produced are also different. There will be large differences in the particle diameter of tailings and obvious differences in the thickness and fineness of tailings, which may lead to the deposition and agglomeration of tailings in sand bins and affect the normal production. However, the research results in this field are rarely reported, and it is urgent to put forward more effective solutions.

The tailings of Huanggang iron mine in Inner Mongolia have a large proportion and obvious difference in thickness. After flocculation settlement, silting and consolidation of sand silts occur, which greatly affect the normal filling operation. Based on this, this study takes the full tailings' filling slurry of Huanggang iron mine as the research object, obtains the reasons for tailings silting and consolidation through analysis, and puts forward a set of coarse and fine tailings' filling system, in order to provide technical support and theoretical guidance for the construction of the full tailings' cemented filling system of Huanggang iron mine.

2. Test and Analysis of Physical and Chemical Properties of Total Tailings

The physical and mechanical properties of the tailings, such as specific gravity, bulk density, porosity, and particle size distribution, were measured by sampling the tailings from Huanggang iron concentrator and laboratory tests were carried out.

2.1. Gravimetric Determination of Total Tailings. Specific gravity is an object of the ratio between density of the tailings and density of water, as a dimensionless quantity. Specific gravity refers to the ratio between the density of liquid or solid at a specific temperature and pressure and the maximum density of pure water at standard atmospheric pressure. Specific gravity of laboratory samples is usually measured by the pyrogen flask method, as shown in Figure 1.

The gravity determination test for the tailings of Huanggang mining was conducted for three times. The average value of the three test results was taken to obtain the gravity of the whole tailings. The test results are presented in Table 1.

It can be seen from Table 1 that the average value of the three test results of the gravity of total tailings in Huanggang iron mine was 3.23. Compared with the gravity of tailings in [9–16], the gravity of total tailings in Huanggang iron mine was large. When the slurry is formed, the settlement performance is good, the settlement speed is fast, and the bulk density of the slurry is large.

2.2. Determination of Bulk Density of Whole Tailings. The constant volume weighing method was used for the measurement, that is, the test material was loaded into the standard funnel, a standard liter bucket was placed below, the material fell freely to avoid vibration, and the weight of the balance was scraped flat after the bucket was full. The loose bulk density of the test material was calculated after several measurements, and the measurement process is shown in Figure 2.

Three tests were conducted for the determination of the dense bulk density and loose bulk density of the whole tailings in Huanggang mining. The results of the three tests were averaged to obtain the dense bulk density and loose bulk density of the whole tailings. The test results are shown in Table 2.

It can be seen from Table 2 that the average values of the three test results of loose and dense bulk density of the whole tailings in Huanggang iron mine were 2.16 and 2.46, respectively. Compared with the bulk density of the tailings in [9–16], the bulk density of the total tailings in Huanggang iron mine was also large, and the difference between the loose bulk density and the dense bulk density was small, which can reflect from the side that the porosity of the total tailings was small.

2.3. Porosity Analysis of Total Tailings. Porosity was calculated using

$$\eta = 1 - \frac{\gamma}{\rho_0}, \tag{1}$$

where η is the porosity of the whole tailings, %, $\gamma$is the bulk density of the whole tailings, g/cm^3, and ρ_0 is the true density of the whole tailings.

According to the data in Tables 1 and 2, the porosity of the whole tailings in loose and dense states is calculated by substituting it into equation (1), as shown in Table 3.

It can be seen from Table 3 that the loose porosity and dense porosity of the total tailings in Huanggang iron mine were 33.12% and 23.84%, respectively, which are smaller

Figure 1: Gravity bottle weighing.

Table 1: Gravity of total tailings.

Description	Units	First test	Second test	Third test	Average value
Total tailings	g/m^3	3.22	3.25	3.23	3.23

Figure 2: Bulk density determination process.

than those in [9–16]. The porosity of the tailings can reflect the strength and water retention of the tailings to a certain extent. The total tailings in Huanggang iron mine had high strength and poor water retention.

2.4. Total Tailings' Particle Size Distribution. The grain size distribution of filling aggregate is also called the gradation of materials, which refers to the percentage content of different particle sizes in granular materials. The particle size distribution of filling material determines the whole process of the filling process and has a great influence on preparation, transportation, and filling body quality. The particle size composition of the whole tailings was analyzed by Malvern 3000 laser particle size tester, which is shown in Figure 3.

The results of particle size distribution of the whole tailings are presented in Table 4 and shown in Figure 4, respectively, and the uniformity coefficient Cu and curvature coefficient Cc obtained are 7.05 and 1.02, respectively.

The measurement results of physical and mechanical properties of Huanggang Mining's tailings show that

(1) From the size of filling materials, the size of Huanggang iron tailings is relatively coarse. The proportion of −200 mesh (<74 μm) particles is only 21.41%, the proportion of 38 μm is about 11%, and the median particle size is 181.57 μm. Compared with the tailings in [9–16], the tailings of Huanggang iron mine were coarser, and the gravity of coarse particle size tailings was larger, and the proportion of fine particle size tailings was smaller. The difference between coarse particle size and fine particle size tailings was obvious. It is necessary to pay attention to the blockage caused by the settlement of coarse particles. The coarse particle size is beneficial to the strength development of filling body, but the less fine particles will affect the transportability of slurry.

(2) From the perspective of filling material gradation, the uneven coefficient and curvature coefficient of filling material were both outside the normal range. Compared with the tailings in [9–16], the composition and distribution of tailings in Huanggang iron mine were uneven, and the gradation was poor. The curvature coefficient was slightly larger than the optimal value, indicating that there was a slight loss of fine particles. Tailings of Huanggang iron mine had great abrasion on the pipeline and were easy to be separated, which was not conducive to long-distance pipeline transportation.

3. Technical Reform Scheme and Results of Sand Silo

The original filling process of Huanggang iron mine adopts natural settlement and concentration of tailings. Due to the coarse particle size, large ratio, and large difference in particle size, the coarser tailings can naturally settle to the bottom of the sand bin for accumulation and concentration, while the finer tailings cannot naturally settle and float in the upper overflow water, and the overflow water is not clear. Therefore, the slurry particles filled into the underground are coarse, the composition distribution is uneven, and the gradation is poor. The segregation occurs in the transportation pipeline and the underground goaf, and the pipeline is greatly worn.

In view of the problems existing in the original filling process of Huanggang iron mine, such as low filling concentration, large drainage volume, serious turbidity of overflow water, and failure of filling strength to meet the standard, based on the above test results, the technical improvement scheme of the sand silo was studied.

Table 2: Test results of bulk density of the whole tailings.

Description	Units	First test	Second test	Third test	Average value
Loose bulk density	g/cm^3	2.15	2.18	2.16	2.16
Dense bulk density		2.45	2.48	2.44	2.46

Table 3: Porosity of whole tailings.

Description	Value
Loose porosity (%)	33.12
Dense porosity (%)	23.84

3.1. Technical Reform Scheme. The fine tailings cannot settle naturally; therefore, a set of flocculant settling module is added to wrap coarse and fine tailings with flocculant to form flocculant groups, which settle together to the bottom of the sand bin, so as to realize full tailings' filling and overflow water clarification. Flocculant automatic dosing machine is shown in Figures 5 and 6.

The modified filling process is as follows: the tailings for filling are provided by the concentrator, and the tailings' slurry with a concentration of 15.81% generated in the beneficiation process is precipitated and concentrated by the tailings' concentration pond, and its weight concentration is increased to about 40%. Then, the tailings are sent to the tailings' bin of the filling preparation station by the tailings' slurry pump. High concentration bottom flow mortar was formed after the sand bin was reconstructed and treated with flocculant. Cement is measured by spiral electronic balance according to the flow and concentration of tailings. At the same time, according to the concentration requirements of filling, an appropriate amount of concentration water is added. Concentrated tail mortar, cement, and water are stirred by the original mixing system, and the evenly mixed filling slurry is prepared and transported to the goaf for filling through the filling borehole and underground pipe network. The overall filling process is shown in Figure 7.

Through the sand silo technical reform program, the filling concentration is increased to 75%–80%, and the solid content of overflow water is less than 300 ppm, which greatly improves the strength of the filling body and reduces water dewatering, thus creating economic benefits for the mine.

3.2. Technical Reform Results and Reason Analysis. After the technical reform of the sand bin, the filling concentration increased from 70%~75% to 75%~78% due to the increase of fine particles. The bleeding rate of the filling slurry decreased from 20% to 10%. The flow state of the filling slurry is good, and segregation and stratification no longer appear. The strength of the backfill body increases and basically reaches the strength required by the mining method. The overflow water is clear, and the full tailings' filling and continuous filling are realized. The filling effect after technical modification is shown in Figures 8 and 9, and the change of filling concentration is shown in Figure 10.

As can be seen from Figure 10, in the first 7 days of filling time, the filling slurry concentration of 1 : 4 and 1 : 15 with different cement-sand ratios was 75% or above, with roughly the same change trend and relatively stable filling. After 7 days, the filling concentration decreased sharply from the original 75% to 46% and 33% and finally to 0.

The reason for the sharp decrease in filling concentration is that the silting and compaction degree of tailings in the sand silo is getting deeper and deeper. At the beginning, the slurry concentration is unstable and the material cannot

Figure 3: Particle size analyzer.

Table 4: Results for particle size measurements of the whole tailings.

Particle size	d_{10}	d_{30}	d_{60}	d_{90}
Value (μm)	34	91.2	239.883	549.541

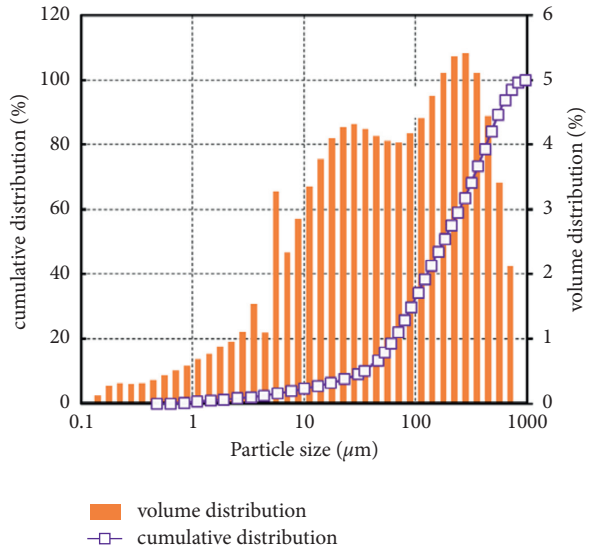

Figure 4: Particle size distribution of the whole tailings.

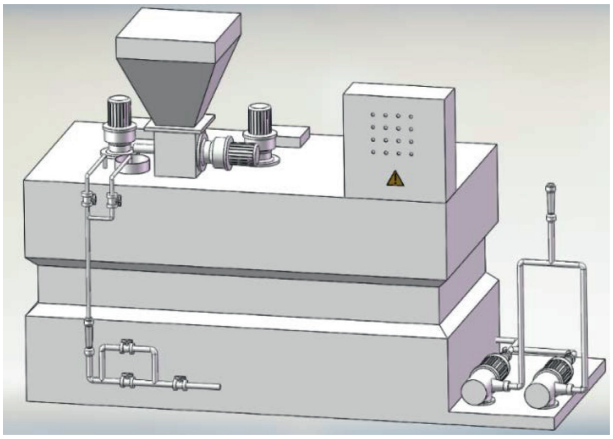

Figure 5: Model of flocculant automatic dosing machine.

Figure 6: Real figure of flocculant automatic dosing machine.

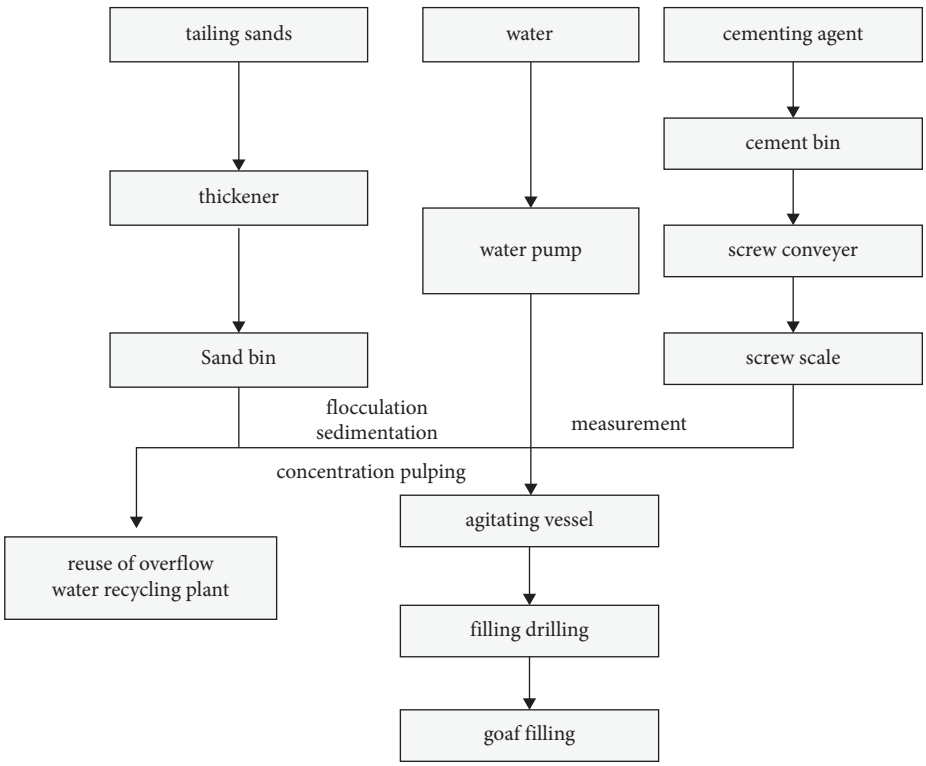

Figure 7: Flowchart of filling process after technical modification.

Figure 8: Overflow water.

Figure 9: Flow pattern of filling slurry.

downfeed in a short time. At the later stage, the slurry concentration is low and the material cannot downfeed for a long time, and the sand surface height is getting higher and higher until the material cannot downfeed in the end. The silting and consolidation of sand silo tailings are shown in Figure 11.

It can be seen from Figure 11 that the hardness of tailings is very high after compaction, and the height of compaction is about 2–4 m, which requires clearance treatment, consuming a lot of time, and labor cost.

After analysis and research, the reasons for silting and compaction of sand silo tailings are as follows: coarse tailing sands particle size is large, coarse tailing sands ratio is too large, −38 micron particle accounted for only 21.41%, adding flocculating agent, the formation of the floccules is not stable, in the process of settling sand storehouse, floccules damage occurs, flocculant wrapped coarse tailing sands materials and a small amount of fine in the sand at the bottom of the silo, and rapid subsidence and a large number of fine tailing sands are under the parcel of flocculant slowly settling in tailing sand materials coarse surface. As a result, the coarse and fine tailings are stratified, and the coarse tailings are accumulated and concentrated for a long time due to the fast settlement speed. Finally, the tailings are silted and consolidated, and the slurry cannot down feeding.

4. Study on the Solution of Tailings' Silting Consolidation

In view of the causes of silting and consolidation of silo tailings, in order to reduce the cost, this study improved the original filling system of Huanggang iron mine and added a new hydrocyclone. Based on this, a set of coarse and fine silo filling system was proposed to solve the problem of silting and consolidation of silo tailings. The process flow of the filling system of coarse and fine tailings' compartments is shown in Figure 12. The tailings of the concentrator are pumped to the filling station by a slurry pump. Firstly, the tailings with large particle size difference are divided into coarse tailings and fine tailings by hydrocyclone so that the fine tailings enter the I sand bin and the coarse tailings enter the II sand bin. Then, the flocculant is added to the flocculation settlement of the coarse and fine tailings by the flocculant automatic dosing device and then mixed and filled to the underground.

In the filling system of coarse and fine tailings' bin shown in Figure 12, according to the concentration and ratio requirements of different filling slurry, the opening and closing degrees of sand discharge valve 1 and sand discharge valve 2 under the sand bin are adjusted, respectively, to control the flow size of fine sand bin and coarse sand bin. The flow can be displayed by electromagnetic flowmeter 1 and electromagnetic flowmeter 2, to control the proportion of coarse and fine tailings in the filling slurry and achieve the reasonable particle size composition and concentration requirements.

By flocculation, sedimentation, and concentration of coarse tailings and fine tailings with different particle sizes in different sand bins, the problems of unstable flocs,

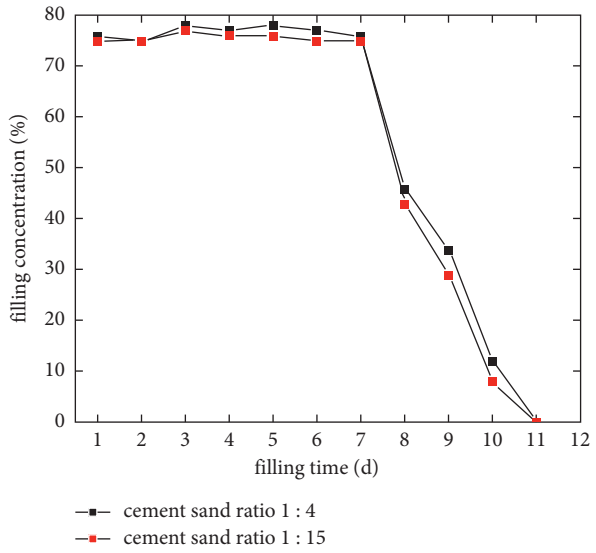

Figure 10: Variation of filling concentration.

Figure 11: Deposition and consolidation of tailings.

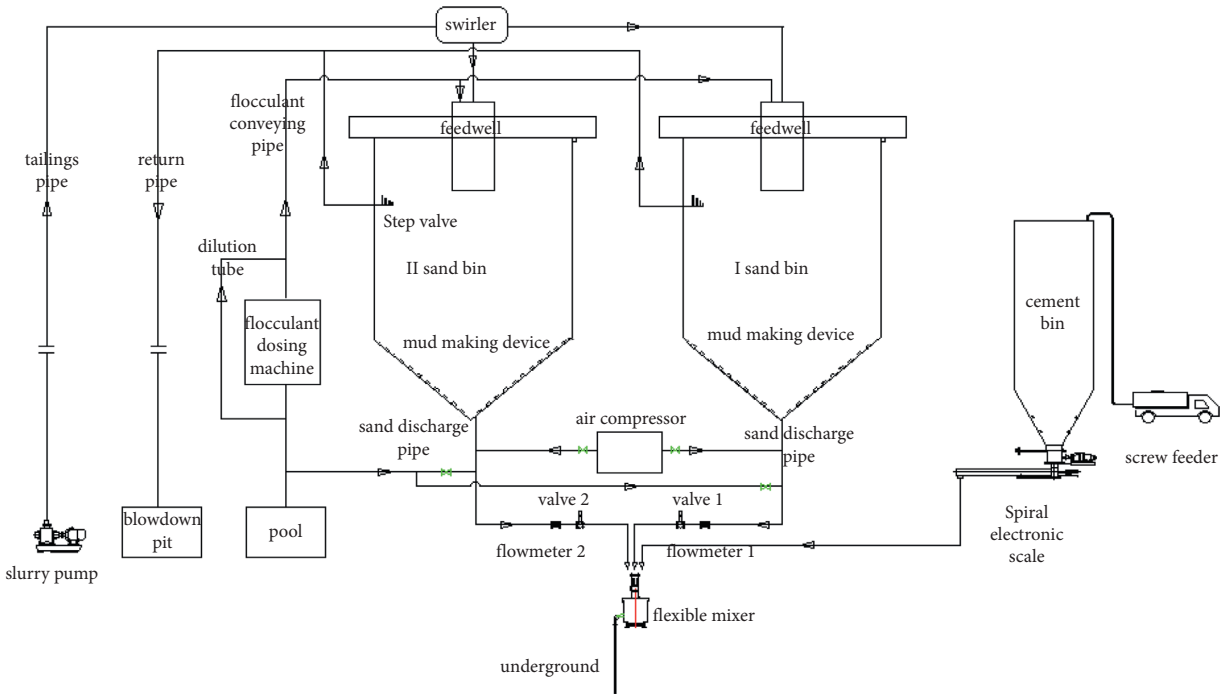

Figure 12: Technical process of the filling system for coarse and fine tailings' compartments.

separation of coarse and fine tailings, deposition and agglomeration of tailings, the shutdown of filling station, and influence of normal filling operation can be effectively avoided after adding flocculants.

5. Conclusion

In this study, the causes of siltation and compaction of tailings in Huanggang iron mine were analyzed, and a set of coarse and fine tailings' filling system is proposed. The following conclusions are drawn:

(1) The particle size difference of tailings in Huanggang iron mine increases, and the formed flocs are unstable. The coarse tailings settle to the bottom of the sand bin before the fine tailings, and the compression time is too long, resulting in the phenomenon of deposition and agglomeration.

(2) Coarse tailings and fine tailings are flocculated in different sand bins, which can avoid the phenomenon of siltation and hardening of tailings in sand bins.

(3) According to the different requirements of the concentration and proportion of the filling slurry, the proportion of coarse sand and fine sand in the filling slurry can be controlled by controlling the flow rate of the coarse sand bin and the fine sand bin, to achieve the reasonable particle size composition and concentration requirements.

The research results are expected to provide technical support and theoretical guidance for the construction of cemented tailings' filling system in Huanggang iron mine.

Data Availability

The data used to support the findings of this study are included within the article.

Conflicts of Interest

The authors declare that they have no conflicts of interest.

Acknowledgments

This work was supported and financed by National Key Research and Development Program of the 13th Five-Year Plan (no. 2018YFC0604603 and 2018YFC0604606), all of which are greatly appreciated.

References

[1] C. Chong, L. Wu, and Z. Yalei, "Research and application of nesting paste filling mining technology," *Mining Research and Development*, vol. 39, no. 7, pp. 24–27, 2019.

[2] X. Yu, Z. Donghe, and J. Huazhe, "Application of upward horizontal layered cemented filling method in Duda Lead-Zinc Mine," *Mining Technology*, vol. 17, no. 2, pp. 1–3, 2011.

[3] W. Lihong, B. Aihua, and L. Yuanyuan, "Development and outlook on the filling method in China," *Mining Research and Development*, vol. 37, no. 3, pp. 1–7, 2017.

[4] W. Zhiyaun, Z. Wenru, and Z. Qianyong, "Research and practice on safe and efficient mining of orebody under complex conditions," *Mining Research and Development*, vol. 38, no. 5, pp. 10–12, 2018.

[5] C. Yang, X. Mengguo, and C. Aiping, "Optimization of filling mining method based on coordination degree measurement model," *Mining Research and Development*, vol. 38, no. 3, pp. 6–10, 2018.

[6] Z. Fengtian, G. Weijun, and X. Yinpei, "The combination of deep hole caving mining technology with sublevel filling method of chibuluma copper mine in Zambia," *Mining Research and Development*, vol. 39, no. 7, pp. 5–9, 2019.

[7] Z. Jiaqi, L. Jingbo, and Y. Xuyan, "Application of upward horizontal layered dry filling mining method in Daliuhang Gold Mine," *Mining Technology*, vol. 17, no. 4, pp. 6–8, 2017.

[8] Z. Yongfeng, Z. Xiongtian, and M. Hongfu, "Research of efficient mining method in slowly inclined medium thick orebody," *Metal Mine*, no. 6, pp. 19–23, 2016.

[9] Z. Tongtong, W. Yongyan, and Y. Zhuoqun, "Effect of loading rate on strength characteristics of layered backfill," *Science Technology and Engineering*, vol. 21, no. 34, pp. 14535–14541, 2021.

[10] X. Wenbin, L. Bin, and W. Yubing, "Experiment design and analysis on the permeability characteristic cemented unclassified tailings backfill," *Mining Research and Development*, vol. 41, no. 12, pp. 99–103, 2021.

[11] C. Jie, C. Yunkai, and H. Qingxiang, "Study on rheological characteristic of high-aeolian-sand filling materials," *Mining Research and Development*, vol. 41, no. 12, pp. 109–113, 2021.

[12] Z. Aiqing, L. Jinyun, and W. Aixiang, "Experimental study on vibration dehydration mechanism of full tailings based on discrete element dynamics," *Mining Research and Development*, vol. 41, no. 12, pp. 119–123, 2021.

[13] W. Fan, H. Bin, and H. Yafei, "Calculation and application of friction loss in slurry pipeline transportation with paste filling," *Journal of Mining and Safety Engineering*, vol. 38, no. 6, pp. 1158–1166, 2021.

[14] R. Zhuen, W Aixiang, and W. Yimin, "Multiple response optimization of key performance indicators of cemen paste backfill of total solid waste," *Chinese Journal of Engineering*, vol. 8, pp. 1–9, 2021.

[15] Z. Meidao, R. Yunzhang, and X. Wenfeng, "Orthogonal experiment on optimization of filling ratio of full tailings paste," *Gold Science and Technology*, vol. 29, no. 05, pp. 740–748, 2021.

[16] C. Gezhong, L. Cuiping, and R. Zhuen, "Influence of flocculation conditions on floc structure and solid-liquid separation in cemented paste filling," *Chinese Journal of Nonferrous Metals*, vol. 156, pp. 1–20, 2020.

[17] K. Ruihai, W. Xu, and W. Fengfeng, "Research and application of full tailings cemented filling technology in the zijinshan gold-copper mine," *Mining Research and Development*, vol. 38, no. 3, pp. 20–24, 2018.

[18] M. Dongxu, L. Xiaosheng, and W. Changjun, "Expansive capability reform and application of the full tailings paste filling system in wancheng minning industry," *Mining Research and Development*, vol. 38, no. 03, pp. 11–15, 2018.

[19] Z. Bokun, Y. Xuyan, and H. Tenglong, "Optimization of filling process scheme for sanshandao gold mine based on unascertained measure theory," *Mining Research and Development*, vol. 40, no. 2, pp. 13–18, 2020.

[20] P. Liang, K. Ruihai, and L. Xiaosheng, "Stndy and analysis on the process selection of filling system in a lead-zinc ore,"

Mining Research and Development, vol. 40, no. 3, pp. 28–32, 2020.

[21] W. Jun, Q. Dengpan, and H. Runsheng, "Consecutive discharge tailings model of vertical sand silo and its application," *Chinese Journal of Nonferrous Metals*, vol. 30, no. 1, pp. 235–244, 2020.

[22] J. Ke, K. Ruihai, and Y. Zhongliang, "Study on the optimal concentration and controlling mode of whole tailings flocculation sedimentation," *Gold Science and Technology*, vol. 27, no. 3, pp. 440–448, 2019.

[23] R. Weicheng, Q. Dengpan, and Z. Zhiwei, "Research on the change law of volume fraction of tailings with tailings silo height in vertical tailings silo," *Gold Science and Technology*, vol. 26, no. 1, pp. 64–73, 2018.

[24] Z. Liyi, L. Wensheng, and Y. Peng, "Thickening sedimentation of unclassified tailings under influence of external field based on response surface method," *Chinese Journal of Nonferrous Metals*, vol. 28, no. 9, pp. 1908–1917, 2018.

Hindawi
Advances in Civil Engineering
Volume 2022, Article ID 4077305, 22 pages
https://doi.org/10.1155/2022/4077305

Research Article

Analysis of Crustal Stress and Its Influence on the Stability of the Deep Tunnel in the Huanaote Mining Area

Mingde Zhu,[1,2] **Yantian Yin**,[1,2] **Chao Peng**,[1,2] **Li Cheng**,[1,2] **Yingjie Hao**,[1,2] **Kuikui Hou**,[1,2] **Haoqin Zhang**,[1,2] **and Jie Zhang**[3]

[1]*Deep Mining Laboratory of Shandong Gold Group Co., Ltd., Laizhou 261442, China*
[2]*Shandong Key Laboratory of Deep-sea and Deep-earth Metallic Mineral Intelligent Mining, Laizhou 261442, China*
[3]*School of Civil and Resource Engineering, University of Science and Technology Beijing, Beijing 100083, China*

Correspondence should be addressed to Mingde Zhu; zhumingde@sd-gold.com

Received 7 December 2021; Revised 8 January 2022; Accepted 10 January 2022; Published 1 March 2022

Academic Editor: Lijie Guo

Crustal stress is a critical parameter utilized to analyze the stability of the tunnel in underground hard-rock mining sites. In order to analyze the distribution law of crustal stress and its influence on the stability of the deep tunnel in the Huanaote mining area, the in-situ stress field model of this area was constructed firstly by using the borehole stress relief method. Moreover, the numerical model is established based on three real engineering conditions: the excavation direction is parallel, vertical, and intersection to the measured maximum horizontal principal stress direction, respectively. Results show that, compared with the other two layout schemes, the stress of two side walls reaches peak at 27 MPa, when the excavation direction is intersected to the measured maximum horizontal principal stress direction, which indicates that the support and maintenance of two side walls should be strengthened to ensure the stability of the tunnel and the safety of personnel and equipment in real projects.

1. Introduction

The Huanaote mining area is located in the middle of the Inner Mongolian Plateau. The lowest mining depth is more than 800 meters from the surface, which is the deepest underground hard-rock mining site in Inner Mongolia. The production began at 2020, and varying degrees of rock burst occurred during the development stage between +100 m and +80 m levels. In order to provide scientific reference for the layout and design of stopes and tunnels, in-situ stress measurement must be carried out to obtain the three-dimensional stress state of the mining area [1, 2].

At present, the borehole stress relief method is the most widely used and the most mature technology in the world. The basic data such as initial strain of stress relief are collected on-site, and it will be combined with indoor temperature compensation test, confining pressure calibration, and related rock mechanics test, and the overall distribution of in-situ stress in the mining area will be determined [3–9]. However, the acquisition circuit of the conventional hollow inclusion strain gauge is a conductor, which is easily influenced by temperature change. The Australian ES&S company has launched the HID type of hollow inclusion probe to realize in-situ digitization of data, but there is no temperature calibration algorithm to correct the temperature inaccuracy. Due to the function of the cooling water channel of the drilling rig and the influence of the friction torque in the drill pipe, there is a risk of being twisted when the measuring wire is removed [10–13].

"Double temperature compensation and the in-situ stress relief measurement considering the nonlinearity of rock mass" [14, 15] are carried out firstly to accurately analyze the distribution law of crustal stress in the Huanaote mining area and its influence on the stability of deep tunnel. Based on the field condition, a numerical model is established to simulate the variation law of stress and displacement of the surrounding rock of tunnel under three working conditions: the excavation direction is parallel, vertical, and intersection to the maximum horizontal principal stress, respectively [16–18].

2. Measurement and Analysis of Crustal Stress in the Mining Area

2.1. Instrument for Measuring Crustal Stress. Instruments utilized for in-situ stress measurement are the most significant part in the field test. The measurement equipment mainly includes a stress meter, stress meter mounting rod, digital dynamic signal test system, confining pressure calibrator, high- and low-temperature test chambers, binder with combining drill bit, and core barrels. Envelope stress meter is the first principle to in-situ stress measurement, and its quality determines the accuracy of measurement results. The improved hollow inclusion strain gauge probe (Figure 1) adopts high-strength nonmagnetic aluminum alloy material, and the instrument cavity behind the device is packaged with thermally conductive silica gel, which has good waterproof, heat dissipation, and shock absorption performance.

From the head to the end of the strain gauge, the sequence of strain gauge following the clockwise order is A-B-C. The strain gauge parallel to the borehole direction is 0# strain gauge, which is 45°, 90°, and 135° clockwise. Taking group A strain gauge as an example, 1# strain gauge as circumferential strain gauge is recorded as A90, 2# strain gauge axial strain gauge recorded as A0, 3# (A45) and 4# (A135) strain gauges are ±45° with borehole axis, respectively. Similarly, 5#~12# strain gauges are recorded as B90, B0, B45, B135, C90, C0, C45, and C135, respectively.

2.2. Steps of Ground Stress Measurement and the Stress Relief Method. A horizontal borehole with a 130 mm diameter is drilled on the side wall first (Figure 2-①), and it reached 3–5 times the depth of the tunnel span [19, 20]. The bottom of the hole is flattened with a flat bit, and the horn mouth is punched with a cone bit. Then, a concentric hole with a diameter of 36 mm and a depth of 35~40 cm is punched from the bottom of the hole (Figure 2-②). The stress gauge is sent to the predetermined position in the hole by the installation rod with the directional device (Figure 2-③). After the cementing agent is solidified, the thin-walled drill with a diameter of 130 mm continues to deepen the large pores, so that the rock around the strain gauge is gradually separated from the surrounding rock, which results in stress relief of the core (Figure 2-④). In the process of stress relief, the strain values measured by each strain gauge in the strain gauge are automatically recorded by the bridge conversion device and the data collector. According to instructions, strain data are recorded every 2 cm footage of advance.

After the stress relief is completed, the strain data stored in the data collector will be printed out by the computer, and the stress relief curve is drawn, which represents the curve of the strain value of each strain gauge with the stress relief depth. Then, according to the temperature change of the acquisition circuit measured by the synchronous dual temperature channel, the temperature calibration test is carried out to reduce the temperature influence in the circuit, and the release curve corrected by dual temperature compensation is obtained. The final stable value of the curve is used as the original data for calculating the in-situ stress.

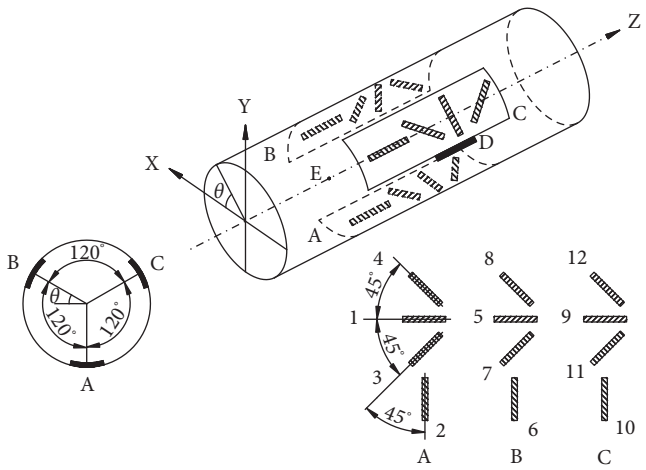

Figure 1: Improved hollow inclusion technique [19].

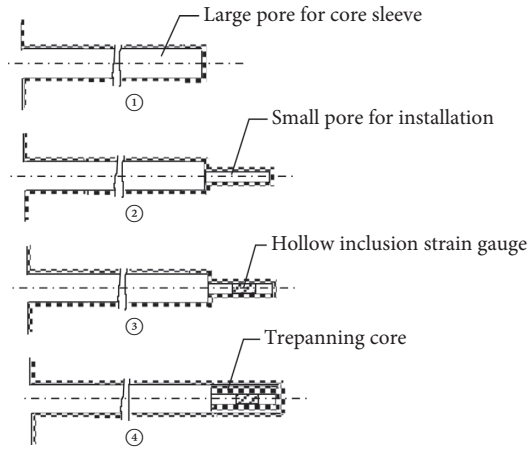

Figure 2: Trepanning stress relief method [19].

The confining pressure calibration test is carried out with the original core obtained from the on-site casing release, and the strain value caused by the confining pressure during the measurement process of the hollow inclusion strain gauge is corrected. The elastic modulus, Poisson's ratio, and K coefficient of rock are obtained from the temperature-calibrated stress-relief strain and confining pressure calibration test results. The stress value of original rock is calculated by Formula (1)~(4).

$$\varepsilon_\theta = \frac{1}{E}\left\{\left(\sigma_\chi + \sigma_y\right)k_1 + 2\left(1-\nu^2\right)\right.$$
$$\left.\left[\left(\sigma_y - \sigma_\chi\right)\cos 2\theta - 2\tau_{xy}\sin 2\theta\right]k_2 - \nu\sigma_z k_4\right\},$$
$$\varepsilon_z = \frac{1}{E}\left[\sigma_z - \nu\left(\sigma_x + \sigma_y\right)\right], \quad (1)$$
$$\gamma_{\theta z} = \frac{4}{E}(1+\nu)\left(\tau_{yz}\cos\theta - \tau_{zx}\sin\theta\right)k_3,$$
$$\varepsilon_{\pm 45^\circ} = \frac{1}{2}\left(\varepsilon_\theta + \varepsilon_z \pm \gamma_{\theta z}\right),$$

where σ_x, σ_y, σ_z, τ_{xy}, τ_{yz}, τ_{zx}—the three-dimensional stress component at the measuring point; ε_θ—circumferential strain value of hole wall; ε_z—axial strain value of hole wall; $\varepsilon_{\pm 45^\circ}$—strain value in the direction of ±45° with borehole axis; $\gamma_{\theta z}$—shear strain value; E—elastic modulus of rock at measuring point; υ—Poisson's ratio of measuring point rock; θ—angle between strain gauge and x axis, where counterclockwise rotation is positive; and k_1, k_2, k_3, k_4—four correction coefficients given by Worotnicki and Walton [21], collectively known as K coefficients, are calculated by the following formula:

$$\left.\begin{aligned} k_1 &= d_1(1-\nu_1\nu_2)\left(1-2\nu_1+\frac{R_1^2}{\rho^2}\right)+\nu_1\nu_2 \\ k_2 &= (1-\nu_1)d_2\rho^2+d_3+\nu_1\frac{d_4}{\rho^2}+\frac{d_5}{\rho^4} \\ k_3 &= d_6\left(1+\frac{R_1^2}{\rho^2}\right) \\ k_4 &= d_1(\nu_2-\nu_1)\left(1-2\nu_1+\frac{R_1^2}{\rho^2}\right)\nu_2+\frac{\nu_1}{\nu_2} \end{aligned}\right\}, \tag{2}$$

where

$$\left.\begin{aligned} d_1 &= \frac{1}{1-2\nu_1+m^2+n\left(1-m^2\right)} \\ d_2 &= \frac{12(1-n)m^2\left(1-m^2\right)}{R_2^2D} \\ d_3 &= \frac{1}{D}\left[m^4\left(4m^2-3\right)(1-n)+x_1+n\right] \\ d_4 &= \frac{-4R_1^2}{D}\left[m^6(1-n)+x_1+n\right] \\ d_5 &= \frac{3R_1^4}{D}\left[m^4(1-n)+x_1+n\right] \\ d_6 &= \frac{1}{1+m^2+n\left(1-m^2\right)} \\ D &= (1+x_2n)\left[x_1+n+(1-n)\left(3m^2-6m^4+4m^6\right)\right] \\ &+(x_1-x_2n)m^2\left[(1-n)m^6+(x_1+n)\right] \end{aligned}\right\}. \tag{3}$$

where R_1—inner radius of hollow inclusion; R_2—installation hole radius; G_1—rigid modulus of hollow inclusion material; G_2—rigid modulus of rock; υ_1—Poisson's ratio of hollow inclusion material; υ_2—Poisson's ratio of rock; and ρ—radial distance of resistance strain gauge in hollow inclusion.

$$\begin{aligned} n &= \frac{G_1}{G_2}, \\ m &= \frac{R_1}{R_2}, \\ x_1 &= 3-4\nu_1, \\ x_2 &= 3-4\nu_2. \end{aligned} \tag{4}$$

2.3. Layout of Measurement Point. This site is developed by shafts, and it is divided into main shaft and air shaft. The main shaft is located outside the rock movement range of footwall in No. 55 exploration line ore body. The net section of the shaft is 5.5 m, and the wellhead elevation is +986.0 m, while the bottom elevation is +30 m. The full depth of the shaft is 956 m, which contains 11 levels from +600 m to +100 m, and the height of each level is 50 m. According to the progress of the infrastructure project in the mining area, seven in-situ stress measuring points are arranged in the five infrastructure levels of +350 m, +300 m, +250 m, +100 m, and +80 m, of which one measuring point is arranged in the level of +250 m, +100 m, and +80 m, and one measuring point is arranged in the two wings of +350 m level and +300 m level, respectively. The layout positions and drilling conditions of each measuring point are shown in Table 1.

2.4. Stress Relief Analysis. According to the data recorded by the resistance strain gauge during the stress relief process of seven boreholes, the stress relief curve is drawn. Based on the temperature variation of the acquisition circuit measured by the synchronous double temperature channel, the stress relief curve is compensated and corrected, and the stress relief curves are as shown in Figure 3.

It can be seen from the stress relief curve that the change of recovery strain with footage depth is basically synchronous in the process of core release. The strain values measured by each strain gauge are generally very small before the lifting depth of the sleeve hole reaches the measured section (i.e., the section where the strain gauge is located). Some strain gauges even measure negative strain values, which is the result of stress transfer caused by casing holes, which is equivalent to "excavation effect." Many curves change in opposite directions when the removal depth of the casing is close to the measured section. The maximum strain occurs when the casing bit passes near the measuring section. When the socket depth exceeds a certain distance from the measured section, the strain value gradually stabilizes and the curve tends to be stable. The final stable value will be used as the original data for calculating in-situ stress.

2.5. Confining Pressure Calibration Test. The calculation of crustal stress requires the elastic modulus and Poisson's ratio of rock at each measuring point. However, the state and mechanical properties of underground rock mass are

Table 1: Position of each measuring point of ground stress and parameters of test holes.

	Location	Coordinate (x, y, z)	Hole depth (m)	Orientation (°)	Dip angle (°)	Burial depth (m)	RQD (%)
1#	350 m level	(557356.94, 5098624.77, 352.3)	9.1	84	3.5	526	42
2#	350 m level	(556825.46, 5099062.66, 352.3)	6.3	180	4	526	92.3
3#	300 m level	(557315.27, 5098571.06, 301.3)	6.2	305	3	576	52.7
4#	300 m level	(556630.72, 5099129.99, 301.3)	7.0	215	4.3	576	98.9
5#	250 m level	(557255.03, 5098459.76, 252.1)	8	180	4	626	78.4
6#	100 m level	(557367.82, 5098517.70, 102.3)	6	25	4	776	97.5
7#	80 m level	(557171.35, 5098497.59, 81.8)	6.1	172	4.5	796	98

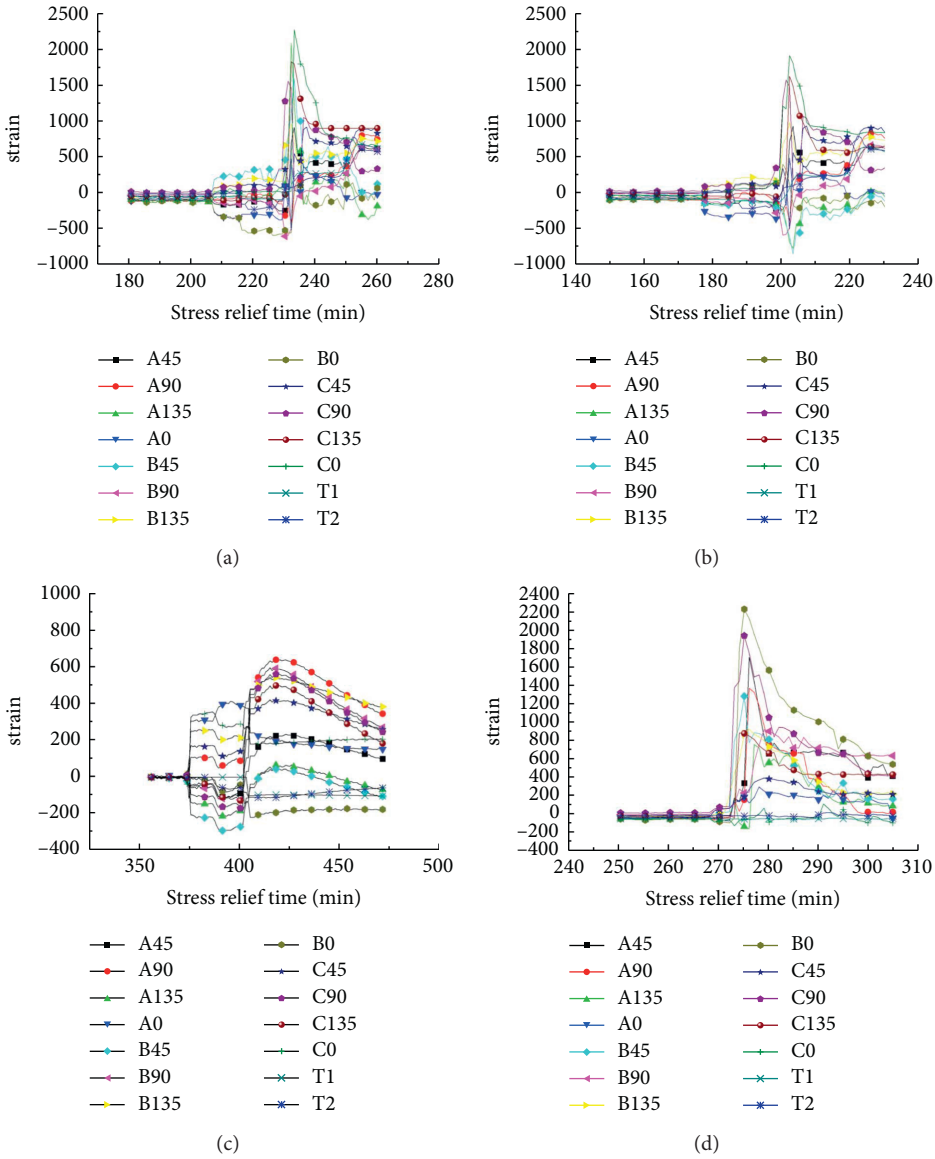

Figure 3: Continued.

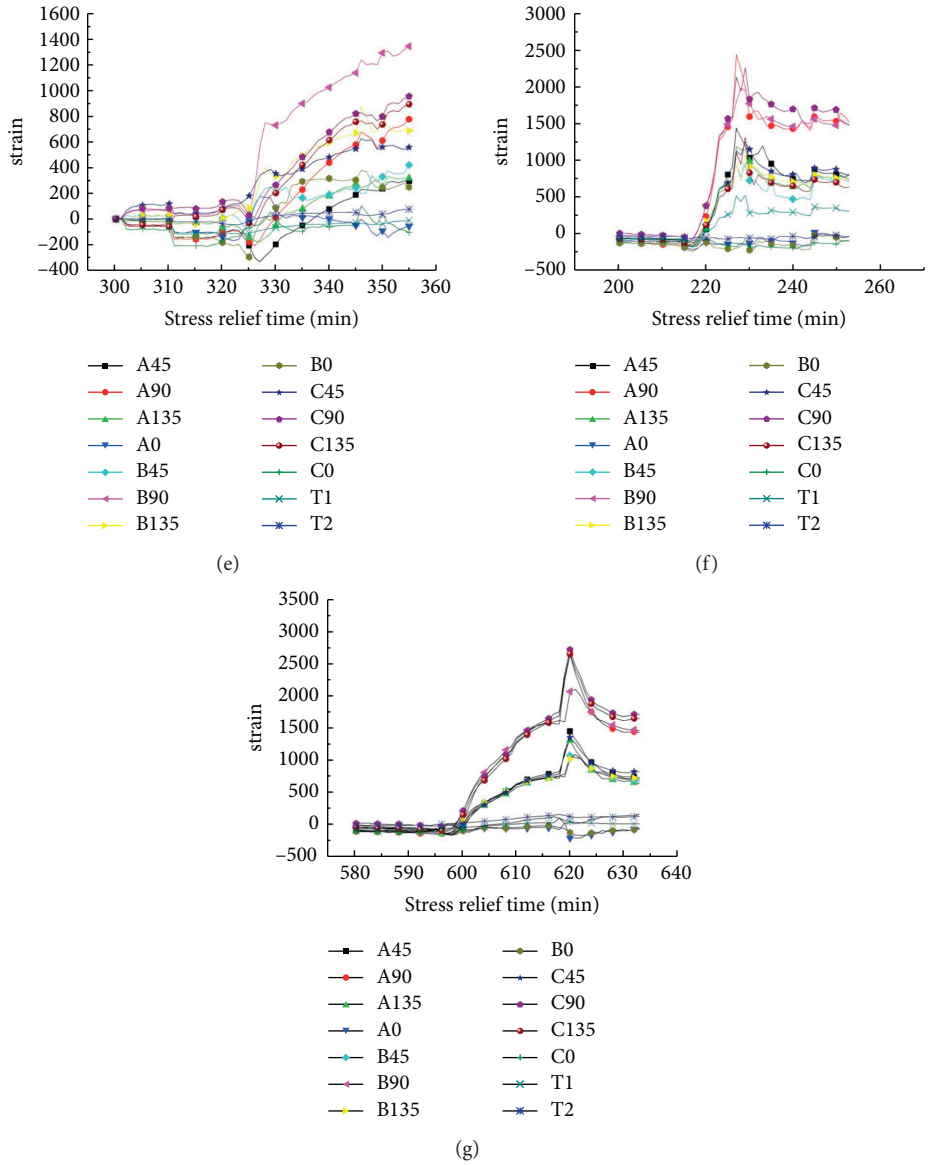

Figure 3: The relief curve of double temperature compensation correction: (a) 350 m level 1# measuring point, (b) 350 m level 2# measuring point, (c) 300 m level 3# measuring point, (d) 300 m level 4# measuring point, (e) 250 m level 5# measuring point, (f) 100 m level 6# measuring point, and (g) 80 m level 9# measuring point.

extremely complex, and the properties of two neighboring rock mass could have a critical variation. In order to ensure the accuracy of in-situ stress calculation results, the rock elastic modulus and Poisson's ratio must be able to truly represent the original rock where the strain gauge is located. It has a great significance for measurement accuracy and crustal stress calculation to conduct confining pressure calibration tests by using the original rock core obtained by the borehole stress relief method.

After the stress relief is completed, the hollow inclusion strain gauge is still bonded in the central hole. By applying confining pressure to the core of the sleeve hole, the strain value caused by confining pressure in the measurement process of the hollow inclusion strain gauge is corrected. From the measured confining pressure-strain curve, the elastic modulus and Poisson's ratio of the rock can be calculated according to the thick wall tube theory [3, 21].

The elastic modulus and Poisson's ratio of surrounding rock are calculated by using the hollow inclusion strain obtained in the second loading-unloading process as the effective data. The elastic modulus, Poisson's ratio, and K coefficient of surrounding rock at each measuring point are calculated according to formulas (5), (7), and (8). The calculation results are shown in Table 2.

$$E = K_1\left(\frac{P_0}{\varepsilon_\theta}\right)\frac{R^2}{R^2 - r^2},$$
$$\nu = \frac{\varepsilon_z}{\varepsilon_\theta}. \tag{5}$$

Table 2: Elastic modulus and Poisson's ratio at each measuring point.

Point	E (GPa)	υ	K_1	K_2	K_3	K_4
350 m level	36.18	0.141	1.123	1.114	1.015	0.967
350 m level	36.10	0.140	1.124	1.117	1.005	0.997
300 m level	35.010	0.131	1.2641	1.1508	1.0078	0.9885
300 m level	36.14	0.143	1.1557	1.1059	1.0816	0.9776
250 m level	35.14	0.132	1.1616	1.1608	1.1078	0.9971
100 m level	36.22	0.141	1.216	1.108	1.105	0.9885
80 m level	36.18	0.142	1.325	1.210	1.134	0.9842

2.6. The Distribution Law of Crustal Stress. Based on the formula between the strain of the hollow inclusion and the three-dimensional stress component, combined with the measured rock mechanics parameters and the stress relief curve of the sleeve core, utilizing the least square method of curve fitting, the three-dimensional in-situ stress measurement results of each measuring point are calculated as shown in Table 3.

Results show that the distribution of in-situ stress field in the Huanaote mining area has the following rules:

(1) Each measuring point has two principal stresses closing to the horizontal direction, and the inclination angle varies from 2.73° to 34.87°, while a principal stress is close to the vertical direction, with a 20° to the vertical direction.

(2) The direction of the maximum principal stress is close to horizontal, and all the maximum horizontal principal stress directions in seven measuring points follow the NE-SW direction, which is basically consistent with the maximum principal stress direction of the regional tectonic stress field. Six of the maximum principal stresses at seven measuring points have an angle less than or equal to 10° with the horizontal plane, which are almost parallel. For the ratio of the maximum horizontal principal stress ($\sigma_{\mathrm{h.max}}$) to the vertical principal stress (σ_v) in seven measuring points, they are all more than 1.5 times, with the maximum value of 1.89 times, compared with the minimum value of 1.57 times. The average value is 1.76 times (Table 4). Results show that the stress field in the Huanaote mining area is dominated by horizontal tectonic stress, rather than self-weight stress. The size and direction of the maximum horizontal principal stress are the first principle to the stability of tunnel surrounding rock.

(3) There is a positive correlation between the depth and maximum horizontal principal stress ($\sigma_{\mathrm{h.max}}$), minimum horizontal principal stress ($\sigma_{\mathrm{h.min}}$), and vertical principal stress (σ_v), respectively. Moreover, this correlation approximates to a linear growth.

2.7. Crustal Stress Field Model. In order to obtain an accuracy variation of stress field with depth, the linear regression method is used to analyze the stress values in measured points. The regression equations of the maximum horizontal principal stress, the minimum horizontal principal stress, and the vertical principal stress with depth (formulas (6)–(8)) and the regression curve (Figure 4) are obtained. The regression equation represents the ground stress field model of the mining area, which gives the mechanical boundary conditions of the mining area necessary for numerical simulation, physical simulation research and various quantitative mining design calculation, support reinforcement, and ground pressure control.

Regression equation (ground stress field model):

$$\sigma_{h,\max} = 0.046H - 2.46, \tag{6}$$

$$\sigma_{h,\min} = 0.021H - 1.55, \tag{7}$$

$$\sigma_v = 0.025H - 1.07, \tag{8}$$

where $\sigma_{\mathrm{h,max}}$—maximum horizontal principal stress, MPa; $\sigma_{\mathrm{h,min}}$—minimum horizontal principal stress, MPa; σ_v—vertical principal stress, MPa; and H—burial depth, m.

3. Stability Analysis of Tunnel Surrounding Rock

According to the mine in-situ stress field model and the field engineering environment, the numerical model is established, and FLAC3D software is used to simulate and analyze the variation law of stress and displacement of roadway surrounding rock under three working conditions: the excavation direction is parallel, vertical, and intersection to the measured maximum horizontal principal stress direction, respectively [22–31]. It provides a theoretical basis for the optimization of underground mining preparation engineering.

3.1. The Axial Direction of Tunnel Is Consistent with the Direction of Maximum Principal Stress. Based on the real condition of the 350 m-level 55-line tunnel, a numerical analysis model was established to study the variation characteristics of surrounding rock stress and deformation of the tunnel with excavation face advancing. The physical and mechanical parameters of numerical model rock are shown in Table 5.

The calculation model is simplified to a quasi-three-dimensional case, and the distance between the surrounding boundary and the center of the tunnel is about 5 times to the width of the tunnel, which reduces the influence of boundary conditions on the simulation results. The establishment model and grid division are shown in Figure 5. The horizontal direction width of the vertical tunnel axis is 40 m, the

Table 3: Calculation results of principal stress at each measuring point.

No.	Burial depth (m)	Maximum horizontal principal stress			Minimum horizontal principal stress			Vertical principal stress		
		Value (MPa)	Orientation (°)	Dip (°)	Value (MPa)	Orientation (°)	Dip (°)	Value (MPa)	Orientation (°)	Dip (°)
1#	526	20.74	212.58	−2.73	7.28	122.74	3.32	10.97	−136.72	85.69
2#	526	19.63	267.8	8.38	7.36	177.76	0.25	11.67	86.10	81.61
3#	576	19.91	213.89	−9.10	10.33	306.21	14.10	12.66	92.03	73.11
4#	576	23.0	209.98	−11.75	10.6	123.36	15.83	12.7	−95.09	70.08
5#	626	27.22	250.01	9.99	11.30	332.96	−34.87	15.99	173.69	−53.30
6#	776	35.69	241.39	−0.56	14.69	151.56	16.15	18.82	−30.52	73.84
7#	796	37.97	261.75	9.93	18.57	167.01	25.24	21.25	11.51	62.61

Table 4: Ratio of the maximum horizontal principal stress to vertical principal stress.

No.	1	2	3	4	5	6	7
$\sigma_{h.max}/\sigma_v$	1.89	1.68	1.57	1.80	1.70	1.89	1.78

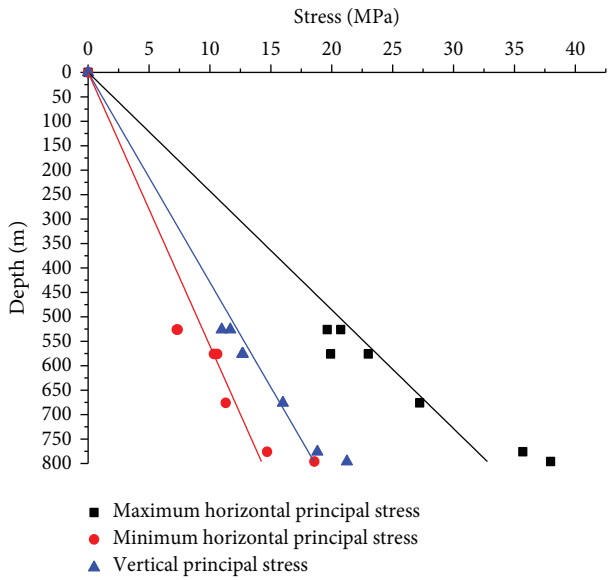

Figure 4: The variation law between $\sigma_{h.max}$, $\sigma_{h.min}$, σ_v, and depth.

Table 5: Geomechanical parameters of rock mass.

Rock mass density ρ (kg·m^{-3})	Elastic model E (GPa)	Friction angle φ (°)	Cohesion c (MPa)	Passion's ratio μ	Tensile strength σ_t (MPa)
2800.0	18.0	36.0	0.7	0.14	0.5

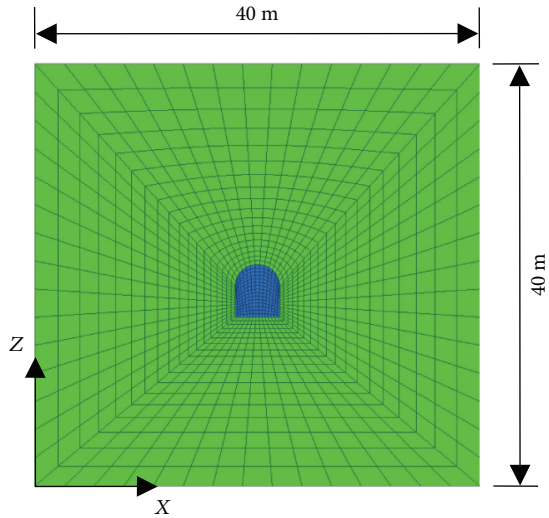

Figure 5: Model and grid partition diagram.

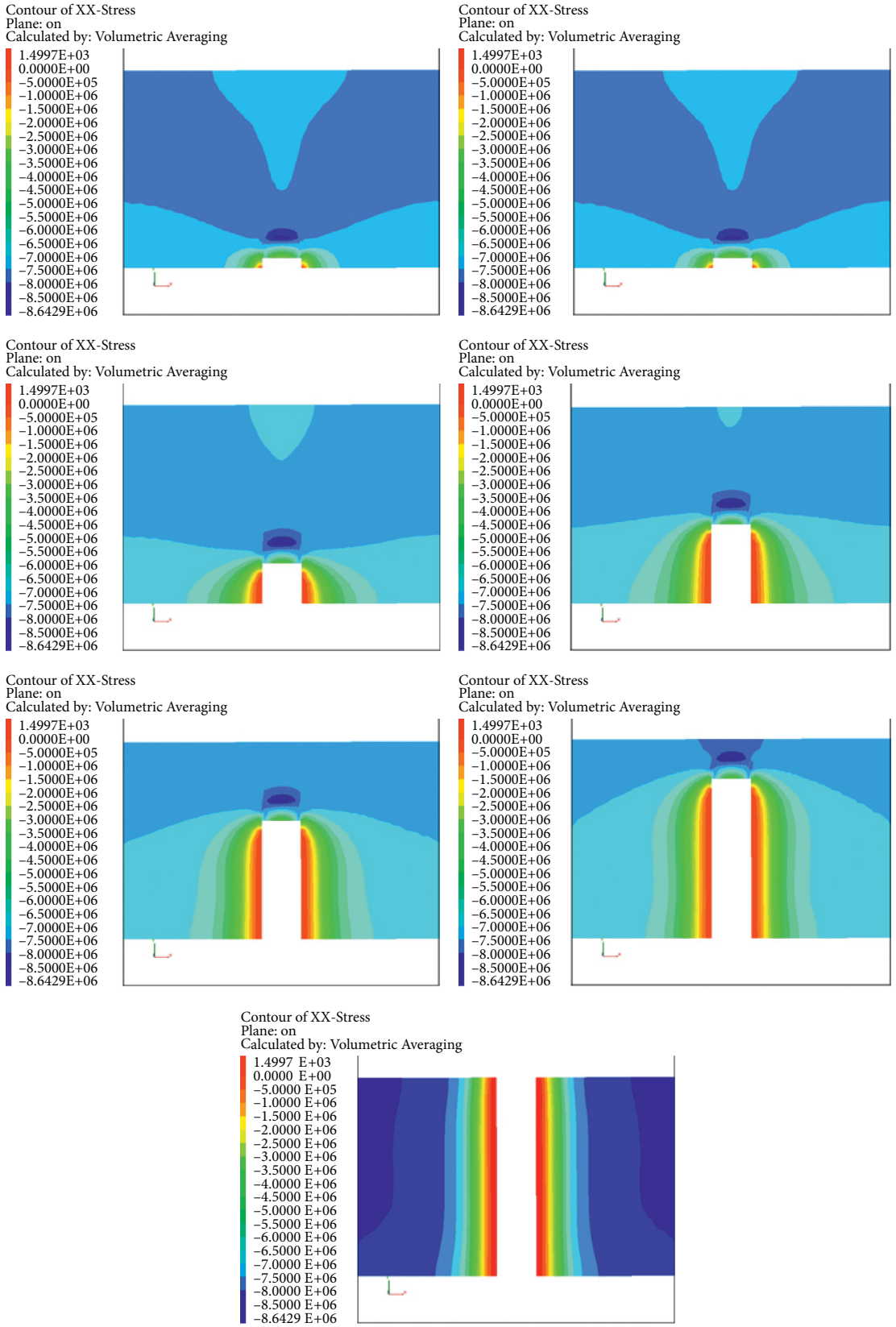

FIGURE 6: Stress development of rock mass in two sides of the tunnel.

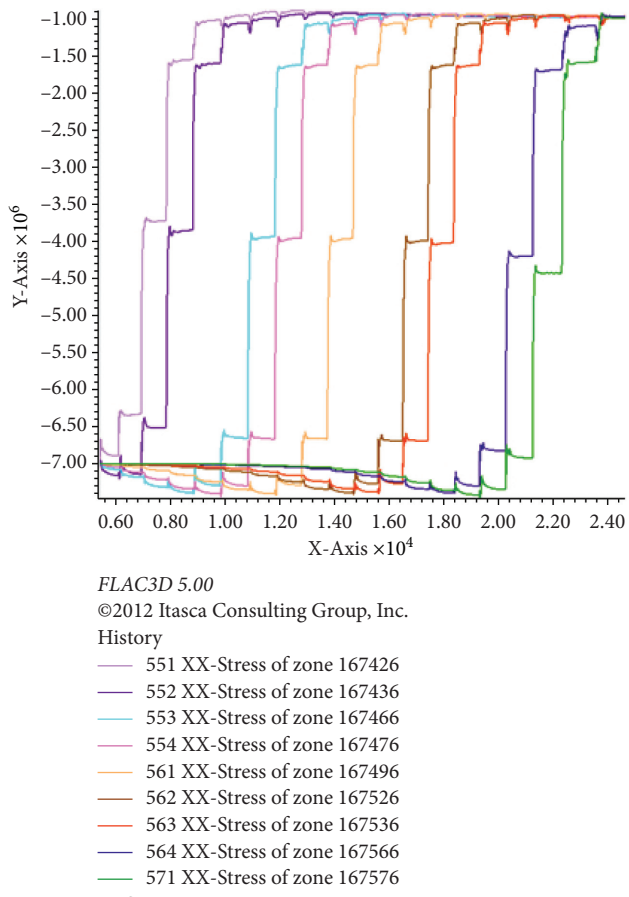

Figure 7: Stress variation curve of side walls.

vertical direction height is 40 m, and the tunnel axis direction length is 20 m. There are 16,400 grid units and 17,661 nodes. The excavation calculation adopts the displacement boundary condition. According to the distribution characteristics of the measured crustal stress field in the mining area, the vertical load applied on the upper boundary is about 10.0 MPa, the maximum horizontal principal stress is 20.0 MPa (y-axis direction), and the minimum horizontal principal stress is 7.0 MPa (x-axis direction).

3.1.1. Disturbance Stress Analysis. The tunnel excavation produces disturbance stress, and the tunnel model sets stress monitoring points at the midpoint of the two sides and the midpoint of the roof every 2 m; at the same time, monitoring points are set at the depth of 1 m to explore the depth of disturbance. With the gradual advancement of the working face, the stress changes of the monitoring points on the two sides of the tunnel are shown in Figure 6.

It can be seen from Figure 6 that the horizontal stress of the 1 m-depth monitoring point after the excavation is about 0.8 MPa, and it reaches the peak between 4.5 and 8.5 MPa in front of excavation face, with a 3.5 m disturbance depth.

The monitoring points are set every 2 meters at the 1 m depth of side walls. The horizontal stress variation curve of two sides during the excavation is shown in Figure 7. It can be seen from the figure that the stress change is large in the range of about 3 m from the excavation face, and the stress of two side walls is reduced by about 7 MPa from the excavation of the tunnel.

Monitoring points are set every 2 m at the 1 m depth inside the tunnel roof. Its vertical stress change during the excavation is shown in Figure 8. It demonstrates that the excavation disturbance has a critical influence on the roof, with a significant stress fluctuation. Moreover, a serious stress variation occurs at 4 m away from the excavation face. The vertical stress of the roof caused by tunnel excavation is reduced to about 8 MPa. Figure 8(b) is the vertical stress variation cloud map of the tunnel roof. It can be seen that the roof experiences compressive stress, which is about 0.3 MPa, and the stress is mostly concentrated in the bottom corner and arch shoulder of the tunnel. Meanwhile, the maximum stress inside the side wall reaches 16.5~17.5 MPa.

3.1.2. Analysis of Tunnel Convergence Displacement. The total length of the tunnel model is 20 m, and the monitoring point is set at 10 m. The horizontal convergence curve of the two side walls during the excavation is shown in Figure 9. It indicates that the horizontal displacement of the wall reaches 26 mm after the excavation. When the monitoring point is not reached, the displacement increases slowly. After the

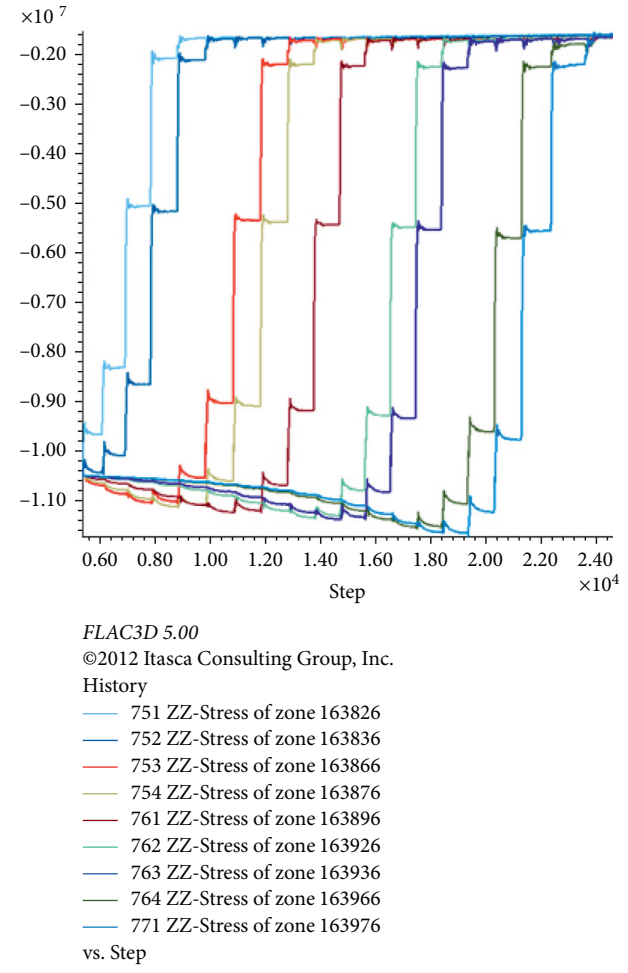

(a)

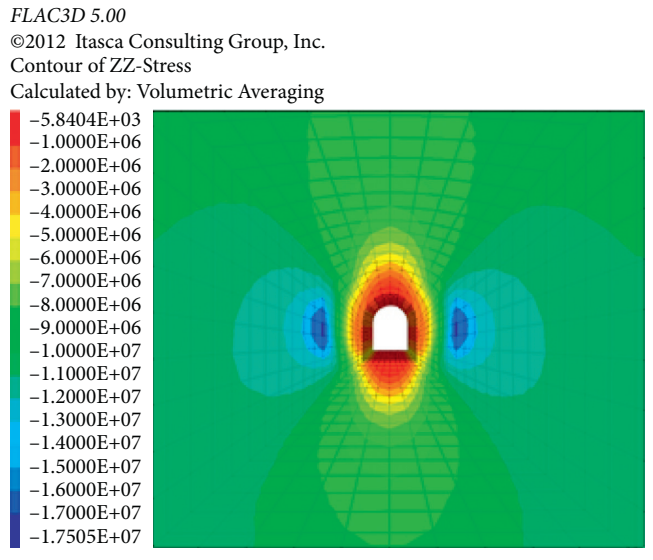

(b)

Figure 8: Variation of vertical stress of tunnel roof: (a) stress variation curve of tunnel roof and (b) stress variation cloud map of tunnel roof.

excavation happened at the monitoring point, the wall displacement increases significantly (12 mm), and the horizontal displacement change of the excavation disturbance in the depth range of 3 m is within 20 mm. With the advancing of working face, the displacement gradually stabilized. Figure 9(c) is the monitoring point in the middle of the side

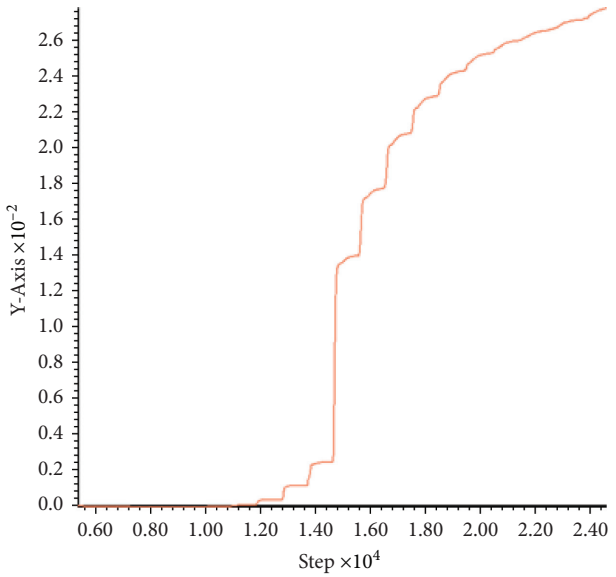

(a)

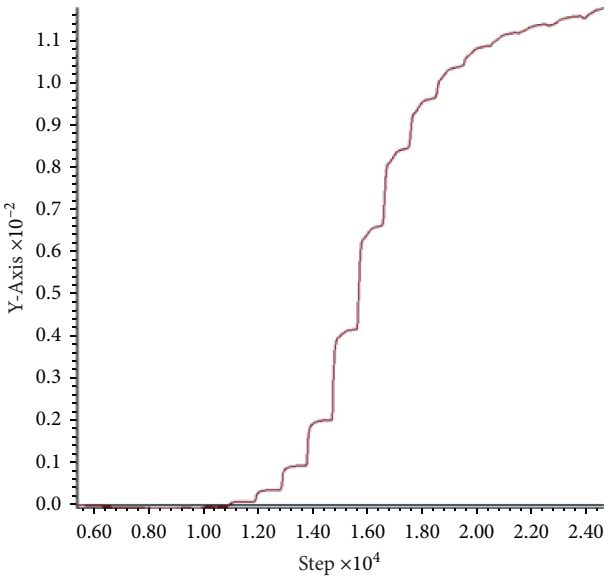

(b)

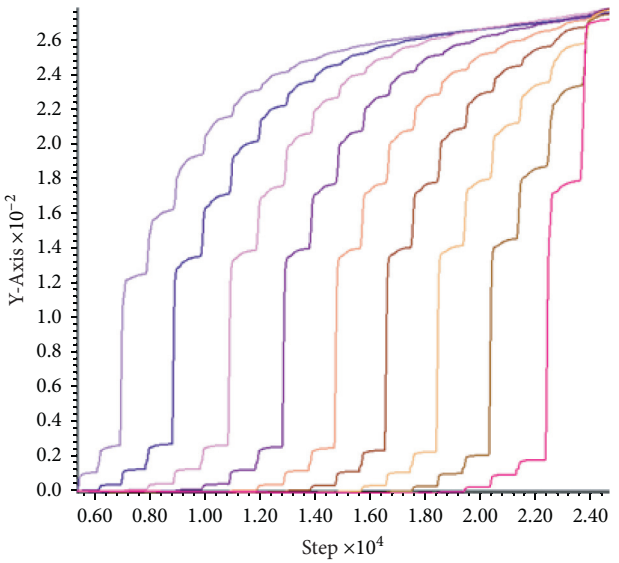

(c)

Figure 9: Horizontal displacement curve of tunnel sides: (a) displacement variation curve of the left side wall, (b) displacement variation curve of 1 m depth in the left side wall, and (c) displacement variation curve of the monitoring point.

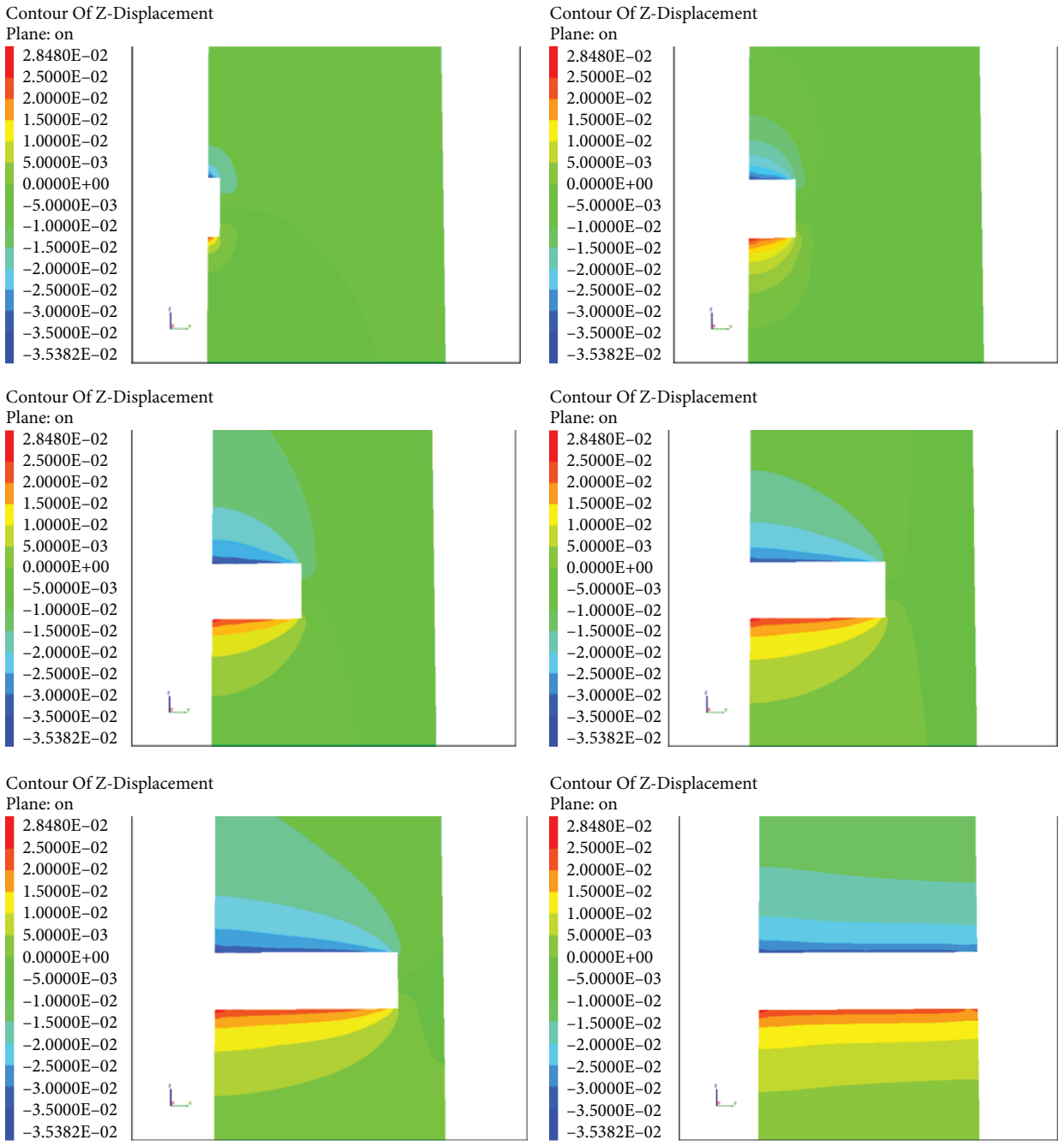

Figure 10: Development of vertical displacement of rock mass in the middle of tunnel roof.

wall set every 2 m in the excavation face of the tunnel. It demonstrates that the excavation of the tunnel has a great displacement influence on two side walls. The displacement change within 4 m from the excavation face is large, and the displacement outside 5 m is basically stable. Therefore, the excavation face of the tunnel is within 4~5 m, which indicates a major region for supporting.

Tunnels adopt the full-face excavation method. With the excavation, the vertical displacement development of rock mass in the middle of tunnel roof is shown in Figure 10.

The variation of roof vertical displacement affected by excavation is shown in Figure 11. Monitoring points are set every 2 m on the roof of the tunnel excavation face. After the excavation, its displacement reaches about 30 mm, compared with 24 mm at depth of 1 m. When the monitoring point is not reached, the displacement increases slowly. After the excavation occurs at the monitoring point, the displacement of the roof increases significantly (9 mm), while the displacement of the wall at 1 m depth is 4 mm. It has the most significant changes in the 2 m range of excavation.

3.2. Vertical Working Condition of Tunnel Axial Direction and Maximum Principal Stress Direction. Based on the

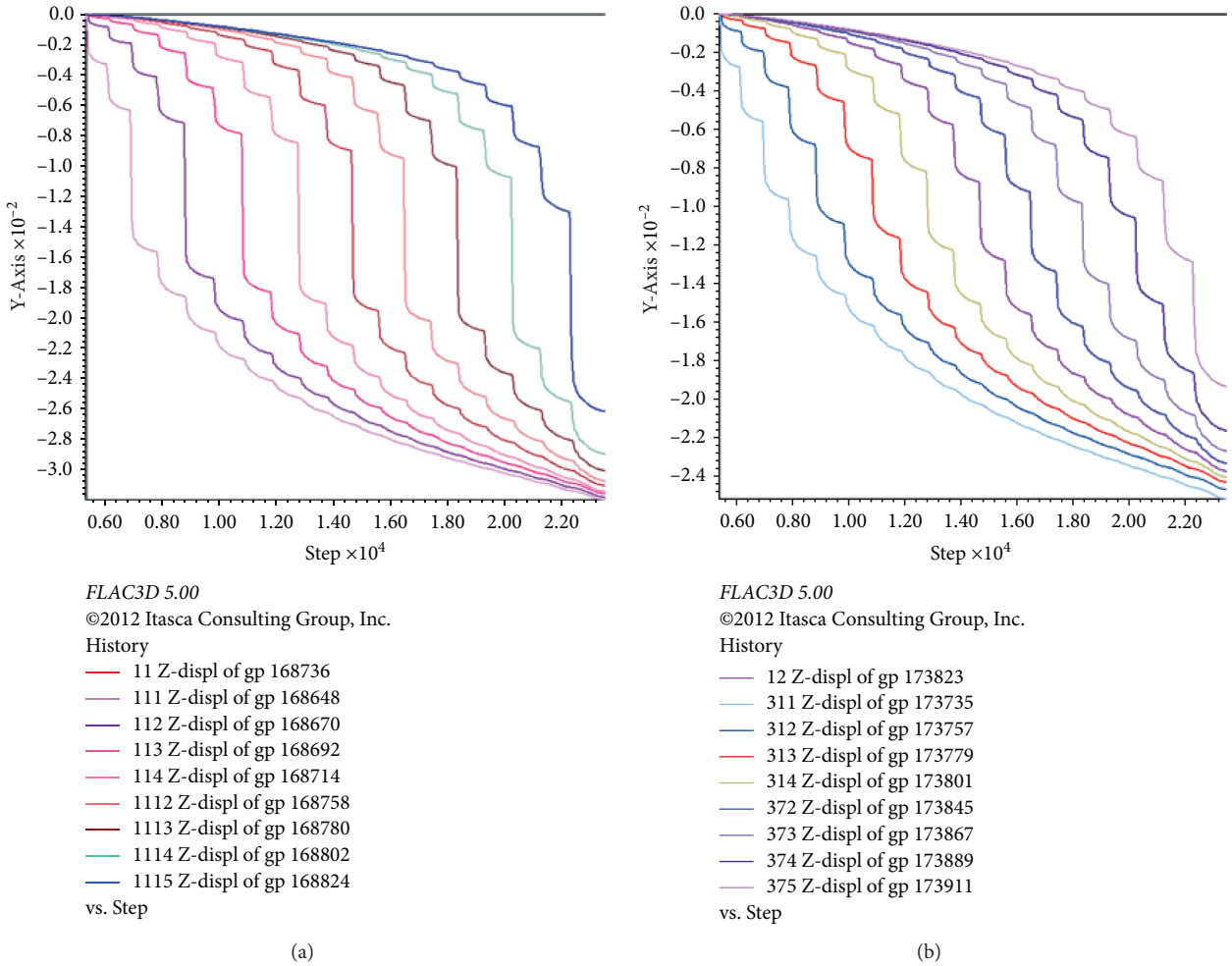

Figure 11: Vertical displacement curve of tunnel roof: (a) displacement variation curve of tunnel roof and (b) displacement variation curve of tunnel roof at 1 m depth.

engineering background of the 350 m horizontal 55-line tunnel, a numerical model was established to study the variation characteristics of stress and deformation of surrounding rock when the axial direction of tunnel is perpendicular to the direction of maximum principal stress.

3.2.1. Mining Stress Analysis. The tunnel model sets stress monitoring points every 2 m at the midpoint of the two side walls and the midpoint of the roof. With the gradual advancement of the working face, the horizontal stress changes of the monitoring points of the two sides of the tunnel are shown in Figure 12.

It can be seen from Figure 12 that the horizontal stress of the two side walls after the excavation is stable within 2 MPa; and the stress disturbance at 4 m away from the excavation surface began to stabilize. The stress range of the two side walls is about 5 m, and the stress change value is within 12 MPa.

Monitoring points are set at 1 m depth of tunnel roof with 2 m space, and the change of vertical stress of roof during excavation is shown in Figure 13. It can be seen from Figure 13(a) is that the stress fluctuation of roof is relatively obvious, and the stress changes greatly within the range of about 4 m from the excavation face. The vertical stress of the roof is reduced by about 7 MPa due to tunnel excavation and finally stabilized at about 3 MPa. Figure 13(b) shows the cloud map of the stress variation of tunnel roof, which the roof stress is small, within 0.6 MPa; the stress is mostly concentrated in the bottom corner of the tunnel and the arch shoulder, and the maximum stress in the side wall is as high as 13.4 MPa. At the depth of 2 m, the maximum principal stress is up to 35 MPa.

3.2.2. Analysis of Tunnel Convergence Displacement. The horizontal convergence curve of the two side walls during the excavation is shown in Figure 14. After the excavation, the horizontal displacement reaches 45 mm; when the monitoring point is not reached, the displacement increases slowly. When the excavation reaches the monitoring point, the displacement increases significantly to 12 mm. The displacement of the monitoring point within 4 m depth from the excavation face changes significantly.

The variation of the vertical displacement at roof influenced by excavation is shown in Figure 15. After the

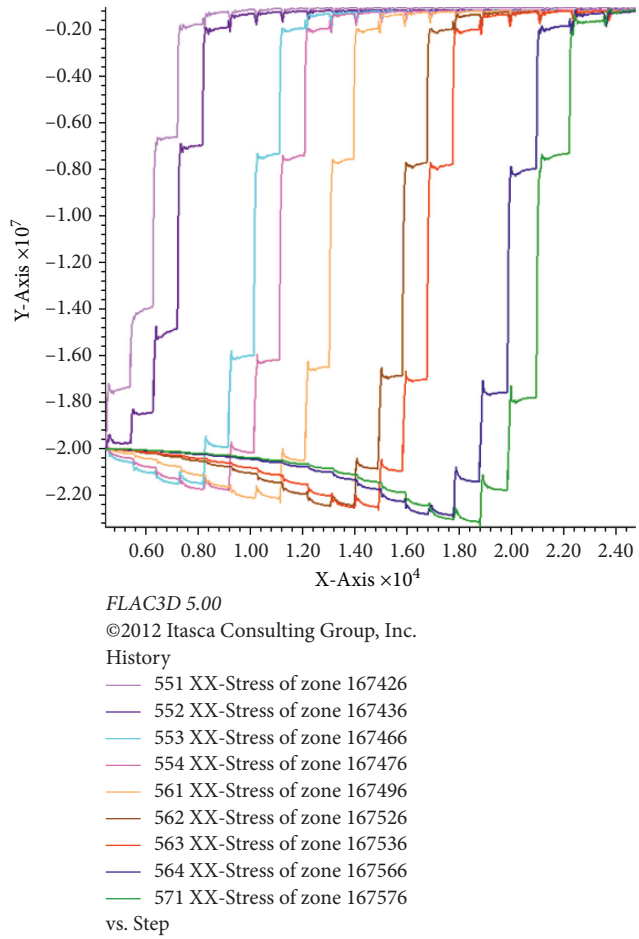

Figure 12: Horizontal stress variation curve of two sides of tunnel.

excavation, the vertical displacement of the roof is about 34 mm, and the displacement at the depth of 1 m of the roof is 11 mm. When the monitoring point is not reached, the displacement increases slowly. When the excavation reaches the monitoring point, the displacement of the roof increases significantly to 15 mm, and the displacement of the wall at 1 m depth is less than 4 mm; the displacement changes in the 3 m range of excavation are obvious.

3.3. The Actual Heading Direction of Tunnel Intersects with the Direction of Maximum Principal Stress. Taking the contact tunnel of 100 m horizontal hoist room as the engineering background, the FLAC3D numerical analysis model is established to study the surrounding rock stress and deformation characteristics when the actual tunneling direction intersects with the maximum principal stress direction. The chamber mouth of the winch room is the 6# in-situ stress measuring point. The angle between the tunneling direction and the direction of the maximum principal stress is 52°. The establishment of the model and the meshing are shown in Figure 16. The x-axis direction is the minimum principal stress direction, with the length of 60 m. The y-axis direction is the maximum principal stress direction, and the width is 20 m. The height of the z-axis direction is 40 m. The length of the tunnel axis direction is 20 m. The total number of meshing units is 122,930, combined with 81,045 nodes.

3.3.1. Mining Stress Analysis. The tunnel adopts the full-section excavation method, and the maximum principal stress distribution variation rule for each 2 m excavation is shown in Figure 17. The stress concentration area after the excavation is mainly located at 2 m ahead of the excavation section, about 24 MPa, and the stress concentration is up to 27 MPa at about 2 m inside the rock mass of the two side walls. Affected by the model boundary, the stress concentration position at the early stage of excavation is distributed in the right side wall, and at the late stage of excavation, it is distributed in the left side wall. During the excavation process, the stress on the right side of the excavation face is greater than that on the left side, and the difference between the two sides is within 0.5 MPa.

The principal stress variation curve and the principal stress change cloud diagram of the tunnel model roof monitoring point are shown in Figure 18. In Figure 18(a), the initial stress value of excavation is about 18 MPa. With the gradual excavation of the tunnel, the stress redistributes and concentrates in front of the excavation section, which

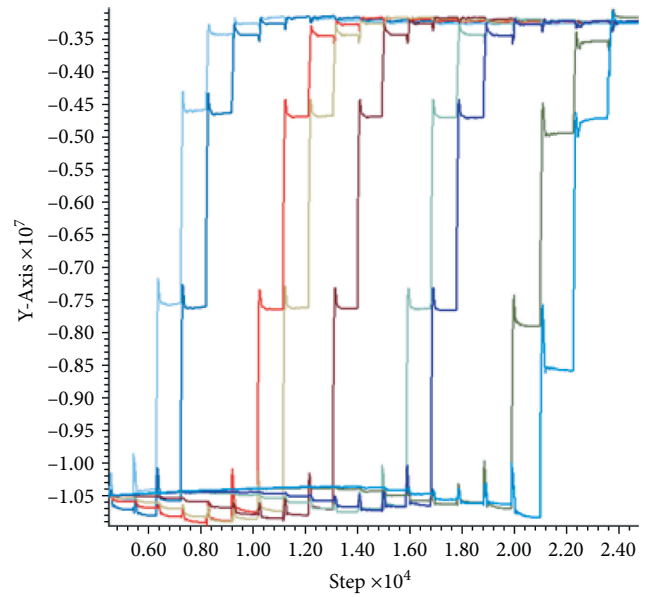

(a)

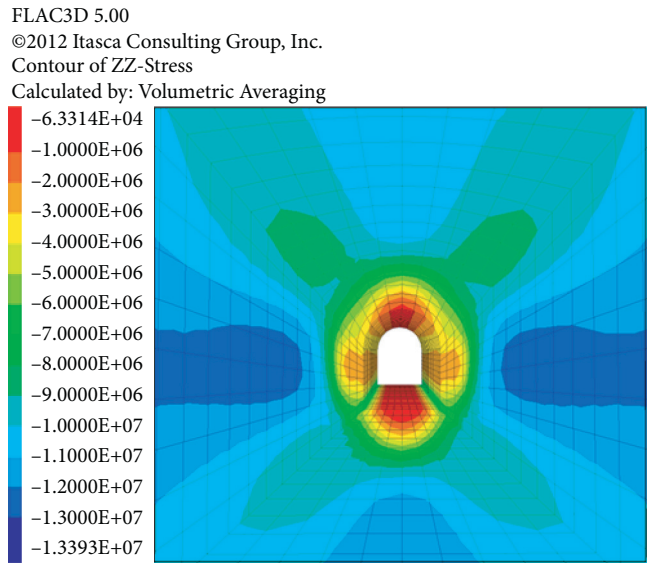

(b)

Figure 13: Vertical stress variation of tunnel roof: (a) Stress variation curve of tunnel roof, (b) Stress variation cloud map of tunnel roof.

the maximum value is 24.59 MPa, while the stress value of the roof monitoring point is 21 MPa. When the excavation reaches the monitoring point, the stress decreases rapidly and finally stabilizes at about 6 MPa, and the stress variation is 15 MPa. In Figure 18(b), the change trend of the minimum principal stress is basically the same as that of the maximum

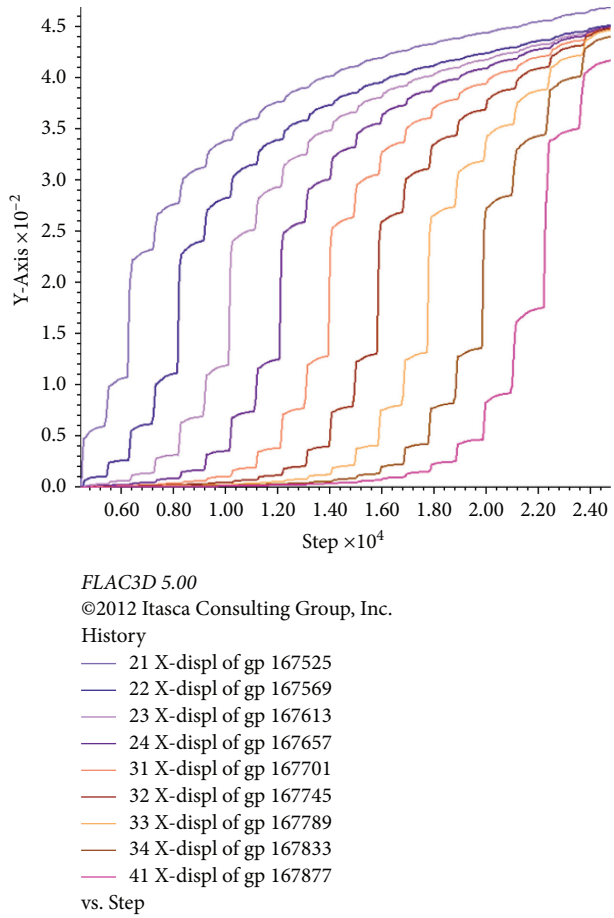

Figure 14: Horizontal displacement curve of the two sides of tunnel.

principal stress, and the stress difference is 3 MPa. The tensile stress appears in the middle of the roof and floor, and the stress value is about 0.23 MPa.

3.3.2. Analysis of Tunnel Convergence Displacement. The length of y axis in the model is 20 m, and the monitoring point is set at 10 m. The convergence curve of the roof direction during the excavation is shown in Figure 19. After the excavation, the maximum displacement of the roof is 32 mm (1# curve), the vertical displacement of the tunnel roof at 1 m depth is 28 mm (3# curve), and the maximum displacement of the tunnel floor is 8 mm (2# curve). According to the displacement curve of the monitoring point, the excavation of the tunnel not only leads to the deformation of the excavated tunnel but also produces the displacement change in the unexcavated area. When the monitoring point is not reached, the displacement slowly increases to 6 mm, which is the displacement change caused by stress release. When it reaches the monitoring point, the displacement of the monitoring point increases significantly to 10 mm; with the continuous advancement of the working face, the displacement growth rate gradually decreases. In order to effectively control the continuous deformation of surrounding rock caused by tunnel section excavation, support measures should be taken in time.

3.4. Stability Analysis of Surrounding Rock under Different Working Conditions. According to the tunnel excavation direction and the measured direction of the maximum horizontal principal stress under parallel, vertical, and intersecting conditions, simulation results of surrounding rock stress and displacement are shown in Table 6:

(1) When the tunneling direction is parallel to the measured maximum horizontal principal stress direction, the displacement of two sides of the tunnel, the displacement of roof, and the displacement at the depth of 1 m of roof are the least, indicating that the stability of the tunnel is better when the tunneling direction of the tunnel is parallel to the measured maximum horizontal principal stress direction.

(2) When the tunnel excavation direction is perpendicular to the measured maximum horizontal principal stress direction, the displacement of the two side walls, roof, the displacement variation of the roof at 1 m depth, and the maximum stress of the roof are all greater than the other two conditions, indicating that the stability and safety of the tunnel are worst when the tunnel excavation direction is perpendicular to the measured maximum horizontal principal stress direction.

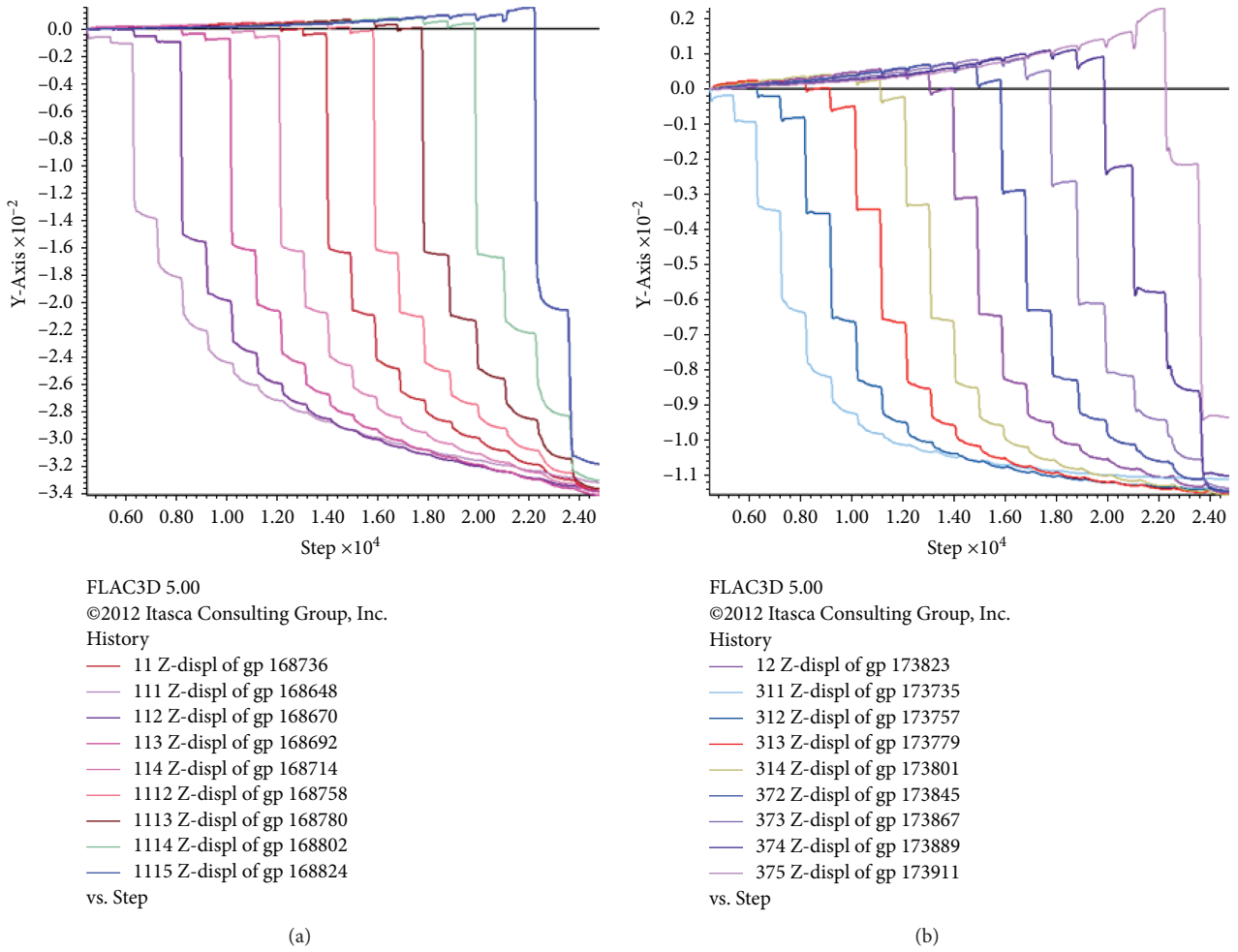

Figure 15: Vertical displacement curve of tunnel roof: (a) displacement curve of tunnel roof and (b) displacement curve of tunnel roof at 1 m depth.

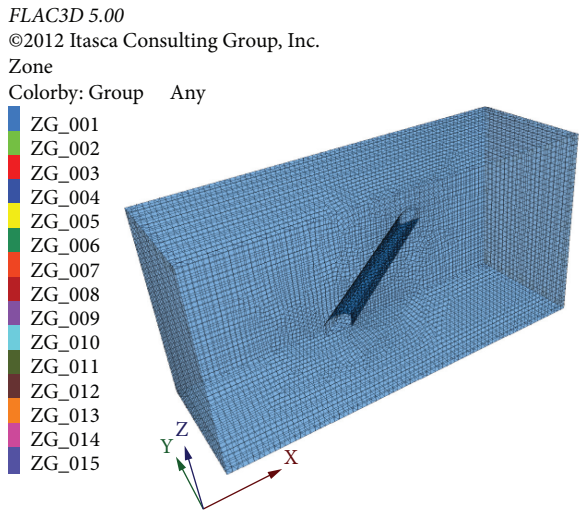

Figure 16: Model and grid partition diagram.

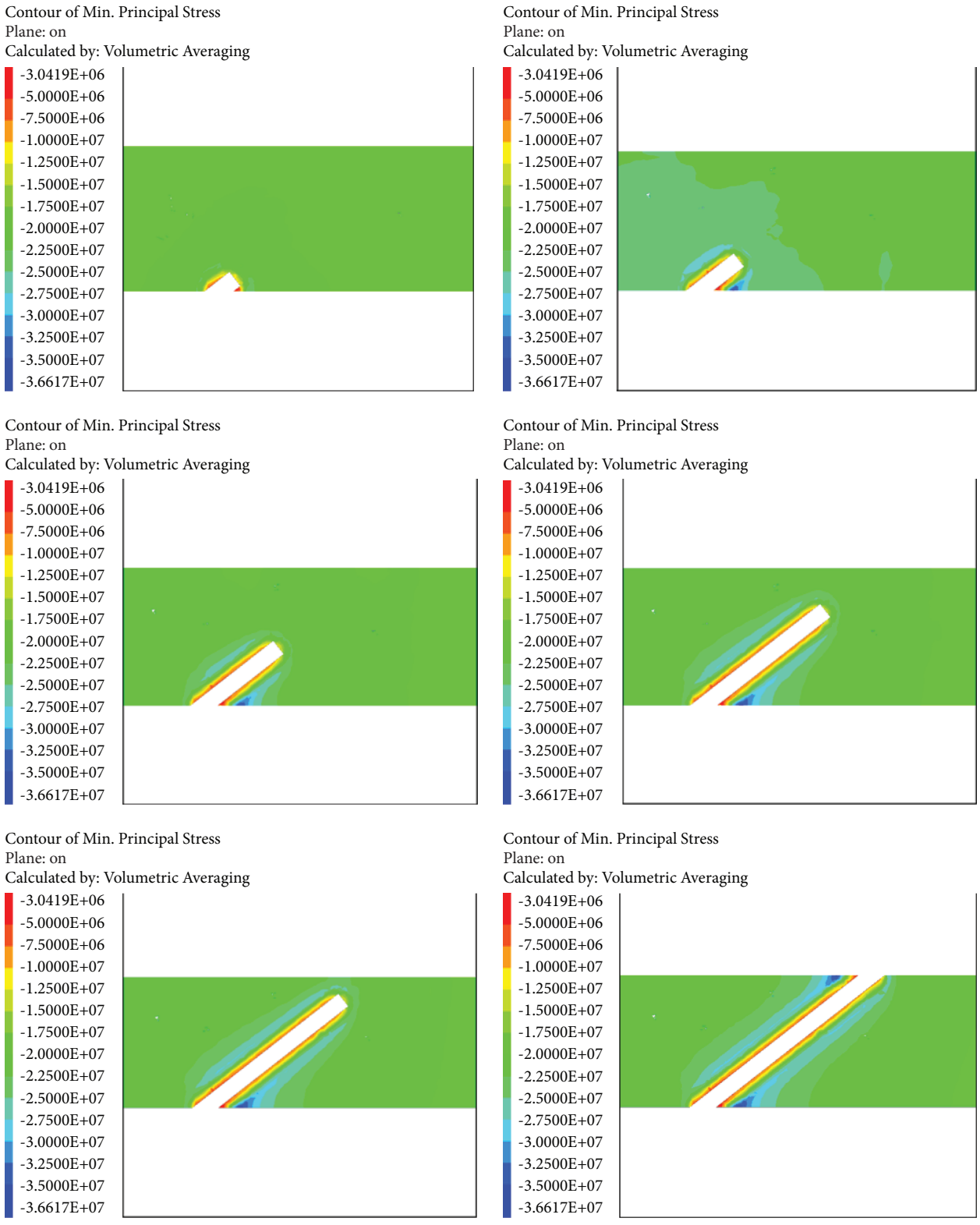

Figure 17: The maximum principal stress distribution cloud chart of tunnel.

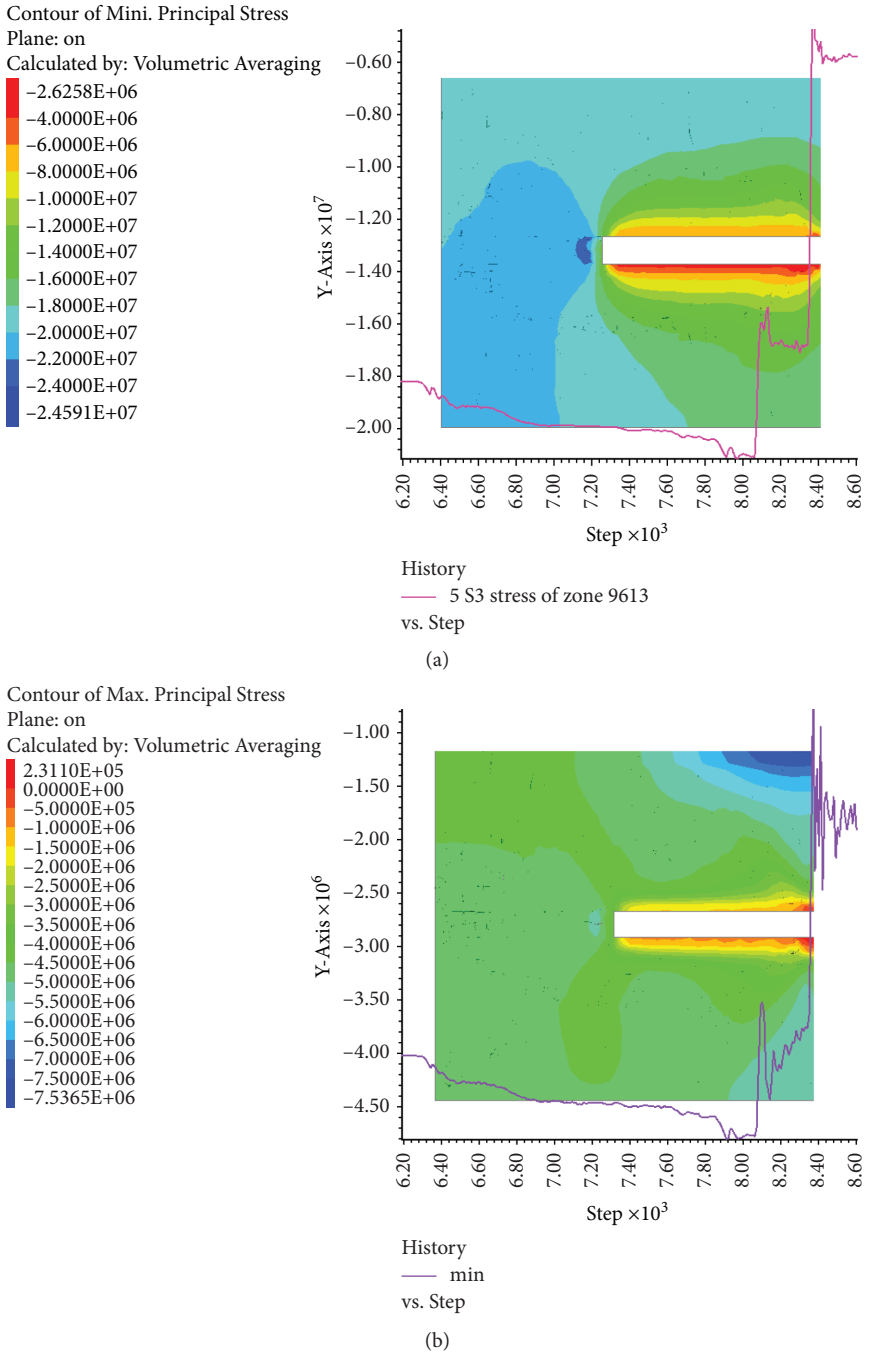

Figure 18: Variation of tunnel roof stress: (a) maximum principal stress and (b) minimum principal stress.

(3) When the actual excavation direction intersects with the measured maximum horizontal principal stress direction, the maximum stress of the two side walls reaches 27 MPa, which is far greater than the other two conditions. In the actual construction process, the support and maintenance of the two sides of the

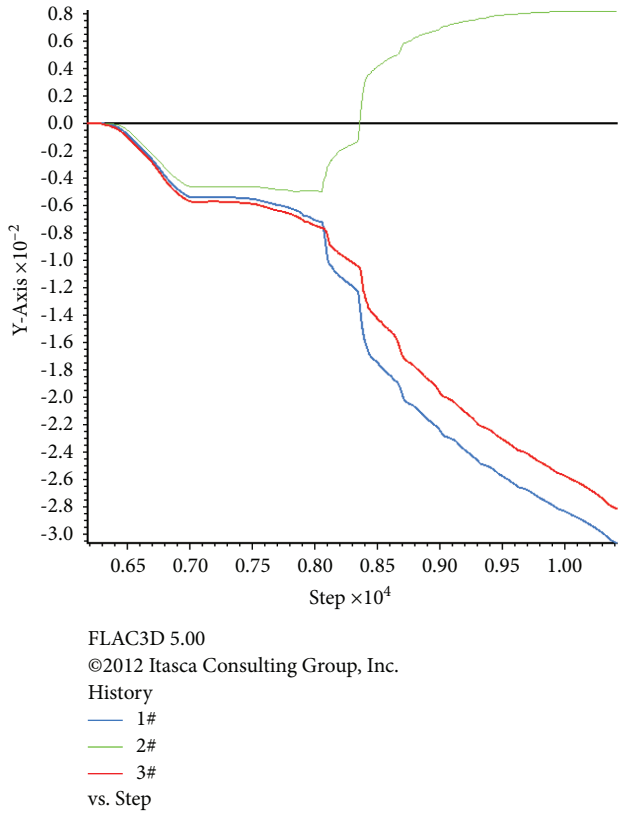

Figure 19: Vertical displacement curve of tunnel roof.

Table 6: Mining stress and deformation of surrounding rock under different working conditions.

	Horizontal displacement of two side walls (mm)	Roof displacement (mm)	Roof displacement at 1 m depth (mm)	Maximum stress of two side walls (MPa)	Maximum stress of roof (MPa)
Conditions 1	26	30	24	17	30
Conditions 2	45	34	31	13.4	35
Conditions 3	35	32	28	27	24.5

*Conditions 1: the axial direction of tunnel is consistent with the direction of maximum principal stress; Conditions 2: axial direction of tunnel perpendicular to direction of maximum principal stress; Conditions 3: the actual heading direction of tunnel intersects with the direction of maximum principal stress.

tunnel should be strengthened to ensure the stability of the tunnel and the safety of personnel and equipment.

4. Conclusion

The in-situ stress field model of the Huanaote mining area is constructed by "double temperature compensation and considering the nonlinear measurement technology of in-situ stress relief of rock mass." On this basis, a numerical model is established according to the field engineering environment to simulate and analyze the variation law of stress and displacement of tunnel surrounding rock under three working conditions: parallel, vertical, and intersecting between the direction of tunnel excavation and the direction of measured maximum horizontal principal stress. Following conclusions are obtained:

(1) The direction of the maximum horizontal principal stress changes in the range of 212~267°, its value changes in the range of 20~37 MPa, and the lateral pressure coefficient of each measuring point changes in the range of 2.05~2.85. The horizontal tectonic stress in the mining area is large, and the horizontal tectonic stress is dominant. The size and direction of the maximum horizontal principal stress are the key to the stability of tunnel surrounding rock.

(2) The vertical principal stress is the intermediate principal stress, whose dip angle changes in the range of 53.30~ 85.69°, and the value changes in the range of 10.97~21.25 MPa, which is close to the self-weight stress of overlying rock mass.

(3) When the tunneling direction is parallel to the direction of the measured maximum horizontal

principal stress, the displacement of the two side walls, roof, and 1 m depth of the roof are the least, indicating that the stability of the tunnel is better when the tunneling direction of the tunnel is parallel to the direction of the measured maximum horizontal principal stress.

The mine is a newly built mine. During the design and construction of subsequent development and mining preparation engineering, it is recommended to excavate the roadway along the direction of the maximum horizontal principal stress to reduce the impact of original rock stress on roadway stability.

(4) When the actual heading direction of the tunnel intersects with the measured maximum horizontal principal stress direction, the maximum stress of the two side walls reaches 27 MPa, which is far greater than the parallel and vertical working conditions of the heading direction of the tunnel and the measured maximum horizontal principal stress direction. In the actual construction process, the support and maintenance of the two side walls should be strengthened to ensure the stability of the tunnel and the safety of personnel and equipment.

Data Availability

The data used to support the findings of this study are available from the corresponding author upon request.

Conflicts of Interest

The authors declare no conflicts of interest

References

[1] Z. F. Song, Y. J. Sun, and X. Li, "Research on In-situ stress measurement and inversion and its influence on tunnel layout in coal mine with thick coal seam and large mining height," *Geotechnical & Geological Engineering*, vol. 36, no. 3, pp. 1907–1917, 2018.

[2] P. Li, M.-f. Cai, Q.-f. Guo, and S.-j. Miao, "Characteristics and implications of stress state in a gold mine in Ludong area, China," *International Journal of Minerals, Metallurgy, and Materials*, vol. 25, no. 12, pp. 1363–1372, 2018.

[3] Y. Liu, J. Yin, and Y. Liu, *Geostress Measurement Method and Engineering Application*, Hubei Science and Technology Press, Wuhan, 2014.

[4] M. Cai, L. Qiao, and H. Li, *Principle and Technology of Ground Stress Measurement*, Science Press, Beijing, China, 1995.

[5] C. Zhang, M. Wu, and Q. Chen, "Review of in-situ stress measurement methods," *Journal of Henan Polytechnic University (Natural Science)*, vol. 31, no. 3, pp. 305–310, 2012.

[6] L. Deng, Y. Yang, and C. Zheng, "In-situ stress measurement analysis and its influence on gas drainage in xinji No.2 coal mine," *Coal Technology*, vol. 40, no. 10, pp. 120–124, 2021.

[7] Z. Yan, Q. Guo, and D. Ma, "In-situ stress measurement and its application in gongchangling underground mine," *Metal Mine*, vol. 10, no. 12, pp. 149–154, 2017.

[8] M. Cai, Q. Guo, and Y. Li, "In situ stress measurement and its application in the 10th Mine of Pingdingshan Coal Group," *Journal of University of Science and Technology Beijing*, vol. 35, no. 11, pp. 1399–1406, 2013.

[9] O. Stephansson and A. Zang, "ISRM suggested methods for rock stress estimation-Part 5: establishing a model for the in situ stress at a given site," *Rock Mechanics and Rock Engineering*, vol. 45, no. 6, pp. 955–969, 2012.

[10] H. Qi and G. Zhou, "Study and application of hollow inclusion stress measuring technique," *Safety In Coal Mines*, vol. 47, no. 12, pp. 141–144, 2016.

[11] H. Gao, S. Yang, and X. Liu, "Hollow inclusion in-situ stress test method and engineering application," *Coal Engineering*, vol. 47, no. 4, pp. 83–85, 2015.

[12] Y. Li, L. Qiao, and Q. Sun, "Analyses of some factors affecting precision in in-situ stress measurement with method of csiro cells," *Chinese Journal of Rock Mechanics and Engineering*, vol. 25, no. 10, pp. 2140–2144, 2006.

[13] D. Wang, Y. Li, and Q. Liu, "Technical research on the method of CSIRO cells to measure ground stress," *Mine Engineering*, vol. 7, no. 2, pp. 144–150, 2019.

[14] Y. Li, Z. Wang, and L. Qiao, "Development of CSIRO cell with the compromised application of instantaneous data-logging,no-power data-connection and twin temperature compensation techniques," *Chinese Journal of Rock Mechanics and Engineering*, vol. 36, no. 6, pp. 1479–2148, 2017.

[15] Y. Li, Z. Liu, L. Qiao, S. Fu, and S. Wu, "Stress monitoring techniques based on the twin temperature compensation method of digital csiro," *Advanced Engineering Sciences*, vol. 50, no. 5, pp. 18–26, 2018.

[16] S. Zhifei, S. Yun-Jiang, and L. Xuan, "Research on in situ stress measurement and inversion, and its influence on roadway layout in coal mine with thick coal seam and large mining height," *Geotechnical & Geological Engineering*, vol. 36, no. 3, pp. 1907–1917, 2018.

[17] J. X. Ren, W. J. Zhang, K. Zhang, and S. Jing, "Characteristics of mining stress in deep-buried and extremely thick coal seam and its influence on adjacent roadways," *Coal Engineering*, vol. 51, no. 1, pp. 77–81, 2019.

[18] Y. Xue, J. Liu, P. G. Ranjith, Z. Zhang, F. Gao, and S. Wang, "Experimental investigation on the nonlinear characteristics of energy evolution and failure characteristics of coal under different gas pressures," *Bulletin of Engineering Geology and the Environment*, vol. 81, no. 1, 2022.

[19] W. Ma, J. Chai, D. Cai et al., "Research on in Situ Stress Distribution of the Railway Tunnels in Southwest China Based on the Complete Temperature Compensation Technology," *Shock and Vibration*, vol. 2021, Article ID 7170850, 14 pages, 2021.

[20] L. Sun, *Numerical Simulation of the Effect on Accuracy of Stress Measurement in the Progress of Drilling*, Institute of Geophysics, China Earthquake Administration, Beijing, China, 2009.

[21] G. Worotnicki and R. Walton, "Triaxial "hollow inclusion" gauges for determination of rock stresses in situ," *International Journal of Rock Mechanics and Mining Sciences & Geomechanics Abstracts*, vol. 13, no. 10, pp. 124-125, 1976.

[22] L. W. Zhao, T. P. Liu, L. I. Ke-Mian, L. I. Jun-Fu, and W. D. Zhang, "Anslyses of the confining pressure formulation about geostress measurement with method of csird cells," *Water Conservancy Science & Technology & Economy*, vol. 18, no. 10, pp. 42–44, 2012.

[23] F. Gao, X. Gao, and H. Kang, "FLAC analysis of mechanical response of surrounding rock mass in deep tunnel," *Chinese Journal of Underground Space and Engineering*, vol. 4, pp. 680–685, 2009.

[24] Y. Xue, J. Liu, X. Liang, S. Wang, and Z. Ma, "Ecological risk assessment of soil and water loss by thermal enhanced methane recovery: numerical study using two-phase flow simulation," *Journal of Cleaner Production*, vol. 334, Article ID 130183, 2022.

[25] H. Xie, H. Zhou, and J. Liu, "Mining-induced mechanical behavior in coal seams under different mining layouts," *Journal of China Society*, vol. 36, no. 7, pp. 1067–1074, 2011.

[26] H. Xiao, X. He, F. Tao, E. Wang, and C. Zhu, "Research on coupling laws between eme and stress fields during deformation and fracture of mine tunnel excavation by flac3d simulation," *Chinese Journal of Rock Mechanics and Engineering*, vol. 24, no. 5, pp. 812–817, 2005.

[27] J. Liu, C. Qingfa, and T. Yin, "Velocity-stress boundary method to generate initial stress field of deep engineering in mine based on FLAC3D," *Metal Mine*, vol. 501, no. 3, pp. 26–31, 2018.

[28] Z. Guo, G. Zhao, and P. Kang, "Study on wallrock deformation by FLAC3D simulation of excavation and support in deep high-stress soft-rock roadway," *Mining and Metallurgical Engineering*, vol. 32, no. 2, pp. 18–22, 2012.

[29] Z. Liu, "Analysis of FLAC3D for the disturbance of deep shaft roadway group," *Coal and Chemical Industry*, vol. 44, no. 4, pp. 21–24, 2021.

[30] D. Yu, Z. Yang, Y. Guo, Y. Yonggang, and W. Bo, "Inversion method of initial geostress in coal mine field based onFLAC3D transverse isotropic model," *Journal of China Coal Society*, vol. 45, no. 10, p. 3427-3434, 2020.

[31] W. Li, "Research on deformation law of surrounding rock under rockburst based on FLAC3D," *China Energy and Environmental Protection*, vol. 41, no. 8, pp. 169–172, 2019.

Hindawi
Advances in Civil Engineering
Volume 2022, Article ID 2706897, 9 pages
https://doi.org/10.1155/2022/2706897

Research Article

Study on Backfill Acoustic Emission Characteristics and Source Location under Uniaxial Compressive

Caixing Shi,[1,2] Yicheng Wu,[3] Lijie Guo ,[1,2] Yue Zhao ,[1,2] and Wenyuan Xu[1,2]

[1]*BGRIMM Technology Group, Beijing 102628, China*
[2]*National Centre for International Research on Green Metal Mining, Beijing 102628, China*
[3]*Wu Shan Copper Mine of Jiangxi Copper Corporation, Ruichang 332204, China*

Correspondence should be addressed to Lijie Guo; guolijie@bgrimm.com

Received 10 January 2022; Accepted 1 February 2022; Published 21 February 2022

Academic Editor: Dawei Yin

This study investigates the acoustic emission (AE) characteristic of cemented tailings backfill (CTB) under uniaxial compressive loading. A classified tailings material source from Wushan Copper Mine was used to prepare cylindrical CTB samples. This study used an SLB10 loading machine for the uniaxial compressive test. A PCI-2 acoustic wave system was attached to the CTB specimen to measure the acoustic emission during loading. Overall, the backfill specimen's uniaxial compressive strength (UCS) is 3.58 MPa. The failure modes of the CTB sample could be divided into five stages, including the pore microfracture compacting stage (stage-a), linear elastic deformation stage (stage-b), yield deformation stage (stage-c), failure stage (stage-d), and residual stage (stage-e). At each stage, the AE characteristic parameters such as the hits per second (HPS), the cumulative number of impacts, energy rate, and total energy vary a lot, which indicates the AE parameter reflects the internal failure evolution of the CTB sample. In stage-a, no apparent AE behavior was measured. In Stage-b, there is no evident macroscopic change in the specimen, while the AE parameters steadily and continuously increase. During stage-c, the number of AE impacts grows sharply, the energy rate increases significantly, and changes suddenly. The cumulative number of AE impacts is 31.3% in stage-d, and the cumulative energy rate is 49.4%, which is the most active stage of acoustic emission activities. The specimen has prominent crack propagation and bifurcation phenomena. In stage-d, the CTB sample was destroyed entirely, and the characteristic parameters of acoustic emission were significantly reduced. Finally, multiple regression analysis methods are introduced into the time difference positioning method to locate the AE source. The positioning results show that the technique can better invert the close relationship between the damage and destruction of the CTB and the generation and penetration of the internal cracks and describe it to a certain extent. The failure surface of the filler specimen has an excellent guiding value for the analysis of the interior failure characteristics of the sample.

1. Introduction

The filling mining method has developed rapidly because of its characteristics of green environmental protection, high resource recovery rate, and practical ground pressure control [1–5]. Especially with the continuous extension of underground mining depth, the advantages of the filling mining method have become more pronounced [6–8]. The strength of cemented tailings backfill (CTB) is a key indicator of the filling mining technology since it is directly related to the safety of subsequent mining operations, and it is a source of worry for mining researchers [9–12]. Wen et al. [13] studied the factors that affect the strength of cemented backfill. The results show that the strength of cemented backfill is affected not only by single factors such as aggregate gradation, solid mass concentration, and cement content but also by the interaction of these factors. Mu et al. [14] studied the relationship between the strength of backfill and ultrasonic wave velocity and established a prediction model for the uniaxial compressive strength (UCS) of backfill based on the ultrasonic pulse velocity. Ercikdi et al. [15] show the linear relationship with a high correlation coefficient that appeared to exist between the UCS and ultrasonic pulse velocity UPV for CTB samples. Therefore, it is of great

significance to study the strength characteristics of the backfill and analyze the failure modes and failure laws at different stages to optimize backfill strength.

The CTB is a multiphase heterogeneous mixture with pores/cracks formed by mixing aggregate, cementing material, water, and solidifying after a certain curing age. It has complex mechanical properties. So it is necessary to study the damage and failure mode of backfill utilizing a new technology. At present, the scanning electron microscope (SEM) [16, 17], CT [18], UT (ultrasonic testing), and acoustic emission testing (AE) are used to study the internal failure mode of rock and soil specimens. When a material or structure is subjected to stress due to its microstructure's unevenness and defects, local stress concentration occurs, resulting in macroscopic manifestations such as plastic deformation, phase transformation, and cracking. In this process, a portion of the strain energy is released in a stress wave. This phenomenon of releasing strain energy in the form of an elastic stress wave is called acoustic emission (AE) [19], and the place where the wave occurs is called the acoustic emission source. AE testing technology uses sensors installed on the surface of materials to receive part of the stress waves transmitted to the surface to form a detection signal. Damage evaluation and research of materials can be realized through the detection, recording, and analysis of these signals [20, 21]. Cheng et al. [22] studied the influence of particle size on the mechanical properties of cemented backfill and obtained the strength of CTB and the characteristic parameters of AE. Sun et al. [23] studied the relationship between the AE signal and the failure of the backfill and constructed the constitutive damage model of the backfill. Zhao et al. [24] studied the relationship between AE event rate, ringing count rate, and stress-time through uniaxial compression and splitting failure tests. Cao et al. [25] investigated the compressive strength behavior and AE characteristics of 180-day cured CTB samples by using four different loading rates. The essential findings provided a scientific reference for studying the dynamic characteristics of CTB samples.

The results show that the AE parameters contain the damage information of the CTB and can describe the damage evolution process of the backfill. Still, the AE detection technique is not used to analyze the AE source.

Considering that wave velocity is also an important index for measuring rock mass failure [26], to comprehensively analyze the failure process of backfill mass, the mechanical properties of Wushan Copper Mine tailings are tested under uniaxial compression conditions. The AE technique analyzed the mechanical and AE characteristics of the backfill, and AE parameters characterized the failure mechanism of the backfill. On this basis, the method of time difference location is used to locate the AE source and verify the failure mechanism of the backfill.

2. Test Analysis

2.1. Basic Physical Properties of Tailings. The tailings used in the test were taken from the flotation workshop of the Wushan copper concentrator. Its density is 3.1 g/cm^3. Figure 1 shows the composition of grain size.

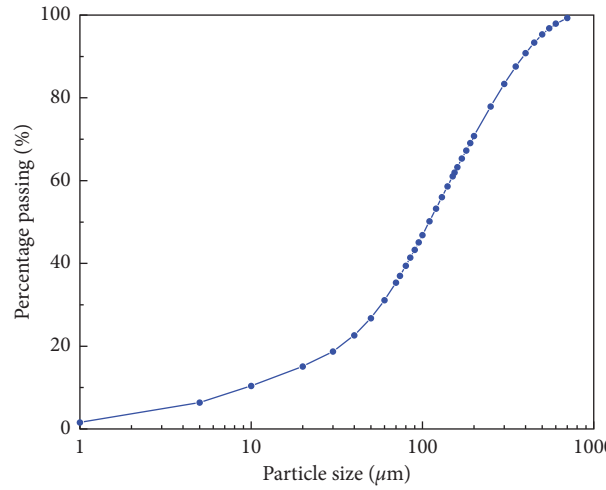

Figure 1: The particle size distribution of classified tailings.

The grain size distribution of the tailings determined as per relevant ASTM D422 is summarized in Figure 1. The grain size analysis shows the tailings contain 60% of the particles finer than 145.6 μm (d_{60}), 30% of the particles finer than 57.4 μm (d_{30}), and 10% of the particles are than 9.4 μm (d_{10}). The grain size analysis also shows it contains 37% of fine particles <74 μm and 22% of fine fractions <40 μm, which identifies the tailings as coarse sand. The calculated uneven coefficient, Cu is 15.54. As summarized in Figure 1, the grain size distribution curve slope is steep, and the curvature coefficient Cc is 2.4. The tailings particles are relatively uniform in size and are, however, poorly graded.

2.2. Sample Preparation. The cylindrical specimens were made according to the standard of ASTM D4832, and the dimensions were diameter × height: 55 mm × 110 mm. The specimen mass fraction is 74%, and the cement content is 20%. The prepared specimens were maintained in the YH-40B curing box with the curing parameters of 20°C, 95% humidity, and 28 days of age.

2.3. Sample Equipment and Method. The test instrument comprises an SLB100 press machine produced by Changchun Machinery and a PCI-2 AE system produced by PAC Company of the USA. Figure 2 shows the A.E. test system. The main shaft adopts displacement control in the experiment, and the loading rate is 0.003 mm/s. The PCI-2 AE system is connected to a computer, which can set, monitor, and store acoustic emission parameters and realize real-time control of AE signal collection. The AE probe contacts the specimen, and a preamplifier is connected between the probe and the acquisition card. The threshold value of the sensor signal acquisition is 45 dB.

In order to reduce the end restraint, two pieces of abrasive reducing paper are placed at both ends of the specimen, and a little butter is put between the two pieces of paper. Four AE probes are fixed on the surface of the CTB according to the space "cross" arrangement. Figure 3 shows the AE test method. The AE measurement point area is

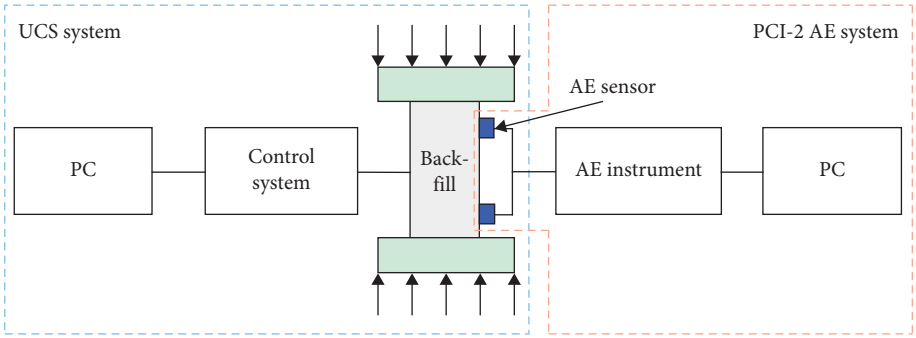

Figure 2: The logic diagram of the SLB100 loading machine and PCI-2 acoustic wave system.

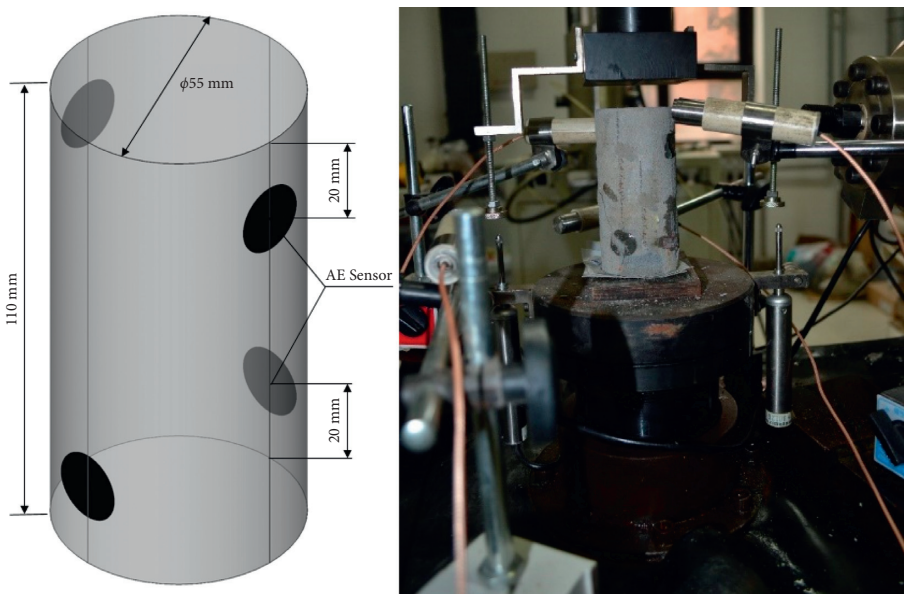

Figure 3: AE test method.

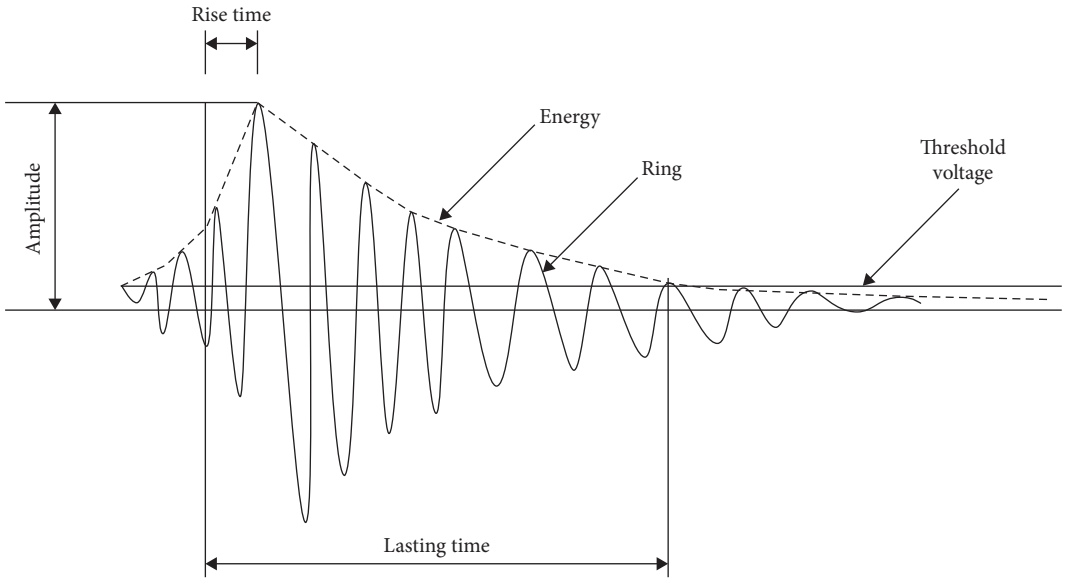

Figure 4: The diagram of acoustic emission characteristic parameters.

smoothed, and the smoothed area is 16 mm × 16 mm. After installing the radial displacement extensometer in the middle of the specimen, the SLB100 press completes the uniaxial loading. The control system and the AE detection system are used to collect the data in uniaxial compression until the loading is completed.

2.4. AE Characteristic Parameters. The CTB is an elasto-plastic material, and the stress wave will be released by the derivation and expansion of internal cracks during loading. The stress waves show different acoustic signals at different time intervals. An AE signal is a complex waveform containing a lot of information. Choosing the appropriate signal processing method to analyze acoustic emission signals is always a complex problem in developing AE detection technology. The characteristic parameter analysis is a standard method for AE signal analysis at present. The AE parameters commonly include impact (waveform) counting, ringing counting, energy, amplitude, lasting time, rise time, and threshold voltage. Figure 4 shows the specific meaning. The AE characteristic parameters are closely related to the signal of the same waveform; they appear or disappear simultaneously. Hence, they have similarities in describing the destruction mechanism of the specimen.

A hit is any signal that exceeds a threshold and causes a channel to acquire data. It reflects AE activities' total amount and frequency. The change in hit number demonstrates the transformation of the internal structure of the specimen. It can be used to characterize microcrack evolution [23, 27]. In this paper, the total number of AE hits per second (HPS) is adopted as the AE parameter for study. Energy is the area under the envelope of signal detection, reflecting the intensity of the signal, and is an important parameter indicating the material failure of the specimen, providing a basis for predicting the material instability failure.

3. AE Test Results and Analysis

In order to study the mechanical properties of backfill under uniaxial compression, the AE characteristic parameters such as HPS, cumulative HPS, energy rate, and energy were investigated. Considering that several groups of filling blocks' mechanical properties and AE characteristics are almost the same, only one group is selected as a type specimen for analysis.

According to the stress-time curve of the backfill under uniaxial compression in Figures 5–8, the UCS of the CTB is 3.58 MPa when the maximum compaction of the backfill is 8.5 KN. At the same time, the compression process of backfill can be divided into five stages, a–e: pore microfracture compacting stage (stage-a), linear elastic deformation stage (stage-b), yield deformation stage (stage-c), failure stage (stage-d), and residual stage (stage-e).

Stage-a: the stress-time curve of the backfill body is concave at the early stage of stress loading (0–53 s), and the number of hit times and energy rate in this stage are less. The cumulative HPS accounts for 2.4% of the total HPS number, and the energy accounts for 0.2% of the total energy. The results show that the AE activity is not active during stage-a, mainly because the CTB is artificially prepared and artificially stirred to ensure the excellent homogeneity and compactness of the filling body. There is less friction between the particles in the CTB during the compression process. There is no change in the appearance of the specimen.

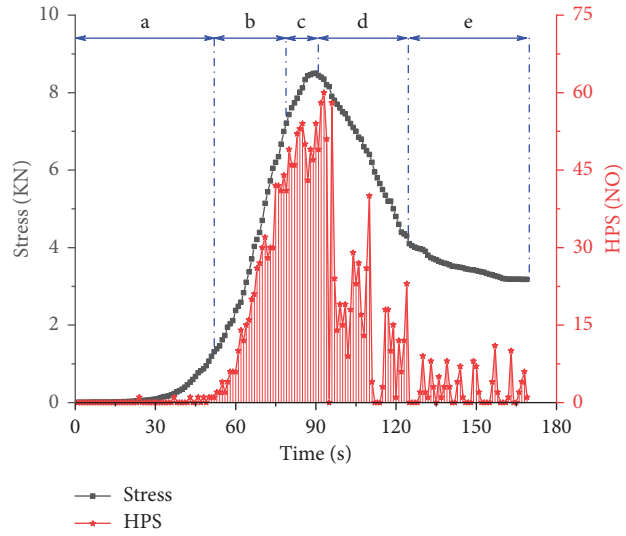

Figure 5: The stress-time curve and AE HPS-time curve of backfill under uniaxial compression.

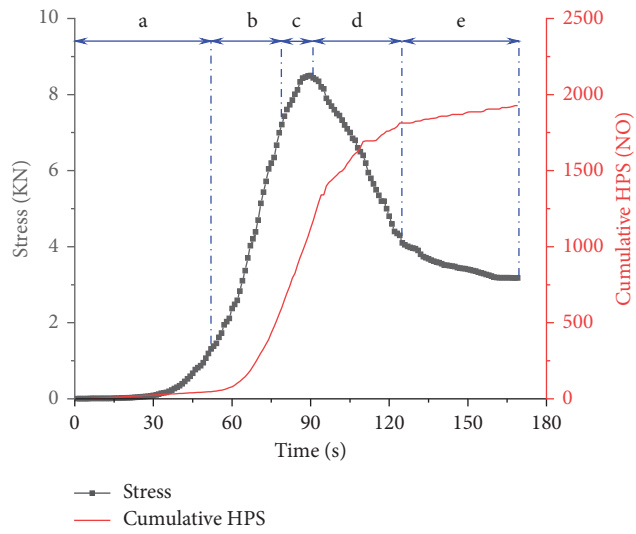

Figure 6: The stress-time curve and AE cumulative HPS-time curve of backfill under uniaxial compression.

Stage-b: with the increase of stress, in the 53 s–80 s period, the CTB enters the linear elastic stage, the loading curve is nearly straight, and the pressure is about 6.99 KN, reaching 82% of the maximum stress. At this stage, the pore/fractures in the backfill continue to compress, and microcracks begin to appear on the soft surface of the interior. The HPS and energy rate increase steadily. The cumulative HPS and energy rate account for 24.8% and 10.6%, respectively. From the

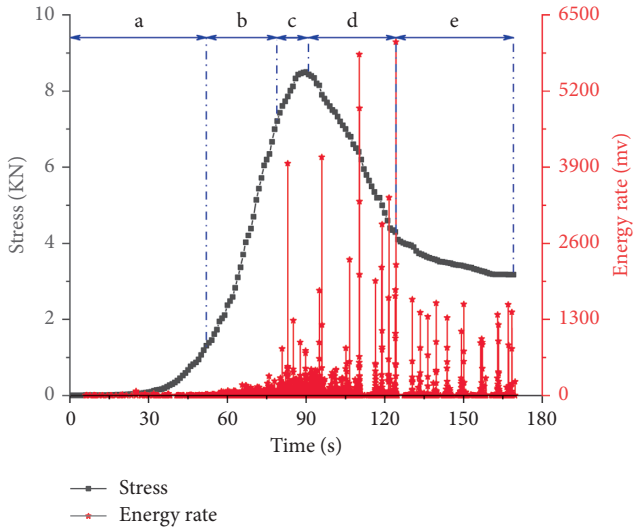

Figure 7: Stress-time curve and AE energy rate-time curve of backfill under uniaxial compression.

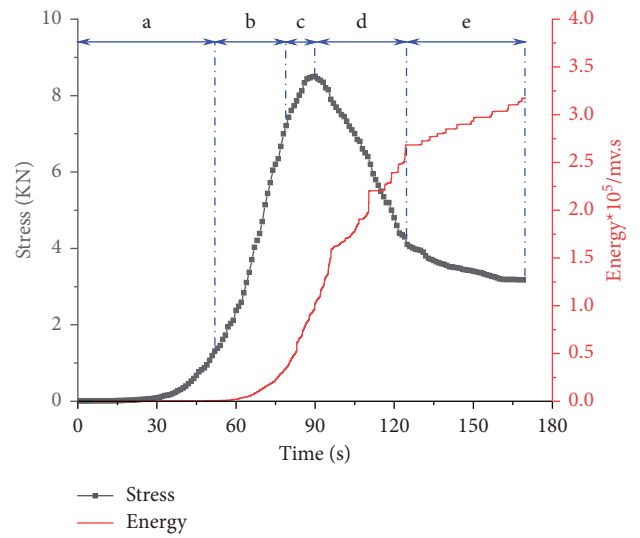

Figure 8: Stress-time curve and AE energy-time curve of under uniaxial compression.

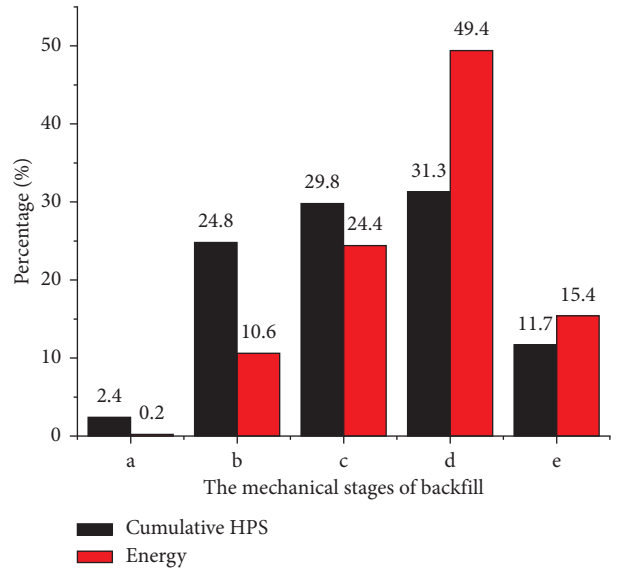

Figure 9: The proportion of A.E. signals in different stages.

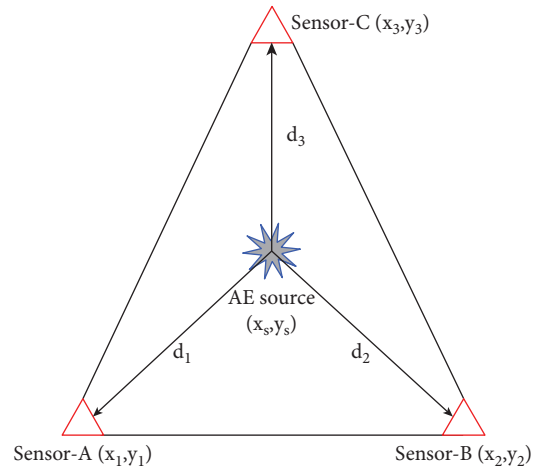

Figure 10: The schematic diagram of acoustic emission source positioning.

experimental process, there is no noticeable change in the macroscopic structure of the CTB, only a slight abscission at the end.

Stage-c: during the 80 s–91 s, the slope of the stress-time curve gradually decreases until it becomes zero, the loading stress reaches its peak value, the backfill enters the yield softening stage, and plastic deformation occurs. The microcracks will cause the stress adjustment of the stress frame after the grain bond fracture, which will lead to an increase in the stress near the grain and failure when the pressure near the grain reaches bond strength. The change in the stress transfer path and the weakening of the mechanical framework showed that the number of HPS increased sharply and approached the maximum value. The energy rate also increased obviously. There were two significant, abrupt changes, and the AE activity was active, indicating that pores/fractures in the CTB were accelerated. The accumulative HPS accounted for 29.8% of the total hits, and the accumulative energy rate accounted for 24.4% of the total energy. From the perspective of the test process, at this stage, the filling body began to show cracks on a macro scale, and the cracks continued to expand, gradually showing a certain penetration tendency.

Stage-d: during the period of 91 s to 125 s, after the loading stress reaches its peak value, the backfill body decays sharply, the pressure drops significantly, and the slope of the stress-time curve becomes negative. The number of HPS has been significantly reduced but is still relatively strong. It is mainly due to the continuous accumulation of internal damage as the cracks in the CTB expand and increase, finally

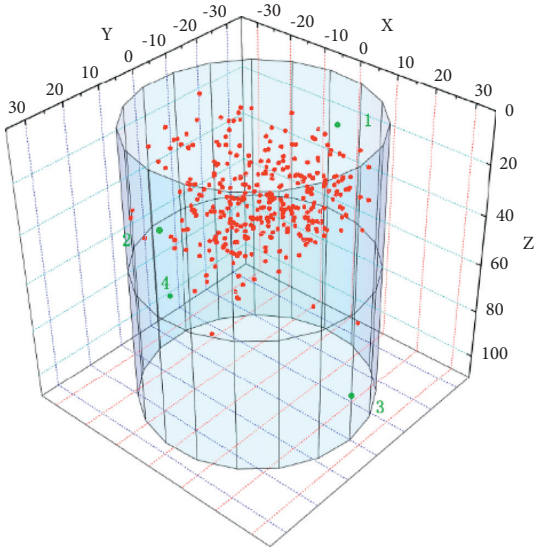

Figure 11: The result diagram of acoustic emission source location result diagram.

Figure 12: The final destruction diagram of the filling body.

forming a macroscopic fracture surface that affects the propagation of elastic waves inside the filling body, resulting in the AE signal being reduced. But the rupture of the backfill will produce many elastic waves, which will make the energy rate abrupt many times and reach the highest value. From the test process, the appearance of the CTB has apparent crack growth and bifurcation phenomena, and the small cracks gradually penetrate the large cracks, causing apparent damage.

Stage-e: during the 125 s to 170 s, the speed of stress reduction is slowed down. Because the filling body still has a specific bearing capacity, the stress is maintained at a lower level and does not decrease to zero. At this stage, the AE HPS in the backfill reduces significantly, and the accumulative hits increase slowly, almost no more. The AE energy rate is a small peak of abrupt change, mainly caused by the sound produced by the partial breakage and shedding of the filling body. In this stage, the accumulative HPS accounts for 11.7% of the total hits, and the accumulative energy rate accounts for 15.4% of the total energy. The filling specimen mainly shows the block sliding along the macroscopic fracture surface from the test process until failure.

Based on the above analysis, there are five mechanical stages in the failure process of backfill under uniaxial compression, and each stage has a different form. The AE signal also shows prominent stage characteristics, indicating that the AE characteristic parameters can reflect the CTB's internal failure evolution law.

Figure 9 shows the cumulative HPS and energy rate in different mechanical stages. In stage-d, the cumulative HPS is 31.3%, and the cumulative energy rate is 49.4%, all of which reach the maximum value. There are apparent crack propagation and bifurcation in the filling body. And many new cracks are produced simultaneously, which is the most active stage of AE activity. Therefore, it is verified that the characteristic emission parameters can characterize the evolution law of primary crack propagation and penetration in the filling body.

4. Exploration and Analysis of AE Source Location

4.1. Calculation Method for AE Source Location. AE source location is an essential work in the AE test, and it is also an important index in AE detection and evaluation. The main methods of location are time difference location and area location [28–30]. The time difference location is based on the time difference between the AE signals from the same AE source arriving at different sensors, combining the parameters such as wave velocity and the distance between sensors. [31]. Figure 10 shows the principle of source positioning in a two-dimensional plane. This paper studies the AE localization of the CTB under uniaxial compression using the time difference localization method.

For an AE hit, the absolute time of transmission to the sensor is t. The distance d between the sensor and the sound source can be calculated by combining the sound velocity v.

$$d = v * t. \tag{1}$$

According to Pythagorean's theory, the distances between two points in a plane are

$$\mathrm{d} = \sqrt{(x_2 - x_1)^2 + (y_2 - y_1)^2}. \tag{2}$$

Since the absolute time of an AE event cannot be obtained, in this paper, we calculate the absolute distance between different sensors and AE sources. That is

$$t_{\mathrm{i}} - t_1 = \frac{(d_i - d_1)}{v}. \tag{3}$$

From the available data from formulas (2) and (3), we get

$$t_i - t_1 = \frac{\left[\sqrt{(x_i - x_s)^2 + (y_i - y_s)^2} - \sqrt{(x_1 - x_s)^2 + (y_1 - y_s)^2}\right]}{v}. \tag{4}$$

In the equation, X_S and Y_S are the AE sources coordinate.

The location of the sound source can be obtained by obtaining multiple sensor data using formula (4) simultaneously. The mathematical method becomes more complicated when it extends to 3D or rolls up the envelope into a 3D object, but the basic principle remains the same.

The standard methods of time difference location are the least square method, Geiger linear location method, multievent location method, etc. [32]. This paper introduces multiple regression analysis to search for the most suitable location among all source location data.

Suppose the observed time difference between the two sensors receiving the hit signal is

$$\Delta t_{i,\mathrm{obs}} = t_i - t_1. \tag{5}$$

The calculated time difference between the two sensors that receive the impact signal is defined as follows:

$$\Delta \mathrm{t}_{i,\mathrm{cal}} = \frac{\left[\sqrt{(x_i - x_s)^2 + (y_i - y_s)^2 + (z_i - z_s)^2} - \sqrt{(x_1 - x_s)^2 + (y_1 - y_s)^2 + (z_1 - z_s)^2}\right]}{v}. \tag{6}$$

Multiple regression analysis is a general-purpose global objective algorithm that minimizes the difference between $\Delta t_{i,\mathrm{obs}}$ and $\Delta t_{i,c1c}$. Therefore, we define the sum of the squares of the difference $\Delta t_{i,\mathrm{obs}}$ and $\Delta t_{i,c1c}$ as χ^2. That is

$$\chi^2 = \sum\left(\Delta t_{i,\mathrm{obs}} - \Delta t_{i,\mathrm{cal}}\right)^2. \tag{7}$$

The χ^2 is called the fitness value, which depends on the coordinated value corresponding to the source location, and the calculation process is an iterative searching process. This article uses the simplex search method to write the locator code to find the minimum value of x_s, y_s, and z_s.

4.2. Results and Analysis of AE Source Location. In order to study the internal failure characteristics of the filling material, the experiment was based on the improved time difference location method to conduct AE localization analysis. Before carrying out the AE test, the average velocity of the sound wave in the CTB was measured at 1147.9 m/s. This indicates that the velocity of wave propagation in the CTB is very fast, and the time from one end to the other end is only 95.8 μs. Therefore, on the basis of fixed acoustic velocity, the AE test is carried out, and the location of the AE source is analyzed. The analysis results are shown in Figure 11. It can be seen that the AE source points are concentrated on the top of the specimen, and the cracks are interspersed and penetrated complicatedly. Through the analysis of internal and external location points, it is deduced that the failure mode of the specimen is mainly splitting failure, which is in good agreement with the actual collapse. It is shown that the improved method can be used to inverse the close relationship between the damage failure of the CTB and the generation and transfixion of internal cracks.

Compared with Figures 11 and 12, some edge cracks of the backfill specimen are not reflected in the process of sound source localization. There are two main reasons for the analysis. First, because of the anisotropy of the backfill material, the acoustic signal will scatter and attenuate in the process of propagation, especially after cracks occur in the specimen. It limits the propagation of AE signals in the CTB.

5. Conclusions

The density of tailings used in the experiment is 3.1 g/cm^3, and their particle size belongs to a discontinuous gradation. Based on the uniaxial compression test of CTB, the mechanical properties and AE characteristics of the whole compression process are analyzed. The main conclusions are as follows:

(1) The UCS of the CTB is 3.58 MPa when the mass fraction is 74%, the cement content is 20%, and the curing age is 28 days. The whole compression process of the backfill can be divided into five stages: the pore microfracture compacting stage, linear elastic deformation stage, yield deformation stage, failure stage, and residual stage.

(2) In the failure stage, the cumulative HPS is 31.3%, and the cumulative energy rate is 49.4%, all of which reach the maximum value. The filling body has apparent crack propagation, bifurcation, and many new cracks, which are the most active stages of AE activity.

(3) The multiple regression analysis methods are introduced in the time difference location method. The positioning results are concentrated on the top of the specimen, and the cracks are interspersed and penetrated complex, which is more consistent with the actual situation. However, some cracks are not reflected in the positioning results, mainly due to the anisotropic characteristics of the CTB material and the iterative calculation with a fixed sound wave velocity.

(4) The AE characteristic parameters can reveal the evolution of the original cracks in the CTB, which indicates that the AE technique is of great value in the analysis of the failure characteristics of the CTB.

Data Availability

The data used to support the findings of this study are available from the corresponding author upon request.

Conflicts of Interest

The authors declare that there are no conflicts of interest regarding the publication of this paper.

Acknowledgments

The authors would like to acknowledge the financial support from the National Key R&D plan Intergovernmental International Scientific and Technological Innovation Cooperation (Grant no. 2021YFE0102900), the Exploration fund of BGRIMM (no. 02-2127).

References

[1] A. Ghirian and M Fall, "Coupled thermo-hydro-mechanical-chemical behaviour of cemented paste backfill in column experiments. Part I: Physical, hydraulic and thermal processes and characteristics," *Engineering Geology*, vol. 164, pp. 195–207, 2013.

[2] A. X. Wu, Y Yang, H. Y. Cheng, and S. M. Chen, "Status and prospects of paste technology in China," *Chinese Journal of Engineering*, vol. 40, no. 5, pp. 517–525, 2018.

[3] Q.-L Zhang, Y.-T. Li, Q.-S. Chen, Y.-K. Liu, Y. Feng, and D.-L. Wang, "Effects of temperatures and pH values on rheological properties of cemented paste backfill," *Journal of Central South University*, vol. 28, no. 6, pp. 1707–1723, 2021.

[4] C. Q Chen, Y. B. Tao, Q. L. Zhang, and C. C. Qi, "The rheological, mechanical and heavy metal leaching properties of cemented paste backfill under the influence of anionic polyacrylamide," *Chemosphere*, vol. 286, Article ID 131630, 2022.

[5] C. X. Shi, L. J. Guo, and X. Z. Chen, "Experimental Study on the Law of flow and segregation of filing slurry in stope," *Gold Science and Technology*, vol. 26, no. 4, pp. 520–527, 2018.

[6] A. Wu, Z. Ruan, R. Bürger, S. Yin, J. Wang, and Y. Wang, "Optimization of flocculation and settling parameters of tailings slurry by response surface methodology," *Minerals Engineering*, vol. 156, Article ID 106488, 2020.

[7] D. S. Gu, "The development tendency of mining science and technology of underground metal mine," *Gold*, vol. 25, no. 1, pp. 18–22, 2004.

[8] W. G. Xiao, *Study on Filling Technology in Deep Mine*, Ph.D, Central South University, Changsha City,China, 2003.

[9] M. Fall, T. Belem, S. Samb, and M. Benzaazoua, "Experimental characterization of the stress-strain behaviour of cemented paste backfill in compression," *Journal of Materials Science*, vol. 42, no. 11, pp. 3914–3922, 2007.

[10] E. Yilmaz, T. Belem, and M. Benzaazoua, "Effects of curing and stress conditions on hydromechanical, geotechnical and geochemical properties of cemented paste backfill," *Engineering Geology*, vol. 168, pp. 23–37, 2014.

[11] Q. S. Chen, K. Luo, Y. M. Wang, X. Li, Q. Zhang, and Y Liu, "In-situ stabilization/solidification of lead/zinc mine tailings by cemented paste backfill modified with low-carbon bentonite alternative," *Journal of Materials Research and Technology*, vol. 17, 2022.

[12] P. Zhang, Q. Gao, Z. J. Wen, and T. Zhang, "Influencing factors on backfill strength and a combined strength prediction model," *Journal of Northeastern University*, vol. 42, no. 02, pp. 232–241, 2021.

[13] Z. J. Wen, B. Xiao, Q. Gao, and S. Yin, "Study on strength influencing factors and strength model of cemented backfill with mixed aggregate," *Arabian Journal of Geosciences*, vol. 14, no. 9, pp. 1–11, 2021.

[14] G. C. Mu, F. Deng, and Z. H. Lai, "Study on the relationship between strength and ultrasound velocity of cemented fill mass," *Industrial Minerals & Processing*, vol. 49, no. 10, pp. 1–3 + 53, 2020.

[15] B. Ercikdi, T. Yılmaz, and G. Külekci, "Strength and ultrasonic properties of cemented paste backfill," *Ultrasonics*, vol. 54, no. 1, pp. 195–204, 2014.

[16] C. E. Krohn and A. H. Thompson, "Fractal sandstone pores: automated measurements using scanning-electron-microscope images," *Physical Review B*, vol. 33, no. 9, pp. 6366–6374, 1986.

[17] A Timur, W. B. Hempkins, and R. M. Weinbrandt, "Scanning electron microscope study of pore systems in rocks," *Journal of Geophysical Research*, vol. 76, no. 20, pp. 4932–4948, 1971.

[18] R. A. Johns, J. S. Steude, L. M. Castanier, and P. V. Roberts, "Nondestructive measurements of fracture aperture in crystalline rock cores using X ray computed tomography," *Journal of Geophysical Research: Solid Earth*, vol. 98, pp. 1889–1900, 1993.

[19] D. Drozdenko, J. Bohlen, S. Yi, P. Minárik, F. Chmelík, and P. Dobroň, "Investigating a twinning-detwinning process in wrought Mg alloys by the acoustic emission technique," *Acta Materialia*, vol. 110, pp. 103–113, 2016.

[20] Z. Moradian, H. H. Ballivy, and B. Gerard, "Detection of cracking levels in brittle rocks by parametric analysis of the acoustic emission signals," *Rock Mechanics and Rock Engineering*, vol. 49, no. 3, pp. 785–800, 2016.

[21] Z.-Z. Zhang, F. Gao, and X.-J. Shang, "Rock burst proneness prediction by acoustic emission test during rock deformation," *Journal of Central South University*, vol. 21, no. 1, pp. 373–380, 2014.

[22] A. P. Cheng, F. S. Dong, P. F. Shu, and Z. X. Fu, "Mechanical properties and acoustic emission characteristics of continuous graded cemented backfill," *Journal of Huazhong University of Science and Technology (Nature Science Edition)*, vol. 49, no. 08, pp. 46–52, 2021.

[23] G. H. Sun, S. S. Wei, and X. X. Liu, "On the damage evolution of fillings based on acoustic emission characteristics," *Journal of Experimental Mechanics*, vol. 32, no. 01, pp. 137–144, 2017.

[24] K. Zhao, X. Yu, S. T. Zhu, Y. Zhou, Q. Wang, and J. Wang, "Acoustic emission investigation of cemented paste backfill prepared with tantalum–niobium tailings," *Construction and Building Materials*, vol. 237117523 pages, 2020.

[25] S. Cao, E. Yilmaz, W. Song, E. Yilmaz, and G. Xue, "Loading rate effect on uniaxial compressive strength behavior and acoustic emission properties of cemented tailings backfill," *Construction and Building Materials*, vol. 213, pp. 313–324, 2019.

[26] S. G. Wang, Y. R. Liu, X. Chen, and Q. Yang, "Failure analysis of pre-cracked specimen based on acoustic emission technique," *Journal of Hydroelectric Engineering*, vol. 38, no. 7, pp. 110–120, 2019.

[27] A. Y. Cao, G. C. Jing, L. M. Dou et al., "Damage evolution law based on acoustic emission of sandy mudstone under different uniaxial loading rate," *Journal of Mining & Safety Engineering*, vol. 32, no. 6, pp. 923–928 + 935, 2015.

[28] L. Geiger, *Probability Method for the Determination of Earthquake Epicenters from the Arrival Time Only*, pp. 60–71, Bulletin of Saint Louis University, Missouri, USA, 1912.

[29] J. A. Nelder and R. Mead, "A simplex method for function minimization," *The Computer Journal*, vol. 7, no. 4, pp. 308–313, 1965.

[30] M. S. Sambridge and B. L. N. Kennett, "A novel method of hypocentre location," *Geophysical Journal International*, vol. 87, no. 2, pp. 679–697, 1986.

[31] A. Tobias, "Acoustic-emission source location in two dimensions by an array of three sensors," *Non-destructive testing*, vol. 9, no. 1, pp. 9–12, 1976.

[32] C. Fu, *Research on Source Location Methods of Acoustic Emission Based on Material of Rock*, Ph.D. thesis, Northeastern University, Shenyang City,China, 2015.